The University Of Sheffield.

# The Crystallisation and Aqueous Durability of Borosilicate Nuclear Waste Glasses

**Peter Bramwell Rose**

A thesis submitted in partial fulfilment of the requirements

for the degree of Doctor of Philosophy

September, 2007

Immobilisation Science Laboratory

Department of Engineering Materials

University of Sheffield

# Abstract

Two simulated (non-radioactive) borosilicate high-level waste (HLW) glasses were supplied by Nexia Solutions; Blend glass and Oxide glass. This work is primarily concerned with identifying the crystal phases present in both as-cast and heat treated (simulating the retarded cooling experienced by 'real' (radioactive) borosilicate HLW glasses after pouring) samples of these two glasses; as well as determining the aqueous durability of these samples. An as-cast Oxide glass sample contained a 'yellow phase' inclusion which was also investigated.

Combined direct current plasma atomic emission spectroscopy (DCP-AES) and X-ray fluorescence spectroscopy (XRF) determined the chemical composition of both glasses. Differential thermal analysis (DTA) identified their glass transition temperatures, whilst Archimedes' principle yielded their densities.

X-ray powder diffraction (XRD), scanning electron microscopy (SEM) and transmission electron microscopy (TEM) identified crystal phases and, in the case of microscopy, determined microstructural homogeneity. As-cast Blend glass samples were compositionally homogeneous and contained $RuO_2$ crystals. Heat treated Blend glass samples contained $Ce_{1-(x+y)}Zr_xGd_yO_{2-(y/2)}$, (Sr,Nd,La) molybdate and lanthanide (Nd,Gd,La,Ce) silicate crystals. As-cast Oxide glass samples were either compositionally homogeneous (Type I microstructure) or compositionally inhomogeneous (Type II microstructure). $RuO_2$, metallic Pd-Te and $(Cr,Fe,Ni)_3O_4$ crystals were observed in both Type I and Type II microstructures, with $Na_3Li(MoO_4)_2 \cdot 6H_2O$ crystals occasionally detected. $Zr_{1-(x+y)}Ce_xGd_yO_{2-(y/2)}$ and lanthanide (Nd,Gd,La,Ce) silicate crystals were only detected in Type II microstructures. Heat treated Oxide glass samples displayed either: extensive crystallisation and matrix cracking (Type A microstructure) or 'banded' crystallisation (Type B microstructure), depending on their parent (as-cast) microstructure (Type I or Type II respectively). $(Na,Sr,Nd,La)MoO_4$, $Ce_{1-(x+y)}Zr_xGd_yO_{2-(y/2)}$ and a Ni-rich crystal phase were detected in both Type A and Type B microstructures. $\alpha$-cristobalite crystals were found exclusively in Type A microstructures, whilst lanthanide (Nd,Gd,La,Ce) silicate and zektzerite crystals were only detected in Type B microstructures.

A modified product consistency test (modified PCT-B) determined the aqueous durability of as-cast and heat treated samples of both glasses. Heat treatment of Blend glass improved its aqueous durability marginally. Heat treatment of Oxide glass

decreased its aqueous durability significantly (as-cast and heat treated Oxide glass samples had Type I and Type A microstructures respectively).

Combined DCP-AES and XRF revealed the chemical composition of the 'yellow phase' inclusion, showing it to be enriched in Mo, Cs, Na, Li, Cr, Ba, Sr and Te compared to Oxide glass. XRD identified the 'yellow phase' inclusion as crystalline, containing $CsLiMoO_4$, $Na_3Li(MoO_4)_2 \cdot 6H_2O$, $(Na,Sr,Nd)MoO_4$ and $Ba_{1-x}Sr_xMoO_4$ (where $0 < x < 0.5$) crystals.

# Acknowledgements

I would like to thank my supervisors Prof. William E. (Bill) Lee, Dr Michael I. Ojovan and Dr Neil C. Hyatt for their guidance, expertise and patience. This thesis has benefited greatly from their input. I would also like to thank the late Prof. Peter F. James for getting me to seriously consider postgraduate research and Prof. John H. Sharp who listened and helped when it mattered. My industrial advisors Charlie R. Scales, Dr Ewan R. Maddrell, Dr Ivan F. Owens and Colin C. Ramshaw supplied glass samples and suggestions. Dr Diane Holland and Dr Russell J. Hand are thanked for taking time out of their busy schedules to act as my thesis examiners and for an interesting and enjoyable viva.

This thesis and I are indebted to Prof. Ian L. Pegg and the Vitreous State Laboratory (VSL) at the Catholic University of America (CUA), Washington, DC. I visited the VSL for 10 weeks during summer 2004 thanks to Prof. Pegg and was allowed full use of the VSL facilities; the compositional and durability data reported herein were generated during the visit. Without the kindness and generosity shown to me by Prof. Pegg and all of the students and staff at the VSL this thesis would not exist. In addition to Prof. Pegg I would like to thank: Dr Chu-Fen Feng for her expert assistance with the modified PCT-B experiments and friendliness; Dr Shan-Tao Lai for demonstrating PCT calculations; Dr Tevfik Bardakci for the use of his office; Dr Charles Viragh for heat capacity and DTA measurements as well as interesting conversations; Dr Isabelle S. Muller for inviting me to the Wolf Trap as well as PCT calculation advice; Kim Klatt for taking me under her wing and introducing me to everybody at the VSL; Dr Keith S. Matlack for allowing me use of the DCP-AES; Su Li, Xiaojin Shi and Yuexia Liu for DCP operation; Rich Cecil for XRF analyses and Aqua Teen Hunger Force appreciation; Erik for viscosity measurements; Dr Hao Gan for help interpreting viscosity data; Caroline Boice for microwave dissolutions and taking me around DC; Dr Weiliang Gong for aiding normalisation of chemical composition data; Kris Smith for hardware and software support in addition to lifts in his car; Nick, Mark, Prof. Pedro B. (Pete) Macedo and Shannon for being fun lunchtime acquaintances; JB, Derek, Igor, Jasbir (Jesse) Singh and Spooner Underwood in the basement level for all their help; Carol Matlack, Meghan Touey and Briana Zakszeski for excellent secretarial assistance; everybody I have forgotten to mention, and finally apologies to Dr Wing K. Kot for destroying his graphite mould. My visit was

immensely enriched by my Millennium North flatmates Bill Brammell and Mitch Yelverton, and latterly by my Capitol Hill flatmate Jen Carrier.

I would like to thank all of the students and staff at the Department of Engineering Materials who have helped me during my time in Sheffield. In particular I would like to thank: Ian Watts and Dean Haylock for glass melting, heat treatments, good humour and generally being the foundations upon which the Department is built; Dr Heath Bagshaw who taught me SEM and TEM operation, as well as sample preparation; Dr David I. Woodward who operated the Tecnai for me and helped immeasurably in the interpretation of electron diffraction patterns; Dawn Bussey who also taught me SEM operation; Dr Peter Korgul for working late so the SEM could be used out of hours; Brian Keeley and Dr Nik Reeves for teaching me how to operate the XRDs; Dr Rick J. Short for measuring the density of glass samples; Phil Staton and Barbara Horsfield for providing excellent help with sample preparation and student practical classes; Bev Lane for DTA measurements; Mel Carter for assistance in student practical classes, Dr Sean D. McLoughlin for glass durability discussions, and Karen Burton for secretarial assistance and all-round helpfulness. Judith K. Watson of the Graduate Research Office is thanked for not kicking me out of the University.

I am grateful to the Engineering and Physical Sciences Research Council (EPSRC) and Nexia Solutions (formerly BNFL) for an industrial CASE studentship. I would also like to express my gratitude to the Sheffield Metallurgical and Engineering Association (SMEA) 2004 Travel Awards, the Tom Jackson Travel Fund, the Laverick-Webster Hewitt Travelling Fellowship, and the Gauntlet Trust of the Armourers & Brasiers' Company and British Alcan Aluminium for their generous financial assistance with my visit to the VSL.

Most of all I would like to thank my parents for everything.

# Contents

# 1 Introduction

In the UK, approximately 20 % of the electricity supply is generated by nuclear power. However, many of the nuclear power stations supplying this electricity will be decommissioned in the near future, meaning an imminent UK electricity shortfall. Concern about global warming and the rising cost of fossil fuels has made building new nuclear power stations an increasingly attractive solution to the imminent shortfall. Although nuclear power stations do not emit $CO_2$ during electricity production, their operation results in spent fuel which is highly radioactive, heat generating and extremely harmful to life. In the UK, spent nuclear fuel is reprocessed to recover uranium and plutonium, the remaining solution being regarded as waste. The liquid waste arising from reprocessing is termed high-level waste (HLW) due to the level of radioactivity and heat it generates. Liquid HLW is currently immobilised by vitrification in a borosilicate glass matrix. This provides a material suitable for storage and eventual disposal, envisioned to be in an underground repository located within a stable geological formation.

During vitrification, some HLW components have limited solubilities in the borosilicate glass melt, typically platinoids (Ru, Pd and Rh), high valence cations (*e.g.* $Mo^{6+}$, $S^{6+}$ and $Cr^{6+}$) and refractory oxides (*e.g.* $Al_2O_3$ and $Fe_2O_3$). These components of limited solubility typically form crystal phases within the glass. Due to the radiogenic heat produced by decaying radionuclides in the glass it will experience retarded cooling from its melting temperature. This retarded cooling can lead to further crystal phases precipitating in the glass. In an underground repository, borosilicate HLW glasses will eventually contact groundwaters. The aqueous durability of these glasses will determine their ability to retain their radionuclide inventory. Therefore the aqueous durability of the crystal phases formed and the effect of their formation on the aqueous durability of the residual glass matrix are highly significant. Further to this, the partitioning of HLW radionuclides between the crystal phases and the residual glass matrix is of great importance.

This work concerns two simulated (non-radioactive) borosilicate HLW glasses produced on full-scale vitrification lines at Sellafield, Cumbria. The aims of this work were to:

- Identify the crystal phases present in both as-cast glasses, as well as determining which radionuclides may preferentially partition to them in 'real' (radioactive) borosilicate HLW glasses.
- Identify the crystal phases which develop after heat treating both as-cast glasses (simulating the retarded cooling experienced by radiogenically heated glasses) and to determine which radionuclides may preferentially partition to these crystal phases in 'real' borosilicate HLW glasses.
- Assess the aqueous durability of both glasses in their as-cast and heat treated states. Thus, the effect of retarded cooling (as would be experienced by 'real' borosilicate HLW glasses) upon these glasses can be understood. Also, to determine the aqueous solubility of identified crystal phases by examination of glass samples after aqueous durability testing.

# 2 Literature Review

## 2.1 Discovery of Radioactivity and Neutron-Induced Fission

Radioactivity was discovered in 1896 by Henri Becquerel as a result of experiments to determine if there was a connection between X-rays (discovered by Wilhelm Röntgen) and naturally-occurring phosphorescence. Becquerel showed that uranium emitted radiation which: (1) caused gases to ionise and (2) could be deflected by electric or magnetic fields (unlike X-rays). Marie and Pierre Curie continued the work on uranium in their Paris laboratory, discovering two new 'active' elements, polonium and radium (from which the term 'radioactive' was coined) (Palmer, 1995). In 1938 Lise Meitner and Otto Frisch interpreted the experimental results of Otto Hahn and Fritz Strassmann (who were attempting to produce transuranic elements), concluding that neutron-induced fission of the uranium nuclei had occurred. Inspired by the possibility of emission of secondary neutrons, and thus a chain reaction, Enrico Fermi and his team created the world's first man-made nuclear reactor in 1942 – Chicago Pile 1 (nuclear reactors were originally known as 'atomic piles') (Greenwood and Earnshaw, 2002). This reactor produced the world's first controlled nuclear chain reaction, its creation being part of the Manhattan Project. The ultimate goal of this project was the production of fission weaponry, realised on the 16$^{th}$ July, 1945 with the Trinity test explosion.

## 2.2 Neutron-Induced Fission and Nuclear Power Generation

For neutron-induced fission to occur, a nucleus of large mass (generally $^{235}U$) captures a neutron (n), then 'fissions' into two smaller nuclei (fission products, FP) and releases either two or three neutrons (on average 2.4 for $^{235}U$) as well as releasing energy:

$$^{235}U + n \rightarrow {}^{236}U \rightarrow 2FP + 2.4n + \text{energy} \qquad (2.1)$$

The released neutrons can induce fission in further suitable nuclei, creating a self-propagating chain reaction (an adjustable neutron absorber is used to control the chain reaction) which is the basis of nuclear reactors. However, the 'fast' neutrons produced during fission (with kinetic energies around 1 MeV) are not very effective at producing fission in further suitable nuclei, so in the majority of nuclear reactors they are slowed-down (moderated) to 'thermal' (or 'slow') neutrons (with similar kinetic energies to the molecules in a room temperature gas; approximately 0.025–1 eV). The majority of nuclear reactors operate using $^{235}U$ fuel. The concentration of $^{235}U$ in natural uranium (0.72 %) is sufficient to sustain a chain reaction although enrichment of uranium fuel is often advantageous due to absorption of neutrons by the fuel cladding and/or moderator. After fission, the fission products collide with neighbouring atoms, converting their kinetic energy into heat. This thermal energy is the basis of nuclear power generation, with the reactor coolant acting as heat-transfer medium.

Nuclear reactors fall into one of two types; fast reactors or thermal reactors. Fast reactors do not moderate (slow) the neutrons released by fission, aiming to 'breed' fissile material as well as produce electricity. In contrast, thermal reactors moderate the neutrons released by fission and can be divided into two groups; gas-cooled and water-cooled. Fast-breeder reactors generally employ a $^{239}Pu$-enriched core surrounded by $^{238}U$ which can 'breed' $^{239}Pu$ by neutron-capture and two subsequent $\beta$-decays. This reactor type is typically cooled by liquid metal (Na and/or K). Gas-cooled reactors are cooled by pressurised $CO_2$ or He gas and are graphite moderated. Water-cooled reactors are cooled and moderated by pressurised $H_2O$ and/or $D_2O$. Nuclear power stations (**Table 2.1**) currently generate approximately 20 % of the UK's electricity supply (Nirex, 2002).

**Table 2.1** Nuclear reactor types currently operating in the UK.

| Reactor type | Coolant | Moderator | Fuel | | |
|---|---|---|---|---|---|
| | | | Type | Cladding | $^{235}U/\sum U$ |
| Magnox | Pressurised $CO_2$ | Graphite | U metal rods | Mg alloy | 0.72 % |
| AGR (advanced gas-cooled reactor) | Pressurised $CO_2$ | Graphite | $UO_2$ pellets | Stainless steel | ~3 % |
| PWR (pressurised-water reactor) | Pressurised $H_2O$ | Pressurised $H_2O$ | $UO_2$ pellets | Zr alloy | ~3 % |

With time, the fuel assemblies in these reactors acquire increased levels of fission products, some of which act as neutron poisons, reducing energy production to an uneconomic level. Therefore, after around 3 y in the reactor, spent fuel assemblies are

replaced and sent for storage in a cooling pond as they are highly radioactive and heat-generating.

## 2.3 Reprocessing of Spent Nuclear Fuel

In the UK, spent fuel is reprocessed using the plutonium and uranium recovery by extraction (PUREX) process. The two operational reprocessing plants at Sellafield, Cumbria, are B205 (for spent U metal fuel) and THORP (thermal oxide reprocessing plant, for spent $UO_2$ fuel). Prior to reprocessing, the fuel rods have their cladding mechanically removed. The spent fuel is then dissolved in 6 mol $l^{-1}$ nitric acid before the U and Pu are extracted with tributyl phosphate in kerosene (Marples, 1988). The remaining solution is regarded as waste, as are the undissolved metallic 'fines'.

### 2.3.1 Classification of Radioactive Wastes

In the UK, radioactive wastes are classified as one of four types (Nirex, 2002): very low-level wastes (VLLW), low-level wastes (LLW), intermediate-level wastes (ILW) and high-level wastes (HLW). VLLW can be disposed of with ordinary refuse, each 0.1 $m^3$ of material containing less than 400 kBq ($\beta$ and $\gamma$ activities) or single items containing less than 40 kBq. LLW is not suitable for disposal with ordinary refuse, with a typical maximum activity of $4 \times 10^9$ Bq tonne$^{-1}$ ($\alpha$ activity) and $12 \times 10^9$ Bq tonne$^{-1}$ ($\beta$ and $\gamma$ activities). ILW exceeds the upper boundaries for LLW, requiring shielding but not cooling. It typically has a maximum activity of $2 \times 10^{12}$ Bq $m^{-3}$ ($\alpha$ activity) and $2 \times 10^{14}$ Bq $m^{-3}$ ($\beta$ and $\gamma$ activities). HLW requires both shielding and cooling, with maximum activities in the region of $4 \times 10^{14}$ Bq $m^{-3}$ ($\alpha$ activity) and $8 \times 10^{16}$ Bq $m^{-3}$ ($\beta$ and $\gamma$ activities) (Hewitt, 2001). The liquid waste arising from reprocessing is termed HLW due to its level of radioactivity and heat generation.

### 2.3.2 Chemical Composition of HLWs from Reprocessing

The majority of the HLW arising from spent nuclear fuel reprocessing is comprised of fission products. These include every element in the Periodic Table from Ge to Gd, together with tritium. Relative concentrations depend on the type of fuel, the type of reactor, the fuel's burn-up (Donald *et al.*, 1997; Larkin, 1986; Marples, 1988) and the

cooling time of the fuel assemblies after removal from the reactor (Roth and Weisenburger, 2000). **Figure 2.1** shows the fission product yield for both 'thermal' and 'fast' neutron-induced fission of $^{235}U$. The chemical composition of the fission product portion of calcined Magnox (U metal) fuel reprocessing waste can be seen in **Table 2.2.**

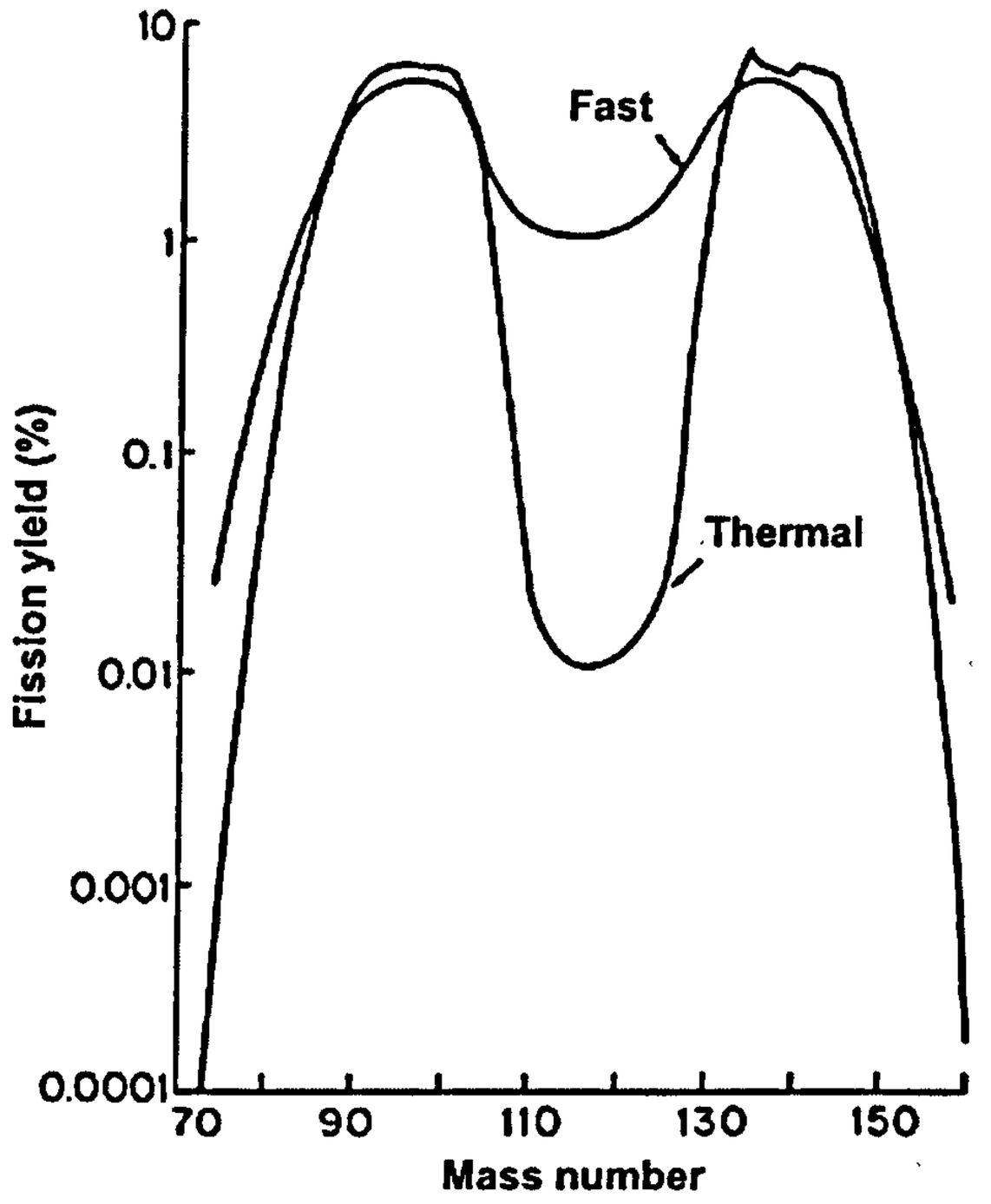


**Figure 2.1** Fission product yield for both 'thermal' and 'fast' neutron-induced fission of $^{235}U$ (adapted from Clarke, 1983).

**Table 2.2** Chemical composition of the fission product portion of calcined Magnox (U metal) fuel reprocessing waste (Marples, 1988). Total added for information only.

| Component | Weight % | Component | Weight % | Component | Weight % |
|---|---|---|---|---|---|
| $MoO_3$ | 14.4 | $Pr_6O_{11}$ | 4.0 | $Rb_2O$ | 1.1 |
| $ZrO_2$ | 13.9 | $Tc_2O_7$ | 3.8 | $Pm_2O_3$ | 0.5 |
| $Nd_2O_3$ | 13.1 | PdO | 3.3 | $Eu_2O_3$ | 0.3 |
| $Cs_2O$ | 9.4 | SrO | 2.9 | $Sb_2O_5$ | 0.2 |
| $CeO_2$ | 8.5 | $Sm_2O_3$ | 2.6 | $Ag_2O$ | 0.1 |
| $RuO_2$ | 7.8 | $Rh_2O_3$ | 2.2 | $Gd_2O_3$ | 0.1 |
| BaO | 4.6 | $Y_2O_3$ | 1.7 | $In_2O_3$ | 0.1 |
| $La_2O_3$ | 4.2 | $TeO_2$ | 1.6 | **Total** | **100.4** |

Other waste components are: unextracted U and Pu; transuranic elements (primarily Np, Am and Cm); fuel additives (such as Fe, Al, Si and Mo); stainless steel corrosion

products (principally Fe, Cr and Ni); contamination from fuel cladding (*e.g.* Mg in Magnox waste); chemical reprocessing additives (older waste streams); soluble poisons (mainly Gd and/or B to avoid criticality) and organic impurities (from the U and Pu extraction stage) (Larkin, 1986).

Initially, the majority of the radioactivity and heat generated by the liquid HLW is due to $^{137}Cs$ and $^{90}Sr$. These (and other) fission products are the major radiological hazard for the first few hundred years, after this period the actinides (Am, Cm, Np, Pu) and $^{99}Tc$ are the major radiological hazard (Clarke, 1983; Donald *et al.*, 1997; Marples, 1988). Thus, it is necessary to isolate HLW from the biosphere for thousands to millions of years. The radioactive half-life ($t_{1/2}$) of individual radionuclides will be categorised as either short-lived ($t_{1/2} \leq ^{137}Cs \approx 30$ y) or long-lived ($t_{1/2} > ^{137}Cs$) in this work.

### 2.3.3 Liquid HLW Storage

The liquid HLW produced from reprocessing is a 6 mol $l^{-1}$ nitric acid solution producing a few kW $m^{-3}$ of heat (depending on its age), as well as high levels of radioactivity. Referred to as highly active liquor (HAL) or raffinate, the solution is stored in double-walled stainless steel tanks which are cooled, air agitated (to avoid sedimentation) and surrounded with thick concrete (as a radiation shield). They are expensive to build and require continuous surveillance (Marples, 1988). The dangers of long-term HAL storage are highlighted by the many leaks which have occurred at the Hanford site in the US, where $^{137}Cs$ and other radionuclides have leaked from their tanks into the ground below (McKinley *et al.*, 2001). However, these tanks are only single-walled and are not made from stainless steel (unlike UK HAL tanks). Thus, it is thought better to solidify the HAL in a physically and chemically durable form which is easier and safer to store, as well as providing a material suitable for eventual disposal (Marples, 1988).

### 2.3.4 Solidified HLW Disposal

The eventual disposal of solidified HLW is envisioned to be in an engineered repository located deep underground within a stable geological formation (IAEA, 2003). Three types of geology have been considered for the location of an underground repository for solidified HLW: salt, clay and igneous rock (granite, basalt or tuff).

Permanent disposal of solidified HLW in an underground repository will be as part of a multibarrier isolation system (Donald *et al.*, 1997; Marples, 1988; Wicks, 1986, 1992). In a multibarrier isolation system, the solidified HLW is contained inside its storage/disposal canisters, which in turn are encased in an 'overpack'. This package is surrounded by 'backfill' within the underground repository. The 'overpack' could consist of either: (1) a thin casing of extremely corrosion resistant material (*e.g.* Ti) or (2) a thicker casing of an iron alloy (*e.g.* cast iron or carbon steel) which would corrode at a slow, predictable rate. The 'backfill' could be either: (1) a clay (*e.g.* bentonite) which swells after emplacement and has a low permeability to water or (2) a cementitious material which will condition the groundwater to a high pH, reducing corrosion of the iron overpack (Donald *et al.*, 1997; Marples, 1988). The man-made, engineered barriers of the multibarrier isolation system are known as the 'near-field', whilst the surrounding geology (the geosphere) is known as the 'far-field' (Marples, 1988).

## 2.4 HLW Vitrification in Borosilicate Glass

The vitrification of UK HLW in a borosilicate glass matrix was selected as a suitable wasteform for storage/disposal due to a number of reasons (Larkin, 1986; Marples, 1988): (1) its ability to incorporate relatively high amounts of the elements present in calcined HLW (typically up to 25 wt% waste oxides); (2) relatively low formation temperature; (3) tolerance to variations in the waste composition; (4) reasonable chemical durability; (5) the radiation stability of the glass structure; (6) ability to accommodate the changes in chemical properties resulting from transmutation (*e.g.* Cs to Ba and Sr to Zr); (7) thermal stability (low levels of crystallisation during cooling); (8) mechanical stability; (9) sufficient reactivity to digest the calcined HLW within the process residence time and (10) relatively simple processing (for remote operation).

### 2.4.1 Borosilicate HLW Glass: Chemistry and Structure

The base glass for the vitrification of UK HLW is a $Li_2O$-$Na_2O$-$B_2O_3$-$SiO_2$ composition.

According to the Zachariasen-Warren model of glass structure, the network forming polyhedra (*e.g.* $[Si\emptyset_4]$, $[B\emptyset_3]$, $[B\emptyset_4]^-$, $[Si\emptyset_3O]^-$) of alkali borosilicate HLW glasses will corner share oxygens (bridging oxygens, BO, shown as Ø) to create a random network structure in which network modifiers (Li, Na and most HLW

components) will occupy interstices within the random network structure (which tends to form rings) as well as charge balancing singly-bonded oxygen atoms (non-bridging oxygens, NBO). Intermediates (such as Al and Fe) can behave as network formers and/or modifiers. The network forming polyhedra $[AlØ_4]^-$ and $[FeØ_4]^-$ (as well as $[BØ_4]^-$) are charge compensated by network modifiers (Shelby, 1997; Wicks, 1992). Both the base glass and the HLW components become part of the random network structure. The Zachariasen-Warren model leads us to believe that borosilicate HLW glasses are relatively homogeneous at the atomic level. However, based on extended X-ray absorption fine structure (EXAFS) data, Greaves (1985) has proposed a modification to the Zachariasen-Warren model whereby network formers and network modifiers are segregated into two interlacing sublattices (the network modifiers cluster together), noting that above a certain network modifier concentration threshold the inter-network (network modifier) regions would form continuous channels (percolation channels).

Further to this more inhomogeneous view of glass structure, neutron diffraction data (Fábián *et al.*, 2007), nuclear magnetic resonance (NMR) data (Bourcier, 1994; Du and Stebbins, 2003) and molecular dynamics (MD) simulations (Gou *et al.*, 2001) have all indicated demixing (non-random distribution) of the borate and silicate network units in 'traditionally' homogeneous borosilicate glasses, with the network modifier(s) preferentially associated with the borate regions (Bourcier, 1994; Gou *et al.*, 2001 and references therein). In support of these results, chemical durability testing of some 'traditionally' homogeneous sodium borosilicate glasses showed that all of the sodium and boron in these glasses could be leached out (due to them forming a percolating network inside the glass), leaving a porous network of vitreous silica (pore diameter 4–6 nm) (Ledieu *et al.*, 2004). The above observations could explain why a 'traditionally' homogeneous borosilicate HLW glass was shown by neutron diffraction (Sinclair *et al.*, 1983) to be inhomogeneous at the nm scale. These findings are perhaps unsurprising since there is unambiguous thermodynamic evidence that like chemical groupings tend to cluster (Wright *et al.*, 2001 and references therein), with amorphous phase separation (APS) representing the limiting case of such clustering. Ojovan *et al.* (2005) found an increased concentration of Mo and Na at the surface of a cast borosilicate HLW glass compared to its bulk, further illustrating that glass components can be inhomogeneously distributed. Some components in multicomponent borosilicate glasses can form oxyanions (**Table 2.3**) which are independent of the borosilicate glass network, located

within inter-network regions together with (charge compensating) network modifying cations.

**Table 2.3** Oxyanions reported in multicomponent borosilicate glasses.

| Oxyanion | Reference(s) |
|---|---|
| Molybdate, $[MoO_4]^{2-}$ | (Calas *et al.*, 2003; Short, 2004; Short *et al.*, 2005) |
| Sulphate, $[SO_4]^{2-}$ | (McKeown *et al.*, 2001, 2004) |
| Chromate, $[CrO_4]^{2-}$ | (Tilquin *et al.*, 1998) |
| Orthophosphate, $[PO_4]^{3-}$ | (Muñoz *et al.*, 2006) |
| Pyrophosphate, $[P_2O_7]^{4-}$ | (Muñoz *et al.*, 2006) |
| Pertechnetate, $[TcO_4]^-$ | (Lukens *et al.*, 2004, 2007) |
| Perrhenate, $[ReO_4]^-$ | (Lukens *et al.*, 2007) |

### 2.4.2 Chemical Composition of Borosilicate HLW Glasses

The UK currently produces two 'real' (radioactive) borosilicate HLW glasses. One vitrifies Magnox (U metal) fuel reprocessing waste (Magnox glass); whilst the other vitrifies oxide ($UO_2$) fuel reprocessing waste and Magnox (U metal) fuel reprocessing waste mixed in a 75:25 oxides ratio, by weight (Blend glass). Simulated (non-radioactive) versions of both Magnox glass and Blend glass have been produced, along with other simulated borosilicate HLW glass compositions, such as one vitrifying simulated oxide ($UO_2$) fuel reprocessing waste (Oxide glass). The chemical composition of a simulated Blend glass (Line 3), a simulated Magnox glass (V26) and a simulated Oxide glass (V33) are shown in **Table 2.4**, whilst their approximate glass transition temperature ($T_g$) and density ($\rho$) ranges are displayed in **Table 2.5**. Also shown in **Table 2.4** is the chemical composition of R7T7 glass, a simulated French borosilicate HLW glass which has a $T_g$ of 502 °C and a $\rho$ of 2.75 g cm$^{-3}$ (Matzke and Vernaz, 1993).

Borosilicate HLW glasses have mean linear thermal expansion coefficients ($\alpha$) of approximately 8–10 × $10^{-6}$ $K^{-1}$ between room temperature and $T_g$ (Donald *et al.*, 1997; Lutze, 1988; Marples, 1988). As borosilicate glass is isotropic, borosilicate HLW glasses will have mean volumetric thermal expansion coefficients ($\beta$) of approximately 24–30 × $10^{-6}$ $K^{-1}$ over the same temperature range. It should be noted that crystallisation of a borosilicate HLW glass may alter the thermal expansion coefficient (TEC) of its residual glass matrix.

**Table 2.4** Chemical composition of simulated borosilicate HLW glasses.

| Glass | Blend[a] | Magnox[a] | Oxide[a] | R7T7[b] |
|---|---|---|---|---|
| **Component** | | **Weight %** | | |
| $Ag_2O$ | — | — | — | 0.03 |
| $Al_2O_3$ | 1.59 | 6.58 | 0.15 | 4.91 |
| $B_2O_3$ | 15.90 | 15.90 | 17.80 | 14.02 |
| BaO | 0.24 | 0.50 | 0.59 | 0.60 |
| CaO | 0.03 | 0.01 | 0.01 | 4.04 |
| CdO | — | — | — | 0.03 |
| $CeO_2$ | 1.86 | 0.84 | 1.33 | |
| $Ce_2O_3$ | | | | 0.93 |
| $Cr_2O_3$ | 0.23 | 0.58 | 0.31 | 0.51 |
| $Cs_2O$ | 1.60 | 1.11 | 1.20 | 1.29 |
| $Fe_2O_3$ | 1.10 | 3.00 | 0.66 | 2.91 |
| $Gd_2O_3$ | 2.92 | — | 2.73 | 0.03 |
| $HfO_2$ | 0.06 | 0.02 | 0.04 | — |
| $K_2O$ | 0.15 | 0.01 | 0.01 | — |
| $La_2O_3$ | 0.87 | 0.48 | 0.72 | 0.56 |
| $Li_2O$ | 3.92 | 4.07 | 3.70 | 1.98 |
| MgO | 1.41 | 5.74 | 0.05 | — |
| $MnO_2$ | — | — | — | 0.25 |
| $MoO_3$ | 2.21 | 1.62 | 2.57 | 1.70 |
| $Na_2O$ | 8.58 | 8.29 | 9.01 | 9.86 |
| $Nd_2O_3$ | 2.77 | 1.44 | 2.37 | 1.59 |
| NiO | 0.21 | 0.37 | 0.51 | 0.42 |
| $P_2O_5$ | 0.11 | 0.26 | 0.10 | 0.28 |
| PdO | — | — | — | 0.33 |
| $Pr_2O_3$ | | | | 0.44 |
| $Pr_6O_{11}$ | 0.85 | 0.44 | 0.72 | |
| $Rb_2O$ | — | — | — | 0.13 |
| $Rh_2O_3$ | — | — | — | 0.12 |
| $RuO_2$ | 1.03 | 0.70 | 1.05 | 0.46 |
| $Sb_2O_3$ | — | — | — | 0.01 |
| $SiO_2$ | 46.28 | 46.10 | 50.50 | 45.48 |
| $Sm_2O_3$ | 0.44 | 0.22 | 0.41 | 0.31 |
| $SnO_2$ | — | — | — | 0.02 |
| SrO | 0.55 | 0.30 | 0.51 | 0.33 |
| $TeO_2$ | 0.31 | — | 0.19 | 0.23 |
| $ThO_2$ | — | — | — | 0.33 |
| $TiO_2$ | 0.06 | 0.01 | 0.02 | — |
| $UO_2$ | — | — | — | 0.52 |
| $Y_2O_3$ | 0.36 | 0.10 | 0.19 | 0.20 |
| ZnO | — | — | — | 2.50 |
| $ZrO_2$ | 2.78 | 1.45 | 2.44 | 2.65 |
| **Total** | **98.42** | **100.14** | **99.89** | **100.00** |

[a] Supplied by Nexia Solutions; [b] (Matzke and Vernaz, 1993)

**Table 2.5** Approximate glass transition temperature ($T_g$) and density ($\rho$) ranges for simulated UK borosilicate HLW glasses (Larkin, 1986; Marples, 1988).

| $T_g$ (°C) | $\rho$ (g cm$^{-3}$) |
|---|---|
| 495–520 | 2.6–2.8 |

## 2.5 HLW Vitrification at Sellafield, Cumbria

Before vitrification, the highly active liquor (HAL) is transferred to a stock tank where half the lithium oxide ($Li_2O$) for the final glass is added as lithium nitrate ($LiNO_3$) (Marples, 1988). The lithium nitrate also aids the incorporation/digestion of elements such as iron and aluminium in the glass melt by forming complex oxides in the calciner which are more reactive than the pure oxide. From the stock tank HAL is continuously metered to a calciner. The calciner is an inclined metal tube rotated in a furnace where the liquid waste is successively evaporated, dried and partially denitrated. During calcination, sugar is added to react with the free nitrate (nitric acid, $HNO_3$) and also reduce ruthenium volatility (Larkin, 1986). At the lower end of the calciner, the calcine falls into an inductively-heated Inconel 601 melting vessel, with base glass frit being added in batches. The glass is melted at approximately 1100 °C and poured into a storage/disposal canister every 8 h, generally leaving a glass 'heel' of ~70 kg in the melter (Marples, 1988). Continuous feed to the melter with batch pouring gives a residence time in the melter of 1–8 h (Larkin, 1986). The glass melts are air sparged to aid homogenisation (although the French employ an inert argon sparge which is expected to create mildly reducing melting conditions) (Short, 2004). The storage/disposal canisters are made from Type 309S stainless steel and hold about 400 kg of glass, requiring two pours to fill them. After filling, the canisters have their lids welded on, before being decontaminated prior to transferral to the vitrified product store (VPS). In the VPS the filled canisters are stacked 10 high and are air-cooled by natural convection (Marples, 1988). A schematic of this process is shown in **Figure 2.2.**

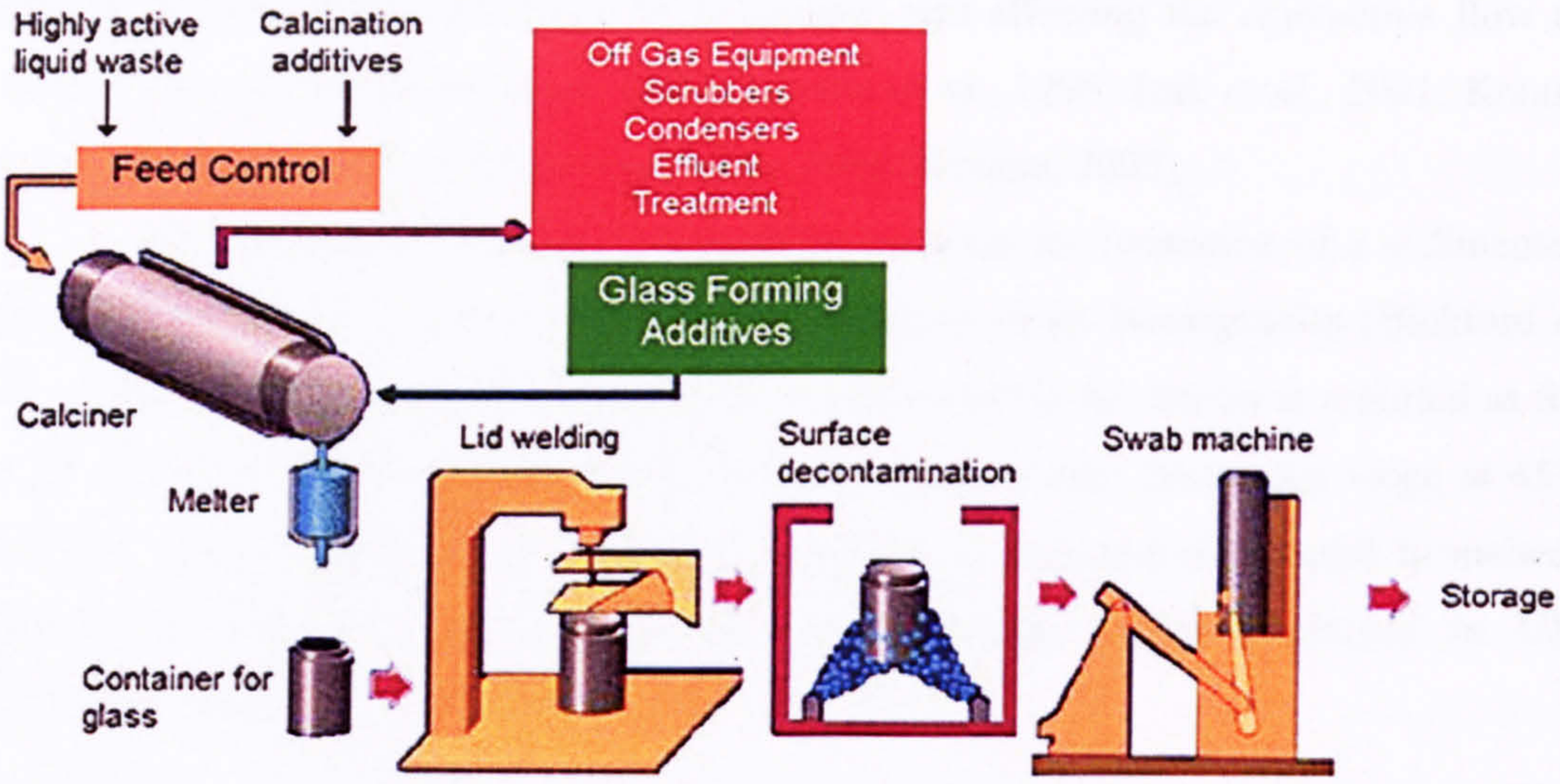


**Figure 2.2** Schematic of the continuous vitrification process (supplied by Nexia Solutions).

## 2.6 HLW Vitrification Issues

### 2.6.1 HLW Glass Melter

Platinum group metals are immiscible within borosilicate HLW glass melts, regardless of melting atmosphere, forming metallic and/or oxide phases (Bickford *et al.*, 1990a; Galoisy *et al.*, 1998; Goldman and Brite, 1986; Krause and Luckscheiter, 1991; Morgan, 2005; Sundaram and Perez, 2000; Yamashita *et al.*, 2004). These platinoid phases (both metallic and oxide) are of higher electrical conductivity than the rest of the glass melt (Bickford *et al.*, 1990a; Demin *et al.*, 1996; Galoisy *et al.*, 1998; Goldman and Brite, 1986; Krause and Luckscheiter, 1991; Marples, 1988; Simonnet and Grandjean, 2005) and can short circuit submerged electrodes (if present). In addition to platinoid phases, only spinel (Hrma, 2002; Izak *et al.*, 2001; LaMont and Hrma, 1998), eskolaite, metallic phases and Zr-containing phases are likely to form at temperatures above 1050 °C (Hrma, 2002). Platinoid phases (Demin *et al.*, 1996; Galoisy *et al.*, 1998; Krause and Luckscheiter, 1991; Marples, 1988; Mendel *et al.*, 1976; Morgan, 2005) and spinel (LaMont and Hrma, 1998; Marples, 1988; Mendel *et al.*, 1976) can agglomerate into 'swarms' in the glass melt and then sediment to the bottom of the glass melter. Sundaram and Perez (2000) report that the larger the 'swarm', the faster it settles. The sedimented phases form a 'sludge' layer (of higher density, viscosity and electrical conductivity) at the bottom of the melter. This 'sludge' layer affects the glass rheology,

causing pouring difficulties (such as blockages) and affecting the convective flow of glass in the melter (Demin *et al.*, 1996; Galoisy *et al.*, 1998; Izak *et al.*, 2001; Krause and Luckscheiter, 1991; LaMont and Hrma, 1998; Morgan, 2005).

Air sparging of the glass melt partially prevents the formation of a sedimented 'sludge' (Krause and Luckscheiter, 1991) and improves its homogeneity (Bickford *et al.*, 1990b; Short, 2004). The relative retention of metals in the melter is reported as Ru > Rh >> Pd > Ag (Smith and Bickford, 2000). Glass melter floors that slope at 45°, coupled with a bottom drain, reduce the retention of sedimented material in melters (Sundaram and Perez, 2000), although this technique is not employed in UK borosilicate HLW glass melters.

### 2.6.2 HLW Glass Melt/Glass Homogeneity

Onset of the limits of HLW incorporation/digestion in the borosilicate glass melt are characterised by (Larkin, 1986): (1) a lumpy pour (indicating insufficient reaction time/rate); (2) bubbles in glass samples; (3) residue build-up in the crucible/melter (showing the limit of incorporation/digestion has been reached); (4) phase separation (principally 'yellow phase'); (5) partially reacted calcine and base glass in glass samples and (6) large-scale crystallisation of glass samples.

Dissolving/relict calcine in glass samples were described as: crystalline, lanthanide- and Zr-rich, and often associated with bubbles (Morgan, 2005). The crystal phases observed within dissolving/relict calcine are lanthanide silicates and Ce-Zr oxides. These crystal phases form due to (localised) supersaturation of their component elements in the glass melt, followed by their precipitation upon cooling (Bouchet *et al.*, 2000). The laboratory-scale glass samples of both Morgan (2005) and Bouchet *et al.* (2000) were melted at approximately 1050 °C for <1 h. 'Residual calcine' in borosilicate HLW glasses reduces their chemical durability (Raman *et al.*, 2003).

Incomplete homogenisation of borosilicate HLW glass melts results in compositional 'banding' of glass samples (Abraitis, 1999; Morgan, 2005). The compositional 'banding' observed by Abraitis (1999) consisted of 'bands' enriched in base glass components (relative to the bulk glass composition) alternating with 'bands' enriched in simulated HLW components (relative to the bulk glass composition) which also exhibited significant crystallisation. The 'bands' enriched in simulated HLW components were of lower chemical durability then the 'bands' enriched in base glass components.

### *2.6.2.1 'Yellow Phase'*

Immiscible 'yellow phase' can form during borosilicate HLW glass melting. 'Yellow phase' is molten at the glass melting temperature (Bickford *et al.*, 1990a; Hall *et al.*, 1976; Morgan, 2005; Morris and Chidley, 1976; Pegg and Joseph, 2001), segregates from the glass melt during feed-to-glass conversion (H. Li *et al.*, 2001; Manara *et al.*, 2007; Morgan, 2005; Sullivan *et al.*, 1995) and is initially nitrate-based (Hrma *et al.*, 2006). Molten 'yellow phase' tends to float on the surface of the glass melt (Bickford *et al.*, 1990a; Buechele *et al.*, 1995; Crichton *et al.*, 1995; Kaushik *et al.*, 2006; Lutze *et al.*, 1979; Manara *et al.*, 2007; Marples, 1988; Morgan, 2005; Morris and Chidley, 1976; Pegg and Joseph, 2001; Schiewer *et al.*, 1982). Molten 'yellow phase' can also be found within the body of the glass melt, as immiscible inclusions (Bickford *et al.*, 1990a; Buechele *et al.*, 1995; Cousi *et al.*, 2004; Hall *et al.*, 1976; Henry *et al.*, 2004; Lutze *et al.*, 1979; Morgan, 2005; Pinet *et al.*, 2006; Short, 2004) and on the inner surface of bubbles (Manara *et al.*, 2007; Morgan, 2005). Relative to the glass melt, molten 'yellow phase': is highly corrosive to metals (*e.g.* Inconel) and ceramics (H. Li *et al.*, 2001; Manara *et al.*, 2007; McKeown *et al.*, 2001; Morgan, 2005; Pegg and Joseph, 2001; Sengupta *et al.*, 2006; Short, 2004; Short *et al.*, 2005; Sullivan *et al.*, 1995), has lower density (Bickford *et al.*, 1990a; Crichton *et al.*, 1995; Dé *et al.*, 1976; Kaushik *et al.*, 2006; Morgan, 2005; Morris and Chidley, 1976; Schiewer *et al.*, 1982), is highly electrically conductive (problematic if electrodes are used in the melter) (Manara *et al.*, 2007; Pegg and Joseph, 2001), is highly oxidising (Krause and Luckscheiter, 1991), has very low viscosity (Bickford *et al.*, 1990a; Morris and Chidley, 1976) and can increase the volatility of some component species (Langowski *et al.*, 1996a and references therein; Sullivan *et al.*, 1995).

'Yellow phase' gets its name from its colour in the solid state, thought to be caused by the presence of chromates (Buechele *et al.*, 1995; Hall *et al.*, 1976; Lutze, 1988). The name 'yellow phase' is misleading as it implies a single phase, solid 'yellow phase' is actually an assembly of crystal phases whose identity and chemical composition will depend on the borosilicate HLW glass composition (Lutze, 1988; McKeown *et al.*, 2001; Morgan, 2005; Morris and Chidley, 1976; Schiewer *et al.*, 1982; Short, 2004). The crystal phases found in solid 'yellow phase' are generally water soluble (Dé *et al.*, 1976; Hall *et al.*, 1976; Kaushik *et al.*, 2006; Kawamura and Ohuchi, 1995; Lutze, 1988; Morgan, 2005; Morris and Chidley, 1976; Schiewer *et al.*, 1982; Short, 2004; Sullivan *et al.*, 1995). Solid 'yellow phase' can be enriched (relative to the

glass) in: molybdate, chromate, sulphate, phosphate, chloride, alkalis and some alkaline earths. These component species preferentially partition to the 'yellow phase' when it is molten. The two most important elements that preferentially partition to 'yellow phase' are caesium (due to short-lived $^{137}Cs$ and long-lived $^{135}Cs$) (Caurant *et al.*, 2007; Dé *et al.*, 1976; Hall *et al.*, 1976; Kaushik *et al.*, 2006; Morgan, 2005; Morris and Chidley, 1976; Muller *et al.*, 1999; Pegg and Joseph, 2001; Schiewer *et al.*, 1982; Sengupta *et al.*, 2006; Sullivan *et al.*, 1995) and strontium (due to short-lived $^{90}Sr$) (Dé *et al.*, 1976; Hall *et al.*, 1976; Kaushik *et al.*, 2006; Morgan, 2005; Morris and Chidley, 1976; Pegg and Joseph, 2001; Schiewer *et al.*, 1982; Sengupta *et al.*, 2006). The actinides uranium (Kaushik *et al.*, 2006) and plutonium (Muller *et al.*, 1999) do not preferentially partition to 'yellow phase'.

The formation of immiscible 'yellow phase' is strongly influenced by REDOX conditions in the glass melt (Buechele *et al.*, 1995; Crichton *et al.*, 1995). 'Yellow phase' formation can be suppressed by melting glasses under reducing condition (Camara *et al.*, 1980, Horneber *et al.*, 1982; Lutze, 1988 and references therein). 'Yellow phase' formation is also reduced by increasing $B_2O_3$ levels in the glass (Caurant *et al.*, 2007; Dé *et al.*, 1976)

### 2.6.3 HLW Solubility in the Glass Melt

The solubilities of many oxides within silicate glass melts are shown in **Table 2.6.** However, borosilicate glass melts have a higher solubility for some of these oxides (Bickford *et al.*, 1990a; Raman, 1998).

**Table 2.6** Approximate oxide solubilities in silicate glass melts (note: actual limits will depend on temperature, glass composition and REDOX conditions) (Pegg and Joseph, 2001).

| Solubility | Oxide |
|---|---|
| >25 wt% | Al, B, Ca, Cs, K, Na, Pb, Rb, Si, U |
| 15–25 wt% | Ba, Fe, La, Li, Mg, Nd, Sr, Zn |
| 5–15 wt% | Be, Bi, Cu, F, Ga, Gd, Ge, Mn, P, Pr, Pu, Th, Ti, V, Zr |
| 1–5 wt% | Am, As, C, Cd, Ce, Cl, Cm, Co, Cr, Dy, Eu, Hf, Mo, Ni, Np, Pm, Re, S, Sb, Se, Sm, Sn, Tc, Te, Tl, W, Y |
| <1 wt% | Ag, Au, Br, Hg, I, N, Pd, Pt, Rh, Ru |

### 2.6.4 HLW Volatility from the Glass Melt

Aside from gases formed in the glass melt, many HLW components have a high volatility, limiting their incorporation into the final HLW glass. This reduces the vitrification efficiency and generates more radioactive waste when the scrubbers are decommissioned. **Table 2.7** lists the off-gas species observed during HLW vitrification. Semi-volatiles can leave the melter as part of an aerosol, whereas particulates can be entrained from the glass melt surface (Langowski *et al.*, 1996a).

**Table 2.7** Off-gas species observed during HLW vitrification (Scott *et al.*, 1985).

| Gases | Semi-volatile | Particulate |
|---|---|---|
| $H_2$, $O_2$, CO, $CO_2$, NO, $NO_2$, $SO_2$, $H_2O$, halogens (*e.g.* $I_2$) | Some compounds of Na, Li, K, Cs, Hg, Cd, Mo, Ru, Sb, Se, Tc, Te, B, and halogens | Fe, Al, Sr, rare-earths, and all other feed components |

### 2.6.5 HLW Glass Pouring

In addition to the problematic (high density, high viscosity and high electrical conductivity) 'sludge' formed at the bottom of HLW glass melters, HLW glass melts may undergo phase transformations during idle periods when the glass melt is at temperatures below the glass formation temperature, or in the pouring system, causing further problems (Lutze, 1988). During HLW vitrification there are two sources of heat: process heat from the glass melter and radiogenic heat produced by decaying radionuclides in the HLW. After pouring the HLW glass into storage/disposal canisters it loses its process heat, however the continued radiogenic heating of the glass results in slow/retarded cooling to the glass transition temperature ($T_g$), taking up to 48 h (Larkin, 1986; Lutze, 1988). The slow cool resulting from this radiogenic heating can lead to glass phase transformations and a subsequent change in glass performance (such as chemical durability) under repository conditions (Bickford and Jantzen, 1986; Dé *et al.*, 1976; D.-S. Kim *et al.*, 1995; Wicks, 1992). Further to this, multiple HLW glass pours into the same canister (as is the case in the UK) will raise the temperature of the pouring interface above $T_g$, increasing the potential for glass phase transformations in this region (Roth *et al.*, 2002). Another issue is that sensitisation (the precipitation of chromium carbide(s) at grain boundaries) of austenitic stainless steel canisters (such as Type 309S) occurs between 500 and 750 °C, lowering their corrosion resistance (ASTM, 2002 and

references therein; Wescott and Slate, 1981). Therefore, there is a trade-off between cooling the poured glass rapidly (to prevent glass phase transformations and canister sensitisation) and cooling the poured glass slowly to prevent significant glass cracking (which increases glass surface area) (Marples, 1988).

### 2.6.6 HLW Glass Irradiation

$\alpha$ irradiation of borosilicate HLW glasses has been reported to either decrease their chemical durability (Lutze, 1988; Trocellier, 2001) or to have a negligible effect on their chemical durability (Marples, 1988 and references therein; Peuget *et al.*, 2006; Wicks, 1992). However, the energetic recoil nuclei from $\alpha$-decays are responsible for most of the effects attributed to $\alpha$ radiation, so the reader must be wary. $\beta$ and $\gamma$ radiation have less effect than $\alpha$ radiation on borosilicate HLW glass properties, whilst nuclear transmutations have no measurable effect (Lutze, 1988). More significantly, Matzke (1984) reports that many crystal phases formed in borosilicate HLW glasses become amorphous (metamict) due to radiation damage, which may lead to swelling of the glass (due to the lower density of the amorphous phases) and possible cracking. However, Lutze (1988) reports this will have a negligible effect on bulk glass properties. Electron irradiation of a sodium borosilicate glass (whose composition was close to the 'traditional' immiscibility region of the ternary $Na_2O$-$B_2O_3$-$SiO_2$ system) using transmission electron microscopy (TEM) induced its amorphous phase separation (APS) (Sun *et al.*, 2004). The effect of $\beta$ and $\gamma$ radiation upon glasses can be simulated by their electron irradiation in the TEM (Sun *et al.*, 2004). Due to the sometimes conflicting reports about the effect(s) of radiation upon borosilicate HLW (and other) glasses, it is suggested to assess them for each glass of interest. A comprehensive review of radiation effects concerning glasses can be found in Weber *et al.* (1997).

## 2.7 Glass Phase Transformations

### 2.7.1 Crystallisation (Devitrification)

Glass crystallisation involves two processes: (1) crystal nucleation and (2) subsequent crystal growth. Nucleation can be either homogeneous or heterogeneous. Homogeneous nucleation is when crystal nuclei occur spontaneously in a homogeneous glass matrix. Heterogeneous nucleation occurs due to the presence of foreign particles/melt insolubles

(*e.g.* platinoids) in the glass or from pre-existing surfaces such as melter/canister walls and the glass melt/atmosphere interface (Paul, 1990; Shelby, 1997).

### 2.7.2 Amorphous Phase Separation (APS)

There are two APS mechanisms which can occur in glass: (1) nucleation and growth and (2) spinodal decomposition. Nucleation and growth is a similar process to that of glass crystallisation; nuclei of different composition from the base glass are formed and grow with time. This type of APS results in the second phase forming spherical particles within the parent glass, with the second phase having little connectivity. Due to the formation process there is a sharp boundary between the two phases. Spinodal decomposition involves a gradual change in composition (as it is diffusion controlled) of the two phases until they reach the immiscibility boundary. Phase separation of this type results in the second phase having a non-spherical structure and both phases having high interconnectivity. During formation the phase boundary is initially diffuse but sharpens with time. The boundary between the two phases formed by APS can act as a nucleation site for subsequent crystallisation. APS can also aid subsequent crystallisation by producing a phase (or phases) with a greater tendency to crystallise than the parent glass (Paul, 1990; Rafferty *et al.*, 2003; Shelby, 1997).

### 2.7.3 Crystalline Phase Separation (CPS)

Formation of an immiscible phase in a glass melt, followed by the crystallisation of this phase upon cooling, is termed CPS (Jantzen *et al.*, 2001).

## 2.8 Crystallisation of Borosilicate HLW Glasses

The following crystal phases have been observed as devitrification products in as-cast and/or heat treated borosilicate HLW glasses (or glasses of similar chemical composition), crystal phases in glass-ceramic HLW forms have been omitted. Hrma (2002) observes that vitrification of HLW rich in components with limited solubilities, coupled with the slow cooling of HLW glass in storage/disposal canisters provides an opportunity for a variety of crystal phases to precipitate. These crystal phases are typically solid solutions and may contain components in proportions not usually seen in

nature. In this work, the term 'wasteform' indicates a borosilicate HLW glass which contains crystals.

### 2.8.1 Platinoid Phases

Omission of Rh from simulated borosilicate HLW glasses has no effect on the formation, size or sedimentation of platinoid phases (Krause and Luckscheiter, 1991). The addition of platinoids to borosilicate HLW glasses has been reported to have negligible (F. Bart *et al.*, 2001) or even a slightly positive (Pacaud *et al.*, 1992), effect on their chemical durabilities. Metallic 'fines' (undissolved by 6 $mol \cdot l^{-1}$ nitric acid during reprocessing) rich in platinoids (Rh, Pd and Rh), Mo and Tc are vitrified in 'real' borosilicate HLW glasses.

#### *2.8.1.1 (Ru,Rh)$O_2$*

(Ru,Rh)$O_2$ has the rutile crystal structure (tetragonal system, space group $P4_2/mnm$). **Table 2.8** notes observations of (Ru,Rh)$O_2$ in borosilicate HLW glasses. They are generally observed with acicular (needle-like) morphologies (F. Bart *et al.*, 2001; Galoisy *et al.*, 1998; Larkin, 1986; Mitamura *et al.*, 1985; Roth and Weisenburger, 2000; Simonnet and Grandjean, 2005), often in clusters or 'swarms'. Granular (Larkin, 1986), 'sponge' (Sundaram and Perez, 2000), grain (Simonnet and Grandjean, 2005) and cubic (F. Bart *et al.*, 2001) morphologies have also been observed.

(Ru,Rh)$O_2$ is an effective nucleating agent (Bickford and Jantzen, 1984; Buechele *et al.*, 1990; Izak *et al.*, 2001; Jantzen *et al.*, 1984; D.-S. Kim *et al.*, 1994; Mitamura *et al.*, 1985), with spinel often reported to nucleate upon it (Bickford and Jantzen, 1984; Buechele *et al.*, 1990; Izak *et al.*, 2001; D.-S. Kim *et al.*, 1994). The existence of (Ru,Rh)$O_2$ in 'real' borosilicate HLW glasses (Cheron *et al.*, 1995) demonstrates its radiation tolerance.

(Ru,Rh)$O_2$ in the 'sludge' layer at the bottom of the melter can incorporate Cr during long melter runs (Kelm and Oser, 1992; Krause and Luckscheiter, 1991). The substitution of $Cr^{4+}$ for $Ru^{4+}$ in $RuO_2$ has been studied by González-Calbet *et al.* (1987).

**Table 2.8** $(Ru,Rh)O_2$ noted in borosilicate HLW glasses.

| Phase | Reference(s) |
|---|---|
| $RuO_2$ | (Abraitis, 1999; F. Bart *et al.*, 2001; Buechele *et al.*, 1990; Galoisy *et al.*, 1998; Hyatt *et al.*, 2004; Izak *et al.*, 2001; Jain *et al.*, 1991; Jantzen *et al.*, 1984; Kahl, 1981; Kawamura and Ohuchi, 1995; D.-S. Kim *et al.*, 1994; Krause and Luckscheiter, 1991; Larkin, 1986; Luckscheiter and Nesovic, 1996; Lutze *et al.*, 1979; Matzke *et al.*, 1984; Mendel *et al.*, 1976; Roth *et al.*, 2002; Simonnet and Grandjean, 2005; Sundaram and Perez, 2000; Turcotte *et al.*, 1980) |
| $(Ru,Rh)O_2$ | (Cheron *et al.*, 1995; Galoisy *et al.*, 1998; Krause and Luckscheiter, 1991; Lutze, 1988; Mitamura *et al.*, 1985; Pacaud *et al.*, 1992; Roth and Weisenburger, 2000; Sundaram and Perez, 2000) |

### *2.8.1.2 Metallic Platinoid Phases*

Metallic Pd and Rh both have the fcc crystal structure (cubic system, space group $Fm\bar{3}m$), forming a complete solid solution above 910 °C (Okamoto, 1994). Even though Te is non-metallic, a solid solution exists between Pd and Te with a maximum Te content of 16.3 at% at 770 °C (Galoisy *et al.*, 1998), with solid solutions of this type having the fcc structure of metallic Pd and Rh. Outside this solid solution region there are at least 10 other crystal phases in the Pd-Te system (Ipser and Schuster, 1986). **Table 2.9** reports metallic platinoid phases observed in borosilicate HLW glasses.

The effectiveness of these metallic phases as nucleating agents is noted by Lutze (1988) and Mitamura *et al.* (1985). They tend to have spherical or tear-shaped morphologies (Galoisy *et al.*, 1998; Mendel *et al.*, 1976).

The extensive number of elements which could conceivably partition to these metallic platinoid phases are noted by Kleykamp (1985) who reports the fission products Mo, Tc, Ru, Rh, Pd, Ag, Cd, In, Sn, Sb and Te form metallic precipitates in spent $UO_2$ fuels. These are generally undissolved by 6 mol $l^{-1}$ nitric acid during reprocessing and are termed metallic 'fines' (Lutze, 1988). Depending on glass melting conditions, it is conceivable that precipitates containing some, if not all, of these fission products could form in 'real' borosilicate HLW glass melts. This is lent weight by Sundaram and Perez (2000) who found Ru, Rh, Pd, Te and Se in metallic phases on the floor of an inactive melter. Observation of metallic Pd-Te in 'real' borosilicate HLW glasses (Cheron *et al.*, 1995) demonstrates its radiation tolerance.

$RuO_2$ can be reduced to metallic Ru (with globular morpohology) in borosilicate HLW melts due to prolonged heating (Krause and Luckscheiter, 1991) as well as reducing melting conditions (Bickford and Jantzen, 1986).

**Table 2.9** Metallic platinoid phases observed in borosilicate HLW glasses.

| Inclusion | Reference(s) |
|---|---|
| Pd-Rh-Te | (Kawamura and Ohuchi, 1995; Krause and Luckscheiter, 1991; Luckscheiter and Nesovic, 1996; Mitamura *et al.*, 1985; Pacaud *et al.*, 1992; Roth and Weisenburger, 2000) |
| Pd-Te | (F. Bart *et al.*, 2001; Cheron *et al.*, 1995; Galoisy *et al.*, 1998; Hyatt *et al.*, 2004; Krause and Luckscheiter, 1991; Lutze, 1988; Sundaram and Perez, 2000) |
| Pd | (Lutze *et al.*, 1979; Mendel *et al.*, 1976; Sundaram and Perez, 2000; Turcotte *et al.*, 1980) |
| Pd-Rh | (Buechele *et al.*, 1990; Sundaram and Perez, 2000) |
| Pd-Ru | (Sundaram and Perez, 2000) |
| Pd-Mo | (Guber *et al.*, 1979) |
| Ru | (Bickford and Jantzen, 1986; Krause and Luckscheiter, 1991) |

### 2.8.2 'Yellow Phase' and Associated Crystal Phases

The qualitative chemical compositions of some 'yellow phase' samples are given in **Table 2.10**. The chemical composition of a sample of 'yellow phase' analysed by Schiewer *et al.* (1982) is given in **Table 2.11**, although Cs, F, Pr, Rb, Ru, Te, La, Nd and Y could not be detected by the techniques employed. The modified phase composition of this sample (as there were obvious errors in the reported phase composition) is reported in **Table 2.12**. The chemical composition ranges of 'yellow phase' samples investigated by Dé *et al.* (1976) are shown in **Table 2.13**.

**Table 2.10** Qualitative chemical compositions of some 'yellow phase' samples.

| Oxide composition | Reference(s) |
|---|---|
| Mo, Li, Cs, Sr, Te, Cr and La | (Morgan, 2005) |
| S, Cr, Mo, P, Na, Li, Cs, Ba, Sr, B, Mg, RE and Si | (Morris and Chidley, 1976) |
| Na, S, Li, Ca, P, Mo, Cr, Fe, Ni, Mn, Zn, Al, B, Si, Mg, Cl, Cs, Se and La | (Sullivan *et al.*, 1995) |
| Alkali, S, Cr, Cs and Sr | (Pegg and Joseph, 2001) |
| S, Na, K, Ca, Cr, Ba and Cs | (Muller *et al.*, 1999) |
| Mo, P, Ca, Zn, Na, B, Zr, Al and Si | (Henry *et al.*, 2004; Pinet *et al.*, 2006) |
| S, Na, Ca, Cr, Fe, Al, U and Ba | (Kaushik *et al.*, 2006) |

**Table 2.11** Chemical composition of the 'yellow phase' sample of Schiewer *et al.* (1982).

| Component | Weight % | Molar % | Component | Weight % | Molar % |
|---|---|---|---|---|---|
| $Al_2O_3$ | 0.53 | 0.41 | $MoO_3$ | 18.11 | 9.92 |
| $B_2O_3$ | 1.00 | 1.13 | $Na_2O$ | 19.13 | 24.34 |
| BaO | 8.14 | 4.18 | $P_2O_5$ | 0.40 | 0.22 |
| CaO | 5.40 | 7.60 | $SO_3$ | 31.14 | 30.69 |
| $CrO_3$ | 9.28 | 7.31 | $SiO_2$ | 0.59 | 0.77 |
| $K_2O$ | 0.51 | 0.43 | SrO | 0.47 | 0.35 |
| $Li_2O$ | 4.47 | 11.80 | Other(s) | 0.59 | 0.38 |
| MgO | 0.24 | 0.47 | **Total** | **100.00** | **100.00** |

**Table 2.12** Modified phase composition of the 'yellow phase' sample of Schiewer *et al.* (1982).

| Component | Weight % | Molar % |
|---|---|---|
| Alkali sulphates | | 58 |
| Alkali chromates | 62 | 8 |
| Alkali molybdates | | 4 |
| $CaMoO_4$ | 20 | 15 |
| $Ba(Sr)CrO_4$ | 9 | 6 |
| Other(s)/residue | 5 | 6 |
| $BaSO_4$ | 4 | 3 |
| **Total** | **100** | **100** |

**Table 2.13** Chemical composition ranges of 'yellow phase' samples analysed by Dé *et al.* (1976).

| Component | Weight % |
|---|---|
| $B_2O_3$ | 2–3 |
| CaO | 0.5–3 |
| $Cs_2O$ | 12–16 |
| $K_2O$ | 0.6 |
| $MoO_3$ | 63–65 |
| $Na_2O$ | 9–14 |
| SrO | 0.3–0.8 |

### *2.8.2.1 Powellites*

Although powellites have been observed in 'yellow phase' (Caurant *et al.*, 2007; Cousi *et al.*, 2004; Schiewer *et al.*, 1982; Turcotte *et al.*, 1982), they generally crystallise within the glass, without the problems associated with 'yellow phase', so the two should not be confused. Powellite ($CaMoO_4$) is of the tetragonal crystal system (space group $I4_1/a$) and is isostructural with scheelite ($CaWO_4$). Powellite can be shown as $AMoO_4$,

where the *A* site can host a range of +1, +2 and +3 valent cations (**Table 2.14**), as well as vacancies, as long as charge neutrality is maintained (Short, 2004).

**Table 2.14** Cations reported on the powellite *A* site (Mokhosoev *et al.*, 1969; Sattler and Nemarich, 1970; Schieber, 1965; Schieber and Holmes, 1964; Shi *et al.*, 1995; Short, 2004; Teller, 1992).

| +1 | +2 | +3 |
|---|---|---|
| Ag, K, Li, Na, Rb | Ba, Ca, Cd, Pb, Sr | Bi, Ce, Dy, Er, Eu, Gd, Ho, La, Nd, Pr, Sm, Tb, Tm, Y, Yb |

Powellites observed in borosilicate HLW glasses are noted in **Table 2.15**. Powellites have been reported with dendritic (Caurant *et al.*, 2007; Mendel *et al.*, 1976; Short, 2004; Short *et al.*, 2005), acicular (F. Bart *et al.*, 2001; Orlhac *et al.*, 1999), di-pyramidal (Orlhac *et al.*, 1999) and diamond (Mitamura *et al.*, 1985) morphologies. Orlhac *et al.* (1999) report that the temperature at which the powellite forms affects its morphology.

Powellite formation in borosilicate HLW glasses reduces the leach rates of elements which segregate to it (Mitamura *et al.*, 1986) and slightly improves the chemical durability of the glass (F. Bart *et al.*, 2001). **Table 2.16** gives the solubility of powellites in various leachants. The formation of powellite in 'real' borosilicate HLW glasses (Cheron *et al.*, 1995) demonstrates its radiation tolerance.

During (high temperature) chemical durability testing of borosilicate HLW glasses, the powellites $(Ca_{0.88}Sr_{0.10}Ba_{0.02})MoO_4$ (Gong *et al.*, 1998) and $(Nd,Pr,La,Ca,Na)MoO_4$ (Abdelouas *et al.*, 1997) formed in/on the altered surface layers of the glass. Powellite is a potential host phase for Am and Cm (Abdelouas *et al.*, 1997).

**Table 2.15** Powellites observed in borosilicate HLW glasses.

| Phase | Reference(s) |
|---|---|
| $BaMoO_4$ | (Turcotte *et al.*, 1982) |
| $CaMoO_4$ | (F. Bart *et al.*, 2001; Caurant *et al.*, 2007; Cheron *et al.*, 1995; Cousi *et al.*, 2004; Guber *et al.*, 1979; Henry *et al.*, 2004; Luckscheiter and Nesovic, 1996; Orlhac *et al.*, 1999; Pacaud *et al.*, 1992; Pinet *et al.*, 2006; Schiewer *et al.*, 1982) |
| $SrMoO_4$ | (Jacquet-Francillon *et al.*, 1982; Kahl, 1981; Lutze *et al.*, 1979; Turcotte *et al.*, 1980) |
| $(Sr,Ba)MoO_4$ | (Mendel *et al.*, 1976) |
| $(Sr,Ba,RE)MoO_4$ | (Mitamura *et al.*, 1985) |
| $(Sr,lanthanides)MoO_4$ | (Jacquet-Francillon *et al.*, 1982; Short, 2004; Short *et al.*, 2005) |
| $Ca(Nd)MoO_4$ | (Caurant *et al.*, 2007; Henry *et al.*, 2004) |
| $Pb(Ca)MoO_4$ | (Feld and Stammler; 1982) |

**Table 2.16** Solubility of powellites in various leachants.

| Leachant | Conditions (temperature and pressure) | Solubility | Reference(s) |
|---|---|---|---|
| Deionised water | Ambient and hydrothermal* | Insoluble | (Komarneni *et al.*, 1983; Schiewer *et al.*, 1982) |
| HCl solution | Ambient | Soluble | (Schiewer *et al.*, 1982) |
| NaCl solution | Hydrothermal* | Insoluble | (Komarneni *et al.*, 1983) |
| KCl solution | Hydrothermal* | Insoluble | (Komarneni *et al.*, 1983) |
| $MgCl_2$ solution | Hydrothermal* | Insoluble | (Komarneni *et al.*, 1983) |
| $Na_2SO_4$ solution | Hydrothermal* | ~5 % soluble | (Komarneni *et al.*, 1983) |

* (100–300 °C; 30 MPa)

### *2.8.2.2 $CsLiMoO_4$*

$CsLiMoO_4$ (cubic crystal system, space group $F\bar{4}3m$) has been observed in 'yellow phase' (Morgan, 2005; Short, 2004), it has a melting point of approximately 770–800 °C (Klevtsova *et al.*, 1980; Morgan, 2005) and is water soluble (Klevtsova *et al.*, 1980).

### *2.8.2.3 Other Associated Crystal Phases*

Other crystal phases reported in, or associated with, 'yellow phase' include: molybdates, sulphates, chromates (**Table 2.17**), phosphates (**Section 2.8.5**) and chlorides (Bickford *et al.*, 1990a; Langowski *et al.*, 1996a; H. Li *et al.*, 1996b; Pegg and Joseph, 2001; Sullivan *et al.*, 1995). The chemical durability of some of the molybdate, sulphate and chromate crystal phases noted in **Table 2.17** are presented in **Table 2.18.**

**Table 2.17** Other molybdate, sulphate and chromate crystal phases reported in, or associated with, 'yellow phase'.

| Type | Phase | Reference(s) |
|---|---|---|
| Molybdates | $Na_2MoO_4$ | (Caurant *et al.*, 2007; Cousi *et al.*, 2004; Horneber *et al.*, 1982) |
| | $Na_2MoO_4 \cdot 2H_2O$ | (Horneber *et al.*, 1982) |
| | Sodium molybdate | (Short, 2004) |
| | Alkali molybdates | (Hall *et al.*, 1976; Matzke and Vernaz, 1993; Schiewer *et al.*, 1982) |
| | Alkaline earth molybdates | (Matzke and Vernaz, 1993) |
| Sulphates | $Na_2SO_4$ ('gall') | (Buechele *et al.*, 1995; Crichton *et al.*, 1995; Kaushik *et al.*, 2006; H. Li *et al.*, 1995, 1996b; Lutze, 1988; McKeown *et al.*, 2001) |
| | $K_2SO_4$ | (Buechele *et al.*, 1995) |
| | $LiNa(SO_4)$ | (Crum *et al.*, 2002) |
| | Alkali sulphates | (Pegg and Joseph, 2001; Schiewer *et al.*, 1982) |
| | $BaSO_4$ | (Kaushik *et al.*, 2006; Morris and Chidley, 1976; Schiewer *et al.*, 1982) |
| | $CaSO_4$ | (McKeown *et al.*, 2001) |
| Chromates | $Na_2CrO_4$ | (Kaushik *et al.*, 2006) |
| | Alkali chromates | (Schiewer *et al.*, 1982) |
| | $BaCrO_4$ | (Kaushik *et al.*, 2006) |
| | $Ba(Sr)CrO_4$ | (Schiewer *et al.*, 1982) |

**Table 2.18** Chemical durability of some of the molybdate, sulphate and chromate crystal phases noted in **Table 2.17.**

| Phase | Durability |
|---|---|
| $Na_2MoO_4$ | Water soluble (Caurant *et al.*, 2007) |
| Alkali molybdates | Water soluble (Schiewer *et al.*, 1982) |
| Alkali sulphates | Water soluble (Schiewer *et al.*, 1982) |
| $BaSO_4$ | Insoluble in water (Morris and Chidley, 1976; Schiewer *et al.*, 1982) and HCl (Schiewer *et al.*, 1982), one of the most thermally stable and chemically durable phases in nature (Kaushik *et al.*, 2006) |
| $Ba(Sr)CrO_4$ | Insoluble in water, soluble in HCl (Schiewer *et al.*, 1982) |
| Alkali chromates | Water soluble (Schiewer *et al.*, 1982) |

### 2.8.3 Spinels

All oxide minerals with the spinel ($MgAl_2O_4$) structure (cubic crystal system, space group $Fd\bar{3}m$) are termed spinels, with complete solid solution existing between many different spinels (D.-S. Kim *et al.*, 1994). Many spinels have been observed in borosilicate HLW glasses (**Table 2.19**) and have better chemical durability than the glass phase (Yan *et al.*, 1995; Zhu *et al.*, 1986), their formation having negligible impact upon overall wasteform chemical durability (Hrma *et al.*, 2005; Lutze, 1988).

Spinels exist in the primary nitrate melt (Izak *et al.*, 2001) and nucleate nearly instantaneously upon cooling the borosilicate HLW glass from its melting temperature (Hrma, 2002; Reynolds and Hrma, 1997). Platinoid phases are noted to be effective spinel nucleation agents (Bickford and Jantzen, 1986; Izak *et al.*, 2001; D.-S. Kim *et al.*, 1994; Sundaram and Perez, 2000). Haematite ($Fe_2O_3$) precipitation often precedes spinel nucleation (Hrma, 2002). Spinels can then provide nucleation sites for other crystal phases, such as clinopyroxenes (Bickford and Jantzen, 1986; D.-S. Kim *et al.*, 1994). Spinels have been noted to contain Rh, Ru (Capobianco and Drake, 1990) and Ti (Hrma *et al.*, 2006). In borosilicate HLW glasses, cubic (Alton *et al.*, 2002) and star-shaped (Alton *et al.*, 2002; Hrma *et al.*, 2000) spinel morphologies have been reported. Spinel is a radiation tolerant crystal phase (Sickafus *et al.*, 2000), demonstrated by its existence in 'real' borosilicate HLW glasses (Cheron *et al.*, 1995; Hrma *et al.*, 2005).

**Table 2.19** Spinels observed in borosilicate HLW glasses.

| Name | Formula | Reference(s) |
|---|---|---|
| Chromite | $FeCr_2O_4$ | (Galoisy *et al.*, 1998; Hrma *et al.*, 2000; D.-S. Kim *et al.*, 1994; H. Li *et al.*, 1996a) |
| Franklinite | $ZnFe_2O_4$ | (Hrma *et al.*, 2005) |
| Magnetite | $Fe_3O_4$ | (Hrma *et al.*, 2000; D.-S. Kim *et al.*, 1994; Zhu *et al.*, 1986) |
| Nichromite | $NiCr_2O_4$ | (Hrma *et al.*, 2000) |
| Trevorite | $NiFe_2O_4$ | (Hrma *et al.*, 2000, 2005; C.-W. Kim *et al.*, 1996; D.-S. Kim *et al.*, 1994; Smith *et al.*, 2004; Turcotte *et al.*, 1980; Yan *et al.*, 1995; Zhu *et al.*, 1986) |
| Cr-Fe-Mn-Ni-Zn spinel | | (F. Bart *et al.*, 2001) |
| Zn-Al-Cr-Fe-Mg spinel | | (Buechele *et al.*, 1995) |
| Cr-Fe-Ni-Zn spinel | | (Kawamura and Ohuchi, 1995) |
| Fe-Cr-Mn-Ni spinel | | (Buechele *et al.*, 1990; Langowski *et al.*, 1996b; Sundaram and Perez, 2000) |
| Fe-Ni-Cr-Zn spinel | | (Pacaud *et al.*, 1992) |
| Fe-Cr spinel | | (Jain *et al.*, 1991) |
| | $(Ni_{0.95}Mn_{0.05})(Fe_{0.92}Cr_{0.08})_2O_4$ | (Bickford and Jantzen, 1984, 1986; Jantzen *et al.*, 1984) |
| | $(Ni_{0.85}Mn_{0.15})(Fe_{0.8}Cr_{0.2})_2O_4$ | (Bickford and Jantzen, 1984, 1986; Jantzen *et al.*, 1984) |
| | $(Fe,Ni,Mn)(Fe,Cr,Mn)_2O_4$ | (H. Li *et al.*, 2003) |
| | $(Mn_{0.3}Fe_{0.3}Zn_{0.4})Cr_2O_4$ | (Hrma *et al.*, 2006) |
| | $(Ni,Fe,Mn)(Fe,Cr)_2O_4$ | (Vienna *et al.*, 1997) |
| | $(Fe,Ni)(Fe,Cr)_2O_4$ | (Izak *et al.*, 2001; D.-S. Kim *et al.*, 1994) |
| | $(Ni,Zn)(Cr,Fe)_2O_4$ | (Cheron *et al.*, 1995) |
| | $(Zn,Ni)(Fe,Cr)_2O_4$ | (Mendel *et al.*, 1976) |
| | $(Fe,Ni,Mn)Fe_2O_4$ | (Bickford and Jantzen, 1986; Zhu *et al.*, 1986) |
| | $Ni(Fe_{0.5}Cr_{0.5})_2O_4$ | (Bickford and Jantzen, 1984) |
| | $(Fe,Ni)Cr_2O_4$ | (Sengupta *et al.*, 2006) |
| | $(Mg,Zn)Cr_2O_4$ | (Lutze, 1988) |
| | $(Ni,Mn)Cr_2O_4$ | (Sundaram and Perez, 2000) |
| | $(Ni,Mn)Fe_2O_4$ | (Jantzen *et al.*, 1984; Sundaram and Perez, 2000; Turcotte *et al.*, 1980; Zhu *et al.*, 1986) |
| | $(Mn,Ni)_3O_4$ | (Jacquet-Francillon *et al.*, 1982) |
| | $ZnCr_2O_4$ | (Orlhac *et al.*, 1999) |

### 2.8.4 Silicate Phases

#### *2.8.4.1 $SiO_2$ Polymorphs*

$SiO_2$ polymorphs noted in borosilicate HLW glasses are shown in **Table 2.20**. The formation of any $SiO_2$ polymorph reduces overall waste form durability (Arbab *et al.*, 2007; D.-S. Kim *et al.*, 1995; Luckscheiter and Nesovic, 1996; Mitamura *et al.*, 1985, 1986; Riley *et al.*, 2002), with preferential leaching around the $SiO_2$ polymorph as the residual glass surrounding these crystals will be $SiO_2$ poor (Mitamura *et al.*, 1985).

These phases have been observed to nucleate on platinoid phases (Lutze, 1988 and references therein; Mitamura *et al.*, 1985). Cristobalite crystals with dendritic as well as globular morphologies have been observed in borosilicate HLW glasses (Caurant *et al.*, 2007).

Amorphous phase separation (APS) of borosilicate HLW glasses has been reported to precede the crystallisation of cristobalite from the vitreous silica phase (Matzke *et al.*, 1984). Voiding (Caurant *et al.*, 2007; Matzke *et al.*, 1984) and cracking (Arbab *et al.*, 2007; Caurant *et al.*, 2007) both in and around cristobalite crystals have also been reported. This has been linked to the rapid $\beta$ to $\alpha$ crystal phase transition of cristobalite (Arbab *et al.*, 2007; Matzke *et al.*, 1984) which occurs between 200 and 280 °C during cooling (Greenwood and Earnshaw, 2002), decreasing the crystal volume and causing stresses in and around crystals if surrounded by a glass matrix (Matzke *et al.*, 1984). There is also a thermal expansion coefficient (TEC) mismatch between cristobalite and borosilicate glass (Jean *et al.*, 1995) which will create stresses. Additions of $Al_2O_3$ are reported to inhibit cristobalite crystallisation in Pyrex glass (Jean *et al.*, 1995). Both cristobalite and tridymite are beam sensitive in the transmission electron microscope (TEM) (McConville *et al.*, 1998), indicating the low radiation tolerance of these phases.

**Table 2.20** $SiO_2$ polymorphs noted in borosilicate HLW glasses.

| Phase | Reference(s) |
|---|---|
| Cristobalite | (Arbab *et al.*, 2007; Caurant *et al.*, 2007; Jacquet-Francillon *et al.*, 1982; Jantzen *et al.*, 2001; Jean *et al.*, 1995; Luckscheiter and Nesovic, 1996; Matzke *et al.*, 1984; Mitamura *et al.*, 1985; Quintas *et al.*, 2007; Riley *et al.*, 2002) |
| Tridymite | (Jantzen *et al.*, 2001; Lutze, 1988 and references therein; Mitamura *et al.*, 1985) |
| Quartz | (Luckscheiter and Nesovic, 1996) |
| Unidentified | (Jantzen *et al.*, 2001; D.-S. Kim *et al.*, 1994, 1995) |

### *2.8.4.2 Clinopyroxenes*

Clinopyroxenes are single-chain silicates of the monoclinic crystal system (D.-S. Kim *et al.*, 1994). Clinopyroxene is a solid solution (Hrma, 2002; D.-S. Kim *et al.*, 1994) of general formula $ABSi_2O_6$ (Webmineral, 2006). Cations noted on the *A* and *B* sites are shown in **Table 2.21.** There can be $Al^{3+}$ for $Si^{4+}$ substitution in clinopyroxenes, such as in augite (**Table 2.22**, due to the presence of $Ti^{4+}$) and esseneite ($CaFe^{3+}AlSiO_6$) (Webmineral, 2006).

**Table 2.21** Cations noted on the clinopyroxene *A* and *B* sites (Webmineral, 2006)

| *A* | *B* |
|---|---|
| $Li^{+}$, $Na^{+}$, $Ca^{2+}$, $Fe^{2+}$, $Mg^{2+}$, $Mn^{2+}$ | $Fe^{2+}$, $Mg^{2+}$, $Mn^{2+}$, $Zn^{2+}$, $Al^{3+}$, $Cr^{3+}$, $Fe^{3+}$, $Mn^{3+}$, $Sc^{3+}$, $V^{3+}$, $Ti^{4+}$ |

Clinopyroxenes have been reported in borosilicate HLW glasses (**Table 2.22**). Clinopyroxenes are unlikely to form in the glass melter but may precipitate in storage/disposal canisters during the slow cool (Bickford and Jantzen, 1984; D.-S. Kim *et al.*, 1994; Menkhaus *et al.*, 2000), often nucleated and grown on spinel crystals (Bickford and Jantzen, 1986). Aegirine (acmite) has been reported to nucleate on $RuO_2$ (Jantzen *et al.*, 1984). Alkali silicates have been reported to nucleate on aegirine (acmite) crystals (Bickford and Jantzen, 1986). Formation of aegirine (acmite) lowers the chemical durability of the wasteform (Bickford and Jantzen, 1984; Jantzen *et al.*, 1984; Lutze, 1988), with Hrma *et al.* (2003) further noting enhanced glass dissolution around aegirine (acmite) crystals. D.-S. Kim *et al.* (1995) however disagree, reporting that clinopyroxene solid solutions have no effect on the chemical durability of the wasteform.

**Table 2.22** Clinopyroxene phases reported in borosilicate HLW glasses.

| Name | Formula | Reference(s) |
|---|---|---|
| Clinopyroxene | | (Hrma, 2002; Hrma *et al.*, 2000; D.-S. Kim *et al.*, 1994, 1995; Vienna *et al.*, 1997) |
| Aegirine (acmite) | $NaFe^{3+}Si_2O_6$ | (Bickford and Jantzen, 1984, 1986; Buechele *et al.*, 1990; Hrma *et al.*, 2003; Jantzen *et al.*, 1984; Kawamura and Ohuchi, 1995; Smith *et al.*, 2004; Spilman *et al.*, 1986) |
| | some Ca for Na substitution | (Spilman *et al.*, 1986) |
| | partial substitution of Fe by Cr | (Plaisted *et al.*, 2001) |
| Diopside | $CaMgSi_2O_6$ | (E. Wang *et al.*, 1994b) |
| | Diopsidic augite $(Mg,Fe^{2+})(Ca,Fe^{2+})Si_2O_6$ | (E. Wang *et al.*, 1994a) |
| | Al-containing diopside $(Ca,Mg,Al)_2(Si,Al)_2O_6$ | (Luckscheiter and Nesovic, 1996) |
| Augite | $(Ca,Na)(Mg,Fe,Al,Ti)(Si,Al)_2O_6$ | (Buechele *et al.*, 1990; Spilman *et al.*, 1986) |
| Omphacite | $(Ca,Na)(Mg,Fe^{2+},Al)Si_2O_6$ | (Muller *et al.*, 1999) |

### *2.8.4.3 Lithium Silicate*

Lithium silicate ($Li_2SiO_3$) has been reported in many borosilicate HLW glasses (Bickford and Jantzen, 1986; Crum *et al.*, 2002; Hrma *et al.*, 2003; Jantzen *et al.*, 1984; D.-S. Kim *et al.*, 1994, 1995; Lutze, 1988 and references therein; Riley *et al.*, 2002; Turcotte *et al.*, 1980). Lithium silicate formation is noted to lead to extensive microcracking of borosilicate HLW glass samples (Turcotte *et al.*, 1980). It has low aqueous durability, raising the leachate pH as it dissolves (Hrma *et al.*, 2003), with lithium silicate formation reducing the chemical durability of the wasteform (Riley *et al.*, 2002). D.-S. Kim *et al.* (1995) disagree however, stating that lithium silicate formation increases the chemical durability of the wasteform.

### *2.8.4.4 Nepheline*

Nepheline ($(Na,K)AlSiO_4$) has a distorted tridymite structure (Haaker and Ewing, 1981). Fe can substitute for Al (Haaker and Ewing, 1981; H. Li *et al.*, 2003), whilst both Cs (Barkatt *et al.*, 1983) and Ca (Haaker and Ewing, 1981) can substitute for Na/K. Nepheline has been observed in borosilicate HLW glasses (Bickford and Jantzen, 1986; Crum *et al.*, 2002; Hrma, 2002; Jacquet-Francillon *et al.*, 1982; Jantzen *et al.*, 1984; D.-S. Kim *et al.*, 1994, 1995; H. Li *et al.*, 1996a, 2003; Lutze, 1988 and references therein; Menkhaus *et al.*, 2000) and nucleates and grows rapidly during the slow cool after pouring (but not in the glass melter) (Hrma, 2002; Menkhaus *et al.*, 2000). The crystallisation of nepheline decreases the chemical durability of the wasteform (Crum *et al.*, 2002; D.-S. Kim *et al.*, 1995; H. Li *et al.*, 1996a, 2003; Lutze, 1988 and references therein; Menkhaus *et al.*, 2000) due to 3 moles of glass former per mole of glass modifier being consumed in its formation (Hrma, 2002; H. Li *et al.*, 1996a, 2003), lowering the chemical durability of the residual glass. Thermal expansion coefficient (TEC) and density mismatch between the nepheline and residual glass cause stressing and microcracking of the waste form (D.-S. Kim *et al.*, 1995). Nepheline becomes metamict (amorphous) upon exposure to the electron beam of a transmission electron microscope (TEM) (Clarke, 1983), indicating the low radiation tolerance of this phase.

### *2.8.4.5 Orthopyroxenes*

Orthopyroxenes are single-chain silicates of the orthorhombic crystal system (D.-S. Kim *et al.*, 1994). They are a solid solution (D.-S. Kim *et al.*, 1994) of general formula $(Fe^{2+},Mg^{2+},Mn^{2+})SiO_3$ or $(Fe^{2+},Mg^{2+},Mn^{2+})_2Si_2O_6$ (Webmineral, 2006). Orthopyroxenes have been noted in borosilicate HLW glasses (**Table 2.23**). Crystallisation of orthopyroxenes has no or negligible effect on the chemical durability of the wasteform (D.-S. Kim *et al.*, 1995). Although this contrasts with Riley *et al.* (2002) who report orthopyroxene crystallisation reduces the chemical durability of the wasteform.

**Table 2.23** Orthopyroxene phases noted in borosilicate HLW glasses.

| Name | Formula | Reference(s) |
|---|---|---|
| Orthopyroxene | $(Mg,Fe)SiO_3$ | (D.-S. Kim *et al.*, 1994, 1995) |
| Enstatite | $Mg_2Si_2O_6$ | (Hall *et al.*, 1976; Marples, 1988) |

### *2.8.4.6 Silicate Apatites*

Silicate apatites are of the hexagonal crystal system (space group $P6_3/m$) and have been observed in borosilicate HLW glasses (**Table 2.24**). Silicate apatites become metamict (amorphous) due to alpha irradiation, indicating they have a low radiation tolerance (Lutze, 1988; Quintas *et al.*, 2007). This change from crystalline to amorphous was accompanied by swelling (density change) which caused microcracking in the surrounding glass phase (Quintas *et al.*, 2007).

**Table 2.24** Silicate apatites observed in borosilicate HLW glasses.

| Phase | Notes | Reference(s) |
|---|---|---|
| $Ca_3Gd_7(SiO_4)_5(PO_4)O_2$ | | (Lutze, 1988; Turcotte *et al.*, 1980) |
| $(Ln_{3.33}\square_{0.67})Ln_6(SiO_4)_6O_2$ | (Ln is a lanthanide cation and □ is a vacancy), some B and Na substitution | (L. Li *et al.*, 2000a) |
| $Ca_{2+x}RE_{8-x}(SiO_4)_6O_{2-0.5x}$ | (RE = Nd or La; $x \approx 0.4$–0.7), possibly some B for Si substitution | (Quintas *et al.*, 2007) |
| $Na_xGd_{9.33-x/3}Si_6O_{26}$ | $(0 < x < 1)$ | (L. Li *et al.*, 2001a) |
| $Na_xLa_{9.33-x/3}Si_6O_{26}$ | $(0 < x < 1)$ | (L. Li *et al.*, 2001b) |
| $Ca_2Gd_8(SiO_4)_6O_2$ | | (Kahl, 1981) |
| $Ca_2Nd_8(SiO_4)_6O_2$ | | (Caurant *et al.*, 2006) |
| $NaGd_9(SiO_4)_6O_2$ | some B for Si substitution | (Zhao *et al.*, 2001) |
| $NaNd_9(SiO_4)_6O_2$ | | (Quintas *et al.*, 2007) |
| $(Na,Ca,RE)_5O(SiO_4)_3$ | | (Kawamura and Ohuchi, 1995) |
| $Ca_{10}(SiO_4)_3(SO_4)_3F_2$ | Fluorellestadite | (Crum *et al.*, 2002) |

### *2.8.4.7 Stillwellite*

Stillwellite ($LnBSiO_5$ where Ln = lanthanide(s)) is of the rhombohedral crystal system (space group $P3_1$) and can incorporate actinides (Th and U) and Ca on its Ln site (Burns *et al.*, 1993). Stillwellite has been described in borosilicate HLW glasses (Hyatt *et al.*, 2004; Lutze, 1988; Mitamura *et al.*, 1985). Hexagonal (Hyatt *et al.*, 2004; Mitamura *et al.*, 1985) and columnar (Mitamura *et al.*, 1985) morphologies have been observed. It is described as a chemically durable crystal phase (Mitamura *et al.*, 1986).

### *2.8.4.8 Zektzerite*

Zektzerite ($LiNaZrSi_6O_{15}$) is of the orthorhombic crystal system (space group *Cmca*) (Ghose and Wan, 1978), with minor amounts of Ti and Hf able to substitute for Zr (Dunn *et al.*, 1977). Acicular crystals of zektzerite have been noted in a borosilicate HLW glass (Hyatt *et al.*, 2004).

### *2.8.4.9 Other Silicate Phases*

There are other silicate phases reported in borosilicate HLW glasses (**Table 2.25**), many of these crystal phases belong to the feldspar, olivine and sodalite groups. In addition to these phases, willemite ($Zn_2SiO_4$) has also been observed (Lutze, 1988; Mendel *et al.*, 1976; Turcotte *et al.*, 1980), its formation leading to thermal expansion coefficient (TEC) mismatch between the crystal and the surrounding glass upon cooling, causing local stresses and cracks in the glass (Lutze, 1988; Mendel *et al.*, 1976). $NaFeSi_2O_6$ (no structural information) has also been noted (Turcotte *et al.*, 1980), its formation resulting in extensive microcracking of the wasteform. $LiAlSi_2O_6$ (no structural information) has also been reported (D.-S. Kim *et al.*, 1995), its formation decreasing the chemical durability of the wasteform. $\beta$-eucryptite ($\beta$-$LiAlSiO_4$) has also been observed (H. Li *et al.*, 1996a), its formation lowering the chemical durability of the wasteform. Olivine crystallisation is reported to reduce the chemical durability of the wasteform (Riley *et al.*, 2002).

**Table 2.25** Other silicate phases reported in borosilicate HLW glasses.

| Name | Formula | Reference(s) |
|---|---|---|
| $\beta$-spodumene | $\beta$-$LiAlSi_2O_6$ | (Healey *et al.*, 1979) |
| Cuspidine | $Ca_4F_2Si_2O_7$ | (Crum *et al.*, 2002) |
| Fluorophlogopite | $K_2(Mg,Fe^{2+})_6(Si_6Al_2O_{20})F_4$ | (E. Wang *et al.*, 1994a) |
| Fluorotremolite | $Ca_2(Mg,Fe^{2+})_5(Si_8O_{22})F_2$ | (E. Wang *et al.*, 1994b) |
| Forsterite | $Mg_2SiO_4$ | (Raman, 1998) |
| Gehlenite | $Ca_2Al_2SiO_7$ | (D.-S. Kim *et al.*, 1994) |
| Hiortdahlite | $(Na,Ca)_3Zr_{1-x}(Si_2O_7)(F,O)_2$ | (Crum *et al.*, 2002) |
| Kirschsteinite | $CaFe^{2+}(SiO_4)$ | (Shanggeng *et al.*, 1990) |
| Krinovite | $NaMg_2CrSi_3O_{10}$ | (D.-S. Kim *et al.*, 1994) |
| Lazurite | $Na_6Ca_2(AlSiO_4)_6SO_4$* | (Crum *et al.*, 2002) |
| Melilite | $(Ca,Na)_2(Al,Mg,Fe^{2+})(Si,Al)_2O_7$ | (Muller *et al.*, 1999) |
| Mullite | $(Al_4SiO_8)_{1.2}$ | (L. Li *et al.*, 2000b) |
| Norbergite | $Mg_2SiO_4 \cdot MgF_2$ | (E. Wang *et al.*, 1994b) |
| Nosean | $Na_8(AlSiO_4)_6SO_4$ | (Crum *et al.*, 2002) |
| Olivine | $MgFeSiO_4$ | (D.-S. Kim *et al.*, 1994, 1995) |
| Pargasite | $(Ca,Na)_{2-3}(Mg,Fe^{2+},Fe^{3+},Al)_5(Al,Si)_8O_{22}F_2$ | (E. Wang *et al.*, 1994a) |
| Parakeldyshite | $Na_2ZrSi_2O_7$ | (Hrma, 2002; Plaisted *et al.*, 2000) |
| Sodalite | $Na_8(AlSiO_4)_6(ClO_4)_2$* | (Crum *et al.*, 2002) |
| Thorite | $\alpha$-$ThSiO_4$ | (Mishra *et al.*, 2007) |
| Titanite | $CaTiSiO_5$ | (Lutze, 1988) |
| Wollastonite | $CaSiO_3$ | (C.-W. Kim *et al.*, 1996; D.-S. Kim *et al.*, 1994) |
| Zircon | $ZrSiO_4$ | (Crum *et al.*, 1997, 2002; Henry *et al.*, 2004; Hrma, 2002; D.-S. Kim *et al.*, 1994, 1995; Pinet *et al.*, 2006; Plaisted *et al.*, 2000; Raman, 1998) |
| Calcium silicophosphate | | (Orlhac *et al.*, 1999) |
| Cerium silicate | | (Lopez *et al.*, 2003) |
| Lithium aluminium silicate | | (D.-S. Kim *et al.*, 1994) |
| Neodymium silicate | | (Lopez *et al.*, 2003) |
| Rare earth silicates | | (Marples, 1988) |
| Sodium aluminosilicate | | (Orlhac *et al.*, 1999) |
| Sodium zirconium silicate | | (D.-S. Kim *et al.*, 1994) |
| | $CaMg_6Al_2Si_6O_{20}F_4$ | (E. Wang *et al.*, 1994a, 1994b) |
| | $Ca_2SiO_4$ | (Kahl, 1981) |
| | $Ca_2ZrSi_4O_{12}$ | (D.-S. Kim *et al.*, 1994) |
| | $Ca_3SiO_5$ | (Kahl, 1981) |
| | $(Ca,Fe,Mg)SiO_3$ | (Kahl, 1981) |
| | $HfSiO_4$ | (Lopez *et al.*, 2003) |
| | $NaAlSiO_4$ | (Turcotte *et al.*, 1980) |
| | $Li_2TiSiO_5$ | (Matzke *et al.*, 1984) |
| | $Ca_{10}Nd_7Si_{20.75}O_{62}$ | (Quintas *et al.*, 2007) |
| | $Na_2Ca_4(PO_3)_2SiO_4$* | (Crichton *et al.*, 1995) |
| | $Na_2ZrSi_2O_7$ | (Crum *et al.*, 1997) |

* Debatable

### 2.8.5 Phosphate Phases

Many phosphate crystal phases have been observed in borosilicate HLW glasses (**Table 2.26**). Phosphate phases have also been reported in 'yellow phase' (Cousi *et al.*, 2004; Henry *et al.*, 2004; Hrma *et al.*, 2006; Pinet *et al.*, 2006; Sullivan *et al.*, 1995). Lithium phosphate ($Li_3PO_4$) formation has been reported as having some effect (Buechele *et al.*, 1990) as well as negligible effect (Langowski *et al.*, 1996b) on wasteform chemical durability. Monazite is more chemically durable than borosilicate glass (Sales *et al.*, 1983), whilst $AlPO_4$ decreased (Langowski *et al.*, 1996b) and $Na_3Nd(PO_4)_2$ marginally improved (Langowski *et al.*, 1996b) the chemical durability of the wasteform. The observation of apatite in 'real' borosilicate HLW glasses (Cheron *et al.*, 1995) demonstrates its radiation tolerance.

**Table 2.26** Phosphate phases observed in borosilicate HLW glasses.

| Name | Formula | Reference(s) |
|---|---|---|
| Apatite | $Ca_{10}(PO_4)F_2$* | (Crum *et al.*, 2002) |
| Fluorapatite | $Ca_5(PO_4)_3F$ | (Crum *et al.*, 2002) |
| Monazite | $(RE)PO_4$ | (Mitamura *et al.*, 1985) |
| Apatite | | (Cheron *et al.*, 1995) |
| Barium phosphate | | (Arbab *et al.*, 2007) |
| Calcium phosphate | | (Henry *et al.*, 2004; Pinet *et al.*, 2006) |
| Lithium phosphate | | (Buechele *et al.*, 1990) |
| Magnesium phosphate | | (Arbab *et al.*, 2007) |
| Oxyapatite | | (Arbab *et al.*, 2007) |
| Sodium barium phosphate | | (Arbab *et al.*, 2007) |
| Sodium magnesium phosphate | | (Arbab *et al.*, 2007) |
| Sodium zinc phosphate | | (Arbab *et al.*, 2007; Henry *et al.*, 2004; Pinet *et al.*, 2006) |
| Zinc phosphate | | (Arbab *et al.*, 2007) |
| | $Li_3PO_4$ | (Jantzen *et al.*, 2001; D.-S. Kim *et al.*, 1994; Langowski *et al.*, 1996b; Sullivan *et al.*, 1995) |
| | $Na_3PO_4$ | (Crichton *et al.*, 1995; H. Li *et al.*, 1995) |
| | $Li_2NaPO_4$ | (Jantzen *et al.*, 2001) |
| | $NaCaPO_4$ | (Cousi *et al.*, 2004) |
| | $Ca_3(PO_4)_2$ | (Jantzen *et al.*, 2001; Yan *et al.*, 1995) |
| | $AlPO_4$ | (Langowski *et al.*, 1996b) |
| | $CePO_4$ | (H. Li *et al.*, 1996b) |
| | $NdPO_4$ | (Langowski *et al.*, 1996b) |
| | $Na_3Gd(PO_4)_2$ | (H. Li *et al.*, 1996b) |
| | $Na_3Nd(PO_4)_2$ | (Langowski *et al.*, 1996b) |

* Incorrect

### 2.8.6 Cerium Oxides

$CeO_2$ with the fluorite crystal structure (cubic system, space group $Fm\bar{3}m$) has been noted in borosilicate HLW glasses (F. Bart *et al.*, 2001; J. M. Bart *et al.*, 2000; Buechele *et al.*, 1990; Cachia *et al.*, 2006; Crum *et al.*, 1997; Guber *et al.*, 1979; Hall *et al.*, 1976; Jacquet-Francillon *et al.*, 1982; Kawamura and Ohuchi, 1995; H. Li *et al.*, 1996b; Lopez *et al.*, 2003; Lutze, 1988; Lutze *et al.*, 1979; Mendel *et al.*, 1976; Mitamura *et al.*, 1985; Orlhac *et al.*, 1999; Pacaud *et al.*, 1992; Turcotte *et al.*, 1980) and is chemically durable (Abdelouas *et al.*, 1997). Elements reported in this crystal phase are shown in **Table 2.27.** Crystals with the fluorite structure are noted as especially stable in displacive radiation damage environments (Sickafus *et al.*, 2000), evidenced by their presence in 'real' borosilicate HLW glasses (Cheron *et al.*, 1995). $Ce_2O_3$ has been observed to form when glasses are melted under reducing conditions (Jain *et al.*, 1991).

**Table 2.27** Elements reported in $CeO_2$ crystals found in borosilicate HLW glasses.

| Element | Reference(s) |
|---|---|
| Pu | (Lutze, 1988) |
| Ru | (F. Bart *et al.*, 2001) |
| Th | (Buechele *et al.*, 1990; Pacaud *et al.*, 1992) |
| U | (Jacquet-Francillon *et al.*, 1982; Pacaud *et al.*, 1992) |
| Zr | (F. Bart *et al.*, 2001; J. M. Bart *et al.*, 2000) |

### 2.8.7 Zirconium Oxides

Undoped zirconia can be of the monoclinic, tetragonal or cubic crystal system, depending on temperature (Yashima *et al.*, 1995). Zirconia (of all three crystal systems) has been observed in borosilicate HLW glasses **(Table 2.28)**, with the cubic zirconia incorporating Ce and occasionally Sm (O'Holleran *et al.*, 1998). The cubic phase (with fluorite structure) can be stabilised at room temperature by doping with the oxides of elements such as Y, Ca, Ce and Gd (Rebollo *et al.*, 2003; Yashima *et al.*, 1995), with cubic $ZrO_2$ being noted as especially stable in displacive radiation damage environments (Sickafus *et al.*, 2000). Stabilization of undoped $ZrO_2$ in cubic form is reported if the crystallites are small enough (<20 nm) (Martínez-Arias *et al.*, 1999 and references therein).

**Table 2.28** Zirconia phases (grouped by crystal system) observed in borosilicate HLW glasses.

| Crystal system | Reference(s) |
|---|---|
| Monoclinic (baddeleyite) | (Crum *et al.*, 1997, 2002; Henry *et al.*, 2004; Hrma, 2002; McKeown *et al.*, 1999; Pinet *et al.*, 2006; Plaisted *et al.*, 2000) |
| Tetragonal | (Henry *et al.*, 2004; Pinet *et al.*, 2006) |
| Cubic | (O'Holleran *et al.*, 1998) |
| Unidentified | (D.-S. Kim *et al.*, 1994) |

### 2.8.8 Uranium and Plutonium Phases

Uranium oxide crystals (with star-shaped morphologies) have been noted in borosilicate HLW glasses (Buechele *et al.*, 1995). Also observed are $PuO_2$ crystals (Bates *et al.*, 1995; Hall *et al.*, 1976; Lutze and Ewing, 1995; Muller *et al.*, 1999) which can incorporate Ce (Lutze and Ewing, 1995; Muller *et al.*, 1999) and Gd (Lutze and Ewing, 1995).

### 2.8.9 Other Metallic Phases

Metallic silver has been reported in borosilicate HLW glasses (H. Li *et al.*, 2003; Short, 2004; Short *et al.*, 2005), generally when they are melted under reducing conditions.

### 2.8.10 All Other Crystal Phases

All the other crystal phases which have been reported in borosilicate HLW glasses but could not be placed in any of the preceding sections are listed in **Table 2.29**. In addition, gadolinium titanate ($(Gd,Cm)_2Ti_2O_7$) with pyrochlore structure (cubic crystal system) has been observed in borosilicate HLW glasses (Lutze, 1988). This crystal phase became metamict (amorphous) due to alpha radiation, indicating it has a low radiation tolerance.

**Table 2.29** All other crystal phases reported in borosilicate HLW glasses.

| Name | Formula | Reference(s) |
|---|---|---|
| Bunsenite | $NiO$ | (C.-W. Kim *et al.*, 1996) |
| Eskolaite | $Cr_2O_3$ | (Healey *et al.*, 1979; Hrma *et al.*, 2006; C.-W. Kim *et al.*, 1996; D.-S. Kim *et al.*, 1994; Langowski *et al.*, 1996b; H. Li *et al.*, 1996b) |
| Fluorspar (fluorite) | $CaF_2$ | (Crichton *et al.*, 1995; Crum *et al.*, 2002; E. Wang *et al.*, 1994a, 1994b) |
| Haematite | $\alpha$-$Fe_2O_3$ | (Hrma, 2002; D.-S. Kim *et al.*, 1994, 1995) |
| Perovskite | $CaTiO_3$ | (Guber *et al.*, 1979; Matzke *et al.*, 1984) |
| Rutile | $TiO_2$ | (Lutze, 1988; Matzke *et al.*, 1984) |
| Suanite | $Mg_2B_2O_5$ | (Hall *et al.*, 1976; Lutze, 1988) |
| Thorianite | $ThO_2$ | (Mishra *et al.*, 2007) |
| Eskolaite with Fe | | (H. Li *et al.*, 1996a) |
| Neodymium oxide | | (Short, 2004) |
| | $(Fe,Ni)CrO_4$ | (Sengupta *et al.*, 2006) |
| | $GdTi_2O_7$* | (Turcotte *et al.*, 1980) |
| | $HfO_2$ | (Lopez *et al.*, 2003) |
| | $TcO_2$ | (Lukens *et al.*, 2004) |
| | $NaCl$ | (Crichton *et al.*, 1995; H. Li *et al.*, 1996b) |
| | $NaF$ | (Crichton *et al.*, 1995; Crum *et al.*, 2002; H. Li *et al.*, 1996b) |

* Incorrect

## 2.9 Amorphous Phase Separation (APS) of Borosilicate HLW Glasses

APS has been observed in many borosilicate HLW glasses (L. Li *et al.*, 2001a; Lutze, 1988 and references therein; Malow, 1989; Quintas *et al.*, 2007; Shanggeng *et al.*, 1990; E. Wang *et al.*, 1994b), this is unsurprising since their compositions lie close to the 'traditional' immiscibility region (Marples, 1988). The 'traditional' immiscibility region for the ternary $Na_2O$-$B_2O_3$-$SiO_2$ system extends up to ~16–20 mol% $Na_2O$ when $SiO_2$ levels are above ~20 mol%, whilst the 'traditional' immiscibility region of the ternary $Li_2O$-$B_2O_3$-$SiO_2$ system is larger still (Mazurin *et al.*, 1984). However, there is still controversy as to where the immiscibility boundary in these borosilicate glass systems actually lie (Tomozawa, 1999). Whether or not APS has occurred in a particular glass is often determined by visual inspection (Du and Stebbins, 2003; Mazurin *et al.*, 1984 and references therein; Tomozawa, 1999), which can only fuel the immiscibility boundary controversy. As the quench rate of an alkali borosilicate glass melt (whose composition is within the 'traditional' immiscibility region) decreases, the domain size of the resultant APS increases (Tomozawa, 1999; Yazawa *et al.*, 2000). Sodium borosilicates which have undergone APS can have domain sizes of <5 nm (Sun *et al.*, 2004), or even

<1 nm (Yazawa *et al.*, 2000). APS of alkali borosilicate glasses results in an alkali borate phase and a vitreous silica phase (Hair and Chapman, 1966). The alkali borate phase is of lower chemical durability, and the vitreous silica phase is of higher chemical durability than the parent glass (Hair and Chapman, 1966; Paul, 1990; Shelby, 1997). As HLW radionuclides tend to partition into the less durable alkali borate phase, this is the phase that will determine the chemical durability of borosilicate HLW glasses in which APS occurs (Sproull *et al.*, 1994). Additions of $Al_2O_3$ suppress APS in alkali borosilicate glasses (Sproull *et al.*, 1994).

## 2.10 Chemical (Aqueous) Durability of Borosilicate HLW Glasses

Chemical durability is a direct measure of the ability of a wasteform to retain its radionuclide inventory (Lutze, 1988). However, as wasteform performance cannot be measured directly over geological time periods it must be evaluated from short-term laboratory tests and/or from comparison with geological occurrences of structurally and chemically similar materials ('natural analogues') (Ebert and Mazer, 1994; Ewing, 2001; Inagaki *et al.*, 1998).

### 2.10.1 Aqueous Corrosion of Silicate Glasses: Overview

Upon glass contacting aqueous solution, water molecules and water-derived ionic species ($H_3O^+$, $OH^-$) diffuse into the glass (hydration). This results in the release of soluble network modifying cations (ion exchange) as well as break-up of the polymeric glass network (hydrolysis), forming silanol groups (Si–OH). The silanol groups may partially repolymerise (condensation), forming a Si-rich gel layer at the glass-solution interface. Further hydration of the Si-rich gel can release silicic acid into solution (dissolution). Precipitation from solution of amorphous and crystalline phases can also occur at the glass-solution interface. All of these processes may occur simultaneously at the molecular level (Abraitis *et al.* 2000; Bourcier, 1991; Bunker, 1994; Ebert and Mazer, 1994). The aqueous corrosion of silicate glasses is shown schematically in **Figure 2.3.**

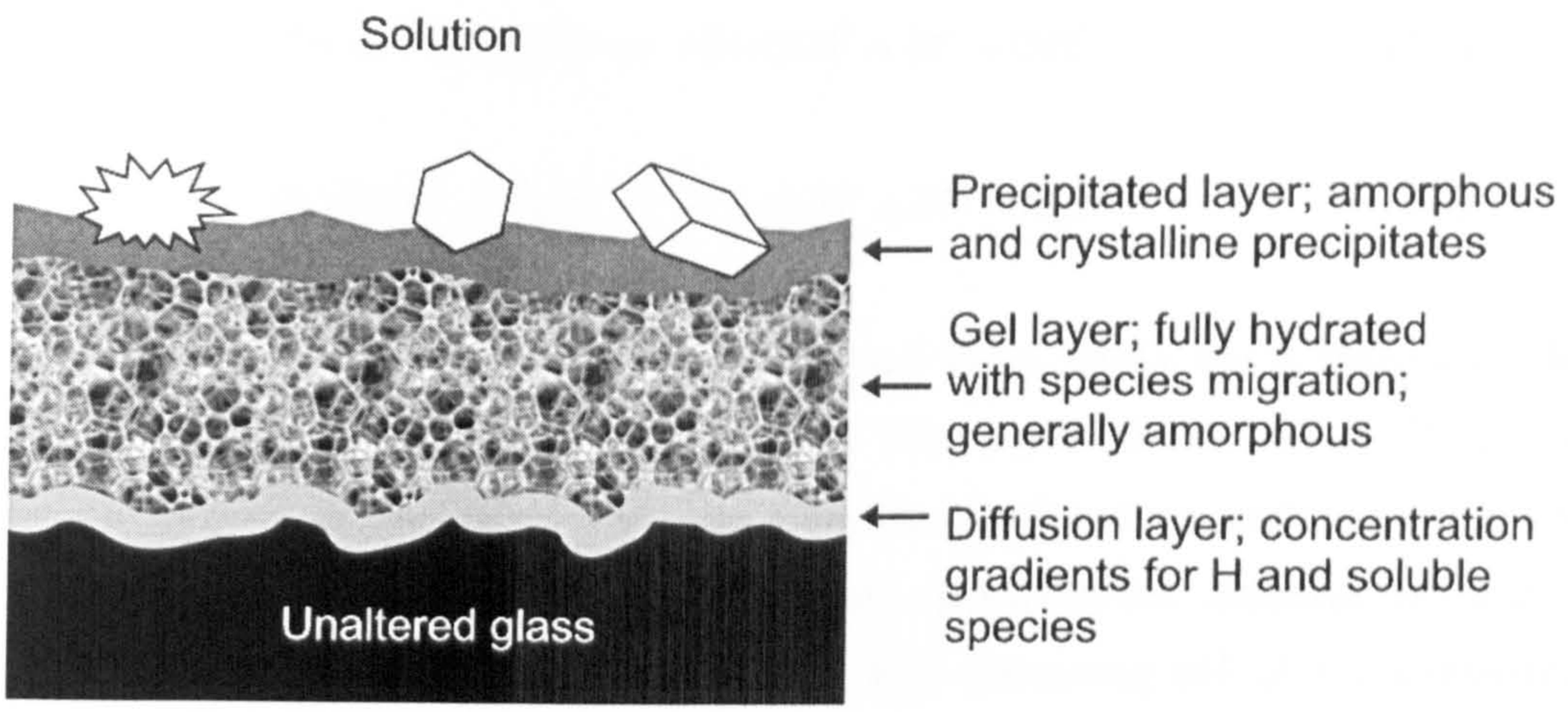


**Figure 2.3** Schematic of the features associated with aqueous corrosion of silicate glasses. Adapted from Bourcier (1991), Inagaki *et al.* (1998) and Wicks (1992).

### 2.10.2 Interdiffusion (Hydration and Ion Exchange)

After aqueous solution contacts glass, water and water-derived ionic species diffuse into the glass (Vernaz *et al.*, 2001). Network modifier channels (percolation channels) are the likely route of water (and water-derived ionic species) infusion into the glass (Greaves, 1990; Hand and Seddon, 1997), assuming the model of glass structure proposed by Greaves (1985) is correct. Formation of water-derived ionic species may be written (Greenwood and Earnshaw, 2002; Hand and Seddon, 1997):

$$2H_2O \leftrightarrow H_3O^+ + OH^- \qquad (2.2)$$

Interdiffusion refers to the concomitant diffusion of water (and $H_3O^+$, $OH^-$) into the glass (hydration) and glass modifier cations out of the glass (ion exchange). Ion exchange occurs on sites within the glass where network modifying cations (such as alkali and alkaline earth cations) charge compensate negative charge centres such as non-bridging oxygens (NBO) and network $[B\emptyset_4]^-$, $[Al\emptyset_4]^-$ and $[Fe\emptyset_4]^-$ groups. Release of a modifying cation via ion exchange may be written (Ebert and Mazer, 1994):

$$\equiv Si\text{–}O^{-}M^{+} + H_2O \rightarrow \equiv Si\text{–}O^{-}H^{+} + M^{+} + OH^{-} \quad (2.3)$$

$$\equiv Si\text{–}O^{-}M^{+} + H_3O^{+} \rightarrow \equiv Si\text{–}O^{-}H^{+} + M^{+} + H_2O \quad (2.4)$$

Ion exchange increases the solution pH (Feng and Pegg, 1994), but is slowed by the build up of alkali and hydroxide in solution (Ebert and Mazer, 1994). Doremus' interdiffusion model (Doremus, 1982) describes the kinetics of ion exchange reactions. Ion exchange rates have Arrhenius temperature dependencies, diminish as inverse square root of time, and decrease as $10^{-0.5pH}$ with increasing pH of the contacting solution (Ojovan *et al.*, 2006).

### 2.10.3 Hydrolysis and Dissolution

Hydrolysis reactions result in cleavage of bridging oxygen (BO, shown as Ø) bonds within the covalently bonded glass network, ultimately resulting in the dissolution of the glass network. Hydrolysis of Si–Ø–Si linkages is thought to occur via nucleophilic attack on the silicon atom by species such as molecular water or hydroxide ions (Ebert and Mazer, 1994). Hydrolysis of a Si–Ø–Si linkage can be written:

$$\equiv Si\text{–}Ø\text{–}Si\equiv + H_2O \leftrightarrow \equiv Si\text{–}OH + \equiv Si\text{–}OH \quad (2.5)$$

$$\equiv Si\text{–}Ø\text{–}Si\equiv + OH^{-} \leftrightarrow \equiv Si\text{–}OH + \equiv Si\text{–}O^{-} \quad (2.6)$$

The above reactions can also occur for BO associated with other network forming elements such as B, Al and Fe (Sheng *et al.*, 1999). High pH accelerates hydrolysis of the glass network, so the pH increase associated with alkali release slows the reactions to release alkali but accelerates the hydrolysis reactions (Ebert and Mazer, 1994).

Release of silicon during glass dissolution requires complete hydrolysis of all network bonds connecting the silicate group (dissolution). The final hydrolytic reaction results in the release of silicic acid (Ebert and Mazer, 1994):

$$\equiv Si\text{–}Ø\text{–}Si(OH)_3 + H_2O \leftrightarrow \equiv Si\text{–}OH + Si(OH)_4 \quad (2.7)$$

$$\equiv Si\text{–}Ø\text{–}Si(OH)_3 + OH^{-} \leftrightarrow \equiv Si\text{–}O^{-} + Si(OH)_4 \quad (2.8)$$

Similar reactions occur for the hydrolysis of other network formers. The release of boron (as boric acid) may be written (Ebert and Mazer, 1994):

$$\equiv Si–Ø–B(OH)_2 + H_2O \rightarrow \equiv Si–OH + B(OH)_3 \quad (2.9)$$

$$\equiv Si–Ø–B(OH)_2 + OH^- \rightarrow \equiv Si–O^- + B(OH)_3 \quad (2.10)$$

The above reactions depolymerise the glass network and produce silanol groups. Increasing concentrations of $H_4SiO_4$ in solution is reported to decrease the glass dissolution rate (Bourcier, 1991; Ebert and Mazer, 1994). A general rate equation has been fashioned to describe the hydrolytic dissolution of silica glass (Aagaard and Helgeson, 1982). The hydrolytic dissolution rate has Arrhenius temperature dependence, increases as $10^{0.5pH}$ with increasing pH of the contacting solution, and results in congruent release of glass constituents into solution.

The hydrolysis of network bonds within the glass network governs the overall rate of dissolution following an initial, short-lived period of ion exchange and surface gel layer formation (Abraitis *et al.*, 2000). However, at reduced temperatures and in silica-saturated conditions, ion exchange reactions can persist for geological timescales (McGrail *et al.*, 2001b; Ojovan *et al.*, 2006).

### 2.10.4 Gel Layer and Precipitated Layer Formation

The silanol groups described above may also undergo condensation reactions, resulting in a reversal of the hydrolysis reaction (**Equation 2.5** and **Equation 2.6**):

$$2(\equiv Si–OH) \leftrightarrow \equiv Si–Ø–Si\equiv + H_2O \quad (2.11)$$

$$\equiv Si–OH + \equiv Si–O^- \leftrightarrow \equiv Si–Ø–Si\equiv + OH^- \quad (2.12)$$

A large proportion of metastable silanol groups undergo condensation to yield highly polymerised Si-rich gels (Bunker, 1987). Reactive sites at the glass surface can also react with solution species (Fleming, 1986), although such polymerisation reactions are pH dependent, according to the reaction:

$$\equiv Si–O^- + H_4SiO_4 \leftrightarrow \equiv Si–Ø–Si(OH)_3 + OH^- \quad (2.13)$$

$$\equiv Si\text{–}OH + H_4SiO_4 \leftrightarrow \equiv Si\text{–}Ø\text{–}Si(OH)_3 + H_2O \qquad (2.14)$$

The amorphous gel layer is metastable and ultimately crystallises at high temperatures and/or with time (Bourcier, 1991; Curti *et al.*, 2006; Frugier *et al.*, 2005; Grambow, 1992; White, 1992). The outer surface of the altered glass (above the gel layer) may comprise a non-continuous precipitation layer which can contain amorphous and crystalline phases (Bourcier, 1991; Lutze, 1988).

Crystal phases formed in the gel layer or precipitated directly from solution onto the glass-solution interface include: smectites such as hectorite, montmorillonite and saponite; aluminosilicates, *e.g.* zeolites; serpentines; transition metal oxides; hydrated calcium silicates, lanthanide phosphates and other silicate phases (Bourcier, 1991; Curti *et al.*, 2006; Frugier *et al.*, 2005; Grambow, 1992; Matzke and Vernaz, 1993).

### 2.10.5 Aqueous Durability of Borosilicate HLW Glasses: Influences

The aqueous durability of borosilicate HLW glasses decreases with increasing temperature of the contacting solution (Donald *et al.*, 1997; Larkin, 1986; Wicks, 1992). Hydrothermal (high temperature, high pressure) conditions may arise in a geological repository due to the radiogenic heat from the vitrified HLW and the pressure of the overburden (Komarneni *et al.*, 1983).

Several borosilicate HLW glass compositions have shown an increase in their aqueous corrosion rates at long reaction times after previously falling to a very low residual rate. Precipitation of secondary phases and their effect on solution chemistry is thought to be responsible for this rate increase (Ebert and Mazer, 1994; McGrail *et al.*, 2001b). The low residual glass corrosion rate (which was thought to be the result of a protective gel layer or solution saturation with respect to silica and other species) is actually due to a dynamic equilibrium that is established between silica dissolution (from the glass and gel layer) and recondensation (of silica onto/into the gel layer), illustrating how secondary phase precipitation would upset this equilibrium and be responsible for corrosion rate changes (Vernaz *et al.*, 2001). The precipitation of secondary phases generally increases the aqueous corrosion rate of borosilicate HLW glasses (Ferrand *et al.*, 2006).

The presence of iron and steel corrosion products can increase the aqueous corrosion rate of borosilicate HLW glasses (Barkatt *et al.*, 1985; Donald *et al.*, 1997;

Lutze, 1988 and references therein; Marples, 1988). Groundwaters contain a large number of cationic and anionic species, as well as colloidal particles. The interaction between vitrified HLW and groundwaters can change the chemistry of both the solid and the solution (Bunker, 1987). Most groundwaters are less aggressive than deionised water, a common leachant in wasteform chemical durability tests, indicating that actual glass corrosion rates in a geological repository will be lower than those determined in the laboratory (Wicks, 1986). The leach rate of borosilicate HLW glasses is at a minimum in neutral pH solutions (pH 5–9) (Abraitis *et al.*, 2000; Clark and Zoitos, 1992; Lutze, 1988; Marples, 1988; Wicks, 1992). Granitic, basaltic and tuffaceous groundwaters are typically neutral to slightly alkaline, whilst salt environments result in neutral to slightly acidic groundwaters (Donald *et al.*, 1997; Lutze, 1988). Both silicic acid (Feng and Pegg, 1994) and boric acid (Feng and Pegg, 1994; Lutze and Grambow, 1992; Macedo *et al.*, 1982) buffer the solution pH increase caused by ion exchange. In acidic to mildly basic media, thick siliceous gels develop which are strongly depleted in alkalis and boron (Abraitis, 1999; Bourcier, 1991; Chêne and Trocellier, 2004; Trocellier *et al.*, 2005). In basic media, gel dissolution is rapid as recondensation is not favoured, resulting in thin or non-existent gel layers whilst alkalis and boron are at nominal concentrations at the glass-solution interface (Abraitis, 1999; Bourcier, 1991; Frugier *et al.*, 2005; Trocellier *et al.*, 2005). The alkalis and boron are strongly depleted at the glass-solution interface in acidic to mildly basic solutions due to the high concentration of $H^+$ in solution increasing the diffusion gradients, and therefore the diffusion rates, of water and water-derived ionic species, as well as those of the alkalis and boron (Bourcier, 1991). The behaviour of silica across the pH spectrum is explained by the good stability of the Si–Ø–Si bond in acidic media compared to basic media (Abraitis, 1999; Trocellier *et al.*, 2005). The majority of transition metals, lanthanides and actinides are noted in the gel layer of corroded glasses but are not detected at significant levels in the leachate solution. This behaviour is pH dependent, with increasingly acidic media leading to their depletion in the gel layer and increasing concentration in solution (Abdelouas *et al.*, 1997; Abraitis, 1999; Barkatt *et al.*, 1981, 1983; Ménard *et al.*, 1998; Plodinec, 1986; Trocellier *et al.*, 2005). However, Pu is generally found in colloidal particles as opposed to the gel or precipitated layers (Ménard *et al.*, 1998; Werme *et al.*, 1990).

Increasing the glass surface area (*SA*) to solution volume (*V*) ratio (*SA*/*V*): reduces the time required for the solution to reach saturation (White, 1992); increases the rate of pH rises during chemical durability testing (Clark and Hench, 1981);

increases the concentration of species in saturated solution (Clark and Hench, 1981; Ebert and Mazer, 1994) and increases the stabilised solution pH (Feng and Pegg, 1994). Chemical durability models for borosilicate HLW glasses consider leaching rates from the glass to be directly proportional to *SA/V* (Bickford *et al.*, 1990a). *SA/V* changes can also affect: gel layer thickness, secondary phase identity and glass leaching mechanism (Feng and Pegg, 1994).

The leach rates of borosilicate glasses are lowest when the alkali oxide to boron oxide content is equimolar (Bunker, 1987; Marples, 1988), with the leach rates further lowered if the alkali oxide content is comprised of equimolar amounts of two different alkali oxides, the 'mixed alkali' effect (Marples, 1988). Wicks (1986) reports that increased waste loading in a borosilicate HLW glass increased its aqueous durability. This is explained by the fact the simulated HLW contained high levels of $Al_2O_3$ and $Fe_2O_3$, which can act as network formers (they are intermediates) (Lutze, 1988). The concentration of lanthanides (La, Nd and Ce) in solution has been noted to show a concentration peak at the beginning of aqueous durability tests and then to rapidly diminish, behaviour which has been linked to the formation of an interphase (gel layer) (Gauthier *et al.* 2000). Increasing alkali oxide and/or boron oxide concentrations in alkali borosilicate glasses reduces their aqueous durability (Hall *et al.*, 1976; Ledieu *et al.*, 2004). For several low aqueous durability borosilicate HLW glasses, gel layer formation is largely complete within 10 d (Barkatt *et al.*, 1983).

As a general rule, glass corrosion rates (during aqueous durability testing) decrease with time in a closed system, but become constant with time in a flowing system with no transport barriers (Clark and Zoitos, 1992; Donald *et al.*, 1997), with flow rate affecting both the pH and chemical composition of the solution (McGrail *et al.*, 2001a). Glass corrosion rates increase with increasing solution flow rates, although a maximum corrosion rate will be reached at high flow rates (Clark and Zoitos, 1992; Ebert and Mazer, 1994; Lutze, 1988; Marples, 1988). Dynamic (flowing) experiments prevent substantial secondary phase precipitation (Ferrand *et al.*, 2006).

The factor governing silica recondensation (onto/into the gel layer) is its transport flux into the environment. The presence of materials with high silica sorption capability (such as clays and some metallic corrosion products) prevents dynamic equilibrium being established between silica dissolution and recondensation until most of the sorption sites have become saturated, during which time the glass dissolution rates are very high. The addition of glass frit or siliceous material to a clay backfill barrier eliminates its sorption capability (Vernaz *et al.*, 2001).

The retention of radionuclides in glass alteration layers influences their release into solution (Gong *et al.*, 1998). Secondary phase precipitation creates new (potential) retention barriers for radionuclides (Abdelouas *et al.*, 1997; Curti *et al.*, 2006), with almost quantitative fixation of many radionuclides in/on secondary phases (Curti *et al.*, 2006).

The presence of Al (Abraitis *et al.*, 2000; Barkatt *et al.*, 1983; Clark *et al.*, 1982; Lutze, 1988; Marples, 1988), Ca and Zn (Lutze, 1988) in a borosilicate glass all improve its aqueous durability. The presence of Mg is also reported to improve the aqueous durability of borosilicate glass (Lutze, 1988). However, the Mg actually removes silica from solution during the formation of clay secondary phases, altering the dynamic equilibrium between silica dissolution and recondensation and promoting glass corrosion (Curti *et al.*, 2006).

The REDOX potential (Eh) of contacting solutions is reported to affect the solubility of multivalent cations. Anoxic (reducing) contacting solutions are reported to reduce the solubility of multivalent cations, thereby increasing the chemical durability of borosilicate HLW glasses (Lutze, 1988). Granitic and basaltic repositories have anoxic groundwaters, tuffaceous and salt repositories have mildly anoxic goundwaters (Lutze, 1988).

## 2.11 Aqueous Durability of Borosilicate HLW Glasses: Effect of Glass Phase Transformations

### 2.11.1 Crystallisation (Devitrification)

Crystallisation of borosilicate HLW glasses has been noted to have a negative (Crum *et al.*, 2002; Lutze, 1988; Mendel *et al.*, 1976; Mitamura *et al.*, 1986; Spilman *et al.*, 1986), positive (Hall *et al.*, 1976; Larkin, 1986) or negligible effect (Kahl, 1981; Shanggeng *et al.*, 1990) on their aqueous durabilities. The cumulative effect of each crystal phase on aqueous durability will determine the effect of crystallisation on the aqueous durability of the wasteform.

The crystallisation of borosilicate HLW glasses is undesirable if: (1) the crystal phases formed are water soluble, especially if HLW radionuclides preferentially partition to these crystal phases; (2) the crystal phases formed deplete the glass matrix of glass formers and intermediates (Bickford and Jantzen, 1984; D.-S. Kim *et al.*, 1995; Sproull *et al.*, 1994; Zhu *et al.*, 1986), resulting in a residual glass of lower chemical

durability than the parent glass and (3) there is preferential corrosion at the glass-crystal interface (Clark and Hench, 1981; Hrma *et al.*, 2003; D.-S. Kim *et al.*, 1995; Sproull *et al.*, 1994; Zhu *et al.*, 1986), which can be due to compositional gradients and/or thermal expansion coeffiecient (TEC) mismatch at these interfaces causing stresses and microcracking (Hrma *et al.*, 2003; D.-S. Kim *et al.*, 1995; Sproull *et al.*, 1994), this is particularly undesirable since HLW radionuclides tend to concentrate at these interfaces (Clark and Hench, 1981; Zhu *et al.*, 1986).

Ideally, a crystallised borosilicate HLW glass would be composed of crystal phases of high chemical durability (to which HLW radionuclides would preferentially partition) homogeneously distributed within a residual glass matrix whose chemical durability is higher than that of its parent glass (due to the formation of the crystal phases). In addition to the above, the crystal phases would be radiation tolerant (including accommodating transmutations), the crystal phases and residual glass matrix would have similar thermal expansion coefficients (TECs) and the crystal phases would not undergo any crystal phase transitions during cooling from their nucleation/growth temperatures (these last two requirements would eliminate stressing/cracking of the wasteform).

### 2.11.2 Amorphous Phase Separation (APS)

**Table 2.30** details the effect of APS on the aqueous durability of alkali borosilicate glasses, depending upon their APS microstructure.

**Table 2.30** Effect of APS on the aqueous durability of alkali borosilicate glasses, depending upon their APS microstructure (Jantzen *et al.*, 2001).

| Type | APS microstructure | APS mechanism | Effect on aqueous durability of glass |
|---|---|---|---|
| A | Vitreous silica phase and alkali borate phase are continuous and interconnected | Spinodal decomposition | Negative |
| B | Vitreous silica droplets dispersed within a continuous alkali borate matrix | Nucleation and growth | Negative |
| C | Alkali borate droplets dispersed within a continuous vitreous silica matrix | Nucleation and growth | Positive |

# 3 Experimental Procedures

## 3.1 Materials and Processing

### 3.1.1 Supplied Glasses

The simulated (non-radioactive) borosilicate HLW glasses used in this work were supplied by Nexia Solutions. They were produced during inactive commissioning of full-scale vitrification lines at Sellafield, Cumbria. Manufacturing the simulated glasses on full-scale vitrification lines (as described in **Section 2.5**) replicates 'real' (radioactive) borosilicate HLW glasses (which are manufactured on similar vitrification lines) better than laboratory-scale glass melts.

The two glasses Nexia Solutions supplied were: (1) simulated Blend glass and (2) simulated Magnox glass. However, chemical analysis (**Table 4.1.1**) revealed the Magnox glass to be erroneously identified Oxide glass, so this work is concerned with the study of: (1) simulated Blend glass and (2) simulated Oxide glass. A description of the simulated reprocessing waste(s) vitrified by these glasses can be found in **Section 2.4.2**. Glass samples were from multiple, unidentified batches. Both glasses were received in the as-cast state and had not been annealed. They have been given identifying codes (**Table 3.1**). A sample of simulated Oxide glass contained a 'yellow phase' inclusion which, after extraction from the glass bulk with a stainless steel spatula, was also investigated during this work. This glass sample had previously been incorrectly identified as both simulated Magnox glass (Short, 2004) and simulated Blend glass (Nexia Solutions).

**Table 3.1** Identifying codes of as-cast simulated borosilicate HLW glasses.

| Code | Description |
|---|---|
| Blend AC | Simulated Blend glass, as-cast |
| Oxide AC | Simulated Oxide glass, as-cast |

### 3.1.2 Glass Heat Treatment

Samples of both as-cast glasses were heat treated to replicate the retarded cooling experienced by 'real' borosilicate HLW glasses after pouring (as described in **Section 2.6.5**). Heat treatments were conducted in a Lenton 1500 W muffle furnace calibrated prior to every use with a calibrated Type K thermocouple. All heat treatments were conducted in an air atmosphere, with glass samples sectioned using a Struers Accutom-5 diamond saw to approximately 1 × 1 × 2 cm in size and then placed on a bed of calcined alumina in a mullite tray. Samples were heated from room temperature to 690 °C at 5 °C $min^{-1}$, held at this temperature for 70 h, cooled to 500 °C at 5 °C $min^{-1}$ for a 1 h anneal and then cooled to room temperature at 5 °C $min^{-1}$. Any calcined alumina adhering to the heat treated glass samples was removed using 120 grit SiC paper and water. Both heat treated glasses have been given identifying codes (**Table 3.2**).

**Table 3.2** Identifying codes of heat treated simulated borosilicate HLW glasses.

| Code | Description |
|---|---|
| Blend HT | Simulated Blend glass, heat treated at 690 °C for 70 h |
| Oxide HT | Simulated Oxide glass, heat treated at 690 °C for 70 h |

## 3.2 Analysis

### 3.2.1 Direct Current Plasma Atomic Emission Spectroscopy (DCP-AES)

A Spectrometrics Incorporated SMI III utilising argon plasma was employed for DCP-AES analysis of glass samples, the 'yellow phase' sample and leachates from chemical (aqueous) durability testing. Glass samples, as well as the 'yellow phase' sample, were analysed to obtain weight percent values of $B_2O_3$ and $Li_2O$ to combine with X-ray fluorescence spectroscopy (XRF) data (**Section 3.2.2**) thereby determining their chemical compositions. Leachates from chemical (aqueous) durability testing (**Section 3.2.8**) were analysed by DCP-AES to yield the concentration of certain elements in solution. A multielement solution standard was tested alongside the sample solutions to ensure the accuracy of the DCP-AES data.

Three samples of each glass (Blend AC and Oxide AC) were crushed in a steel percussion mortar and then ground with an agate pestle and mortar before sieving to <75 $\mu$m. Next, 0.0990–0.1000 g of each glass sample was placed in a Teflon container

for microwave dissolution. The 'yellow phase' sample was ground with an agate pestle and mortar before sieving to <75 $\mu$m. However, due to the small amount of 'yellow phase' available (~0.06 g) the whole sample was analysed by XRF before a single 0.0248 g sample was placed in a Teflon container for microwave dissolution. Microwave dissolution of the samples was undertaken with HF-$HNO_3$ solution (50 % HF and 70 % $HNO_3$ solutions in a 1:5 volume ratio) in a CEM MSP 1000 microwave before analysis. Sample weight and solution volume were required by the attached computer software. Container 'blanks' were analysed to check for possible contamination from the Teflon containers and/or HF-$HNO_3$ solution. A multicomponent borosilicate glass, National Institute of Standards and Technology (NIST) standard reference material 1412 (**Appendix, Table A.1**), was also analysed to ensure the accuracy of compositional data. The elements analysed for in glass and 'yellow phase' samples are shown in **Table 3.3**.

**Table 3.3** Elements analysed for by DCP-AES in glass and 'yellow phase' samples.

| | | |
|---|---|---|
| Al | K | Pb |
| B | Li | Si |
| Ba | Mg | Sr |
| Ca | Mn | Ti |
| Cd | Na | U |
| Cr | Ni | Zn |
| Fe | P | Zr |

Analysis of acidified leachate samples yielded elemental concentrations in solution, reported in mg $l^{-1}$ (interchangeable with $\mu$g $ml^{-1}$ and wtppm). The elements analysed for in leachate samples (together with their detection limits) are shown in **Table 3.4**. Uncertainty for all elements having concentrations greater than 2 mg $l^{-1}$ is 10 % relative.

**Table 3.4** DCP-AES detection limit (DL) of all elements analysed for in leachate samples.

| Element | DL (mg $l^{-1}$) | Element | DL (mg $l^{-1}$) | Element | DL (mg $l^{-1}$) |
|---|---|---|---|---|---|
| Al | 0.63 | La | 0.63 | Ni | 0.84 |
| B | 4.20 | Li | 1.05 | P | 12.60 |
| Ba | 0.04 | Mg | 0.21 | Ru | 1.47 |
| Ca | 0.08 | Mn | 0.84 | Si | 0.84 |
| Cr | 0.21 | Mo | 1.26 | Sr | 0.06 |
| Fe | 1.05 | Na | 0.21 | Ti | 0.42 |
| K | 1.68 | Nd | 0.84 | Zr | 0.42 |

### 3.2.2 X-Ray Fluorescence Spectroscopy (XRF)

An ARL 9400 Sequential XRF analysed glass and 'yellow phase' samples for all elements heavier than boron. UniQuant v4.44 software calculated the oxide composition of samples once their respective DCP-AES data (**Section 3.2.1**) for $B_2O_3$ and $Li_2O$ were entered. The XRF operated with a Cu-filtered Rh X-ray source, gas flow proportional counter employing P-10 gas (90 % argon and 10 % methane) and a scintillation counter. The scintillation counter was used to detect short wavelengths (with the X-ray tube operating at 60 kV and 40 mA) whilst the gas flow proportional counter was used for detecting long wavelengths (with X-ray tube settings of either 40 kV and 60 mA, or 30 kV and 80 mA). The machine used LiF200, LiF220, LiF420, Ge111, and TlAP analysing crystals and operated with a helium atmosphere.

The three samples of each glass (Blend AC and Oxide AC) and one of 'yellow phase' prepared in **Section 3.2.1** were analysed. Approximately 2 g of each glass sample and the whole of the 'yellow phase' sample (~0.06 g) were placed in plastic sample holders for loading into the machine. The mean of the three normalised chemical compositions obtained for both glasses are reported, together with the standard deviation ($1\sigma$) of each component. The chemical composition of the 'yellow phase' is also reported.

### 3.2.3 Differential Thermal Analysis (DTA)

DTA of glass samples was conducted using a Perkin Elmer DTA 7 running Perkin Elmer PYRIS v5.00.02 thermal analysis software. Samples of each glass (Blend AC and Oxide AC) were crushed in a steel percussion mortar and then ground with an agate pestle and mortar before sieving to <75 $\mu$m. For analysis, 25 ± 0.1 mg of glass sample was placed in an alumina crucible, with 25 ± 0.1 mg of alumina reference material placed in an identical alumina crucible. Both sample and reference material were heated from room temperature to 1100 °C at 5 °C $min^{-1}$ in a static air atmosphere. Furnace temperature and $\Delta T$ measurements were taken every 0.1 s. The glass transition temperature ($T_g$) was determined by onset and is reported for both glasses, together with the estimated error of that value.

### 3.2.4 Density Measurement

Archimedes' principle was used to calculate glass density. Bulk samples were weighed in air and then weighed in deionised water at 21 °C. Three samples of each glass (Blend AC and Oxide AC) were tested, with the mean density of each glass being reported, along with the standard deviation ($1\sigma$) of that value.

### 3.2.5 X-Ray Powder Diffraction (XRD)

Philips PW1710 and Siemens D500 diffractometers were used for XRD analysis of glass samples. However, due to the small amount of material (~0.035 g), a STOE STADI P diffractometer was used to analyse 'yellow phase' samples. The Philips and Siemens diffractometers employed Cu $K\alpha$ radiation, whilst the STOE diffractometer used Cu $K\alpha_1$ radiation.

For glass sample analysis (Blend AC, Oxide AC, Blend HT and Oxide HT) both the Philips and Siemens machines operated in reflection mode and scanned from 10° to 80° $2\theta$ at a speed of 0.1° $min^{-1}$ in 0.01° steps. Both X-ray tubes were operated at 40 kV and 30 mA. Glass samples were crushed in a steel percussion mortar, ground with an agate pestle and mortar and sieved to <75 $\mu$m before being placed in aluminium sample holders for loading into the machines. 'Yellow phase' samples were analysed by the STOE machine in transmission mode using an imaging plate position sensitive detector (IP-PSD) with a scan range of –6° to 125° $2\theta$ to record the trace. Eight traces were recorded for each sample and then summed to improve counting statistics. The X-ray tube was operated at 40 kV and 40 mA. 'Yellow phase' samples were ground with an agate pestle and mortar, sieved to <75 $\mu$m, glued to acetate using polyvinyl acetate (PVA), dried and then loaded into the machine. XRD traces were peak-matched to crystal phases detailed in the International Centre for Diffraction Data (ICDD) database using STOE $WinX^{POW}$ v1.06 software. XRD traces from the Philips and Siemens diffractometers were first converted for use in $WinX^{POW}$ by Traces v4.2 and WinFit! v1.12 software. **Table 3.5** lists the ICDD cards matched to crystal phases in glass and 'yellow phase' XRD traces.

**Table 3.5** ICDD cards matched to crystal phases in glass and 'yellow phase' XRD traces.

| ICDD card | Phase | Space group | ICDD card | Phase | Space group |
|---|---|---|---|---|---|
| 24-1103 | $NaLa(MoO_4)_2$ | $I4_1/a$ | 39-1425 | $SiO_2$ | $P4_12_12$ |
| 29-193 | $BaMoO_4$ | $I4_1/a$ | 40-1290 | $RuO_2$ | $P4_2/mnm$ |
| 29-835 | $LiNaZrSi_6O_{15}$ | $Cmca$ | 44-183 | $CuGa_2O_4$ | $Fd\bar{3}m$ |
| 30-157 | $(Ba_{0.5}Sr_{0.5})MoO_4$ | $I4_1/a$ | 46-1043 | Pd | $Fm\bar{3}m$ |
| 30-769 | $Na_3Li(MoO_4)_2 \cdot 6H_2O$ | $R\bar{3}c$ | 49-381 | $AgCeMo_2O_8$ | $I4_1/a$ |
| 34-394 | $CeO_2$ | $Fm\bar{3}m$ | 49-384 | $AgLaMo_2O_8$ | $I4_1/a$ |
| 38-1238 | $CsLiMoO_4$ | $F\bar{4}3m$ | | | |

### 3.2.6 Scanning Electron Microscopy (SEM) with Energy Dispersive X-Ray Spectroscopy (EDX)

SEM analysis of glass samples was conducted using a JEOL JSM 6400 operating at an accelerating voltage of 20 kV and equipped with a Link Analytical EDX unit with a beryllium window. Secondary electron (SE) images and backscattered electron (BE) images were collected from samples, along with EDX spectra.

Glass samples (Blend AC, Oxide AC, Blend HT and Oxide HT) were sectioned to approximately 1 × 1 × 1 cm in size using a Struers Accutom-5 diamond saw before mounting them in cold-setting resin (Struers EpoFix) under vacuum. Mounted samples were then ground with sequentially finer grit SiC papers (from 120 to 1200) and water before polishing to a finish of 1 $\mu$m with diamond pastes. Next, samples were partially painted with Acheson electrodag 1415M silver paint and then carbon coated using an Edwards "Speedivac" model 12E6/1598 coating unit before analysis.

### 3.2.7 Transmission Electron Microscopy (TEM) with Windowless Energy Dispersive X-Ray Spectroscopy (EDX)

TEM analysis of Oxide (but not Blend) glass samples employed a Philips EM 420T(D) and a FEI Tecnai 20, both fitted with windowless Link Analytical EDX units. The microscopes operated with an accelerating voltage of 120 kV and 200 kV respectively. Double tilt holders were employed in both microscopes, allowing samples to be tilted about two axes. Bright-field micrographs and selected-area diffraction (SAD) patterns, as well as windowless EDX spectra, were collected from samples.

Sections of glass samples (Oxide AC and Oxide HT) approximately 500 $\mu$m thick were cut using a Struers Accutom-5 diamond saw. These sections were mounted on a Gatan 623 disk grinder using heat-sensitive resin, both sides then being ground with sequentially finer grit SiC papers (from 120 to 1200) and water to a final section thickness of ~30 $\mu$m. The sections were then cleaned of resin using acetone before 3.05 mm diameter copper rings with a 1 mm diameter aperture were attached using Devcon 5-minute epoxy glue. A Gatan Dual Ion Mill (DuoMill) model 600 then milled the samples to perforation. The dual ion beam miller was operated with an accelerating voltage of 6 kV at a combined gun current of 0.6 mA and an incidence angle of 12°. Samples were then carbon coated using an Edwards "Speedivac" model 12E6/1598 coating unit before analysis. Obtained electron diffraction patterns were indexed using simulated electron diffraction patterns produced with CaRIne Crystallography v3.1 software. The space group, lattice parameters and atomic coordinates of crystal phases were needed for their simulation in CaRIne and were obtained from the Inorganic Crystal Structure Database (ICSD) (**Table 3.6**).

**Table 3.6** References used to produce simulated electron diffraction patterns of identified crystal phases.

| Reference | Crystal structure | Phase | Space group |
|---|---|---|---|
| (Bouvier *et al.*, 2000) | Cubic, Fluorite | $ZrO_2$ | $Fm\bar{3}m$ |
| (Della Giusta *et al.*, 1987) | Cubic, Spinel | $Fe_{0.99}Ni_{0.01}Fe_{1.97}Cr_{0.03}O_4$ | $Fd\bar{3}m$ |
| (Hazen *et al.*, 1985) | Tetragonal, Powellite | $CaMoO_4$ | $I4_1/a$ |
| (Taylor, 1984) | Cubic, Fluorite | $CeO_2$ | $Fm\bar{3}m$ |

Interplanar spacings were calculated using (Williams and Carter, 1996):

$$d = \frac{\lambda L}{R} \tag{3.1}$$

$d$ = interplanar spacing (Å)
$\lambda$ = relativistic wavelength of electrons (Å)
$L$ = camera length (mm)
$R$ = spacing of diffraction maxima from direct beam (mm)

### 3.2.8 Modified Product Consistency Test Method B (PCT-B)

The chemical (aqueous) durability of glass samples was determined using a modified PCT-B (ASTM, 2002). The modification was based upon the pulsed-flow leach test developed by Barkatt and co-workers (Barkatt *et al.*, 1981, 1983, 1985; Macedo *et al.*, 1982) and is similar to the modified PCT-B used by Feng and Pegg (1994). In the pulsed-flow test, leachate is renewed after each sampling with fresh leachant, yielding data at multiple times from a single test sample. The pulsed-flow test is designed to simulate the slow-flow of groundwater in contact with the wasteform, a condition considered likely in geological repositories. Leachate renewal is the main modification to PCT-B, so the majority of experimental details can be found in ASTM (2002), further deviations from this method are noted in the following procedure. Furthermore, elemental concentrations were corrected to take into account the dilution of the leachate after each sampling, yielding more accurate leaching data. The leachate renewal described in this procedure differs from the leachate renewal of pulsed-flow tests as the sampling times are not at regular intervals, so leachant/leachate flow-rates cannot be calculated. Also, the results of this modified PCT-B are not directly comparable to either PCT or pulsed-flow test results, they are only comparable amongst themselves or with results obtained using the method detailed herein.

The tests were conducted in unsensitised Type 304L stainless steel vessels, whilst the leachant was American Society for Testing and Materials (ASTM) Type 1 water. ASTM Type 1 water has a maximum total matter content of 0.1 g $m^{-3}$ and a minimum electrical resistivity of 18 MΩ $cm^{-1}$ at 25 °C. Glass samples were crushed and then sieved to yield a particle size distribution for the 'powders' of 74–149 $\mu$m (ASTM –100 to +200 mesh). Next, 4 g of glass 'powder' were immersed in 40 g of leachant in the precleaned vessels. Using Appendix X1 (ASTM, 2002), the glass densities shown in **Table 4.1.3** and assuming a Gaussian distribution of glass 'powder' sizes the wasteform surface area to leachant/leachate volume ratio (*SA*/*V*) can be calculated for Blend and Oxide glasses (**Table 3.7**).

**Table 3.7** Calculated *SA*/*V* ratio for both glasses.

| Glass | $\rho$ (g $cm^{-3}$) | *SA* ($m^2$ $g^{-1}$) | *SA*/*V* | |
|---|---|---|---|---|
| | | | ($m^{-1}$) | ($m^2$ $l^{-1}$) |
| Blend | 2.82 | $1.907 \times 10^{-2}$ | 1907 | 1.907 |
| Oxide | 2.73 | $1.970 \times 10^{-2}$ | 1970 | 1.970 |

The sealed vessels were then placed in a convection oven preheated to 90 ± 2 °C. All glasses (Blend AC, Oxide AC, Blend HT and Oxide HT) were run in triplicate, along with LRM glass and container 'blanks', both also in triplicate. Low-activity reference material (LRM) is a reference glass (**Appendix, Table A.2**) with well characterised leaching behaviour (Ebert and Mazer, 2000), tested to ensure the accuracy of elemental concentration data. Container 'blanks' are tests run without glass to see if the test vessels are contributing to elemental concentrations in the leachate.

Each test was sampled after 1, 3, 7, 14 and 28 d. At each sampling, 4 ml of leachate were withdrawn from the vessel using a syringe and then filtered through a Whatman 0.45 $\mu$m polysulphone filter, ready for further investigation. An equal amount of fresh leachant (4 ml) was then added to the vessel to maintain a constant *SA/V* ratio before it was returned to the convection oven (1 h after its removal). The pH of the leachate was measured using a pH meter (calibrated every 30 min) immediately after quenching ~2 ml of the 4 ml leachate sample to room temperature. Two 1 ml samples of the remaining leachate were acidified by adding 20 ml of 1 wt% (0.16 mol $l^{-1}$) $HNO_3$ solution to each of them. One acidified sample was sent for DCP-AES analysis (**Section 3.2.1**) with the other kept as a backup.

The elements analysed for in container 'blank' leachate samples were all below their DCP-AES detection limits, indicating the test vessels were not contributing to elemental concentrations in leachate samples. Raw concentrations (means) of elements detected in glass leachate samples during modified PCT-B (including their standard deviations ($1\sigma$)) are presented in the **Appendix** for Blend AC (**Table A.3**), Oxide AC (**Table A.5**), Blend HT (**Table A.7**), Oxide HT (**Table A.9**) and LRM (**Table A.11**). Uncertainty for all elements having concentrations greater than 2 mg $l^{-1}$ is 10 % relative. **Table 3.8** shows that elemental concentration data obtained from the leachates of the LRM reference glass compare well with published data (Ebert and Wolf, 2000), illustrating the validity of the elemental concentration data obtained from the leachates of all glass samples.

**Table 3.8** Measured elemental concentrations (means) in the LRM leachates after 7 d of modified PCT-B compared to those reported for (7 d) PCT-A by Ebert and Wolf (2000). Values given in parentheses indicate standard deviation ($1\sigma$) in the measured values and interlaboratory error in the reference values.

| Element | Concentration (mg $l^{-1}$) | |
|---|---|---|
| | Measured | Reference |
| Al | 13.78 (± 0.19) | 14.3 (± 7.3) |
| B | 30.44 (± 0.24) | 26.7 (± 7.2) |
| Na | 173.83 (± 0.36) | 160 (± 34) |
| Si | 83.50 (± 0.10) | 82.0 (± 12.7) |

Raw elemental concentrations were corrected to allow for the 9:10 dilution of the leachates after each sampling. The following equations were used:

$$
\begin{aligned}
c_{i(c1)} &= c_{i(r1)} \\
c_{i(c2)} &= 0.1c_{i(r1)} + c_{i(r2)} \\
c_{i(c3)} &= 0.1(c_{i(r1)} + c_{i(r2)}) + c_{i(r3)} \\
c_{i(c4)} &= 0.1(c_{i(r1)} + c_{i(r2)} + c_{i(r3)}) + c_{i(r4)} \\
c_{i(c5)} &= 0.1(c_{i(r1)} + c_{i(r2)} + c_{i(r3)} + c_{i(r4)}) + c_{i(r5)}
\end{aligned}
\qquad (3.2)
$$

$c_{i(cn)}$ = corrected concentration of element $i$ in the leachate at $n^{th}$ sampling (mg $l^{-1}$)
$c_{i(rn)}$ = raw concentration (mean) of element $i$ in the leachate at $n^{th}$ sampling (mg $l^{-1}$)

Corrected elemental concentrations in the glass leachates during modified PCT-B are presented in the **Appendix** for Blend AC (**Table A.4**), Oxide AC (**Table A.6**), Blend HT (**Table A.8**) and Oxide HT (**Table A.10**). Only the corrected leachate data were used in the following calculations.

The mass fraction of each element of interest in the Blend and Oxide glasses was calculated using (Abraitis, 1999):

$$f_i = \frac{wt_{ox(i)} \times (m_{i(ox)} / M_{ox(i)})}{100} \qquad (3.3)$$

$f_i$ = mass fraction of element $i$ in the unleached wasteform (unitless)
$wt_{ox(i)}$ = weight percent of the oxide of element $i$ in the unleached wasteform (%)
$m_{i(ox)}$ = mass of element $i$ in the oxide of element $i$ (g $mol^{-1}$)
$M_{ox(i)}$ = molar mass of the oxide of element $i$ (g $mol^{-1}$)
100 = convert percent to fraction

The normalised leaching rate of each element of interest was then calculated for each glass (Blend AC, Oxide AC, Blend HT and Oxide HT) using a modified version of the equation used in ASTM (2002):

$$NR_i = \frac{c_{i(n)} - c_{i(n-1)}}{fi \times SA/V \times (t_n - t_{n-1}) \times 10^3} \qquad (3.4)$$

| | | |
|---|---|---|
| $NR_i$ | = | normalised leach rate of element *i* from the wasteform (g $m^{-2}$ $d^{-1}$) |
| $c_{i(n)}$ | = | concentration of element *i* in the leachate at $n^{th}$ sampling (mg $l^{-1}$) |
| $c_{i(n-1)}$ | = | concentration of element *i* in the leachate at $n-1^{th}$ sampling (mg $l^{-1}$) |
| $f_i$ | = | mass fraction of element *i* in the unleached wasteform (unitless) |
| $SA/V$ | = | wasteform surface area divided by leachant/leachate volume ($m^2$ $l^{-1}$) |
| $t_n$ | = | duration of the test at $n^{th}$ sampling (days) |
| $t_{n-1}$ | = | duration of the test at $n-1^{th}$ sampling (days) |
| $10^3$ | = | convert mg $l^{-1}$ to g $l^{-1}$ |

Finally, the leached fraction of each element of interest was calculated for each glass (Blend AC, Oxide AC, Blend HT and Oxide HT) using a modified version of the equation used by Ledieu *et al.* (2004):

$$LF_i = \left( \frac{c_i \times V}{f_i \times m \times 10^3} \right) \times 100 \qquad (3.5)$$

| | | |
|---|---|---|
| $LF_i$ | = | fraction of element *i* leached from the wasteform (%) |
| $c_i$ | = | concentration of element *i* in the leachate (mg $l^{-1}$) |
| $V$ | = | leachant/leachate volume (l) |
| $f_i$ | = | mass fraction of element *i* in the unleached wasteform (unitless) |
| $m$ | = | mass of wasteform used in the test (g) |
| $10^3$ | = | convert mg $l^{-1}$ to g $l^{-1}$ |
| 100 | = | convert fraction to percent |

The pH (mean) of the glass leachate samples for Blend AC, Oxide AC, Blend HT, Oxide HT and LRM (as well as container 'blank' leachate samples) during modified PCT-B (including their standard deviations ($1\sigma$)) are presented in the **Appendix, Table A.12. Table 3.9** shows that pH data obtained from the leachates of the LRM reference glass compare well with published data (Ebert and Wolf, 2000), illustrating the validity of the pH data obtained from the leachates of all glass samples.

**Table 3.9** Measured pH (mean) of the LRM leachates after 7 d of modified PCT-B compared to that reported for (7 d) PCT-A by Ebert and Wolf (2000). Values given in parentheses indicate standard deviation ($1\sigma$) in the measured value and interlaboratory error in the reference value.

| pH | Measured | Reference |
|---|---|---|
| | 11.03 (± <0.01) | 10.9 (± 0.4) |

## 3.2.9 Leached Glass Analysis

After chemical (aqueous) durability testing (**Section 3.2.8**) the leached glass 'powder' samples were dried in a convection oven (preheated to 90 ± 2 °C) for 24 h. The dried samples were mounted in cold-setting resin (Struers EpoFix) under vacuum. Mounted samples were then ground with sequentially finer grit SiC papers (from 120 to 1200) and water before polishing to a finish of 1 $\mu$m with diamond pastes. Next, samples were partially painted with Acheson electrodag 1415M silver paint before being carbon coated using an Edwards "Speedivac" model 12E6/1598 coating unit. These samples were then analysed by SEM (**Section 3.2.6**).

# 4 Results

## 4.1 Chemical, Thermal and Physical Analysis

**Table 4.1.1** gives the chemical composition of both Blend and Oxide glass. From these compositions we can calculate the waste loading of each glass; waste loading being a measure of the amount of simulated HLW incorporated by the base glass (a $Li_2O$-$Na_2O$-$B_2O_3$-$SiO_2$ composition). The waste loading of Blend glass is 26.99 wt% (12.53 mol%), whilst that of Oxide glass is 19.82 wt% (7.56 mol%). Therefore, Blend glass incorporates more simulated HLW than Oxide glass.

The glass transition temperature ($T_g$) of both Blend and Oxide glass are noted in **Table 4.1.2.** As Oxide glass has a higher $T_g$ than Blend glass it will 'freeze' during cooling at a higher temperature than Blend glass.

**Table 4.1.3** reports the unannealed density ($\rho$) of both Blend and Oxide glass. Blend glass has a greater $\rho$ than Oxide glass.

**Table 4.1.1** Normalised chemical composition (mean) of both glasses (standard deviation ($1\sigma$) given in parentheses). '—' indicates component not present.

| Glass | Blend | | Oxide | |
|---|---|---|---|---|
| **Component** | **Weight %** | **Molar %** | **Weight %** | **Molar %** |
| $Al_2O_3$ | 1.82 (± 0.03) | 1.26 | 0.60 (± 0.04) | 0.40 |
| $B_2O_3$ | 17.11 (± 0.25) | 17.32 | 18.14 (± 0.20) | 17.79 |
| BaO | 0.31 (± 0.04) | 0.14 | 0.57 (± 0.03) | 0.25 |
| CaO | 0.04 (± 0.00) | 0.05 | 0.02 (± 0.00) | 0.02 |
| $CeO_2$ | 1.90 (± 0.05) | 0.78 | 1.33 (± 0.03) | 0.53 |
| $Cr_2O_3$ | 0.27 (± 0.03) | 0.13 | 0.22 (± 0.02) | 0.10 |
| $Cs_2O$ | 2.01 (± 0.21) | 0.50 | 1.32 (± 0.06) | 0.32 |
| $Fe_2O_3$ | 1.17 (± 0.03) | 0.52 | 0.58 (± 0.03) | 0.25 |
| $Gd_2O_3$ | 3.27 (± 0.09) | 0.64 | 2.81 (± 0.09) | 0.53 |
| $HfO_2$ | 0.06 (± 0.01) | 0.02 | 0.04 (± 0.00) | 0.01 |
| $K_2O$ | 0.21 (± 0.01) | 0.16 | 0.05 (± 0.01) | 0.04 |
| $La_2O_3$ | 0.76 (± 0.02) | 0.16 | 0.69 (± 0.03) | 0.14 |
| $Li_2O$ | 4.13 (± 0.01) | 9.74 | 3.88 (± 0.05) | 8.87 |
| MgO | 1.34 (± 0.06) | 2.34 | 0.01 (± 0.01) | 0.02 |
| $MoO_3$ | 2.93 (± 0.36) | 1.44 | 2.67 (± 0.14) | 1.27 |
| $Na_2O$ | 8.53 (± 0.11) | 9.70 | 8.97 (± 0.19) | 9.88 |
| $Nd_2O_3$ | 3.13 (± 0.09) | 0.66 | 2.44 (± 0.06) | 0.50 |
| NiO | 0.24 (± 0.01) | 0.23 | 0.46 (± 0.06) | 0.42 |
| $P_2O_5$ | 0.13 (± 0.01) | 0.06 | 0.11 (± 0.00) | 0.05 |
| PbO | 0.02 (± 0.00) | 0.01 | — | — |
| PdO | — | — | 0.52 (± 0.07) | 0.29 |
| $Pr_6O_{11}$ | 0.97 (± 0.03) | 0.07 | 0.75 (± 0.02) | 0.05 |
| $RuO_2$ | 1.52 (± 0.10) | 0.81 | 1.02 (± 0.15) | 0.52 |
| $SO_3$ | — | — | 0.02 (± 0.01) | 0.02 |
| $SiO_2$ | 43.24 (± 1.12) | 50.71 | 49.19 (± 0.14) | 55.90 |
| $Sm_2O_3$ | 0.50 (± 0.03) | 0.10 | 0.41 (± 0.01) | 0.08 |
| SrO | 0.63 (± 0.03) | 0.43 | 0.48 (± 0.02) | 0.32 |
| $TeO_2$ | 0.36 (± 0.02) | 0.16 | 0.24 (± 0.01) | 0.10 |
| $TiO_2$ | 0.04 (± 0.01) | 0.04 | 0.02 (± 0.00) | 0.02 |
| $Y_2O_3$ | 0.41 (± 0.01) | 0.13 | 0.19 (± 0.01) | 0.06 |
| $ZrO_2$ | 2.95 (± 0.09) | 1.69 | 2.25 (± 0.05) | 1.25 |
| **Total** | **100.00** | **100.00** | **100.00** | **100.00** |

**Table 4.1.2** Glass transition temperature ($T_g$) of both glasses (estimated error given in parentheses).

| Glass | Blend | Oxide |
|---|---|---|
| $T_g$ (°C) | 492 (± 5) | 498 (± 5) |

**Table 4.1.3** Mean density ($\rho$) of both glasses (standard deviation ($1\sigma$) given in parentheses).

| Glass | Blend | Oxide |
|---|---|---|
| $\rho$ (g cm$^{-3}$) | 2.82 (± 0.01) | 2.73 (± 0.01) |

## 4.2 Phase and Microstructural Analysis

### 4.2.1 As-Cast Blend Glass (Blend AC)

Two XRD traces of Blend AC are presented in **Figure 4.2.1.1** to illustrate the consistency of XRD traces obtained from different samples of Blend AC. **Figure 4.2.1.1** reveals peak matches for tetragonal $RuO_2$ (labelled ∇; ICDD card [40-1290]). SEM **(Figure 4.2.1.2)** indicates the glass matrix is compositionally homogeneous.

*$RuO_2$/Metallic Ru*

The tetragonal $RuO_2$ crystal phase identified by XRD **(Figure 4.2.1.1)** has the rutile structure (space group $P4_2/mnm$). SEM revealed acicular $RuO_2$ **(Figure 4.2.1.3)** and 'sponge-like' $RuO_2$/metallic Ru **(Figure 4.2.1.5)** in the glass. Acicular $RuO_2$ (labelled × in **Figure 4.2.1.3)** had an EDX spectrum **(Figure 4.2.1.4)** which showed only Ru. 'Sponge-like' $RuO_2$/metallic Ru (labelled × in **Figure 4.2.1.5)** had an EDX spectrum **(Figure 4.2.1.6)** which showed Ru and Si. **Figure 4.2.1.6** indicates the unusual 'sponge-like' $RuO_2$/metallic Ru is an agglomeration of $RuO_2$/metallic Ru interwoven with silicate glass (suggested by the Si peak).

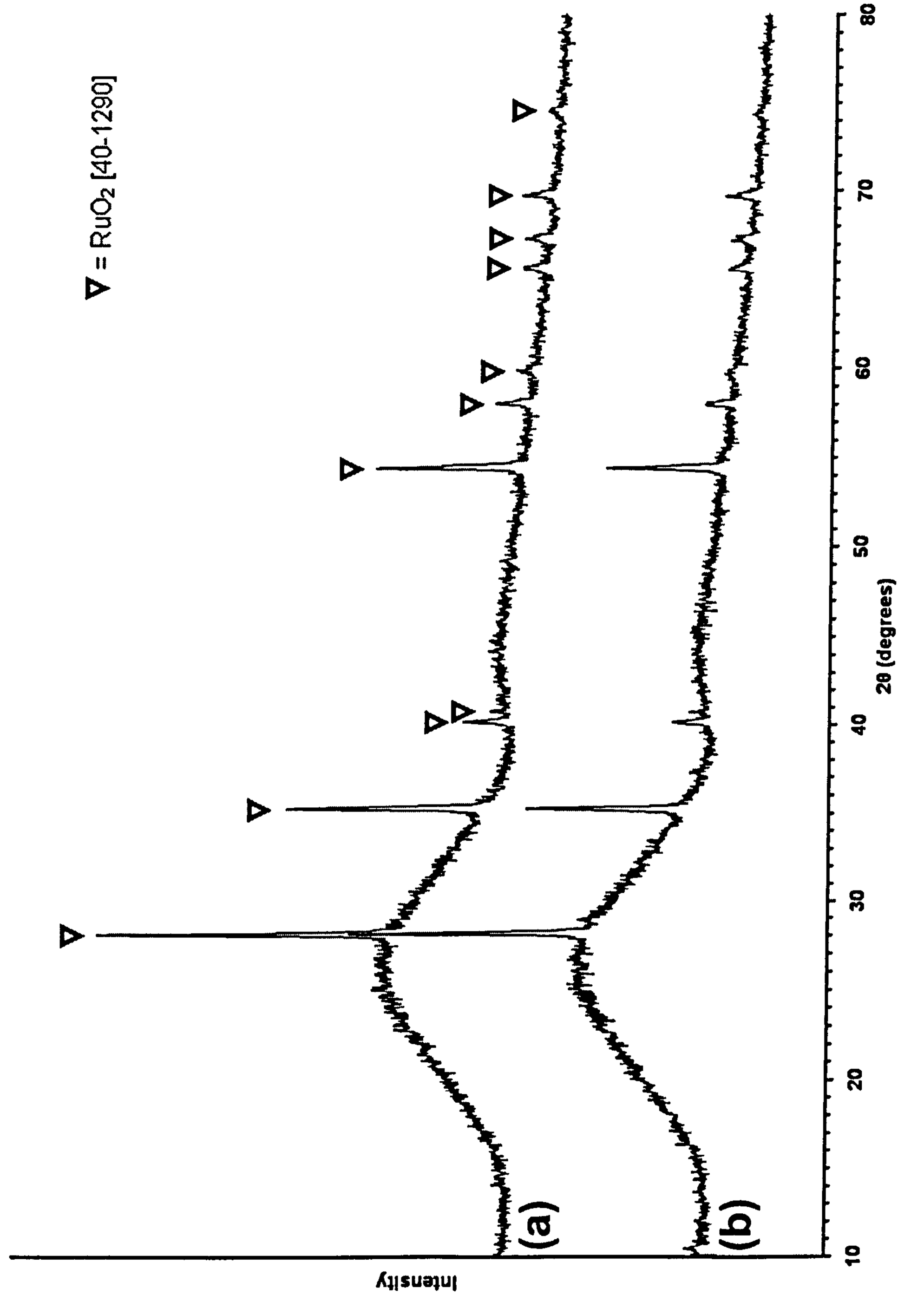


**Figure 4.2.1.1** XRD traces from two Blend AC samples, illustrating their consistency. Peak matches have been labelled, with $RuO_2$ also identified in trace (b).

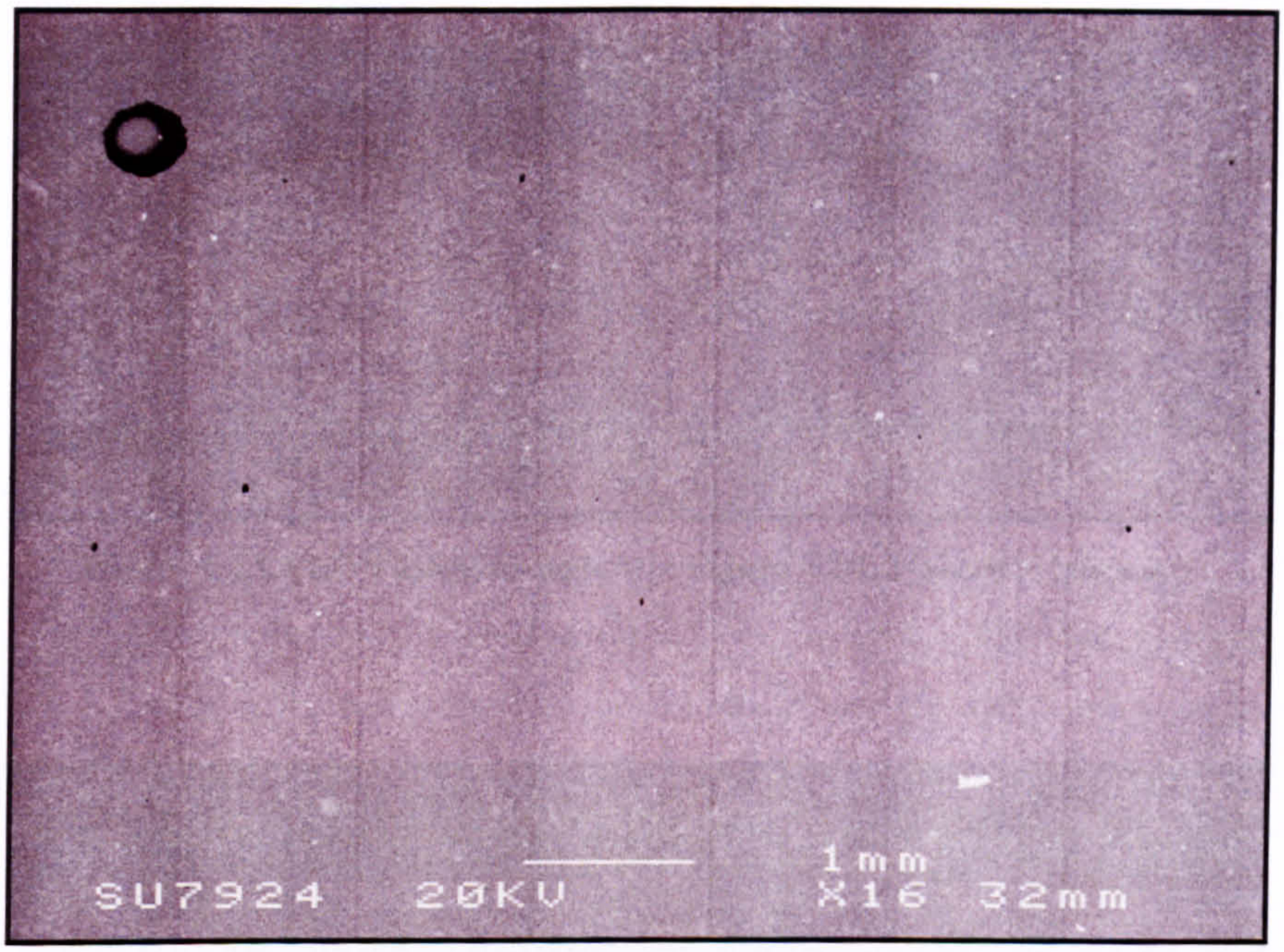


**Figure 4.2.1.2** BE SEM image of a Blend AC sample, indicating a compositionally homogeneous glass matrix.

### *4.2.1.1 $RuO_2$/Metallic Ru*

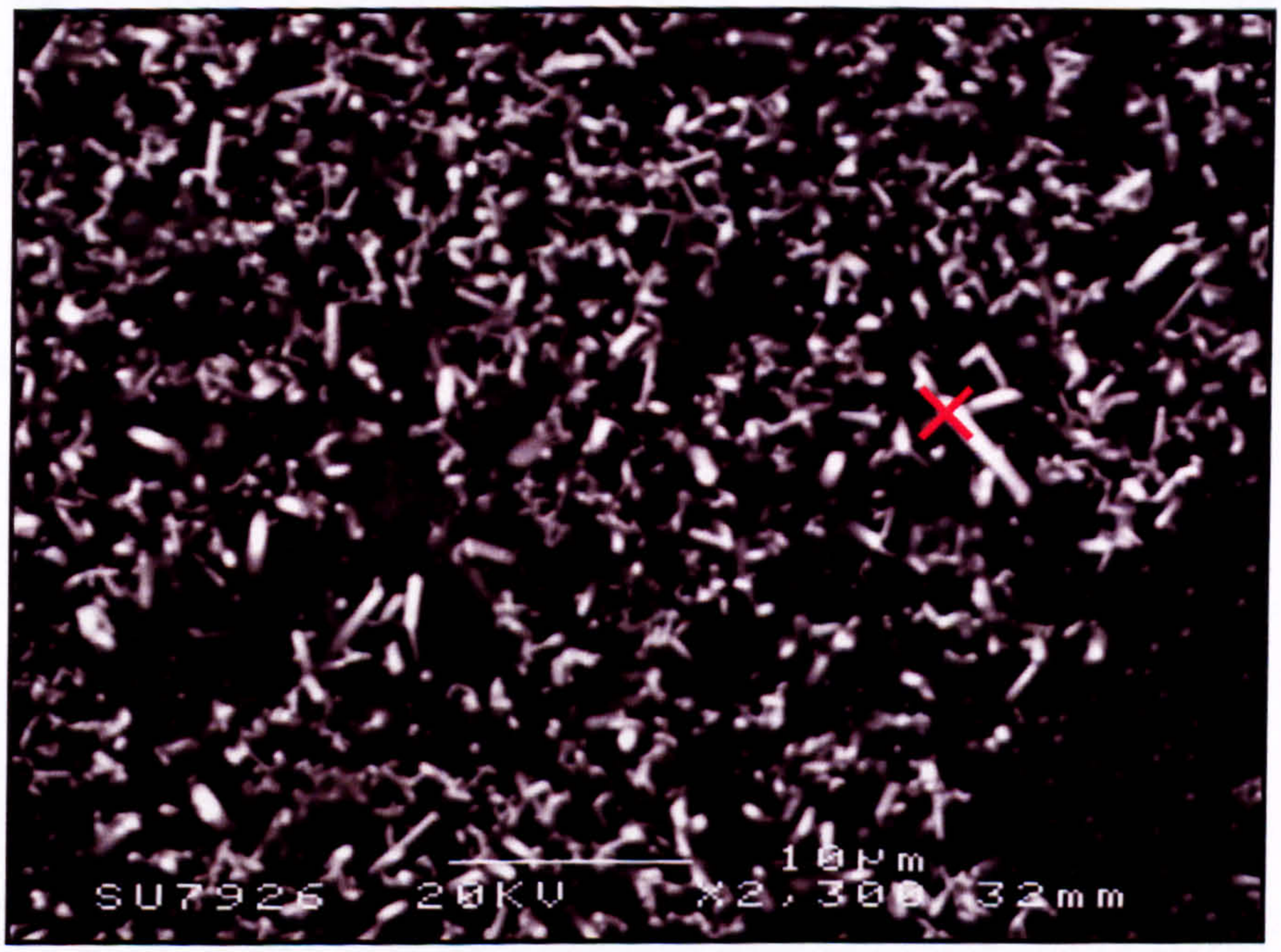


**Figure 4.2.1.3** SE SEM image of a Blend AC sample, revealing acicular $RuO_2$.

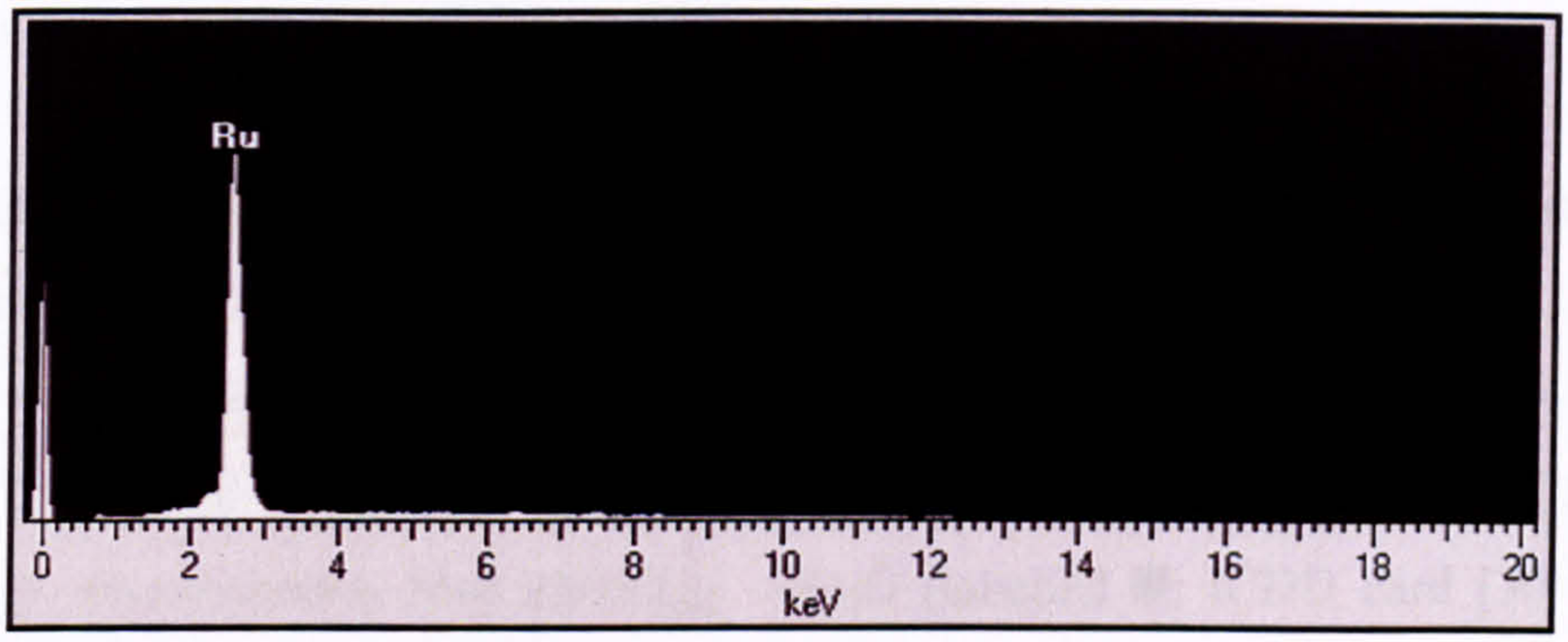


**Figure 4.2.1.4** EDX spectrum from × in **Figure 4.2.1.3** (*y*-axis = Intensity).

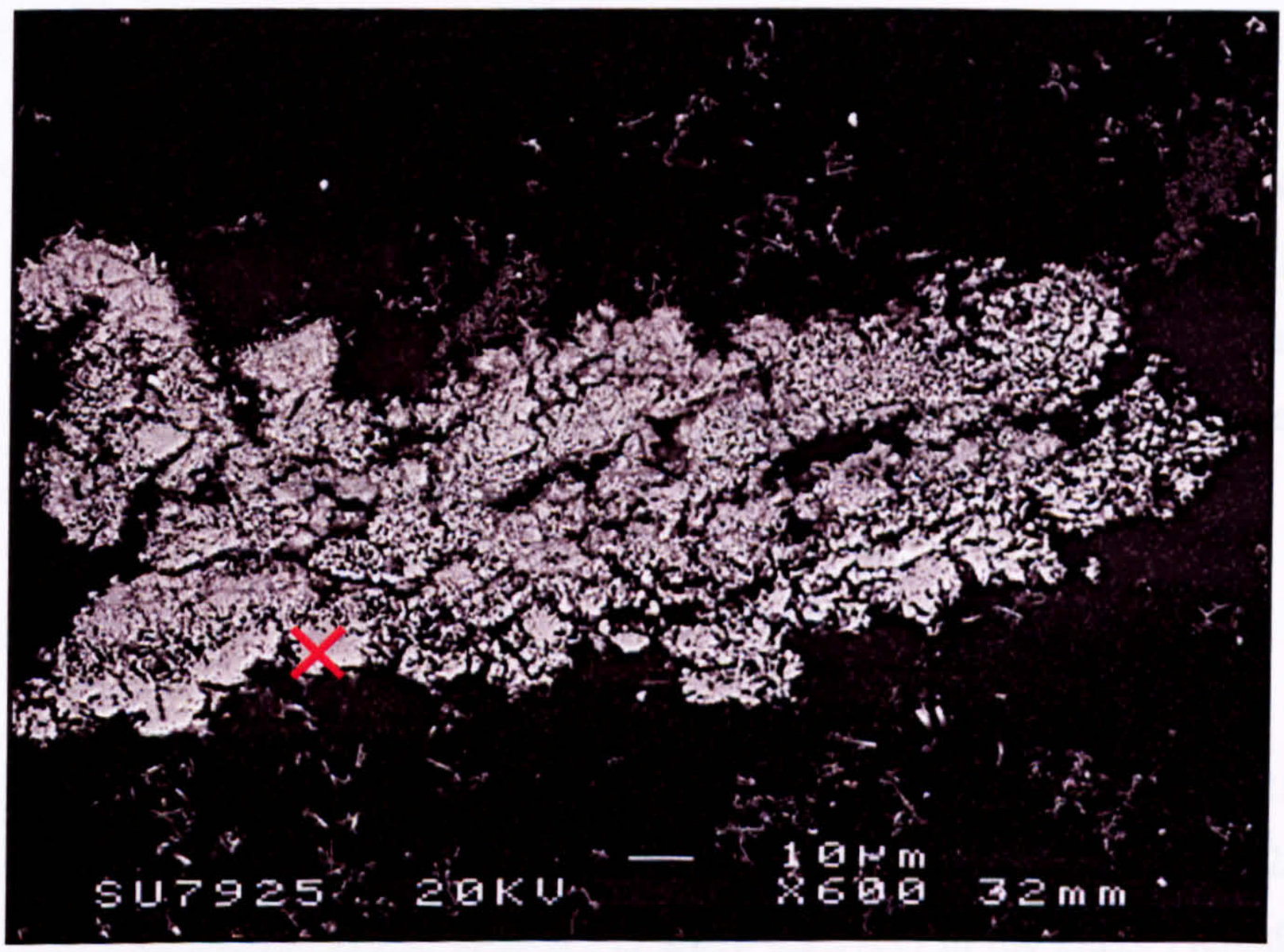


**Figure 4.2.1.5** SE SEM image of a Blend AC sample, revealing an uncommon 'sponge-like' $RuO_2$/metallic Ru agglomeration.

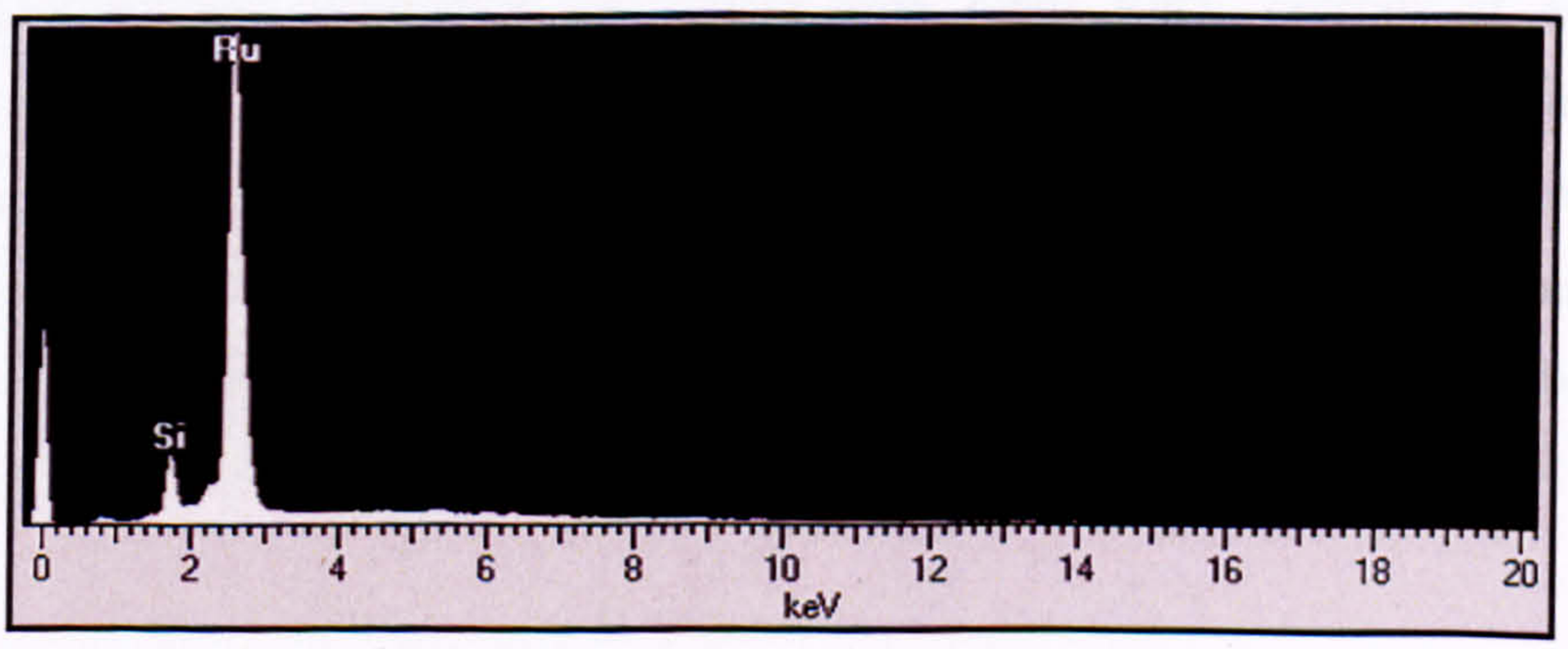


**Figure 4.2.1.6** EDX spectrum from × in **Figure 4.2.1.5** (*y*-axis = Intensity).

### 4.2.2 As-Cast Oxide Glass (Oxide AC)

Two XRD traces of Oxide AC are presented in **Figure 4.2.2.1** to illustrate the inconsistency of XRD traces obtained from different samples of Oxide AC. **Figure 4.2.2.1** reveals peak matches for tetragonal $RuO_2$ (labelled ∇; ICDD card [40-1290]), cubic Pd (labelled ◆; ICDD card [46-1043]), cubic $CuGa_2O_4$ (labelled ○; ICDD card [44-183]), rhombohedral $Na_3Li(MoO_4)_2 \cdot 6H_2O$ (labelled ■; ICDD card [30-769]) as well as unidentified peaks. SEM reveals the glass matrix of some samples is compositionally homogeneous (**Figure 4.2.2.2**), which will be termed Type I microstructure; whilst other samples are compositionally inhomogeneous (**Figures 4.2.2.3** and **4.2.2.4**), which will be termed Type II microstructure. Type II microstructures display compositional 'banding' as well as dissolving/relict calcine. Glass samples with different microstructures will not be from the same batch. A linescan of this compositional 'banding' (**Figures 4.2.2.4** and **4.2.2.5**) shows the bright 'bands' (indicating higher average atomic number in that region) are enriched in Ce, Cs, Gd, Mo, Nd, Ni and Zr (simulated HLW components) whilst being depleted in Si, relative to the bulk glass composition.

*$RuO_2$/Metallic Ru*

The tetragonal $RuO_2$ crystal phase identified by XRD (**Figure 4.2.2.1**) has the rutile structure (space group $P4_2/mnm$). SEM revealed acicular $RuO_2$ (**Figures 4.2.2.6** and **4.2.2.10**) and globular $RuO_2$/metallic Ru (**Figure 4.2.2.11**) in the glass. Acicular $RuO_2$ (labelled × in **Figure 4.2.2.6**) had an EDX spectrum (**Figure 4.2.2.7**) which showed only Ru. **Figures 4.2.2.10** and **4.2.2.11** both had EDX spectra (from × in both images) near identical to **Figure 4.2.2.7.** TEM investigation of an acicular $RuO_2$ crystal (labelled × **Figure 4.2.2.8**) showed it in contact with other $RuO_2$ crystals at each end. Windowless EDX (**Figure 4.2.2.9**) showed Ru and O in its spectrum, as well as Cu from the support ring. Cracks radiating from a large acicular $RuO_2$ crystal are visible in **Figure 4.2.2.10.** A linescan (**Figures 4.2.2.4** and **4.2.2.5**) reveals that $RuO_2$/metallic Ru crystals are randomly distributed throughout the glass bulk. $RuO_2$ is found in both Type I and Type II microstructures.

*Metallic Pd-Te*

The cubic Pd crystal phase identified by XRD (**Figure 4.2.2.1**) has the fcc structure (space group $Fm\bar{3}m$). SEM revealed spheroidal metallic Pd-Te (**Figure 4.2.2.12**) and globular metallic Pd-Te (**Figure 4.2.2.16**) in the glass. Spheroidal metallic Pd-Te (labelled × in **Figure 4.2.2.12**) had an EDX spectrum (**Figure 4.2.2.13**) which showed Pd and Te. **Figure 4.2.2.16** had an EDX spectrum (from × in the image) near identical to **Figure 4.2.2.13**. A spheroidal metallic Pd-Te crystal investigated by TEM (labelled × **Figure 4.2.2.14**) had a windowless EDX spectrum (**Figure 4.2.2.15**) which showed Pd and Te, as well as Cu from the support ring, but no O. Pd-Te is found in both Type I and Type II microstructures.

*$(Cr,Fe,Ni)_3O_4$*

The cubic $CuGa_2O_4$ crystal phase peak matched using XRD (**Figure 4.2.2.1**) is spinel (space group $Fd\bar{3}m$). This crystal phase is not present in the glass (as neither Cu nor Ga are present, as can be seen in **Table 4.1.1**); rather, a spinel crystal phase with matching lattice parameters but different chemical composition is present. SEM revealed facetted $(Cr,Fe,Ni)_3O_4$ (**Figures 4.2.2.17** and **4.2.2.22**) in the glass. Facetted $(Cr,Fe,Ni)_3O_4$ (labelled × in **Figure 4.2.2.17**) had an EDX spectrum (**Figure 4.2.2.18**) which showed Cr, Fe, Ni and some Ru. **Figure 4.2.2.22** had an EDX spectrum (from × in the image) near identical to **Figure 4.2.2.18**. A facetted $(Cr,Fe,Ni)_3O_4$ crystal investigated by TEM (labelled × **Figure 4.2.2.19**) had a windowless EDX spectrum (**Figure 4.2.2.20**) which showed Cr, Fe, Ni, O and some Ru, as well as Cu from the support ring. The electron diffraction patterns from the facetted $(Cr,Fe,Ni)_3O_4$ crystal (**Figure 4.2.2.21**) reveal it has the spinel crystal structure (cubic system, space group $Fd\bar{3}m$) and is the likely origin of the peaks incorrectly matched to $CuGa_2O_4$ in the XRD trace (**Figure 4.2.2.1**). An agglomeration of facetted $(Cr,Fe,Ni)_3O_4$ crystals is observed by SEM in **Figure 4.2.2.22**. $(Cr,Fe,Ni)_3O_4$ is found in both Type I and Type II microstructures.

*$Na_3Li(MoO_4)_2 \cdot 6H_2O$*

The rhombohedral $Na_3Li(MoO_4)_2 \cdot 6H_2O$ crystal phase identified by XRD (**Figure 4.2.2.1**) has the space group $R\bar{3}c$ and was hydrated by atmospheric $H_2O$. This crystal phase was not observed in glass samples by either SEM or TEM, probably due to the use of water in sample preparation.

*$Zr_{1-(x+y)}Ce_xGd_yO_{2-(y/2)}$*

SEM revealed globular $Zr_{1-(x+y)}Ce_xGd_yO_{2-(y/2)}$ (**Figure 4.2.2.23**) in the glass. Globular $Zr_{1-(x+y)}Ce_xGd_yO_{2-(y/2)}$ (labelled × in **Figure 4.2.2.23**) had an EDX spectrum (**Figure 4.2.2.24**) which showed Zr, Ce and Gd. A globular $Zr_{1-(x+y)}Ce_xGd_yO_{2-(y/2)}$ crystal investigated by TEM (labelled × **Figure 4.2.2.25**) had a windowless EDX spectrum (**Figure 4.2.2.26**) which showed Zr, Ce, Gd and O, as well as Si from the surrounding glass and Cu from the support ring. Also visible within the globular $Zr_{1-(x+y)}Ce_xGd_yO_{2-(y/2)}$ crystal are 'contrast features' approximately 10–20 nm in size (**Figure 4.2.2.25**). The electron diffraction pattern from the globular $Zr_{1-(x+y)}Ce_xGd_yO_{2-(y/2)}$ crystal (**Figure 4.2.2.27**) reveal it to be nano-crystalline (as it yielded a ring diffraction pattern) and that it has the fluorite crystal structure (cubic system, space group $Fm\bar{3}m$). Interplanar spacings of the cubic $Zr_{1-(x+y)}Ce_xGd_yO_{2-(y/2)}$ crystal phase were determined (**Table 4.2.2.1**) using **Figure 4.2.2.27**. The values obtained are too low for cubic-stabilised zirconia and this is thought to be due to an inaccurately calibrated camera length. SEM indicates globular $Zr_{1-(x+y)}Ce_xGd_yO_{2-(y/2)}$ is associated with: bubbles (**Figure 4.2.2.23**), larger hexagonal lanthanide (Nd,Gd,La,Ce) silicate crystals (**Figure 4.2.2.28**), and by extension, is a component crystal phase of dissolving/relict calcine (**Figure 4.2.2.3**). This phase is not associated with the unidentified XRD peaks in **Figure 4.2.2.1**. $Zr_{1-(x+y)}Ce_xGd_yO_{2-(y/2)}$ is found exclusively in Type II microstructures.

*Lanthanide (Nd,Gd,La,Ce) Silicate*

SEM revealed hexagonal lanthanide (Nd,Gd,La,Ce) silicate (**Figure 4.2.2.28**) in the glass. Hexagonal lanthanide (Nd,Gd,La,Ce) silicate (labelled × in **Figure 4.2.2.28**) had an EDX spectrum (**Figure 4.2.2.29**) which showed Si, Nd, Gd, La and possibly Ce. This crystal phase was not observed in glass samples by TEM. SEM indicates hexagonal

lanthanide (Nd,Gd,La,Ce) silicate is associated with: bubbles (**Figure 4.2.2.28**), smaller globular $Zr_{1-(x+y)}Ce_xGd_yO_{2-(y/2)}$ (**Figure 4.2.2.28**), cracking in and around itself (**Figure 4.2.2.28**) and is a component crystal phase of dissolving/relict calcine particles/granules (**Figure 4.2.2.3**). This phase is likely associated with the unidentified XRD peaks in **Figure 4.2.2.1**. Lanthanide (Nd,Gd,La,Ce) silicate is found exclusively in Type II microstructures.

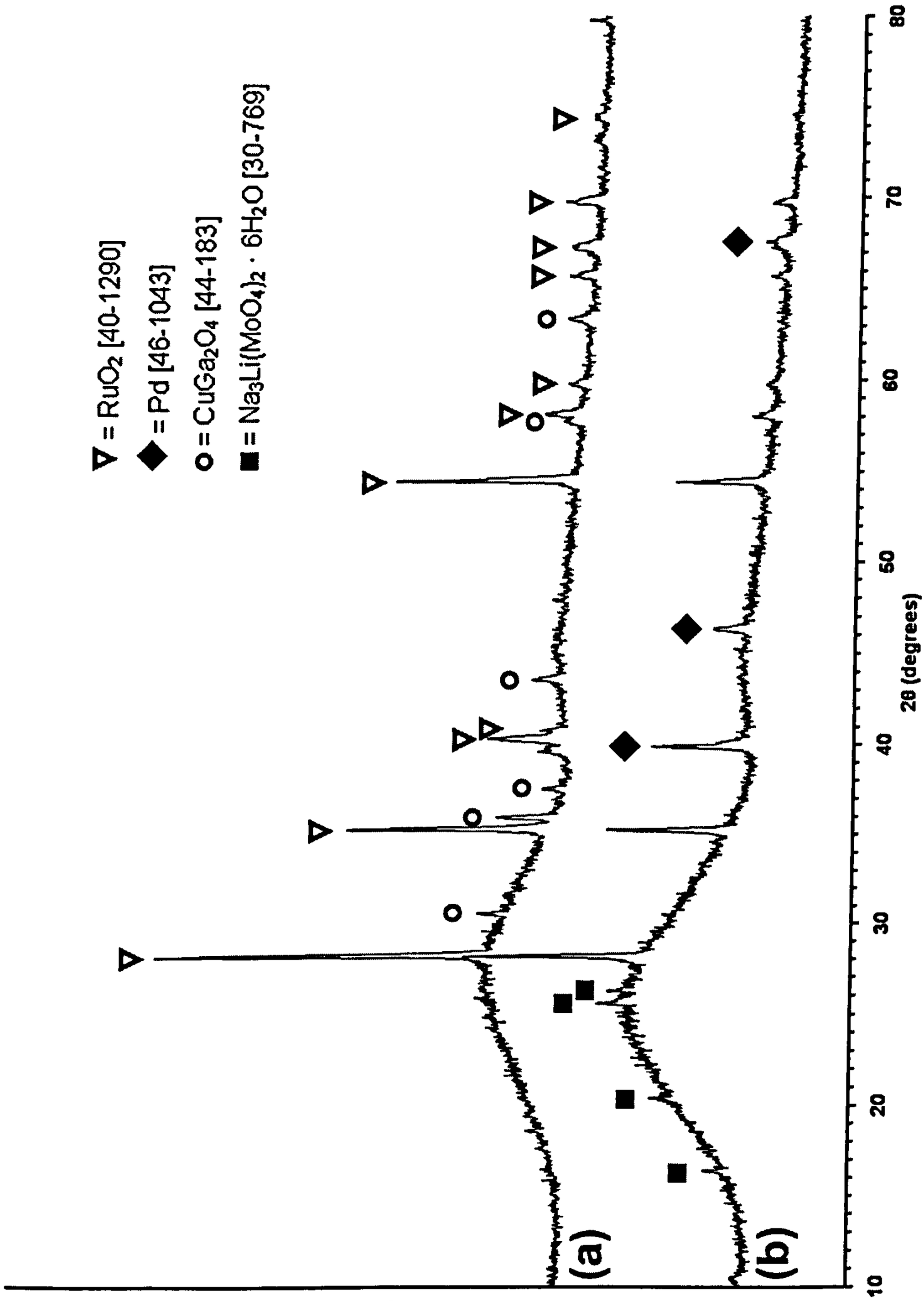


**Figure 4.2.2.1** XRD traces from two Oxide AC samples, illustrating their inconsistency. Peak matches have been labelled, with $RuO_2$ also identified in trace (b).

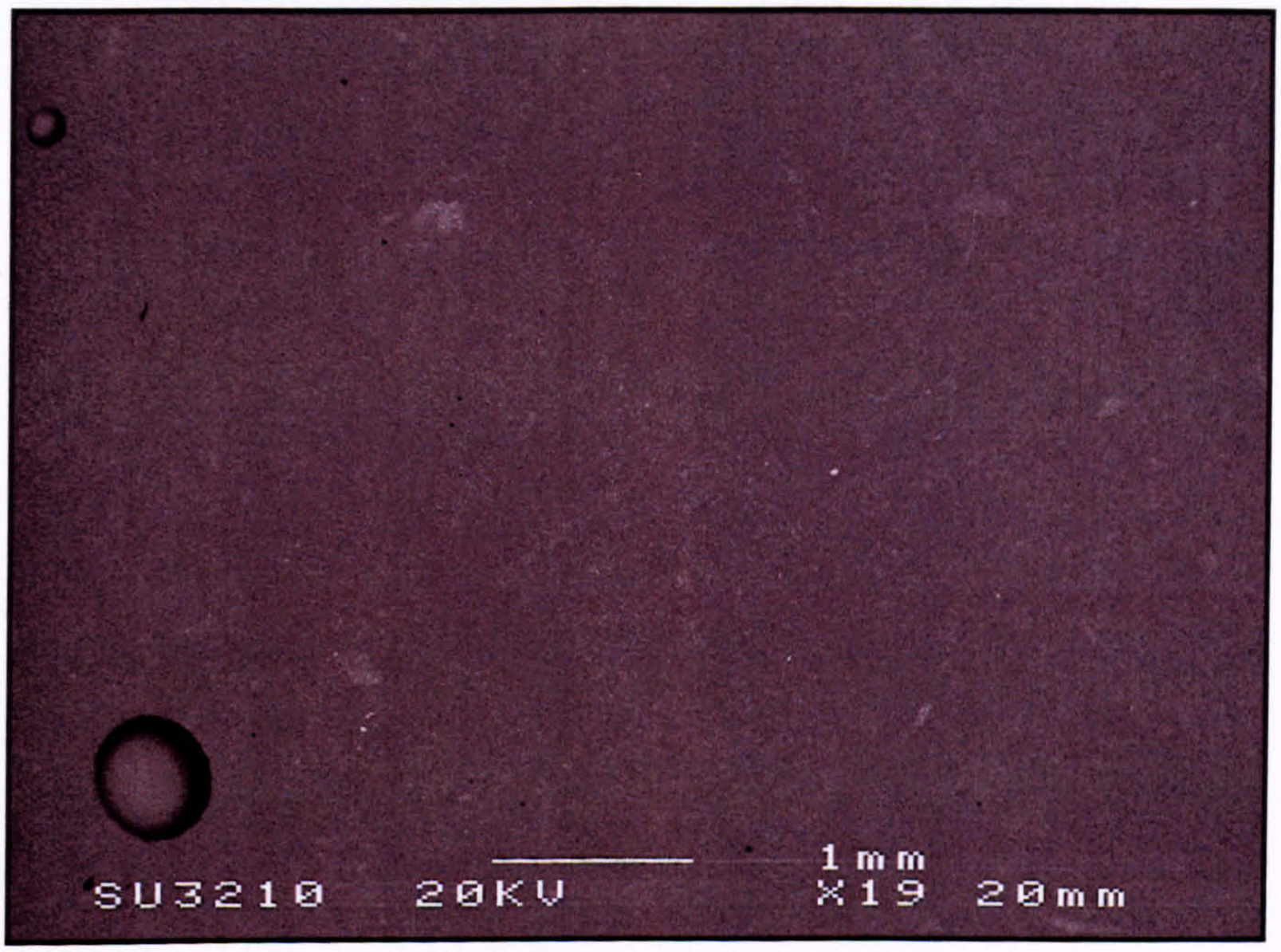


**Figure 4.2.2.2** BE SEM image of an Oxide AC sample, indicating a compositionally homogeneous glass matrix. This image is typical of images obtained from samples with Type I microstructures.

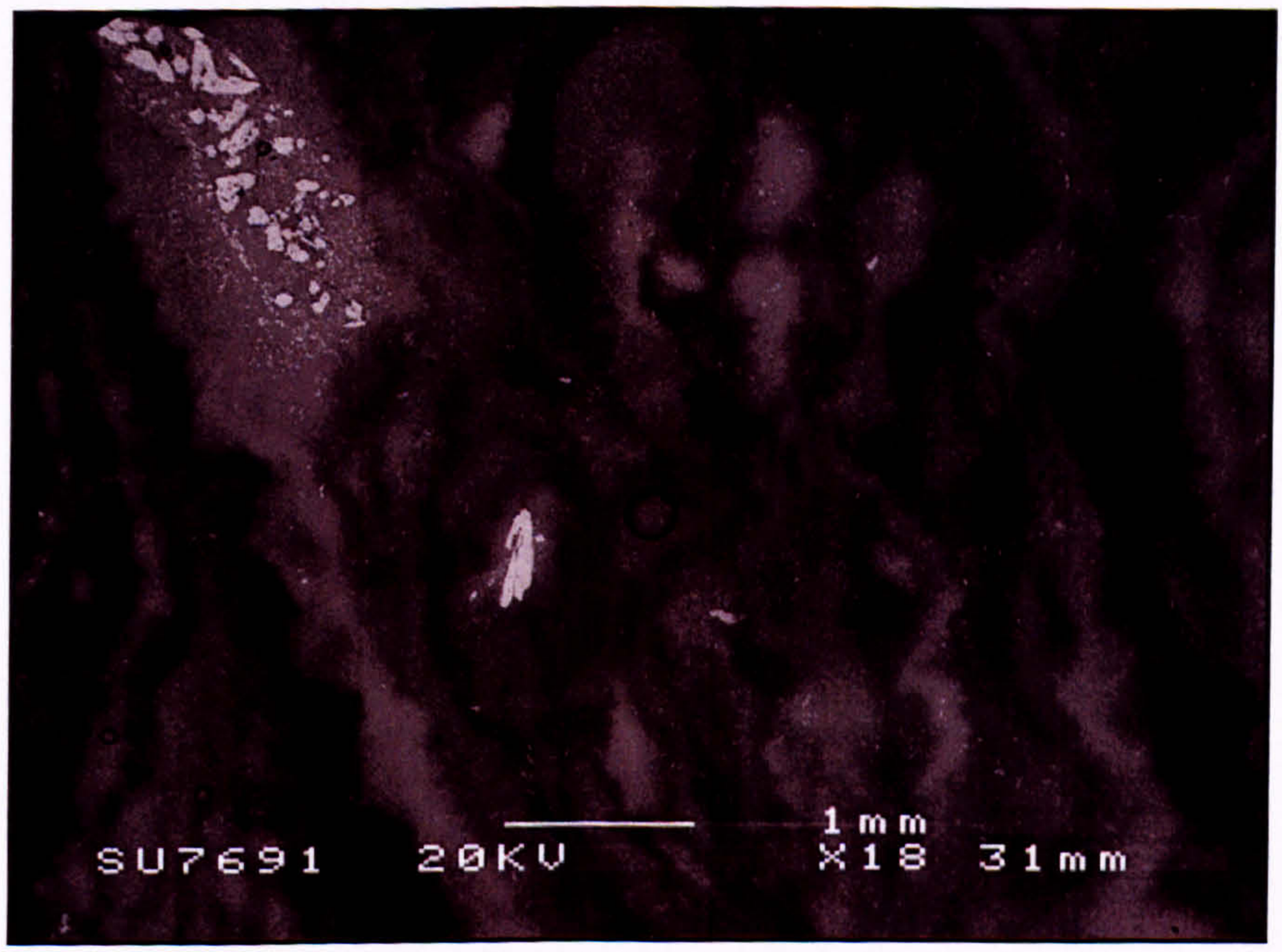


**Figure 4.2.2.3** BE SEM image of an Oxide AC sample, indicating a compositionally inhomogeneous glass matrix. This image displays compositional 'banding' and dissolving/relict calcine, typical of images obtained from samples with Type II microstructures.

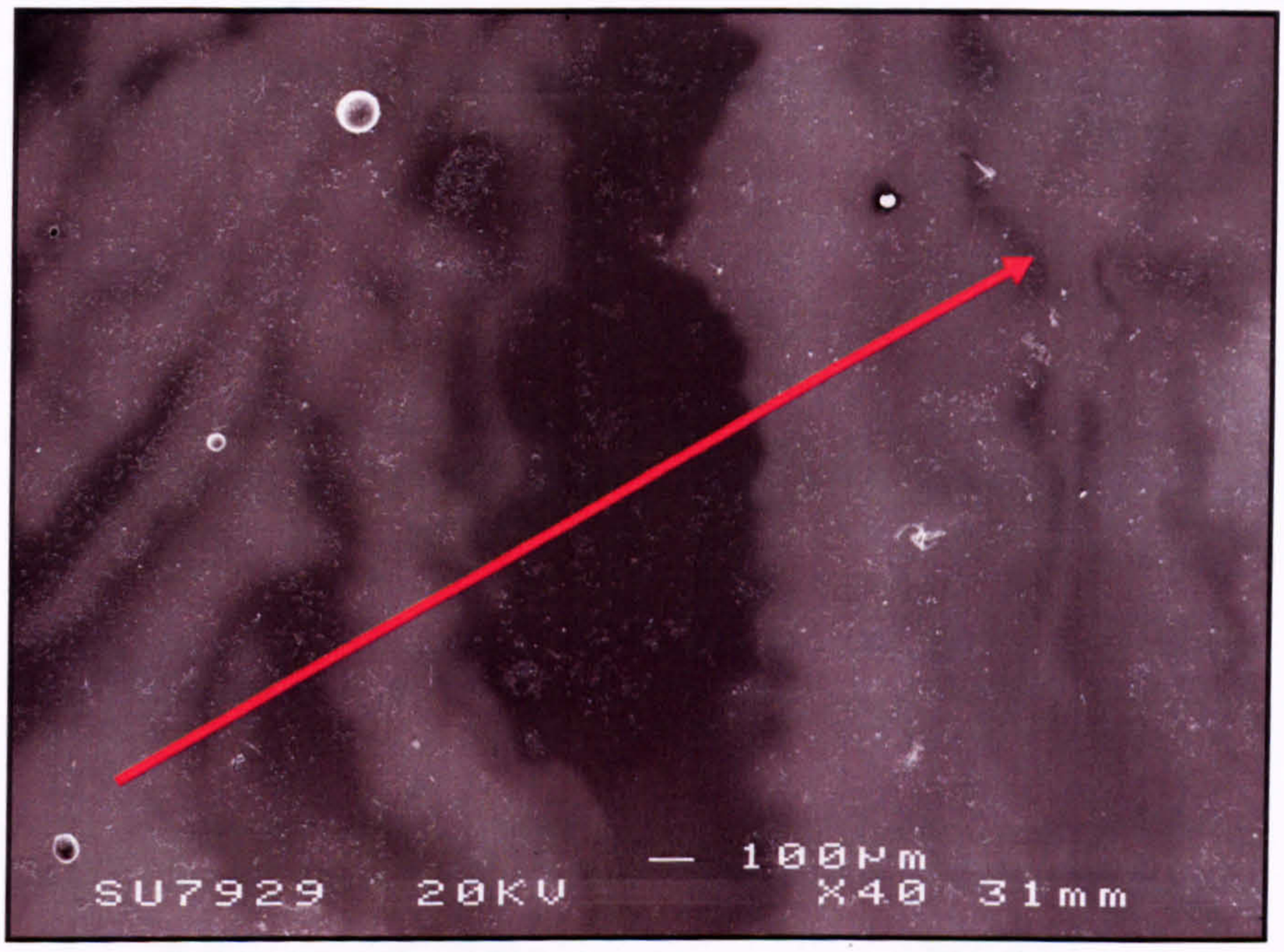


**Figure 4.2.2.4** BE SEM image of an Oxide AC sample with Type II microstructure. The red arrow indicates the location and direction of a linescan performed across compositional 'banding' (linescan length ≈ 2.3 mm).

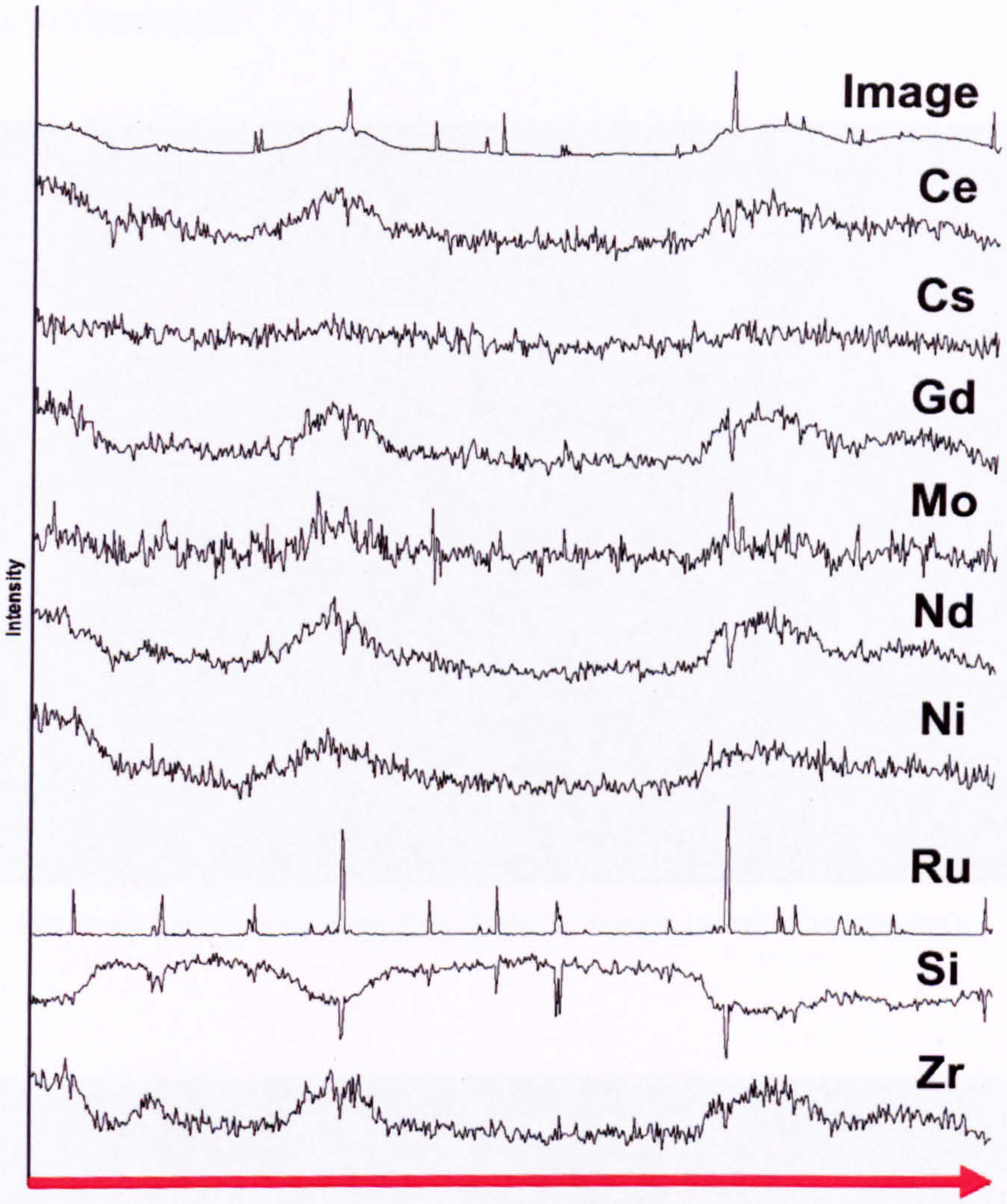


**Figure 4.2.2.5** Linescan performed where indicated in **Figure 4.2.2.4** ($x$-axis $\approx$ 2.3 mm).

### *4.2.2.1 $RuO_2$/Metallic Ru*

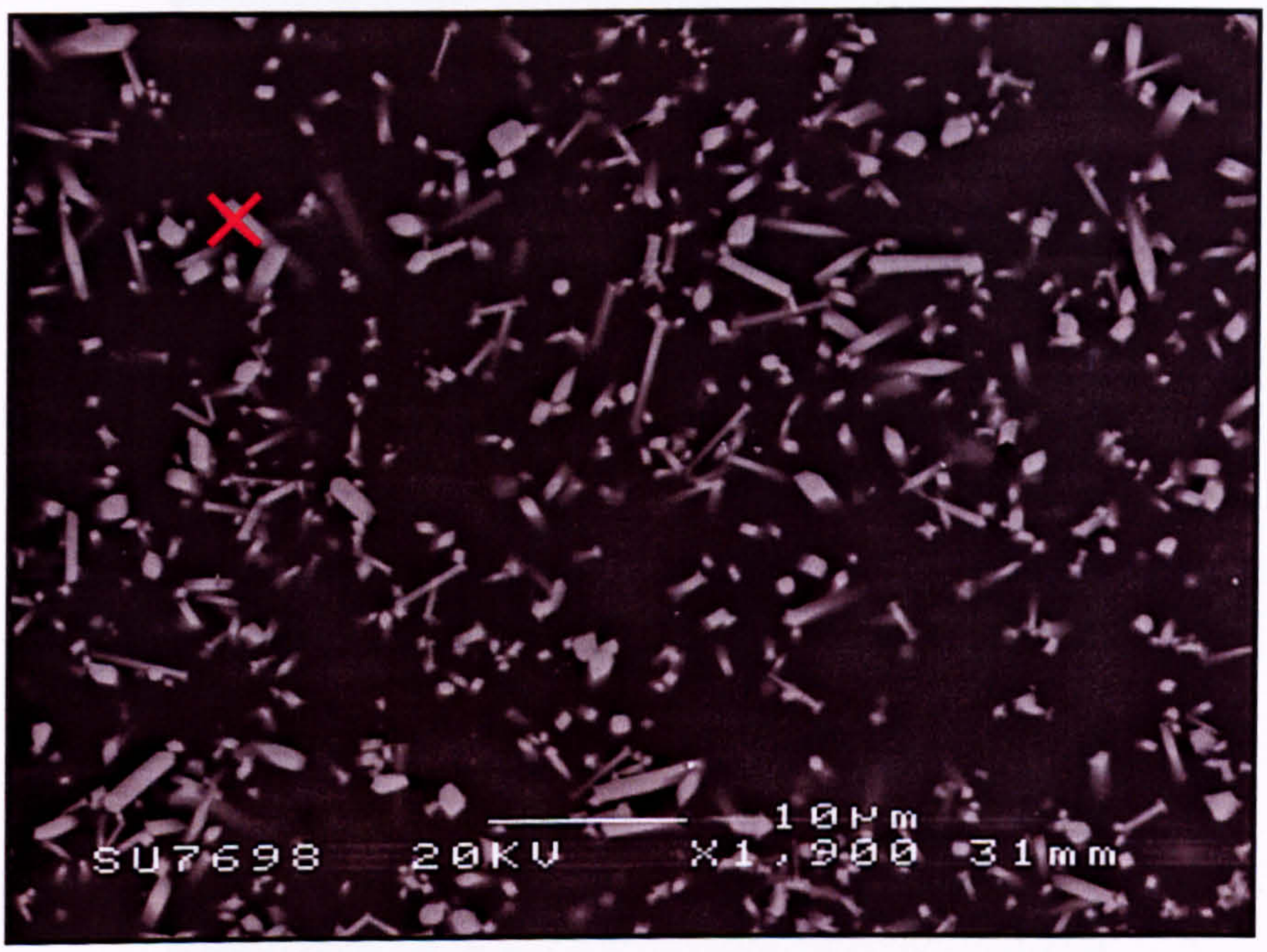


**Figure 4.2.2.6** BE SEM image of an Oxide AC sample, revealing acicular $RuO_2$.

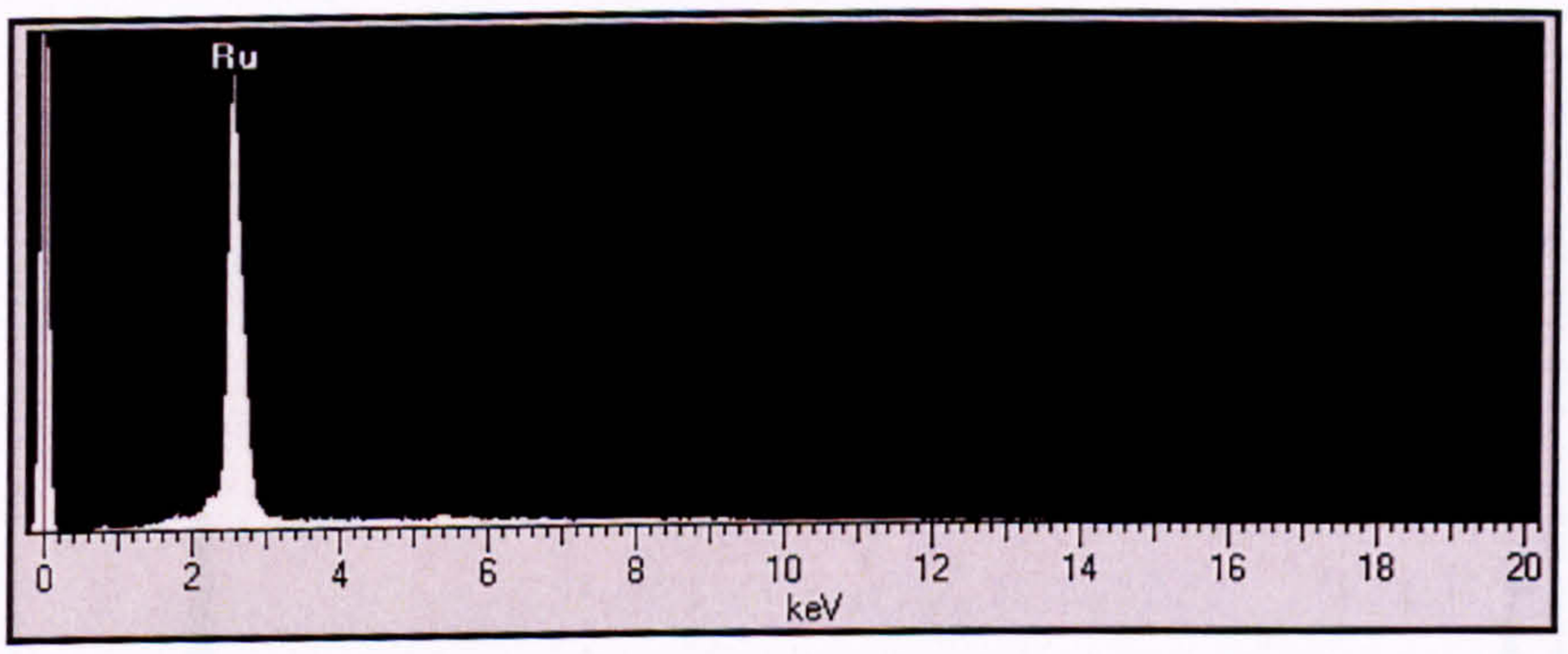


**Figure 4.2.2.7** EDX spectrum from × in **Figure 4.2.2.6** (*y*-axis = Intensity).

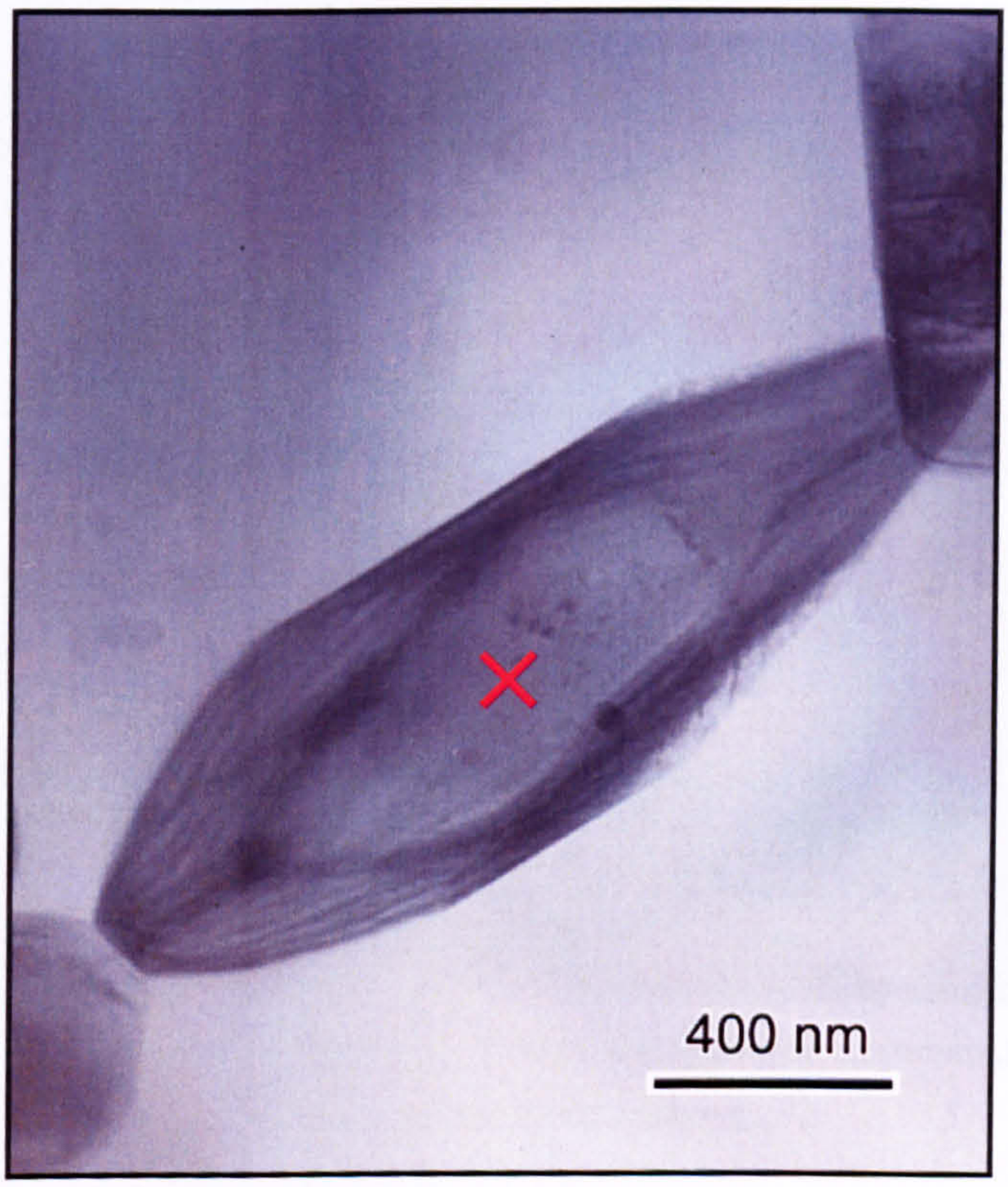


**Figure 4.2.2.8** Bright-field TEM micrograph of an Oxide AC sample, revealing an acicular $RuO_2$ crystal.

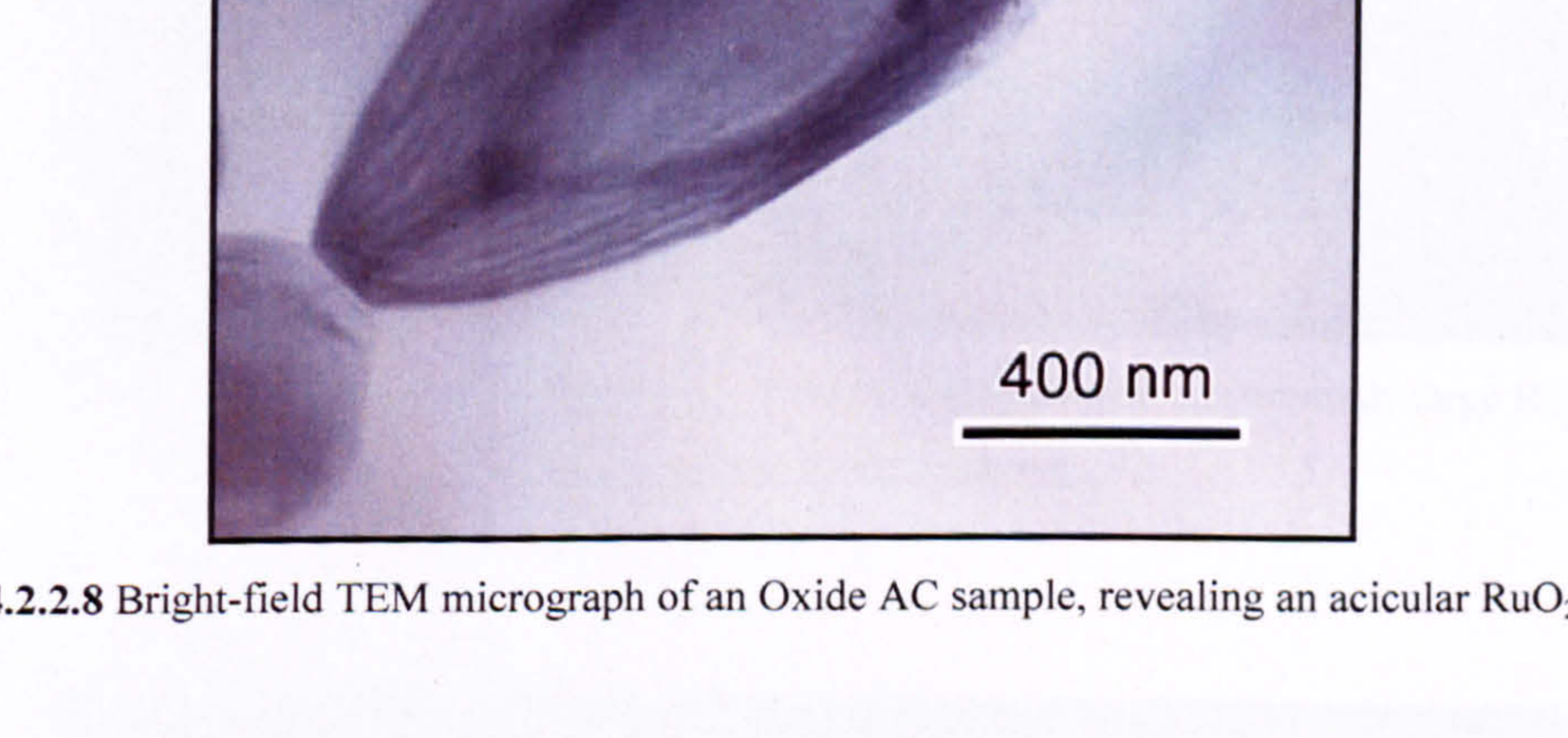


**Figure 4.2.2.9** Windowless EDX spectrum from × in **Figure 4.2.2.8** (*x*-axis = keV; *y*-axis = Intensity).

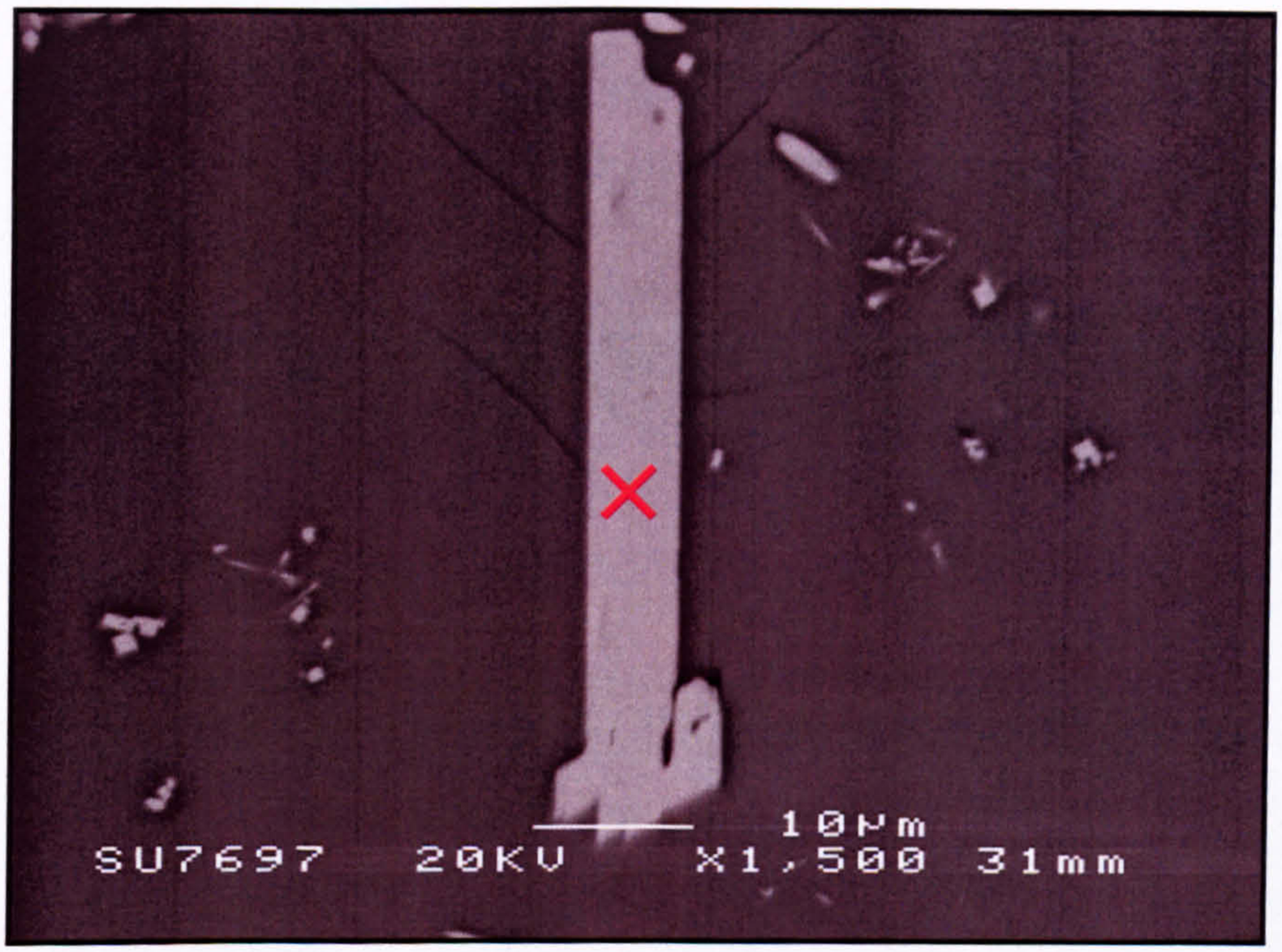


**Figure 4.2.2.10** BE SEM image of an Oxide AC sample, revealing an uncommonly large $RuO_2$ crystal with cracks radiating from it.

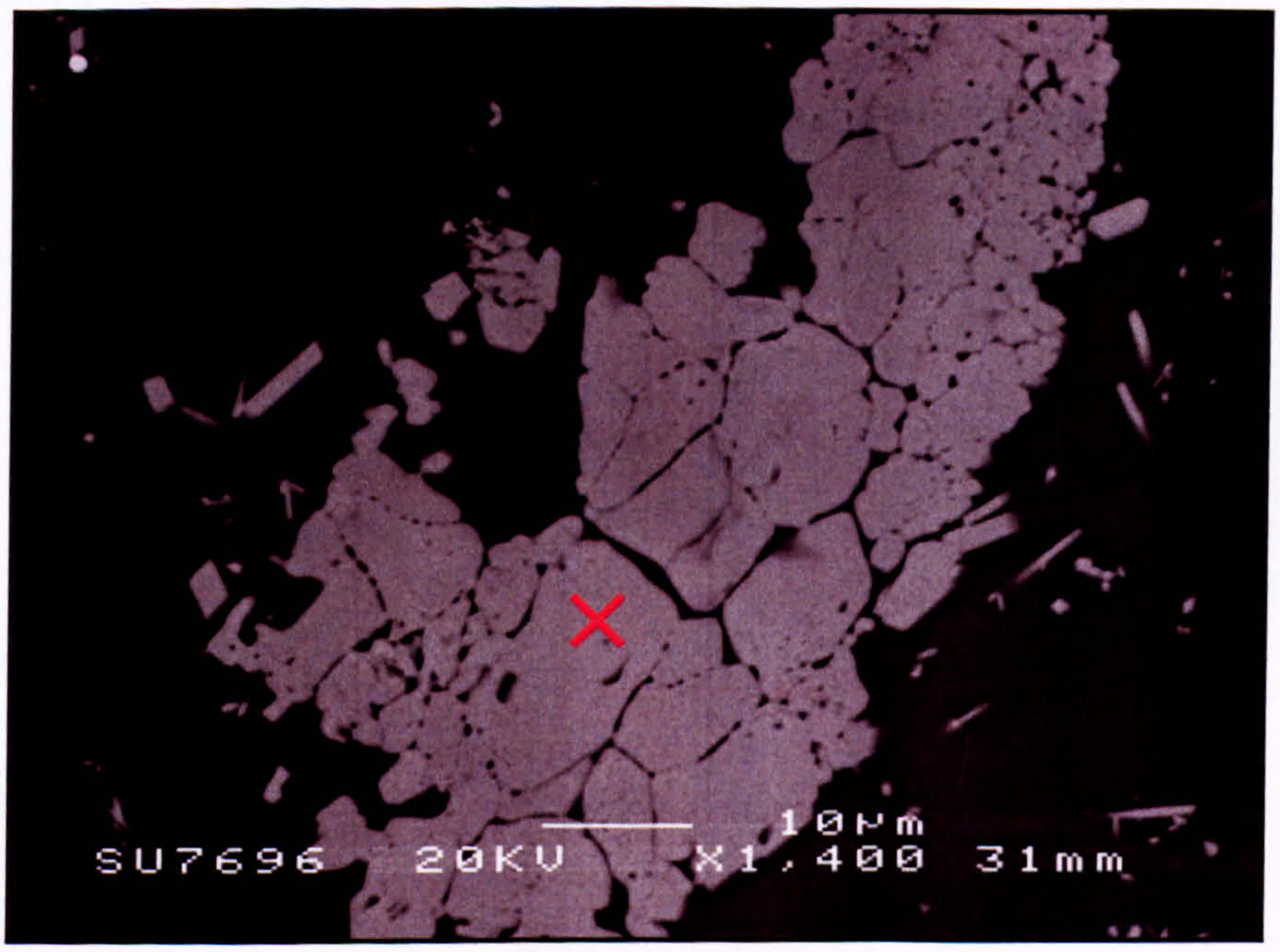


**Figure 4.2.2.11** BE SEM image of an Oxide AC sample, revealing uncommon globular $RuO_2$/metallic Ru.

*4.2.2.2 Metallic Pd-Te*

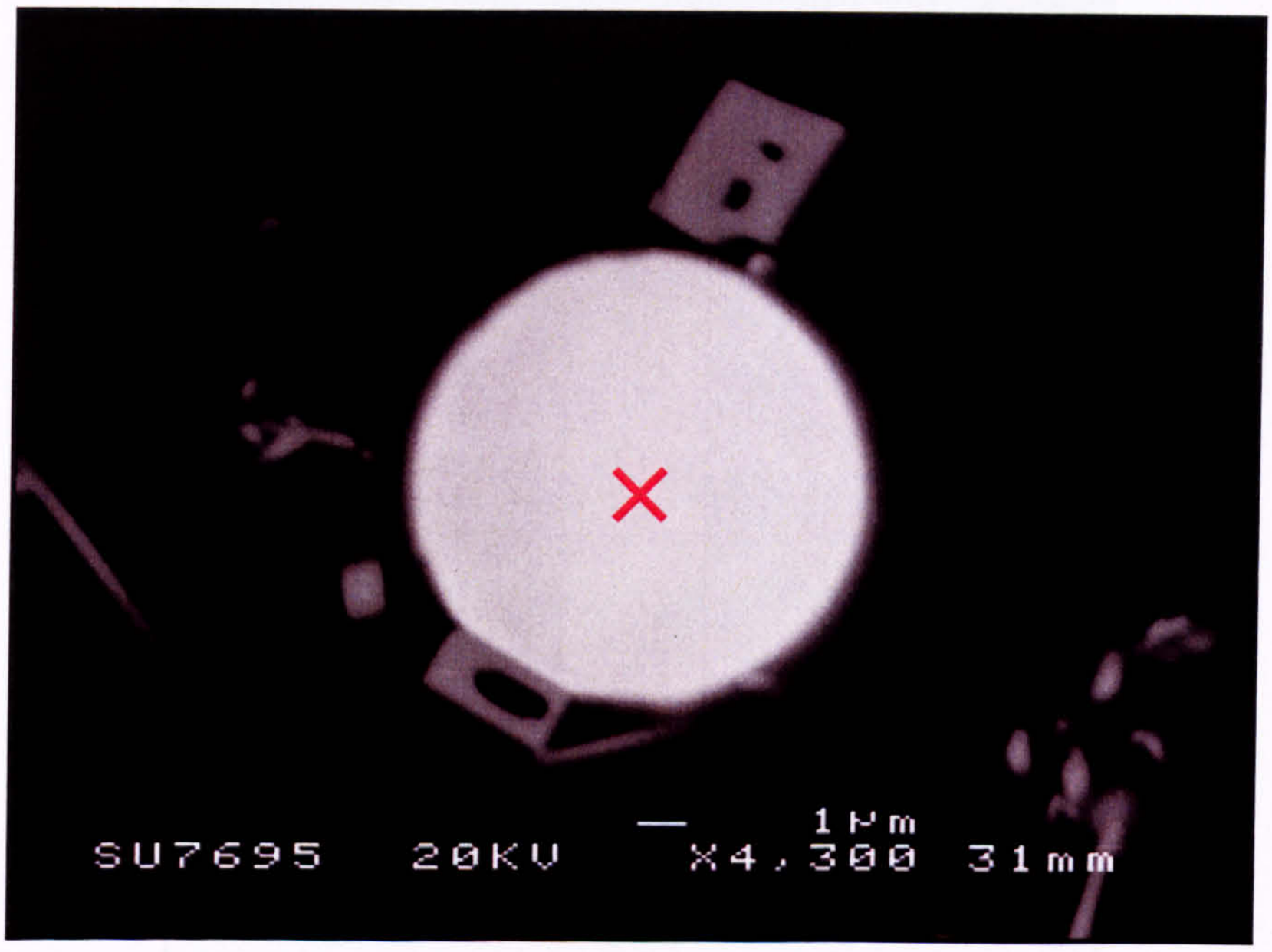


**Figure 4.2.2.12** BE SEM image of an Oxide AC sample, revealing spheroidal metallic Pd-Te.

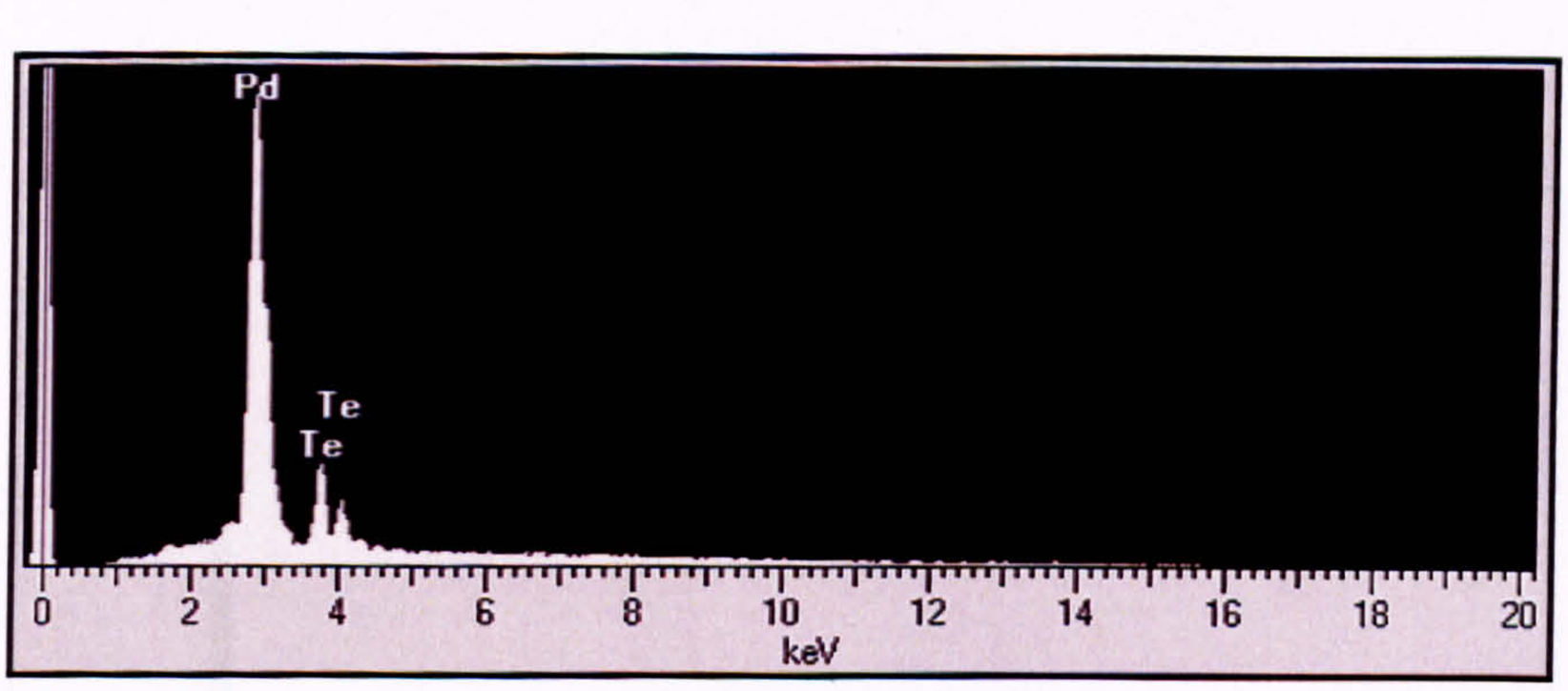


**Figure 4.2.2.13** EDX spectrum from × in **Figure 4.2.2.12** (*y*-axis = Intensity).

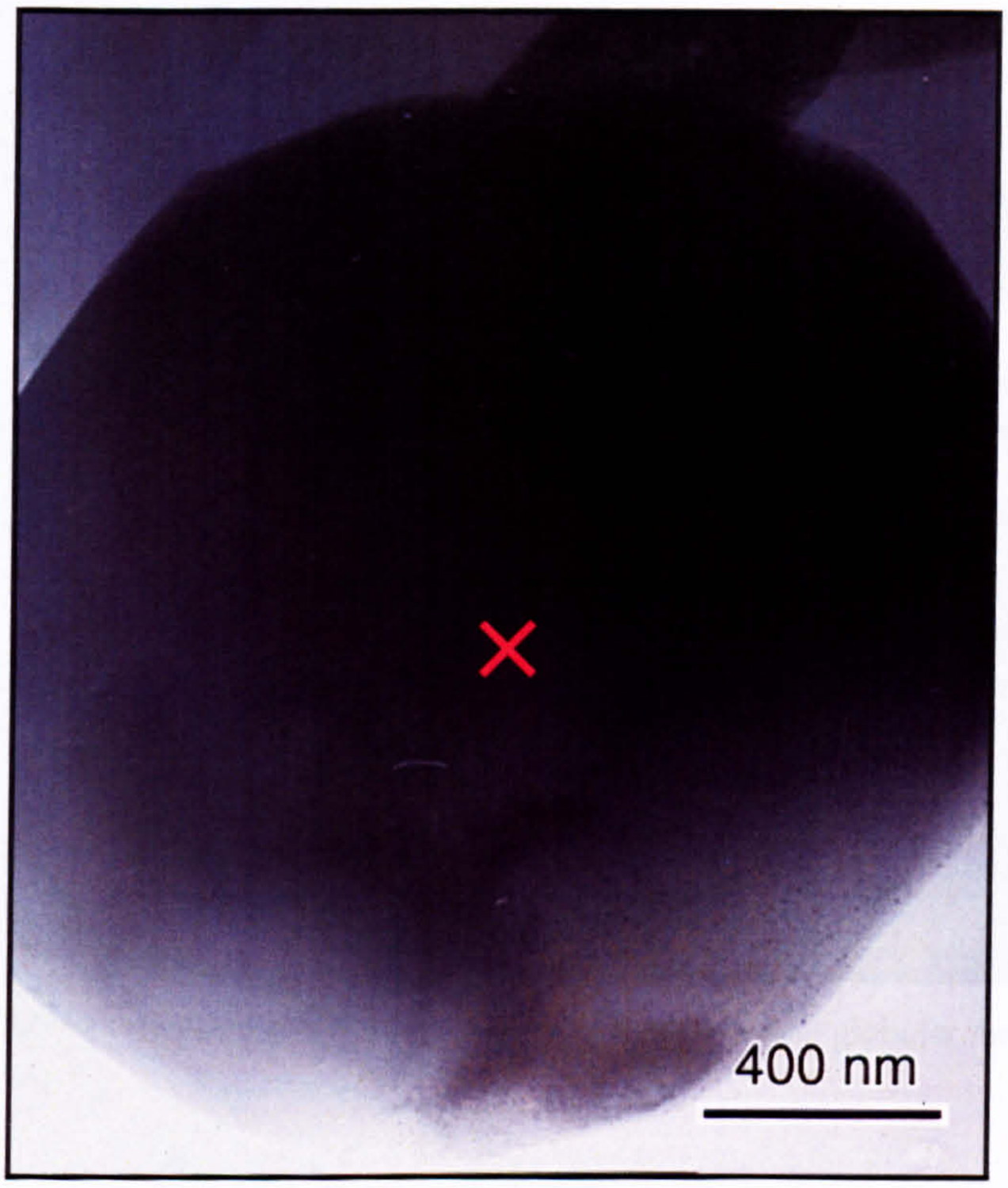


**Figure 4.2.2.14** Bright-field TEM micrograph of an Oxide AC sample, revealing spheroidal metallic Pd-Te.

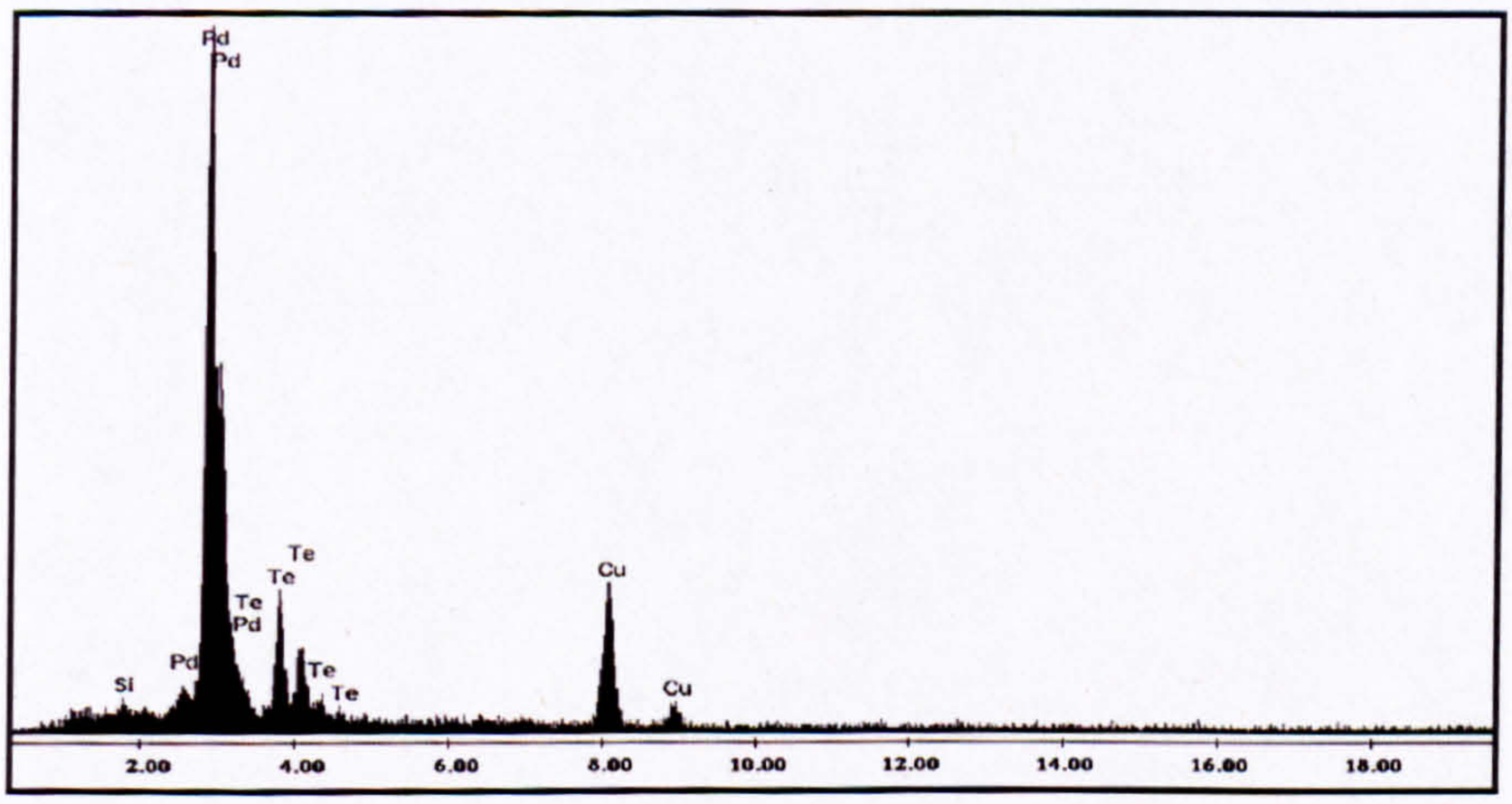


**Figure 4.2.2.15** Windowless EDX spectrum from × in **Figure 4.2.2.14** (*x*-axis = keV; *y*-axis = Intensity).


**Figure 4.2.2.16** SE SEM image of an Oxide AC sample, revealing globular metallic Pd-Te.

### *4.2.2.3 $(Cr,Fe,Ni)_3O_4$*

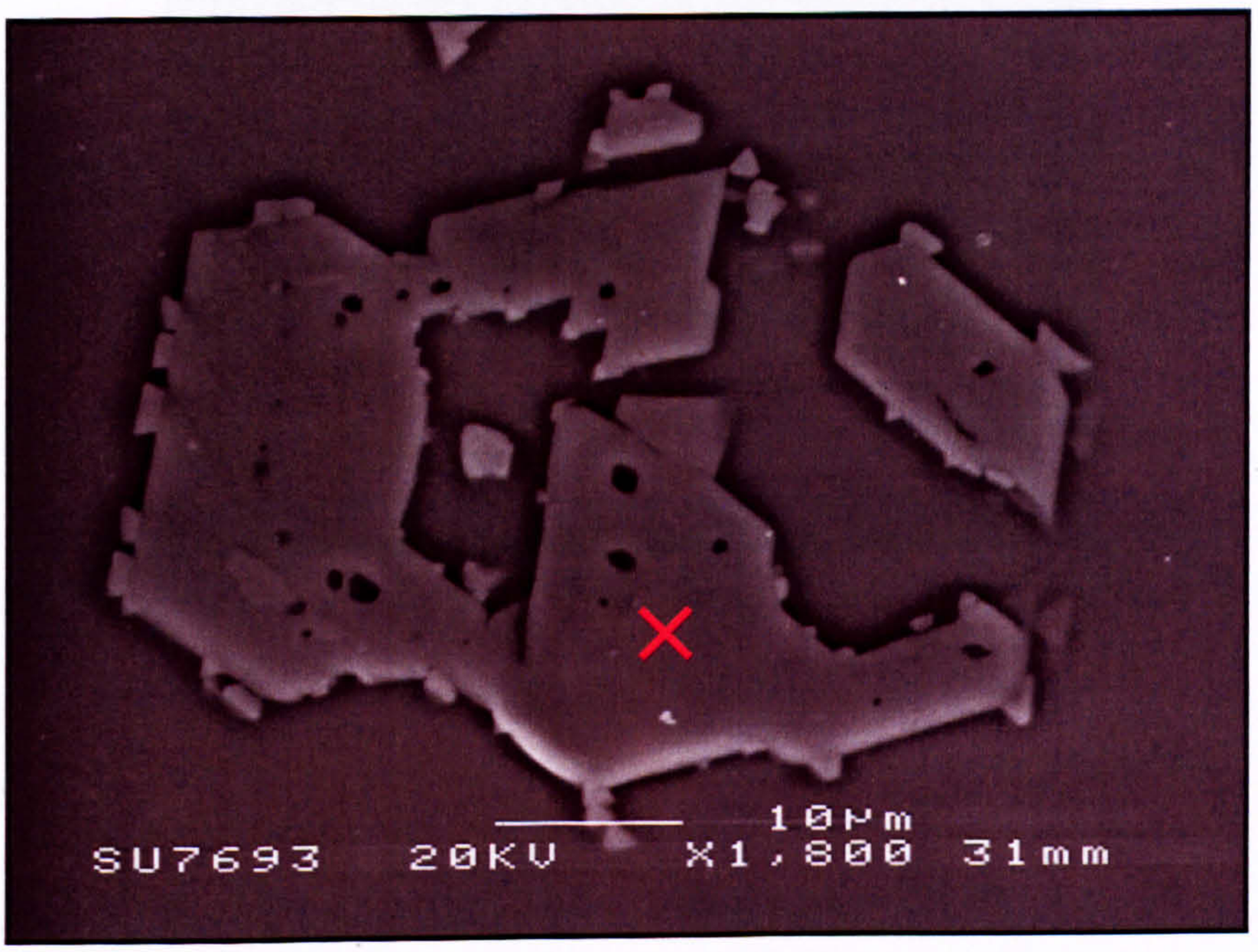


**Figure 4.2.2.17** SE SEM image of an Oxide AC sample, revealing a facetted $(Cr,Fe,Ni)_3O_4$ crystal.

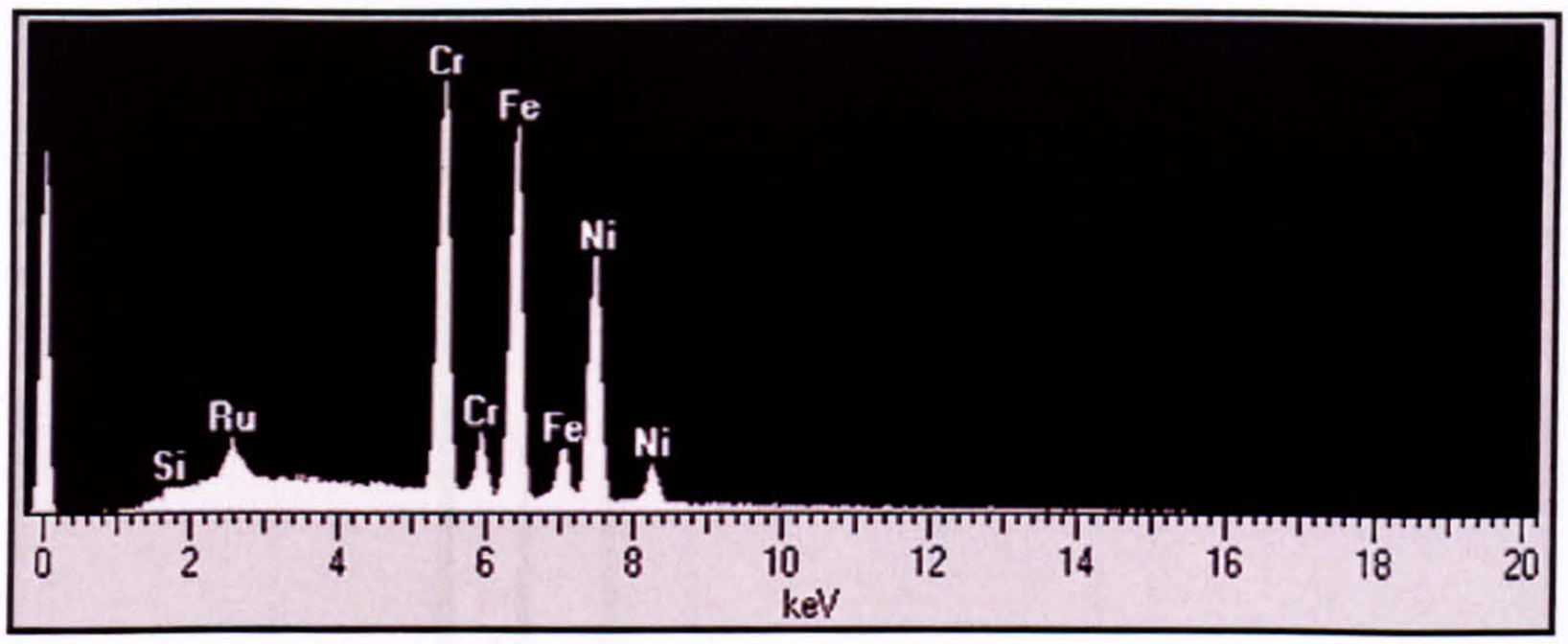


**Figure 4.2.2.18** EDX spectrum from × in **Figure 4.2.2.17** (*y*-axis = Intensity).

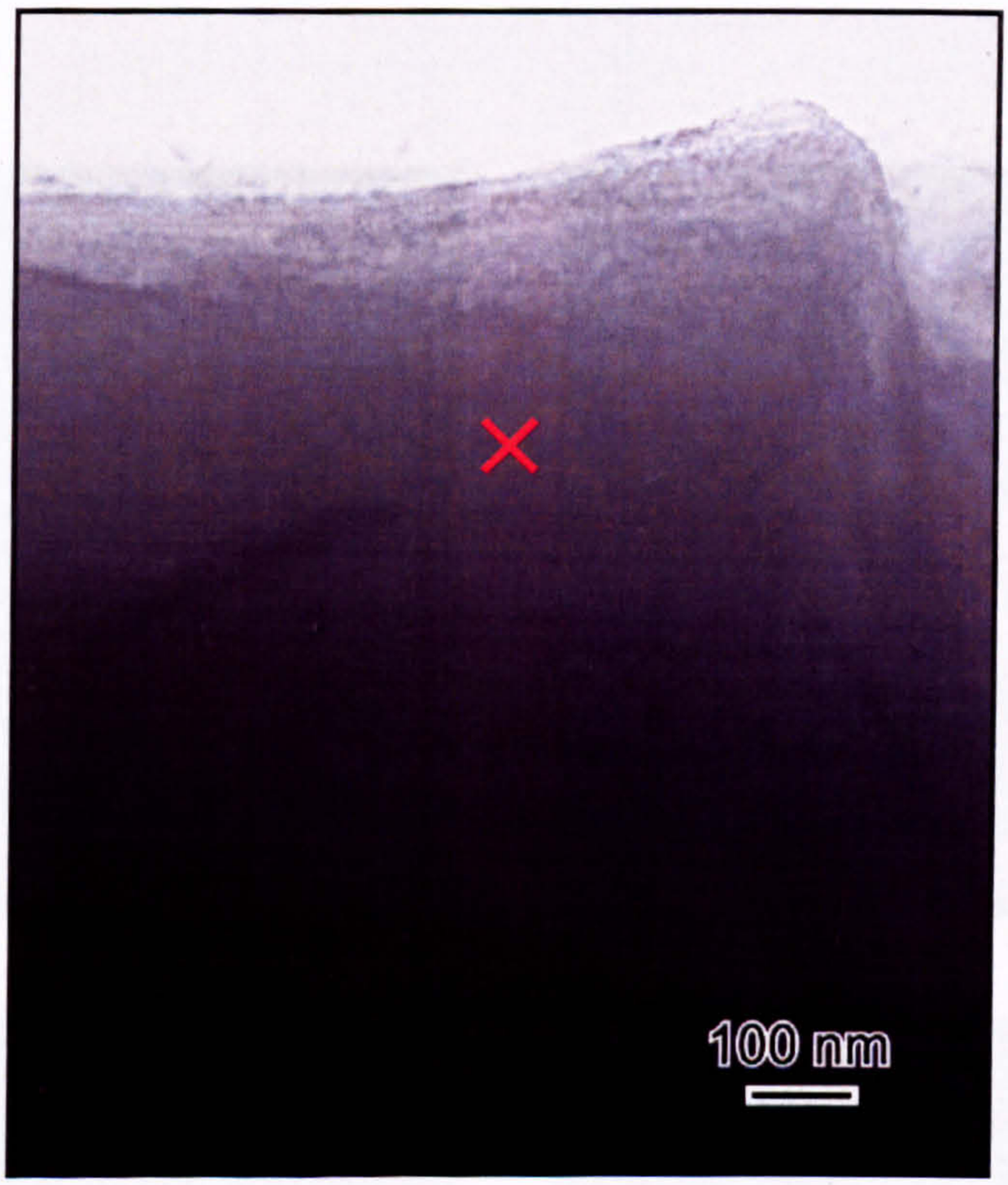


**Figure 4.2.2.19** Bright-field TEM micrograph of an Oxide AC sample, revealing a facetted $(Cr,Fe,Ni)_3O_4$ crystal.

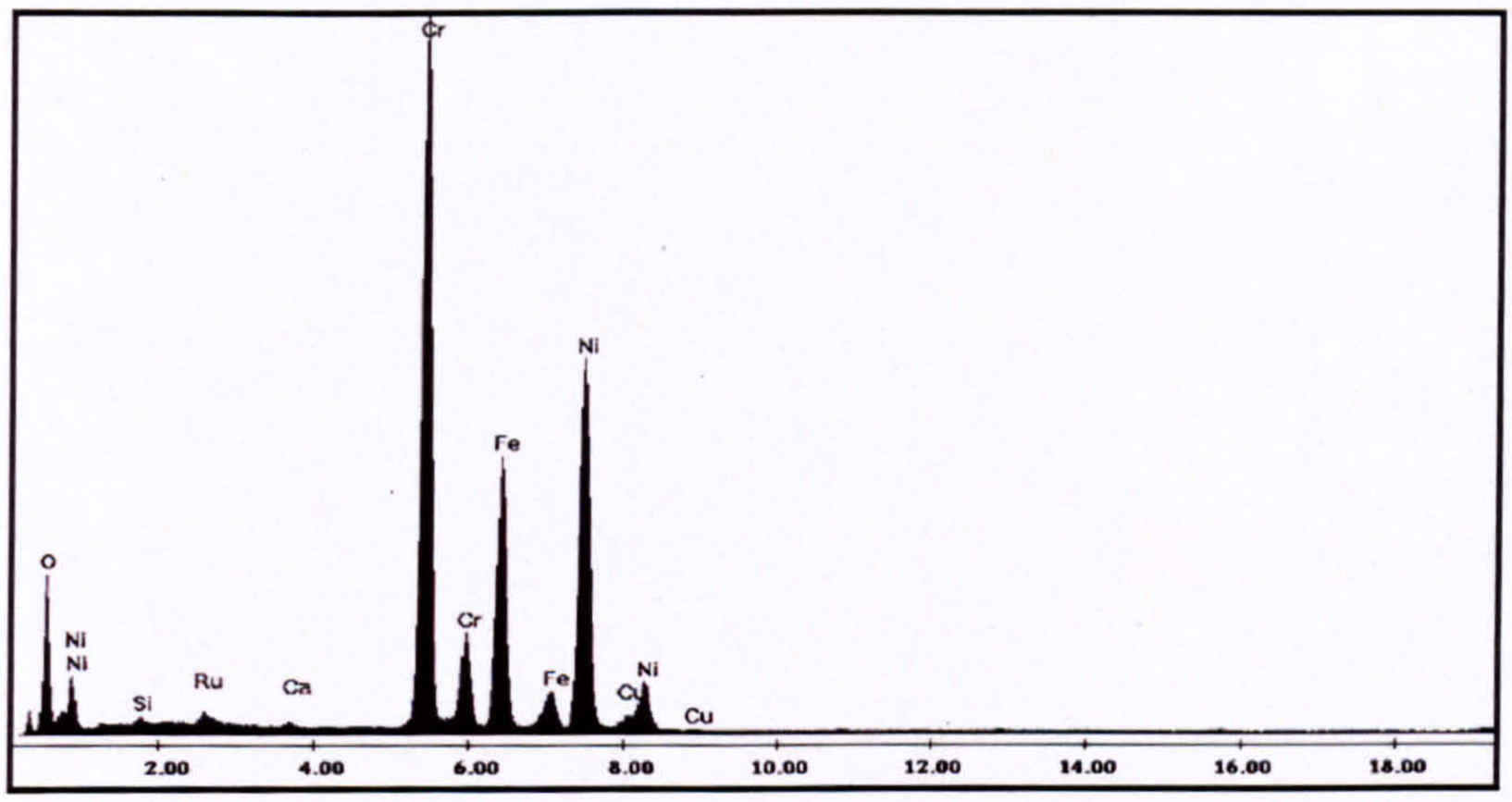


**Figure 4.2.2.20** Windowless EDX spectrum from × in **Figure 4.2.2.19** (*x*-axis = keV; *y*-axis = Intensity).

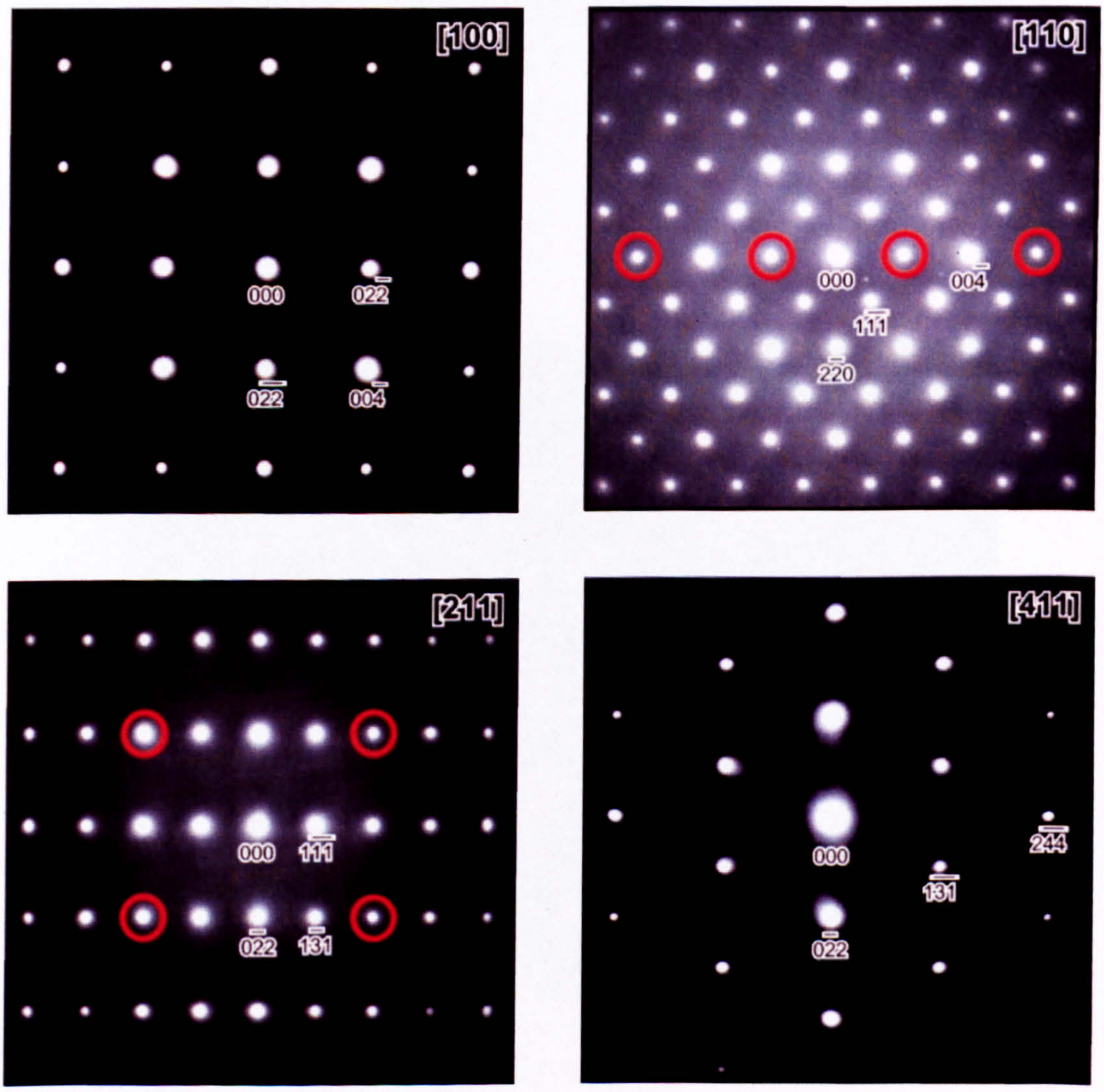


**Figure 4.2.2.21** Electron diffraction patterns from × in **Figure 4.2.2.19**, indexed and identified as the spinel crystal structure using data from Della Giusta *et al.* (1987). Spots arising from double diffraction are circled in red.

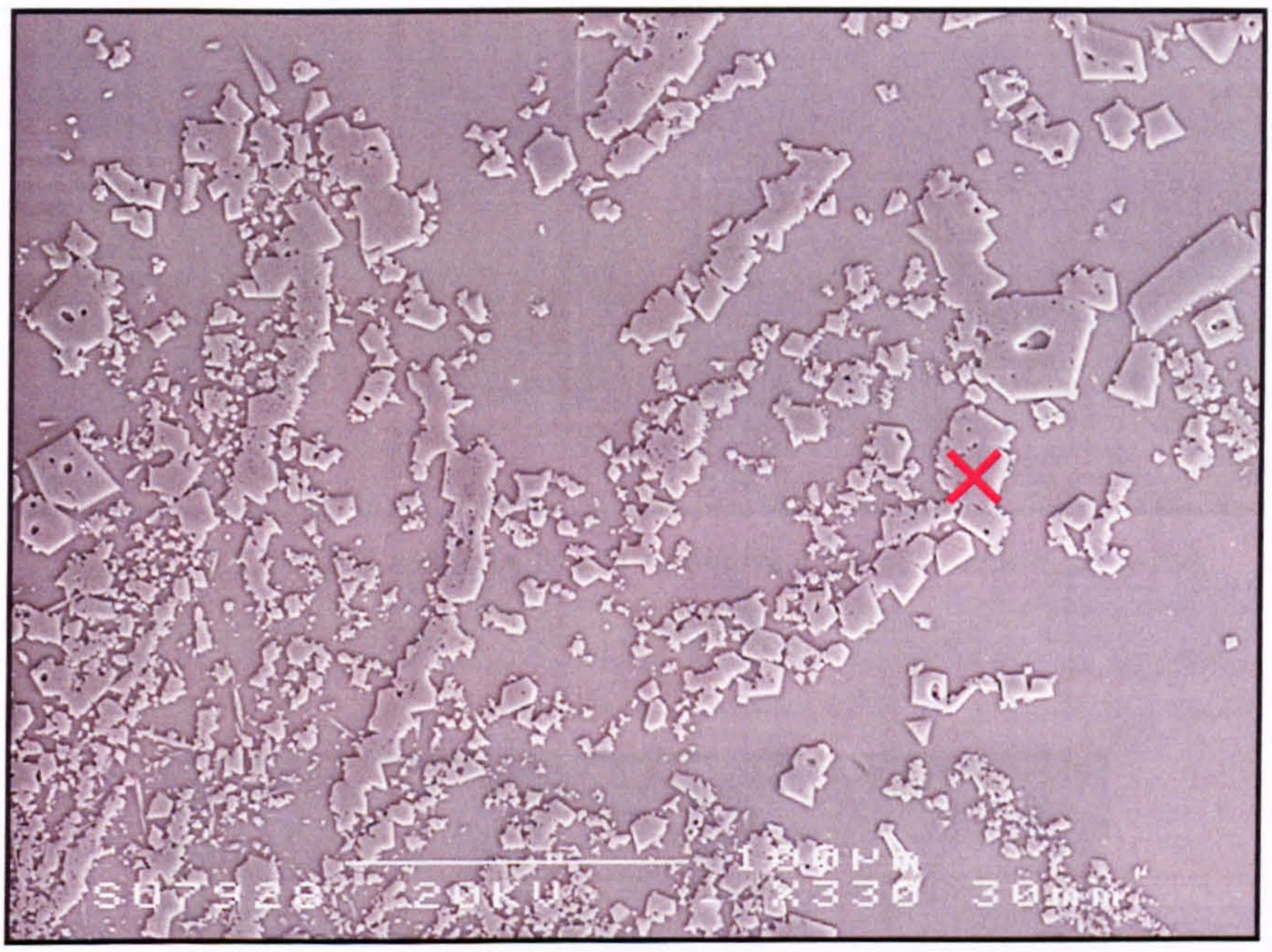


**Figure 4.2.2.22** SE SEM image of an Oxide AC sample, reveals an agglomeration of facetted $(Cr,Fe,Ni)_3O_4$ crystals.

### *4.2.2.4* $Zr_{1-(x+y)}Ce_xGd_yO_{2-(y/2)}$

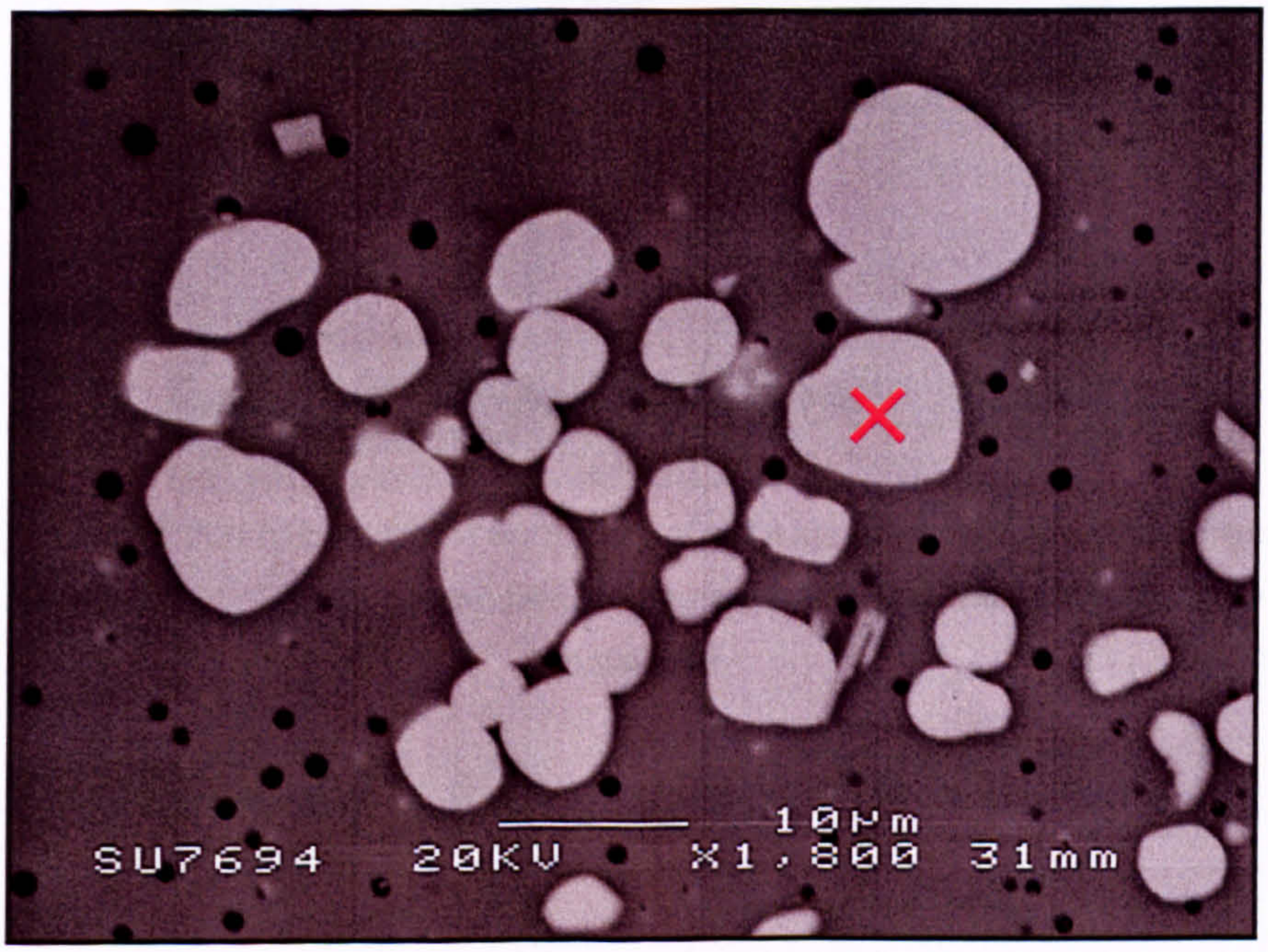


**Figure 4.2.2.23** BE SEM image of an Oxide AC sample, revealing globular $Zr_{1-(x+y)}Ce_xGd_yO_{2-(y/2)}$ (light grey) and bubbles (black).

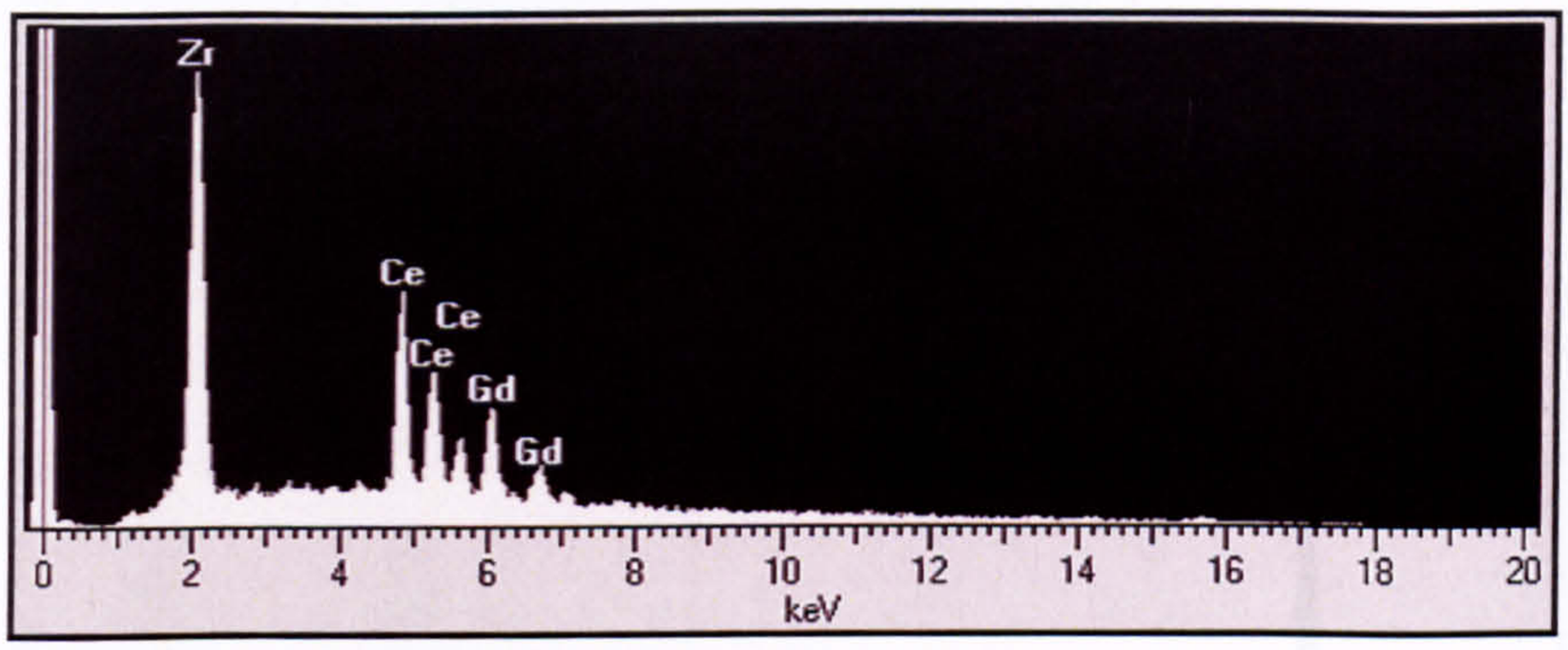


**Figure 4.2.2.24** EDX spectrum from × in **Figure 4.2.2.23** (*y*-axis = Intensity).

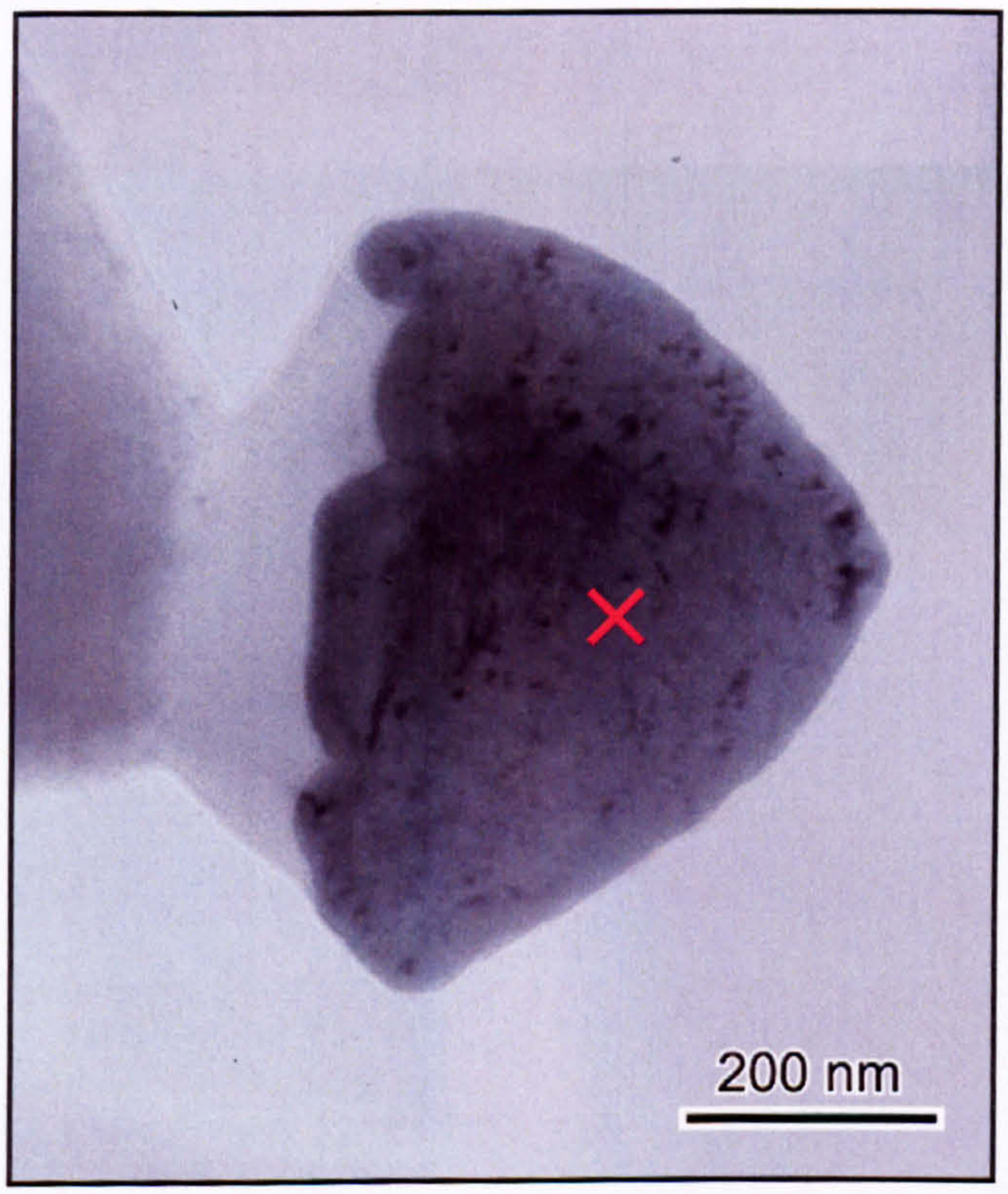


**Figure 4.2.2.25** Bright-field TEM micrograph of an Oxide AC sample, revealing globular $Zr_{1-(x+y)}Ce_xGd_yO_{2-(y/2)}$. Visible 'contrast features' approximately 10–20 nm in size are due to nano-crystallinity.

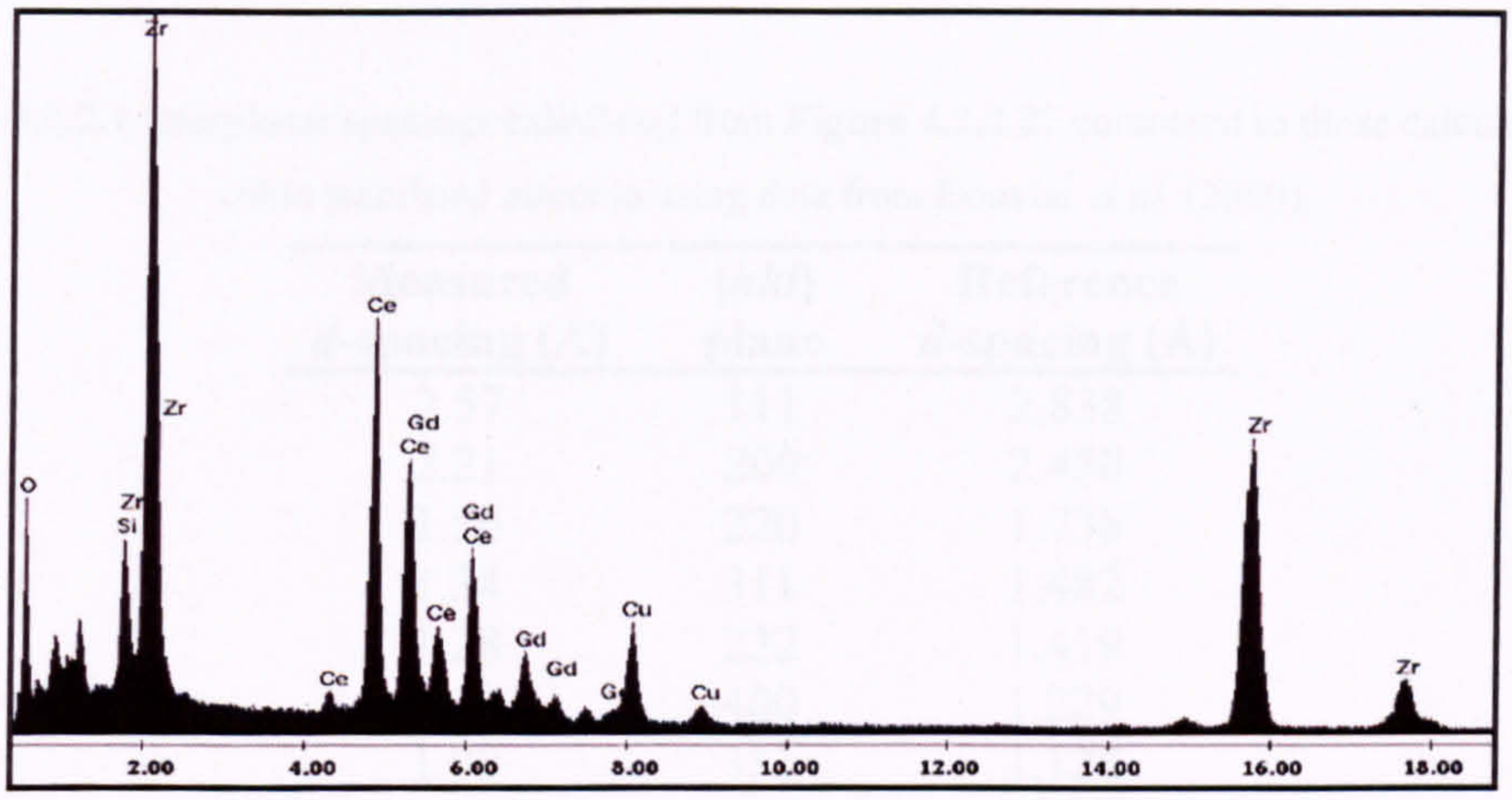


**Figure 4.2.2.26** Windowless EDX spectrum from × in **Figure 4.2.2.25** (*x*-axis = keV; *y*-axis = Intensity).

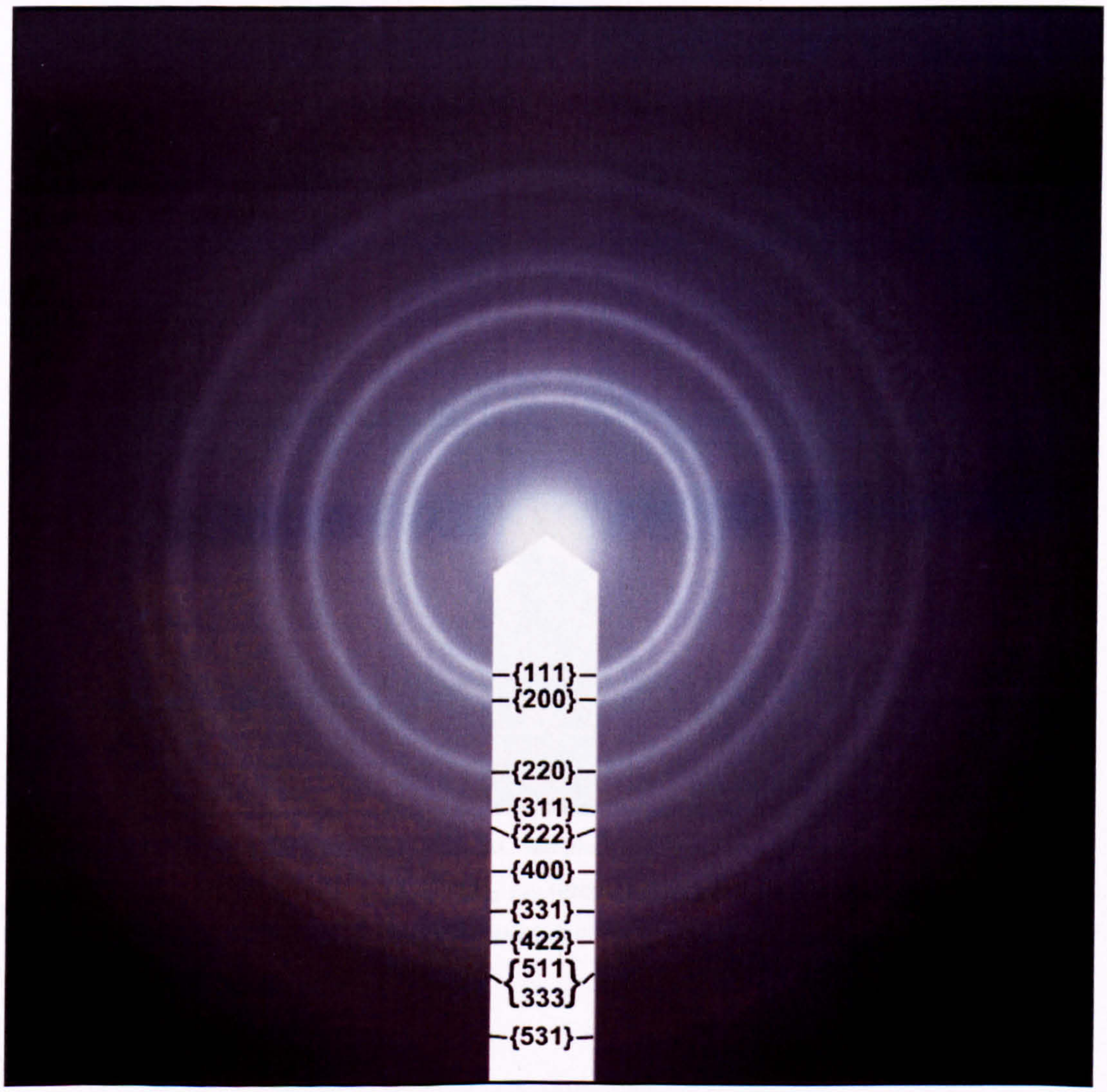


**Figure 4.2.2.27** Electron diffraction pattern from × in **Figure 4.2.2.25**, indexed and identified as the fluorite crystal structure using data from Bouvier *et al.* (2000). Ring pattern due to nano-crystallinity.

**Table 4.2.2.1** Interplanar spacings calculated from **Figure 4.2.2.27** compared to those calculated for cubic-stabilised zirconia using data from Bouvier *et al.* (2000).

| **Measured *d*-spacing (Å)** | **{*hkl*} plane** | **Reference *d*-spacing (Å)** |
|---|---|---|
| 2.57 | 111 | 2.838 |
| 2.21 | 200 | 2.458 |
| 1.56 | 220 | 1.738 |
| 1.34 | 311 | 1.482 |
| 1.28 | 222 | 1.419 |
| 1.10 | 400 | 1.229 |
| 1.00 | 331 | 1.128 |
| 0.91 | 422 | 1.003 |
| 0.85 | 511, 333 | 0.946 |
| 0.73 | 531 | 0.831 |

### *4.2.2.5 Lanthanide (Nd,Gd,La,Ce) Silicate*

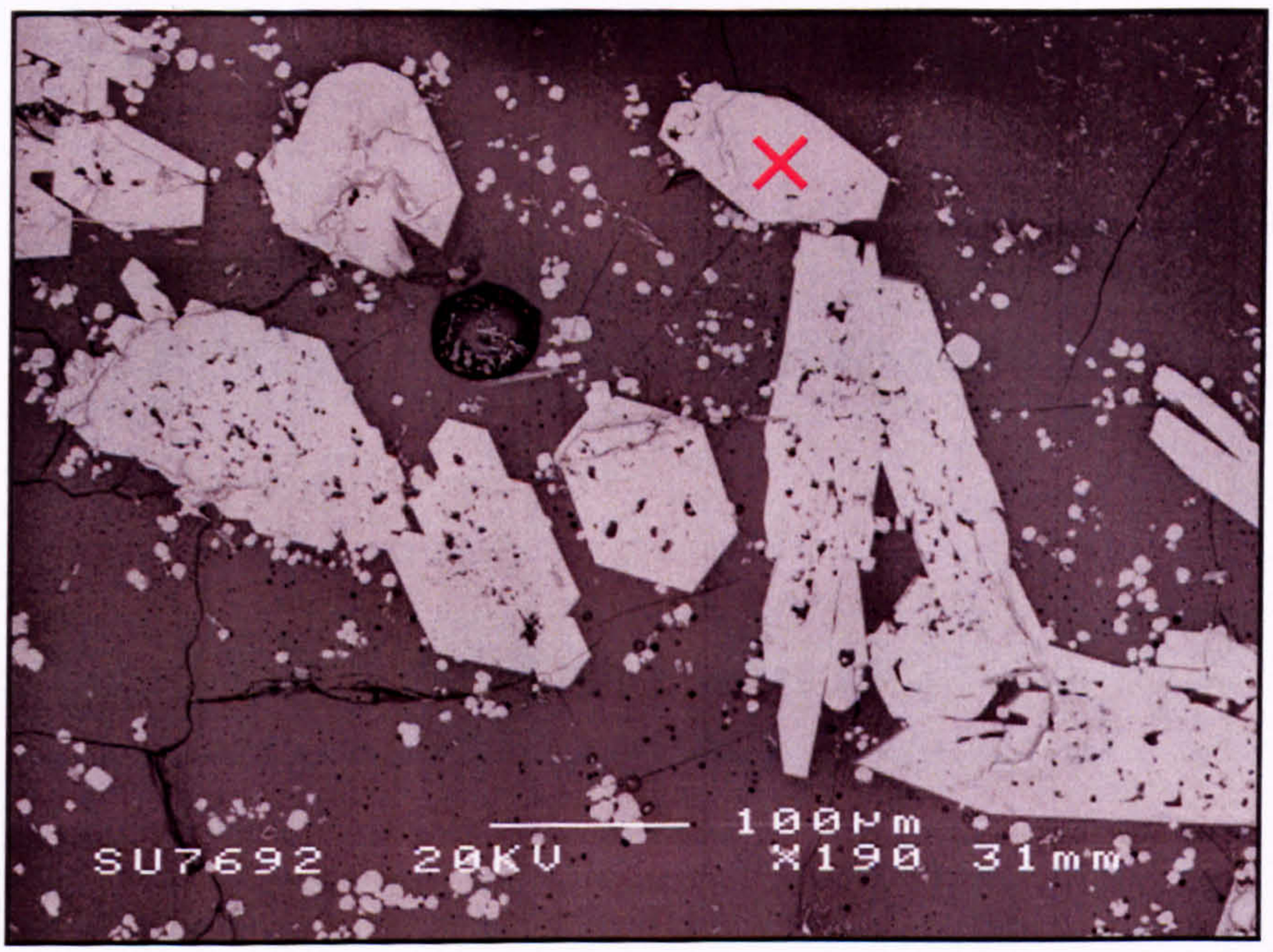


**Figure 4.2.2.28** BE SEM image of an Oxide AC sample, revealing hexagonal lanthanide (Nd,Gd,La,Ce) silicate (light grey), globular $Zr_{1-(x+y)}Ce_xGd_yO_{2-(y/2)}$ (grey), bubbles (black) and cracking. Image is of the interior of dissolving/relict calcine.

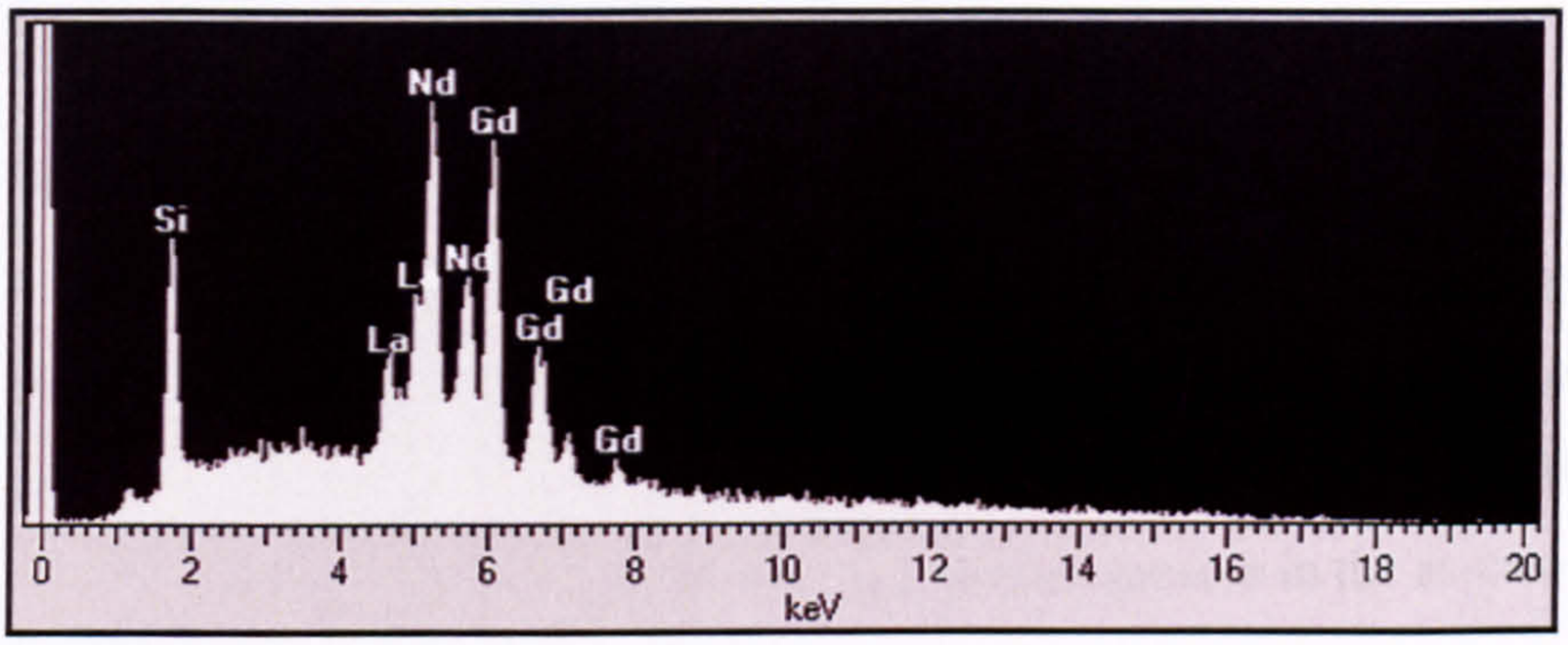


**Figure 4.2.2.29** EDX spectrum from × in **Figure 4.2.2.28** (*y*-axis = Intensity).

### 4.2.3 Heat Treated Blend Glass (Blend HT)

Two XRD traces of Blend HT (Blend glass heat treated at 690 °C for 70 h) are presented in **Figure 4.2.3.1** to illustrate the consistency of XRD traces obtained from different samples of Blend HT. **Figure 4.2.3.1** reveals peak matches for tetragonal $RuO_2$ (labelled ∇; ICDD card [40-1290]), cubic $CeO_2$ (labelled ■; ICDD card [34-394]) as well as unidentified peaks. Tetragonal $RuO_2$ was already present in the as-cast glass.

$Ce_{1-(x+y)}Zr_xGd_yO_{2-(y/2)}$

The cubic $CeO_2$ crystal phase identified by XRD (**Figure 4.2.3.1**) has the fluorite structure (space group $Fm\bar{3}m$). SEM revealed spheroidal $Ce_{1-(x+y)}Zr_xGd_yO_{2-(y/2)}$ (**Figure 4.2.3.2**) in the glass. Spheroidal $Ce_{1-(x+y)}Zr_xGd_yO_{2-(y/2)}$ (labelled × in **Figure 4.2.3.2**) had an EDX spectrum (**Figure 4.2.3.3**) which showed Ce, Zr and Gd. Spheroidal $Ce_{1-(x+y)}Zr_xGd_yO_{2-(y/2)}$ (the small white phase in **Figure 4.2.3.8**) is sometimes associated with facetted lanthanide (Nd,Gd,La,Ce) silicate (the large grey phase in **Figure 4.2.3.8**).

*(Sr,Nd,La) Molybdate*

SEM revealed dendritic (Sr,Nd,La) molybdate (**Figure 4.2.3.4**) in the glass. Dendritic (Sr,Nd,La) molybdate (labelled × in **Figure 4.2.3.4**) had an EDX spectrum (**Figure 4.2.3.5**) which showed Mo, Sr, Nd and La. A (Sr,Nd,La) molybdate dendrite was observed to nucleate and grow on $RuO_2$ (**Figure 4.2.3.4**). This phase is not associated with the unidentified XRD peaks in **Figure 4.2.3.1**.

*Lanthanide (Nd,Gd,La,Ce) Silicate*

SEM revealed acicular lanthanide (Nd,Gd,La,Ce) silicate (**Figure 4.2.3.6**) and facetted lanthanide (Nd,Gd,La,Ce) silicate (**Figures 4.2.3.8** and **4.2.3.9**) in the glass. Acicular lanthanide (Nd,Gd,La,Ce) silicate (labelled × in **Figure 4.2.3.6**) had an EDX spectrum (**Figure 4.2.3.7**) which showed Si, Nd, Gd, La and Ce. **Figures 4.2.3.8** and **4.2.3.9** both had EDX spectra (from × in both images) near identical to **Figure 4.2.3.7**. Acicular lanthanide (Nd,Gd,La,Ce) silicate was associated with a $RuO_2$-rich region in **Figure 4.2.3.6**; whilst facetted lanthanide (Nd,Gd,La,Ce) silicate (the large grey phase in **Figure 4.2.3.8**) was sometimes associated with spheroidal $Ce_{1-(x+y)}Zr_xGd_yO_{2-(y/2)}$ (the

small white phase in **Figure 4.2.3.8**). This phase is likely associated with the unidentified XRD peaks in **Figure 4.2.3.1.**

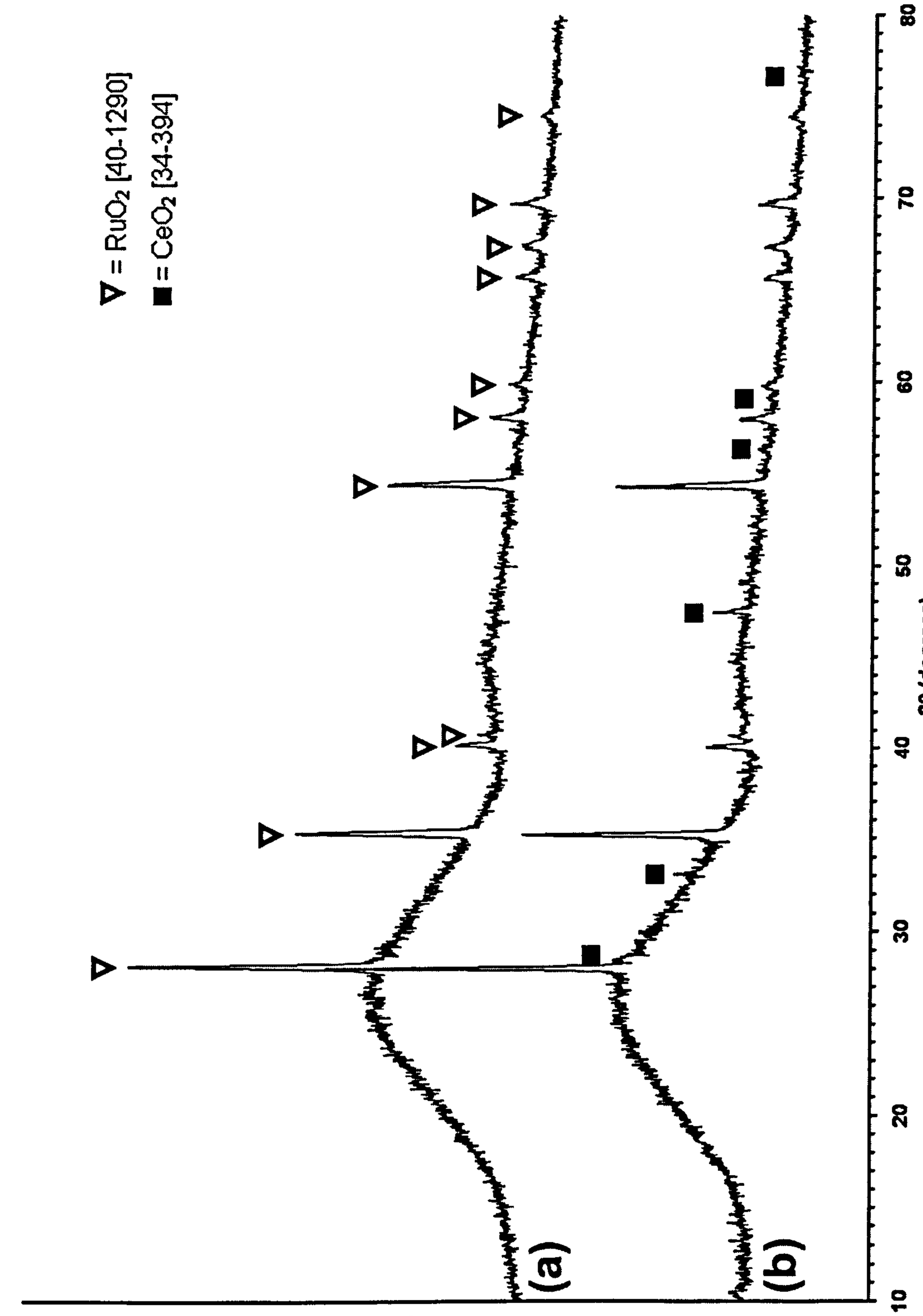


**Figure 4.2.3.1** XRD traces from two Blend HT samples, illustrating their consistency. Peak matches have been labelled, with $RuO_2$ also identified in trace **(b)**.

### *4.2.3.1* $Ce_{1-(x+y)}Zr_xGd_yO_{2-(y/2)}$

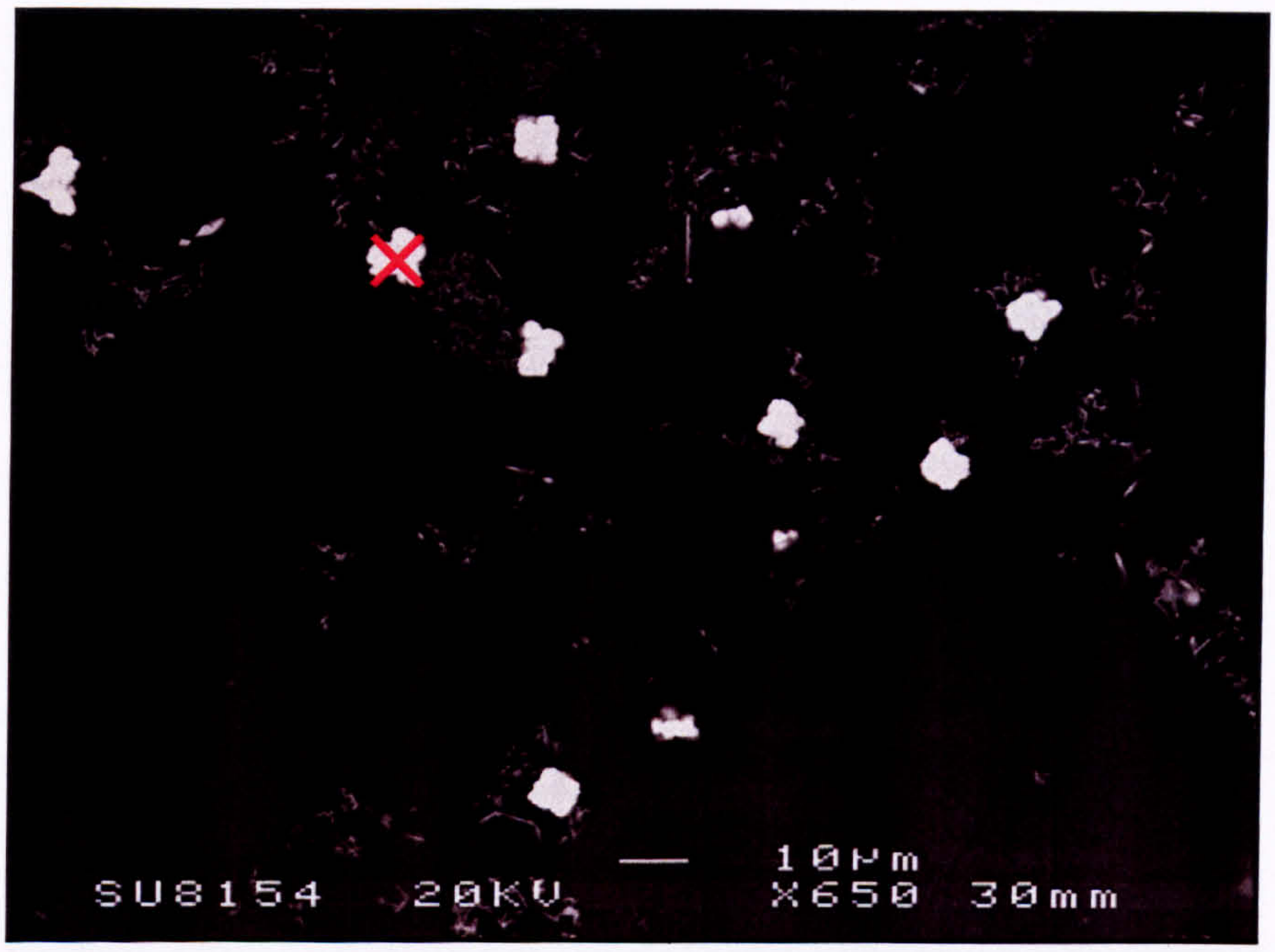


**Figure 4.2.3.2** BE SEM image of a Blend HT sample, revealing spheroidal $Ce_{1-(x+y)}Zr_xGd_yO_{2-(y/2)}$.

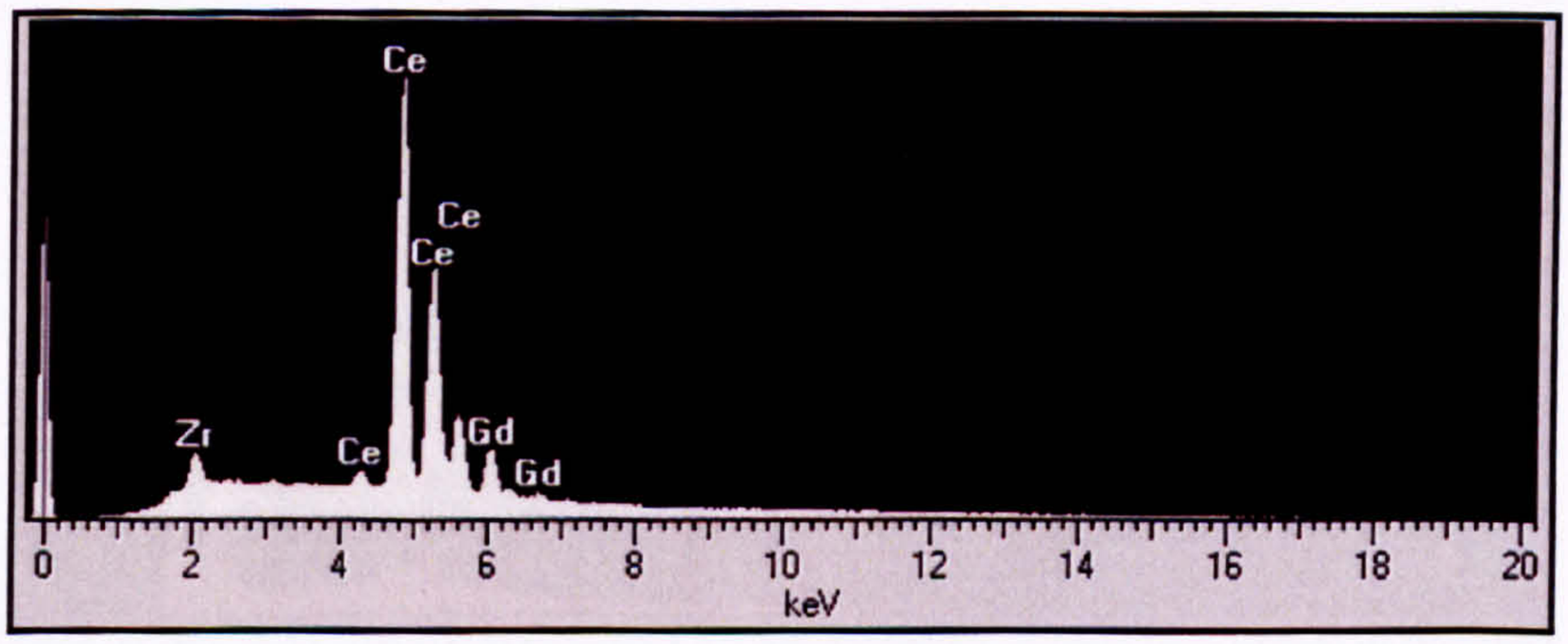


**Figure 4.2.3.3** EDX spectrum from × in **Figure 4.2.3.2** ($y$-axis = Intensity).

### *4.2.3.2 (Sr,Nd,La) Molybdate*

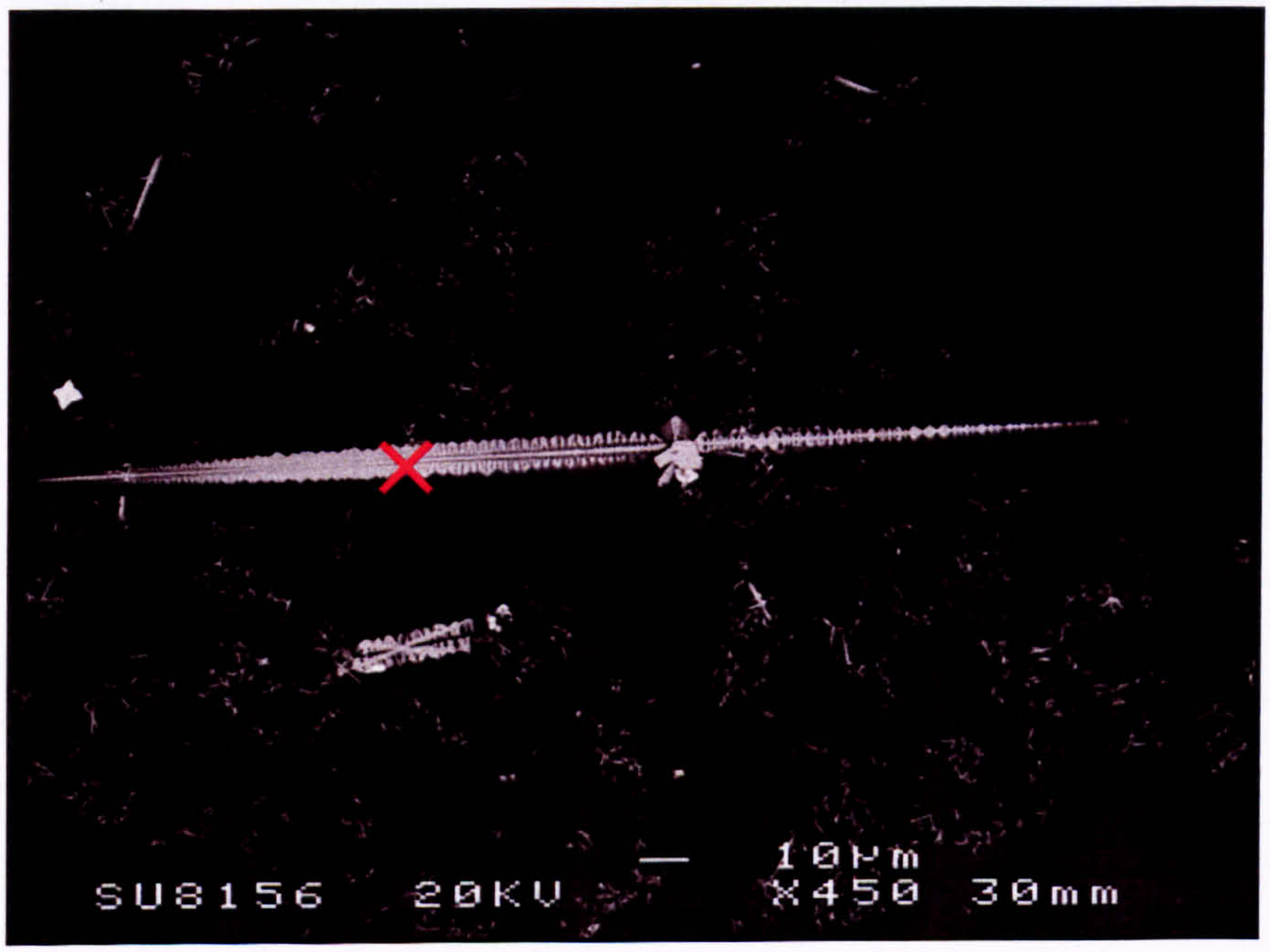


**Figure 4.2.3.4** BE SEM image of a Blend HT sample, revealing dentritic (Sr,Nd,La) molybdate, a large crystal of which has nucleated and grown on $RuO_2$.

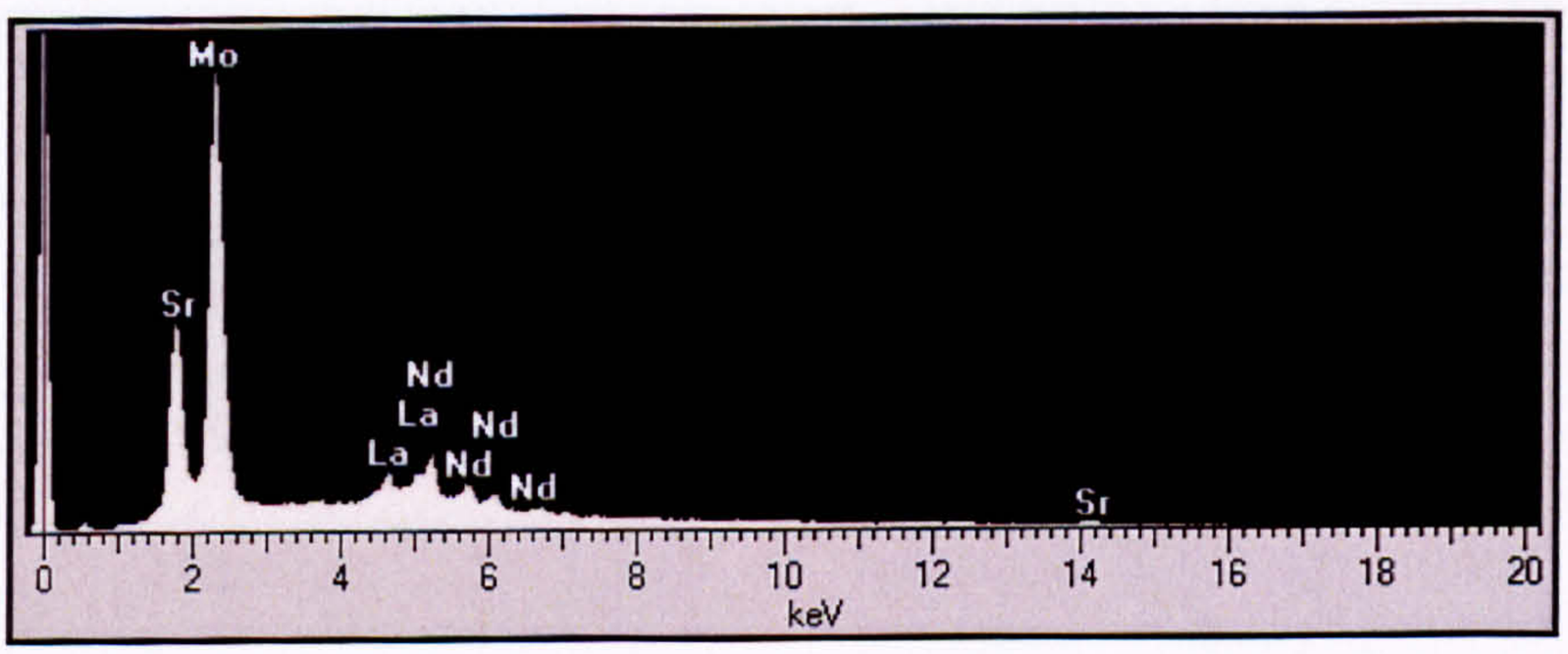


**Figure 4.2.3.5** EDX spectrum from × in **Figure 4.2.3.4** (*y*-axis = Intensity).

### *4.2.3.3 Lanthanide (Nd,Gd,La,Ce) Silicate*

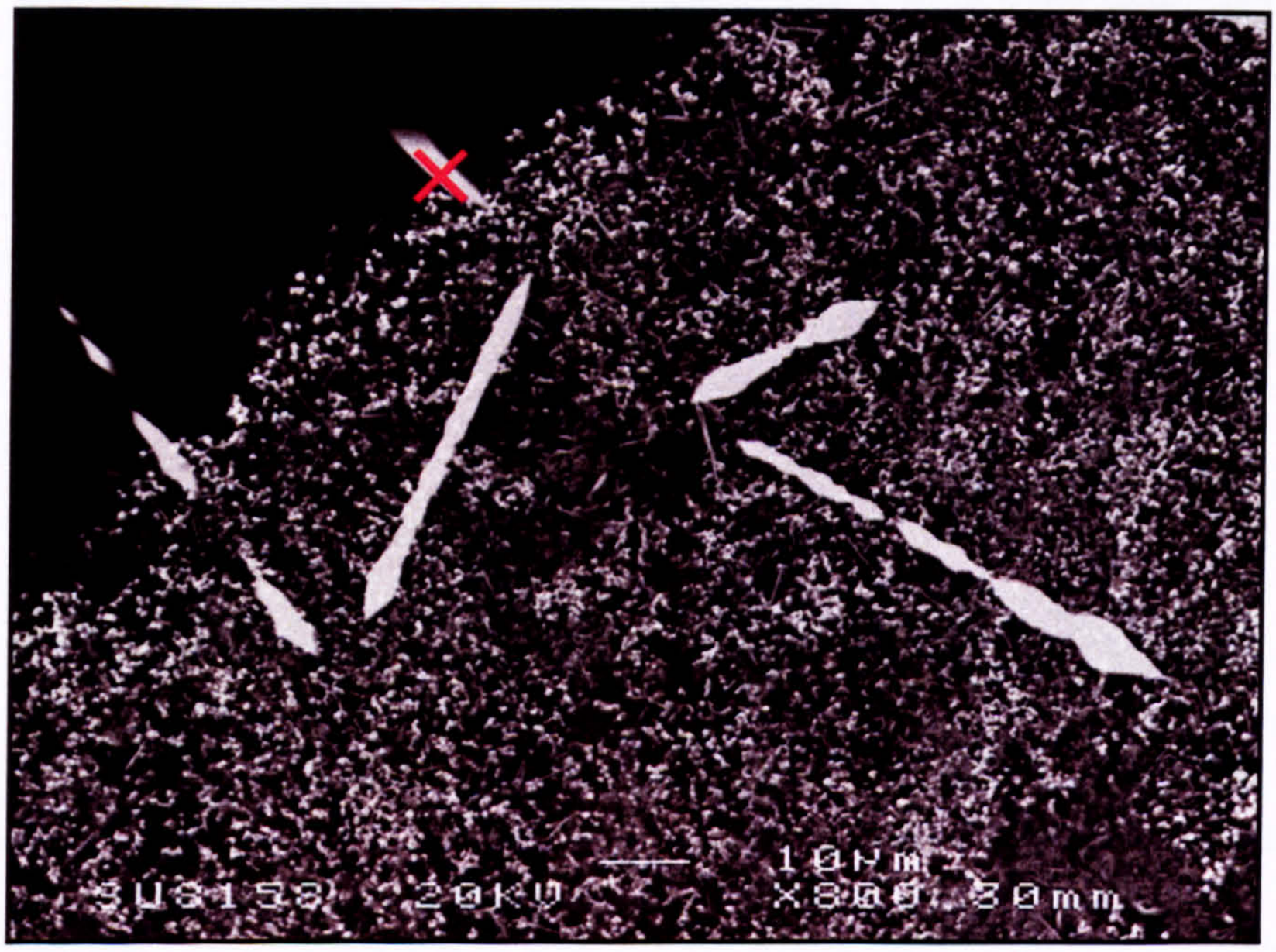


**Figure 4.2.3.6** BE SEM image of a Blend HT sample, revealing acicular lanthanide (Nd,Gd,La,Ce) silicate (white) in a $RuO_2$-rich region (grey).

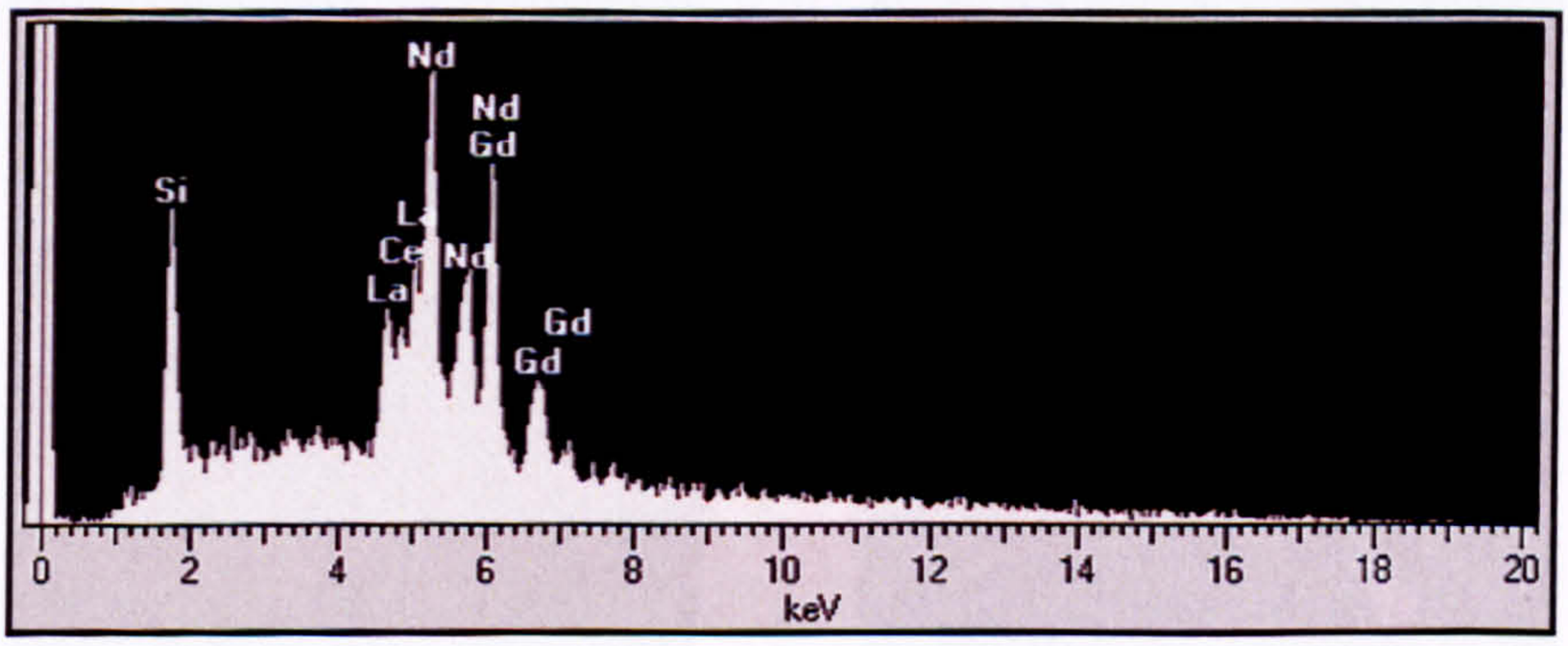


**Figure 4.2.3.7** EDX spectrum from × in **Figure 4.2.3.6** (*y*-axis = Intensity).

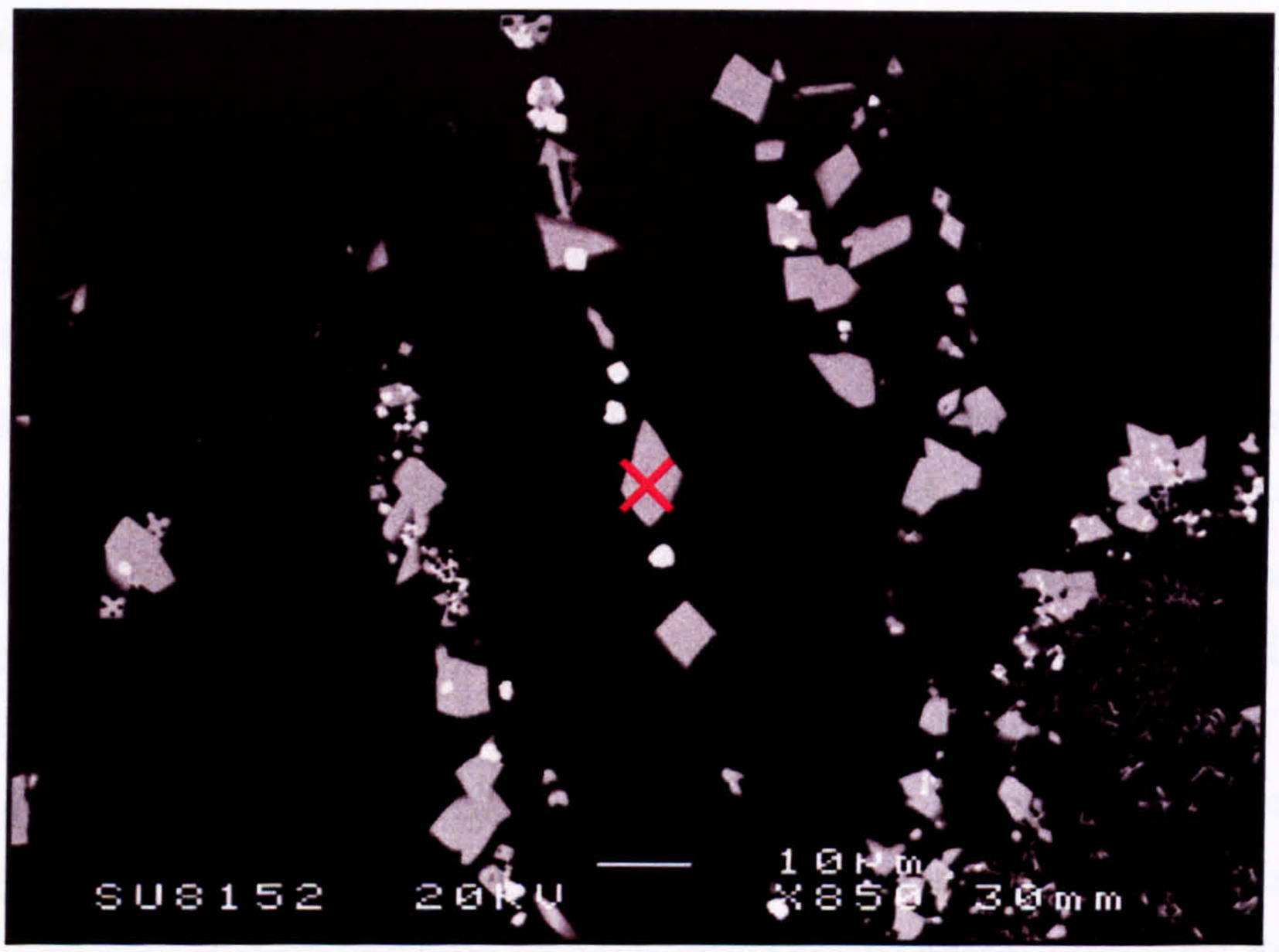


**Figure 4.2.3.8** BE SEM image of a Blend HT sample, revealing facetted lanthanide (Nd,Gd,La,Ce) silicate (grey) associated with spheroidal $Ce_{1-(x+y)}Zr_xGd_yO_{2-(y/2)}$ (white).


**Figure 4.2.3.9** BE SEM image of a Blend HT sample, revealing facetted lanthanide (Nd,Gd,La,Ce) silicate.

### 4.2.4 Heat Treated Oxide Glass (Oxide HT)

Two XRD traces of Oxide HT (Oxide glass heat treated at 690 °C for 70 h) are presented in **Figure 4.2.4.1** to illustrate the inconsistency of XRD traces obtained from different samples of Oxide HT. **Figure 4.2.4.1** reveals peak matches for tetragonal $RuO_2$ (labelled ▽; ICDD card [40-1290]), cubic Pd (labelled ◆; ICDD card [46-1043]), tetragonal $SiO_2$ (labelled □; ICDD card [39-1425]), tetragonal $NaLa(MoO_4)_2/AgLaMo_2O_8$ (labelled ✚; ICDD cards [24-1103]/[49-384]), cubic $CeO_2$ (labelled ■; ICDD card [34-394]), orthorhombic $LiNaZrSi_6O_{15}$ (labelled ○; ICDD card [29-835]) as well as unidentified peaks – four of which are labelled in red and have *d*-spacings (Å) of 5.74, 4.50, 3.03 and 2.83. A peak matched to orthorhombic $LiNaZrSi_6O_{15}$ (*d*-spacing of 2.88 Å) has a significantly greater intensity than expected, indicating there is contribution from an unidentified crystal phase. Tetragonal $RuO_2$ and cubic Pd were already present in the as-cast glass. SEM reveals glass samples have one of two different microstructures. The first microstructure shows extensive crystallisation (**Figures 4.2.4.2** and **4.2.4.3**) and extensive sample cracking (**Figure 4.2.4.4**). Indications are that this was the Type I microstructure before heat treatment, so will be termed Type A microstructure. The second microstructure displays 'banded' crystallisation (**Figure 4.2.4.5**) and phases not observed in the first microstructure. Indications are that this was Type II microstructure before heat treatment, so will be termed Type B microstructure. **Figure 4.2.4.1(a)** is typical of XRD traces obtained from glass samples with Type A microstructures. **Figure 4.2.4.1(b)** is typical of XRD traces obtained from glass samples with Type B microstructures.

*$SiO_2$*

The tetragonal $SiO_2$ crystal phase identified by XRD (**Figure 4.2.4.1**) is $\alpha$-cristobalite (space group $P4_12_12$, or its enantiomorph $P4_32_12$). SEM revealed dendritic $\alpha$-cristobalite (**Figures 4.2.4.6** and **4.2.4.8**) in the glass. Dendritic $\alpha$-cristobalite (labelled × in **Figure 4.2.4.6**) had an EDX spectrum (**Figure 4.2.4.7**) which showed only Si. **Figure 4.2.4.8** had an EDX spectrum (from × in the image) near identical to **Figure 4.2.4.7.** This crystal phase was not observed in glass samples by TEM. Extensive cracking in and around dendritic $\alpha$-cristobalite is observed by SEM in **Figure 4.2.4.8.** $\alpha$-cristobalite is found exclusively in Type A microstructures.

*(Na,Sr,Nd,La)$MoO_4$*

The tetragonal $NaLa(MoO_4)_2/AgLaMo_2O_8$ crystal phases peak matched using XRD **(Figure 4.2.4.1)** are powellites (space group $I4_1/a$). These crystal phases are not thought to be present in the glass; rather, a powellite crystal phase with matching lattice parameters but different chemical composition is present. SEM revealed dendritic (Na,Sr,Nd,La)$MoO_4$ **(Figures 4.2.4.9, 4.2.4.14** and **4.2.4.15)** in the glass. Dendritic (Na,Sr,Nd,La)$MoO_4$ (labelled × in **Figure 4.2.4.9**) had an EDX spectrum **(Figure 4.2.4.10)** which showed Mo, Sr, Nd and La. **Figures 4.2.4.14** and **4.2.4.15** both had EDX spectra (from × in both images) near identical to **Figure 4.2.4.10**. A dendritic (Na,Sr,Nd,La)$MoO_4$ crystal investigated by TEM (labelled × in **Figure 4.2.4.11**) had a windowless EDX spectrum **(Figure 4.2.4.12)** which showed Mo, Sr, Na, Nd and La, as well as Cu from the support ring. The electron diffraction patterns from the dendritic (Na,Sr,Nd,La)$MoO_4$ crystal **(Figure 4.2.4.13)** reveal it has the powellite crystal structure (tetragonal system, space group $I4_1/a$) and is the likely origin of the peaks incorrectly matched to $NaLa(MoO_4)_2/AgLaMo_2O_8$ in the XRD trace **(Figure 4.2.4.1)**. Using SEM, (Na,Sr,Nd,La)$MoO_4$ has been noted to nucleate and grow on $RuO_2$ crystals **(Figure 4.2.4.9)** and metallic Pd-Te crystals **(Figure 4.2.4.14)**. (Na,Sr,Nd,La)$MoO_4$ is found in both Type A and Type B microstructures.

*$Ce_{1-(x+y)}Zr_xGd_yO_{2-(y/2)}$*

The cubic $CeO_2$ crystal phase identified by XRD **(Figure 4.2.4.1)** has the fluorite structure (space group $Fm\bar{3}m$). A spheroidal $Ce_{1-(x+y)}Zr_xGd_yO_{2-(y/2)}$ crystal investigated by TEM (labelled × in **Figure 4.2.4.16**) had a windowless EDX spectrum **(Figure 4.2.4.17)** which showed Ce, O, Zr and Gd, as well as Si from the surrounding glass and Cu from the support ring. The electron diffraction patterns from the spheroidal $Ce_{1-(x+y)}Zr_xGd_yO_{2-(y/2)}$ crystal **(Figure 4.2.4.18)** reveal it has the fluorite crystal structure (cubic system, space group $Fm\bar{3}m$), matching the XRD data **(Figure 4.2.4.1)**. 'Twinning' of spheroidal $Ce_{1-(x+y)}Zr_xGd_yO_{2-(y/2)}$ crystals can be seen in **Figure 4.2.4.16**. Using SEM, compositional 'zoning' of a spheroidal $Ce_{1-(x+y)}Zr_xGd_yO_{2-(y/2)}$ crystal is noted in **Figures 4.2.4.30** and **4.2.4.31** (at the start of the linescan), with the core of the crystal more enriched in Zr than the exterior of the crystal, and the exterior more

enriched in Ce and Gd than the core. $Ce_{1-(x+y)}Zr_xGd_yO_{2-(y/2)}$ is predominantly found in Type B microstructures.

*Ni-Rich Phase*

A Ni-rich phase investigated by TEM (labelled **(b)** in **Figure 4.2.4.19**) had a windowless EDX spectrum (labelled **(b)** in **Figure 4.2.4.20**) that shows it is composed of Ni and O (with some Cr and Fe), as well as Si from the glass matrix, Ru from the $RuO_2$ core, and Cu from the support ring. The electron diffraction pattern from the Ni-rich phase (**Figure 4.2.4.21**) reveals it is crystalline, although it could not be indexed or identified. Clusters of acicular Ni-rich phases have been noted to nucleate and grow on $RuO_2$ (**Figures 4.2.4.19** and **4.2.4.22**) and metallic Pd-Te (**Figure 4.2.4.23**). Clusters of acicular Ni-rich phases are also observed by SEM (**Figure 4.2.4.30**). This phase is likely associated with the unidentified XRD peaks in **Figure 4.2.4.1**. The Ni-rich phase is predominantly found in Type B microstructures.

*Lanthanide (Nd,Gd,La,Ce) Silicate*

SEM reveals acicular/platey lanthanide (Nd,Gd,La,Ce) silicate (**Figure 4.2.4.24**) in the glass. Acicular/platey lanthanide (Nd,Gd,La,Ce) silicate (labelled **×** in **Figure 4.2.4.24**) has an EDX spectrum (**Figure 4.2.4.25**) which shows Si, Nd, Gd, La and Ce. An acicular/platey lanthanide (Nd,Gd,La,Ce) silicate crystal investigated by TEM (labelled **×** in **Figure 4.2.4.26**) had a windowless EDX spectrum (**Figure 4.2.4.27**) which showed Si, O, Nd, Gd, La and Ce, as well as Cu from the support ring. The electron diffraction pattern from the acicular/platey lanthanide (Nd,Gd,La,Ce) silicate phase (**Figure 4.2.4.28**) reveal it is crystalline, although it could not be indexed or identified. Acicular/platey lanthanide (Nd,Gd,La,Ce) silicate (located at the end of the linescan) has a lower concentration of Si than the residual glass matrix (**Figures 4.2.4.30** and **4.2.4.31**). This phase is likely associated with the unidentified XRD peaks in **Figure 4.2.4.1**. Lanthanide (Nd,Gd,La,Ce) silicate is found exclusively in Type B microstructures.

*$LiNaZrSi_6O_{15}$*

The orthorhombic $LiNaZrSi_6O_{15}$ crystal phase identified by XRD (**Figure 4.2.4.1**) is zektzerite (space group *Cmca*). SEM revealed acicular zektzerite (**Figures 4.2.4.29** and **4.2.4.30**) in the glass. Acicular zektzerite observed in **Figure 4.2.4.30** was confirmed as zektzerite by a linescan (**Figure 4.2.4.31**) which revealed the acicular zektzerite had a higher concentration of Si and Zr than the residual glass (which appeared black compared to the dark grey zektzerite). This crystal phase was not observed in glass samples by TEM. Extensive cracking in and around acicular zektzerite is observed by SEM in **Figure 4.2.4.30**). Acicular zektzerite crystals (labelled ×) penetrating lanthanide (Nd,Gd,La,Ce) silicate crystals can be seen in **Figure 4.2.4.29**. Zektzerite is found exclusively in Type B microstructures.

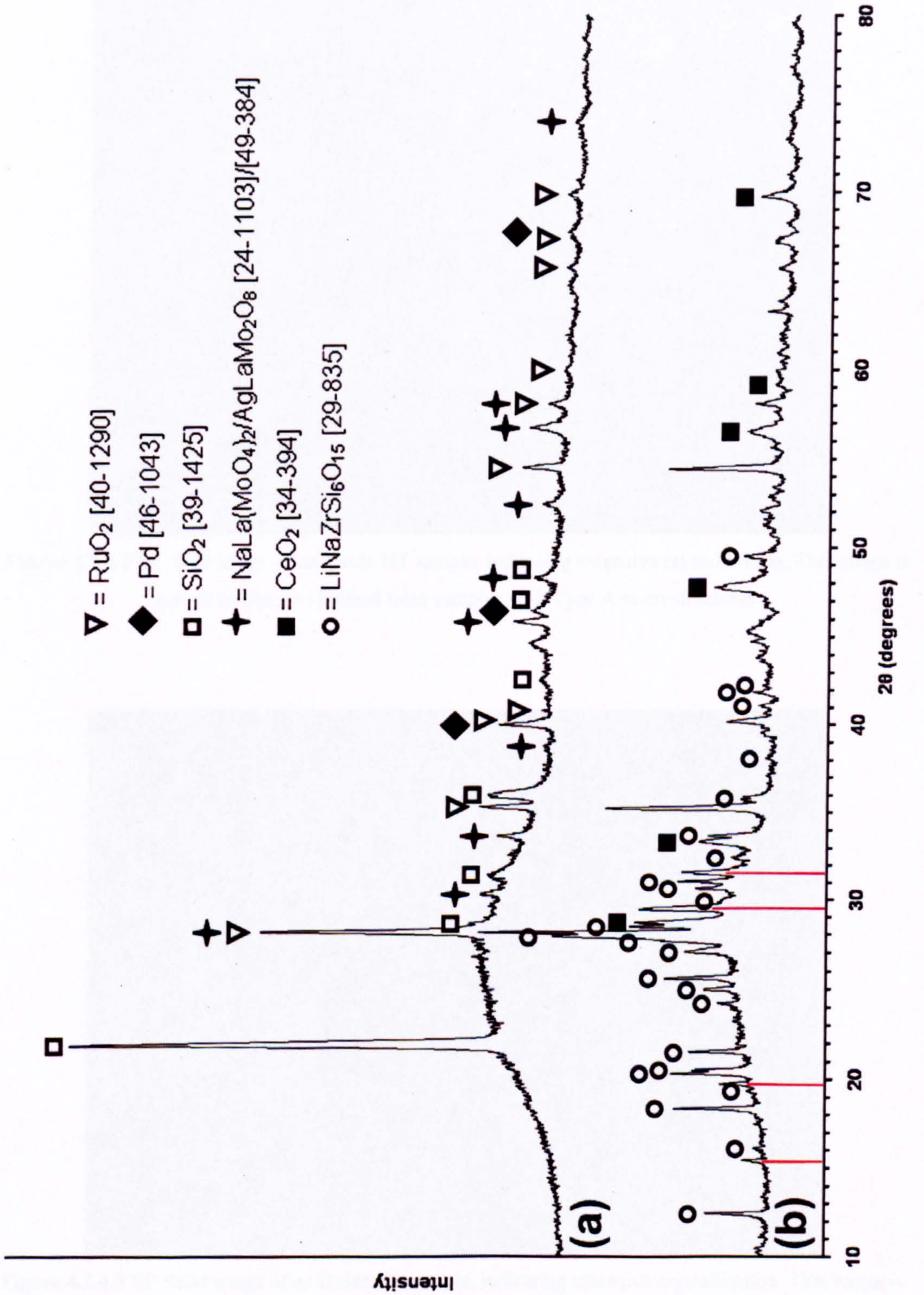


**Figure 4.2.4.1** XRD traces from two Oxide HT samples, illustrating their inconsistency. Peak matches have been labelled, with $RuO_2$ also identified in trace **(b)**. Four unidentified peaks have been labelled in red and have *d*-spacings (Å) of 5.74, 4.50, 3.03 and 2.83. Trace **(a)** is typical of traces obtained from samples with Type A microstructures. Trace **(b)** is typical of traces obtained from samples with Type B microstructures.

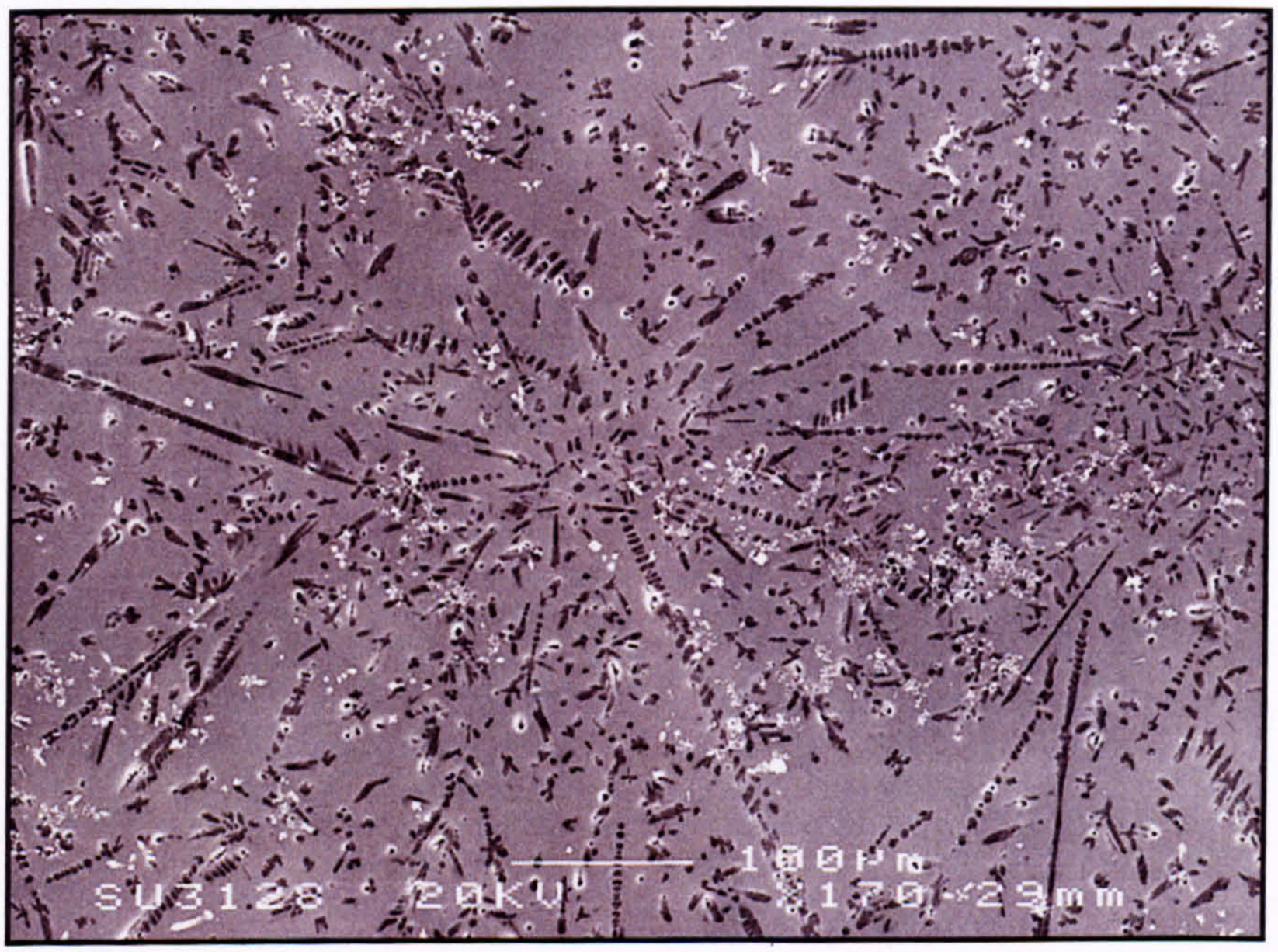


**Figure 4.2.4.2** SE SEM image of an Oxide HT sample, indicating extensive crystallisation. This image is typical of images obtained from samples with Type A microstructures.

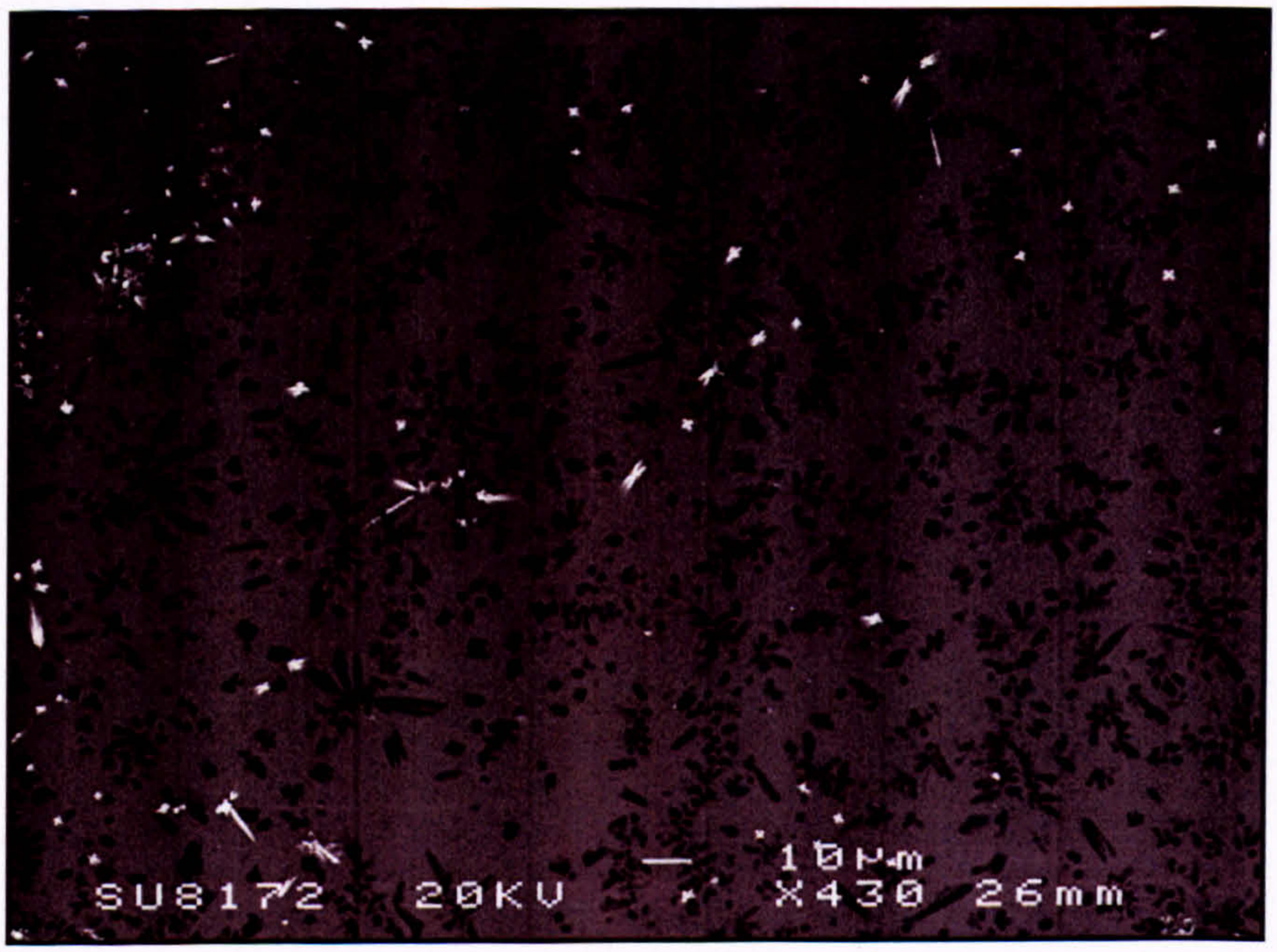


**Figure 4.2.4.3** BE SEM image of an Oxide HT sample, indicating extensive crystallisation. This image is typical of images obtained from samples with Type A microstructures.

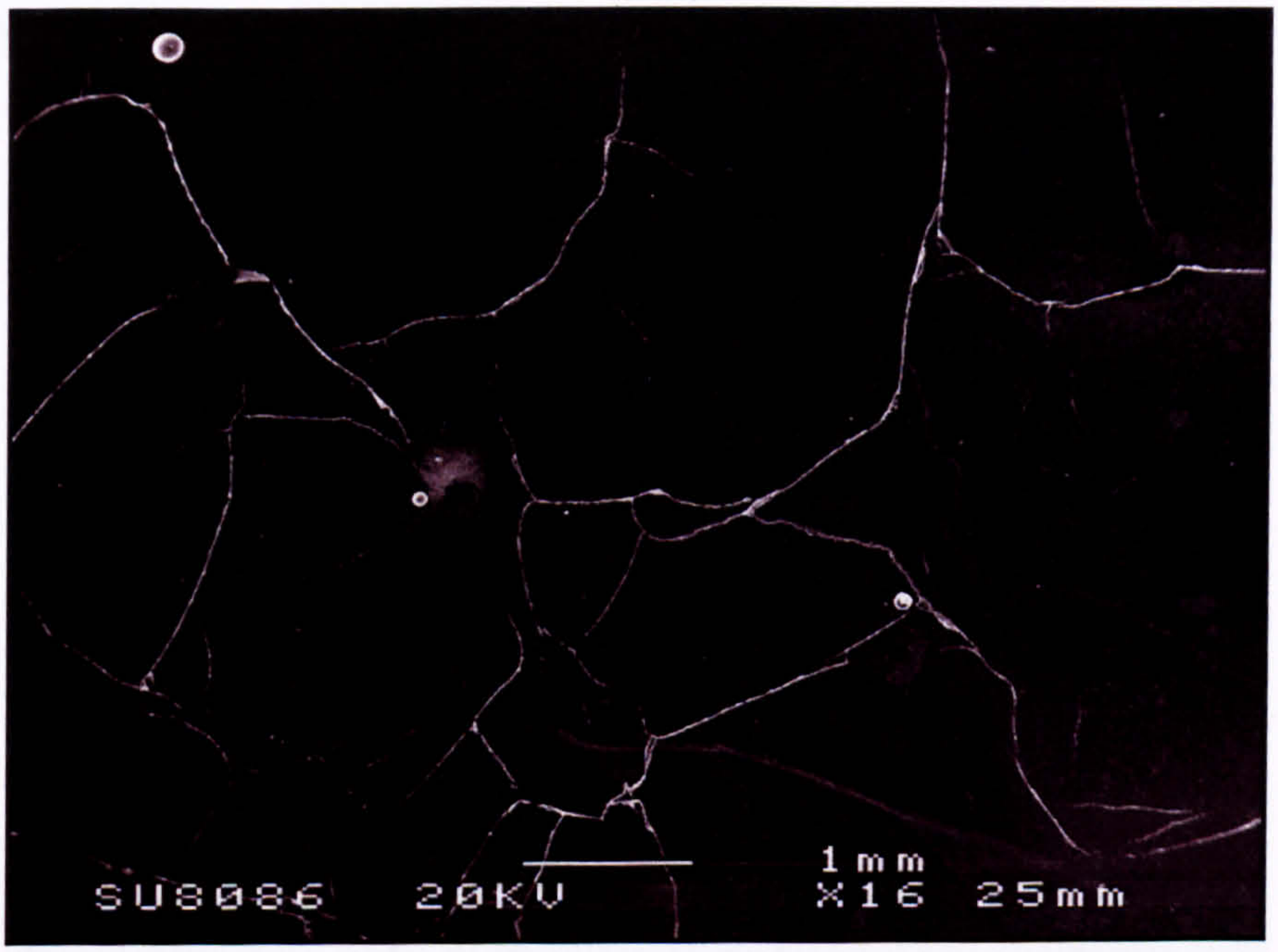


**Figure 4.2.4.4** SE SEM image of an Oxide HT sample, indicating extensive sample cracking. This image is typical of images obtained from samples with Type A microstructures.


**Figure 4.2.4.5** BE SEM image of an Oxide HT sample, indicating 'banded' crystallisation. This image is typical of images obtained from samples with Type B microstructures.

### *4.2.4.1 $SiO_2$*

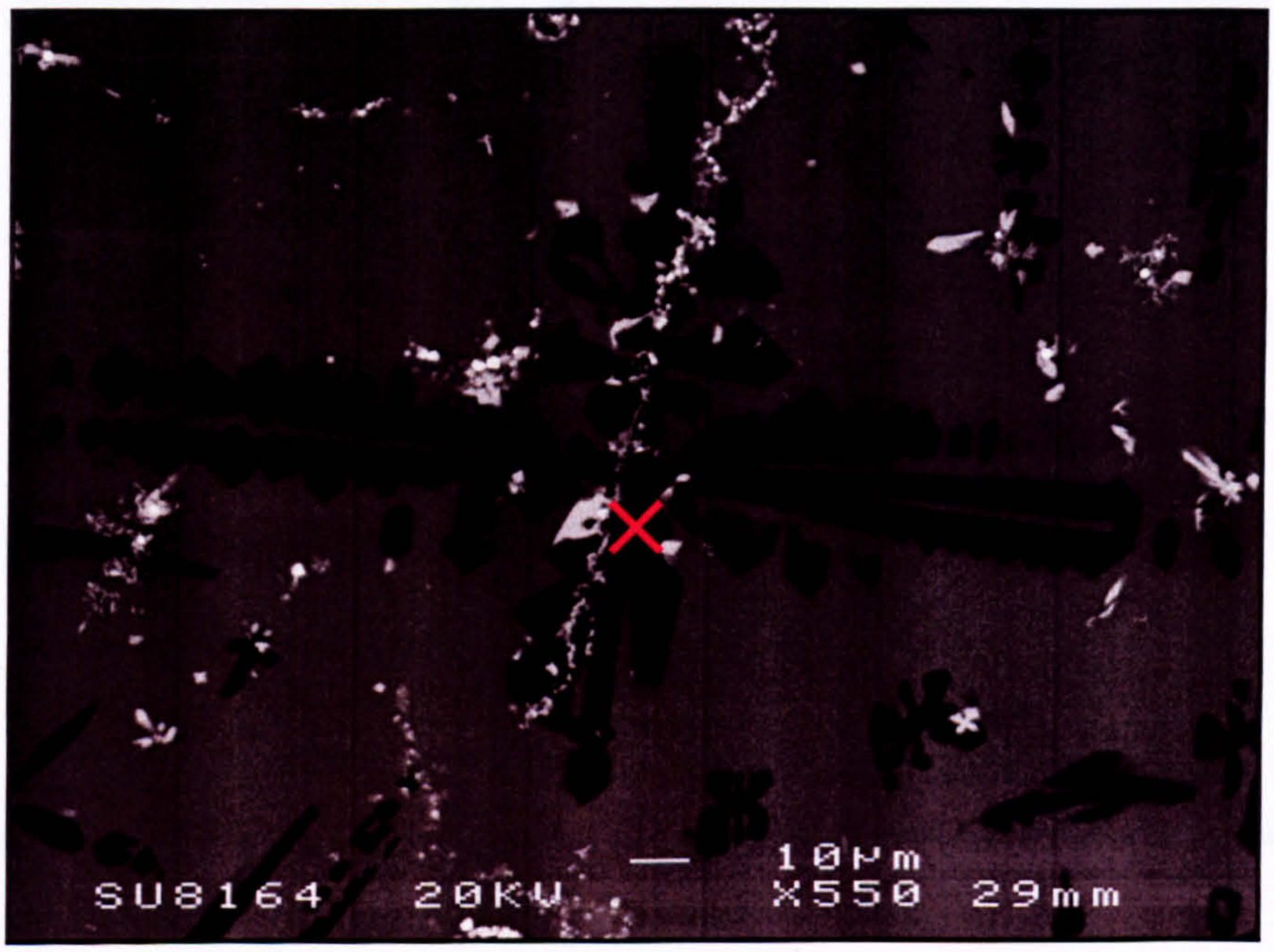


**Figure 4.2.4.6** BE SEM image of an Oxide HT sample, revealing dendritic $\alpha$-cristobalite.

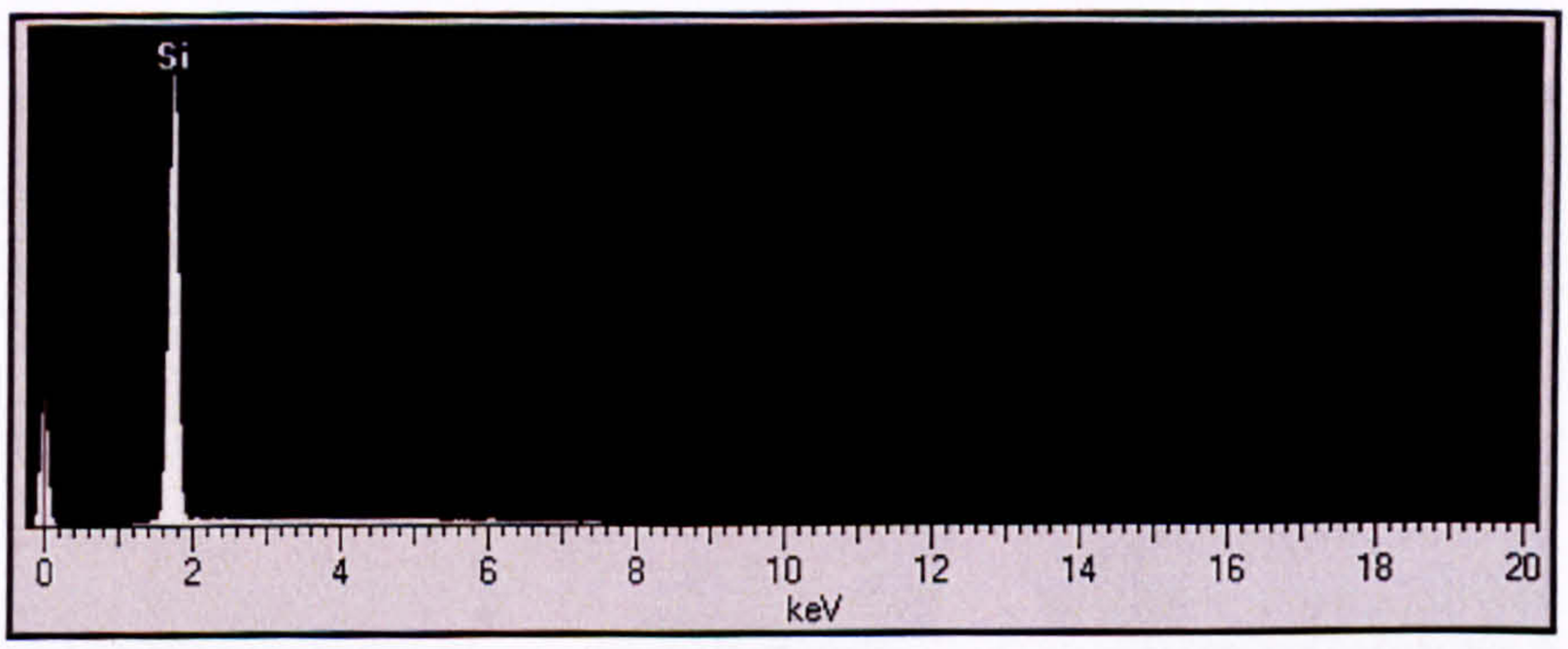


**Figure 4.2.4.7** EDX spectrum from × in **Figure 4.2.4.6** ($y$-axis = Intensity).

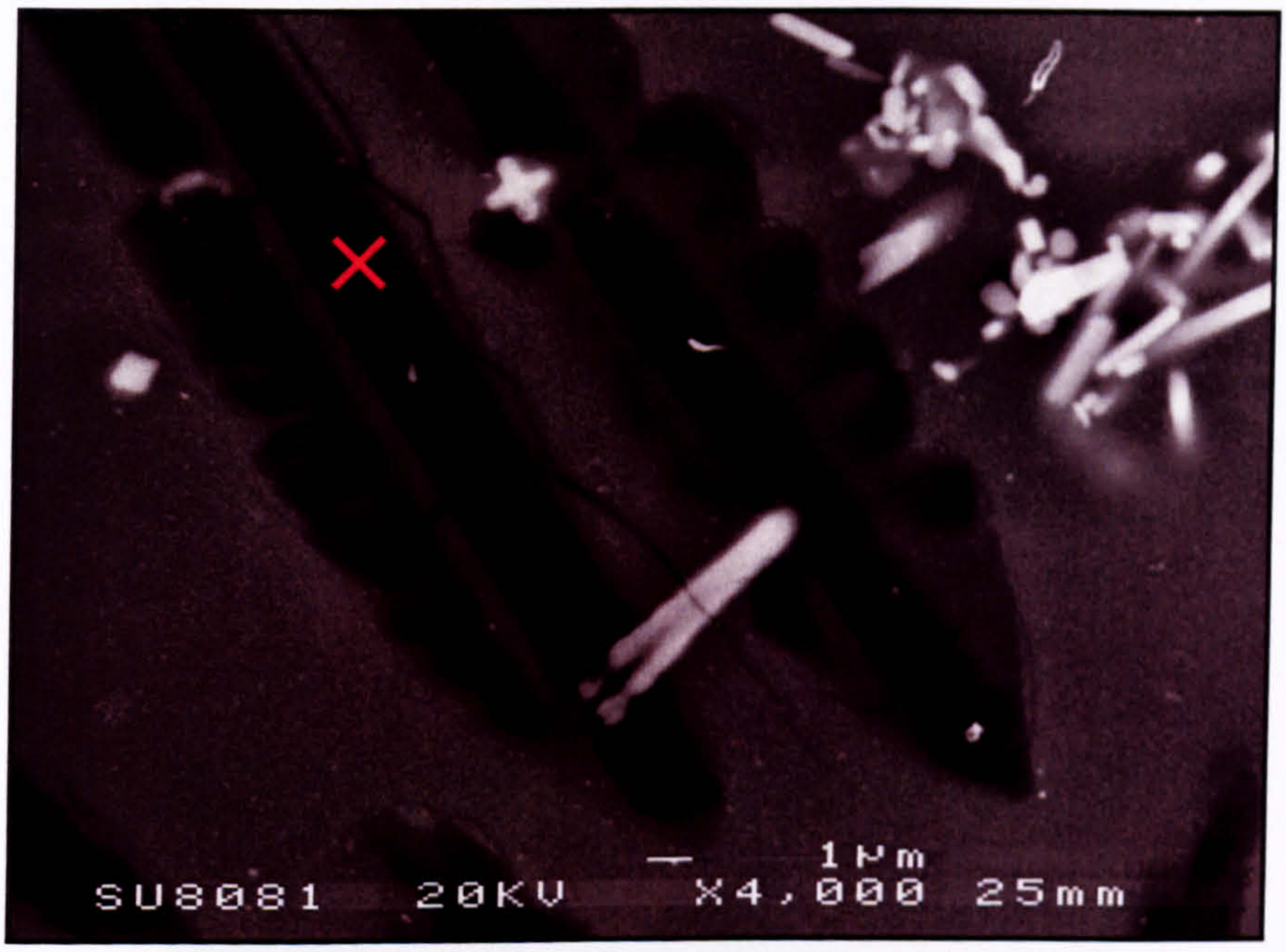


**Figure 4.2.4.8** SE SEM image of an Oxide HT sample, revealing extensive cracking in and around dendritic $\alpha$-cristobalite.

### *4.2.4.2 (Na,Sr,Nd,La)$MoO_4$*

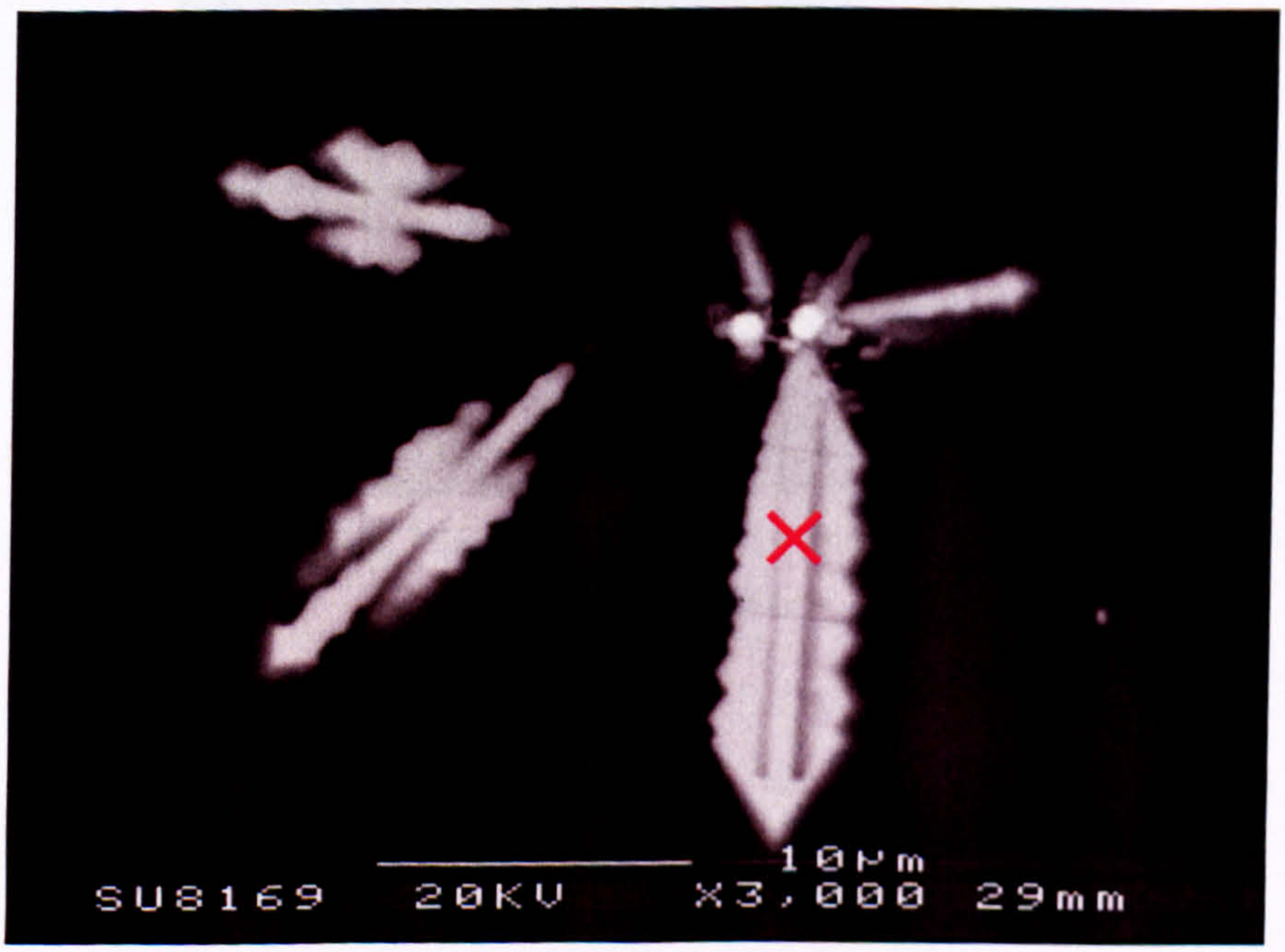


**Figure 4.2.4.9** BE SEM image of an Oxide HT sample, revealing dendritic (Na,Sr,Nd,La)$MoO_4$, a crystal of which has nucleated and grown on $RuO_2$.

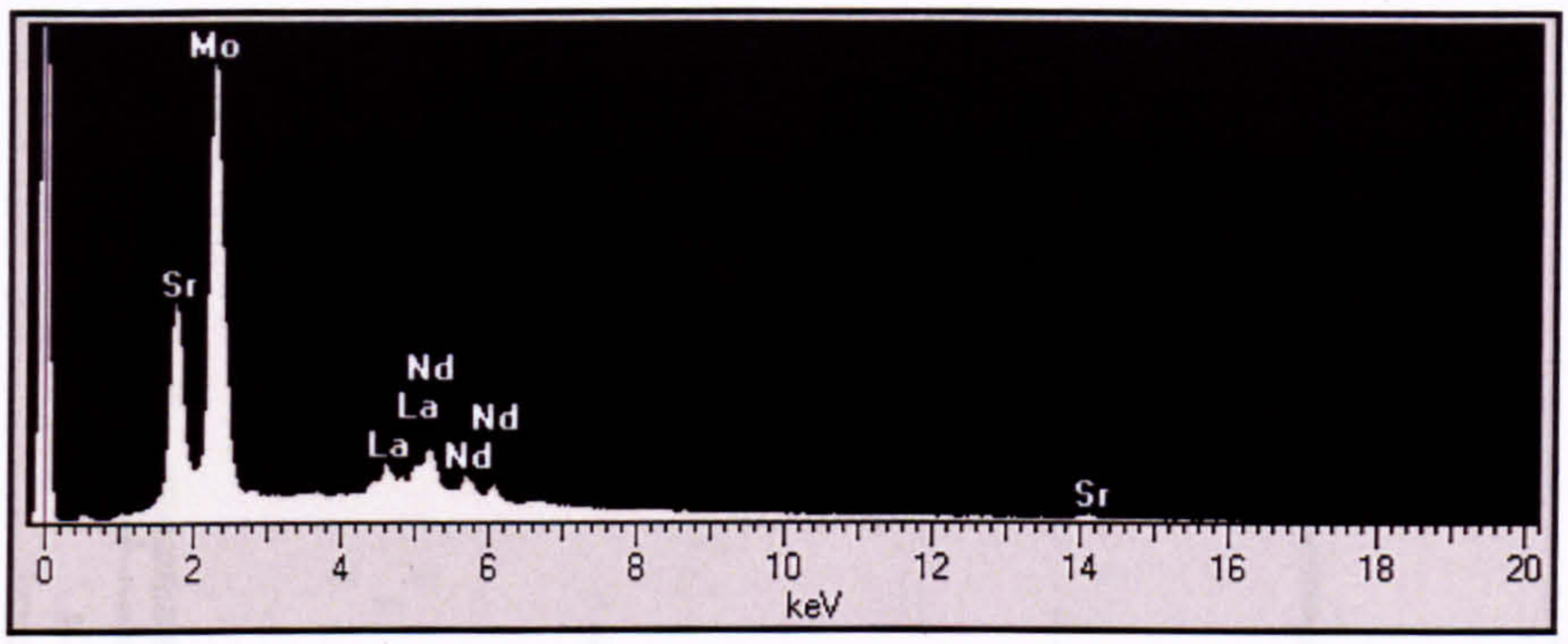


**Figure 4.2.4.10** EDX spectrum from × in **Figure 4.2.4.9** ($y$-axis = Intensity).

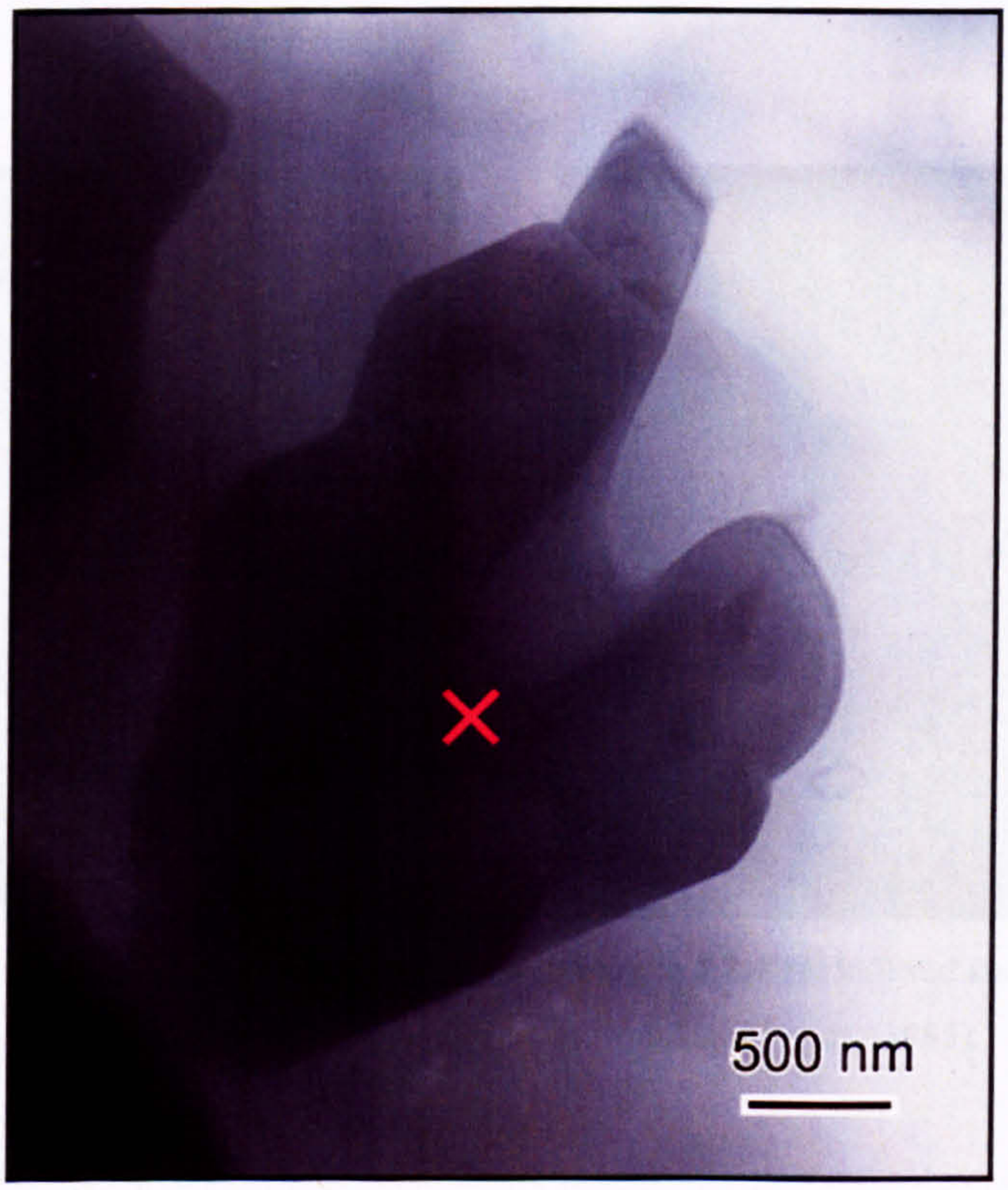


**Figure 4.2.4.11** Bright-field TEM micrograph of an Oxide HT sample, revealing dendritic $(Na,Sr,Nd,La)MoO_4$.

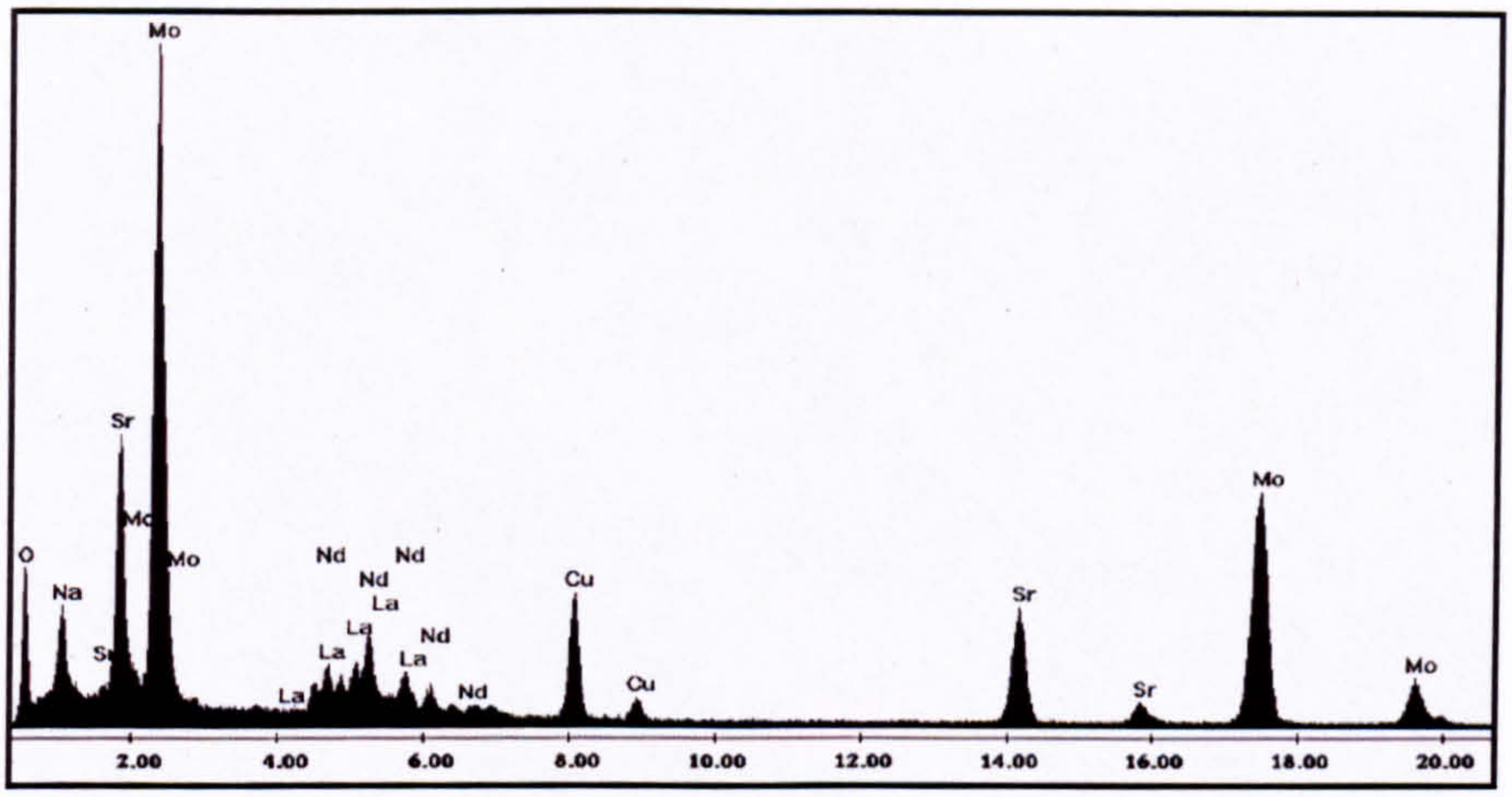


**Figure 4.2.4.12** Windowless EDX spectrum from × in **Figure 4.2.4.11** (*x*-axis = keV; *y*-axis = Intensity).

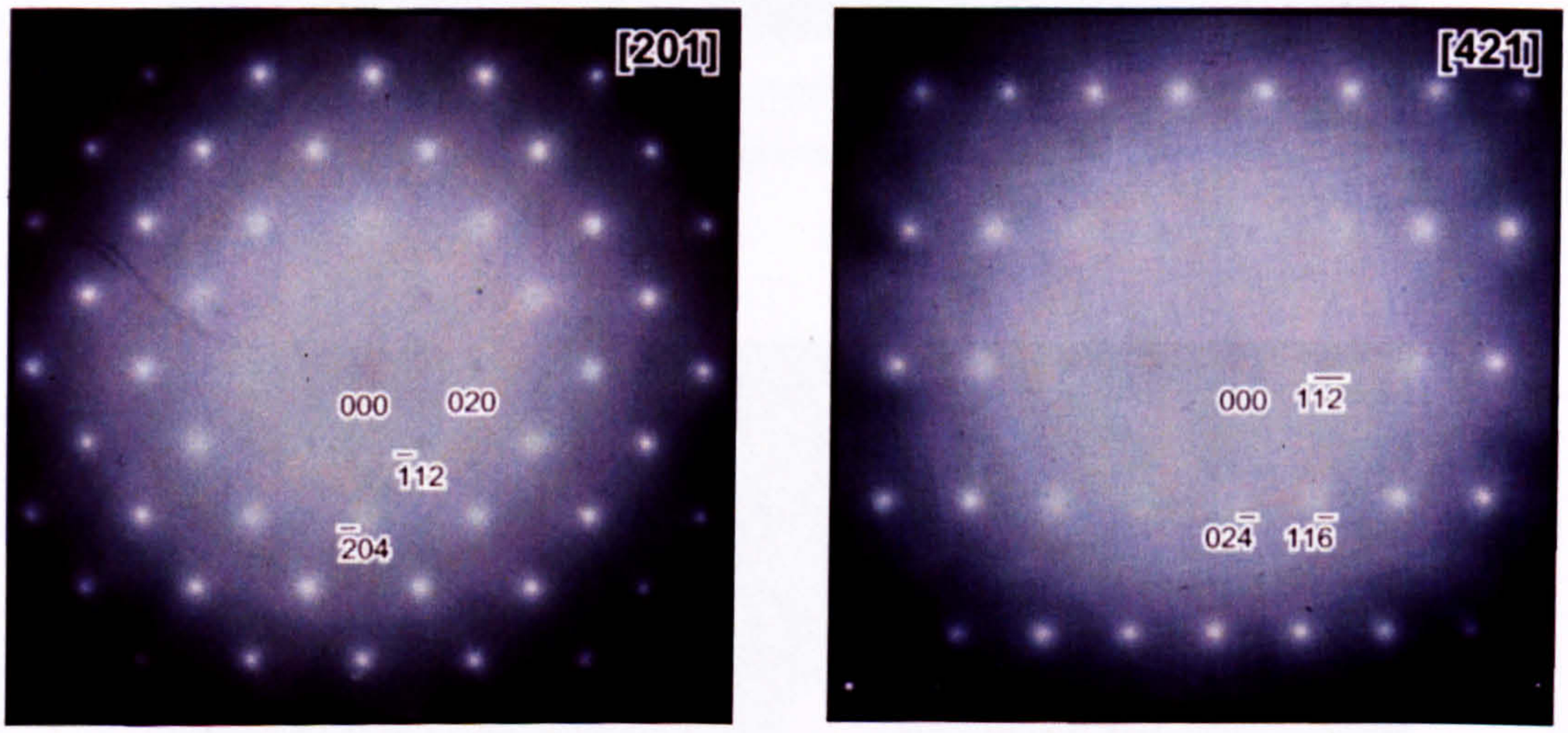


**Figure 4.2.4.13** Electron diffraction patterns from × in **Figure 4.2.4.11**, indexed and identified as the powellite crystal structure using data from Hazen *et al.* (1985).

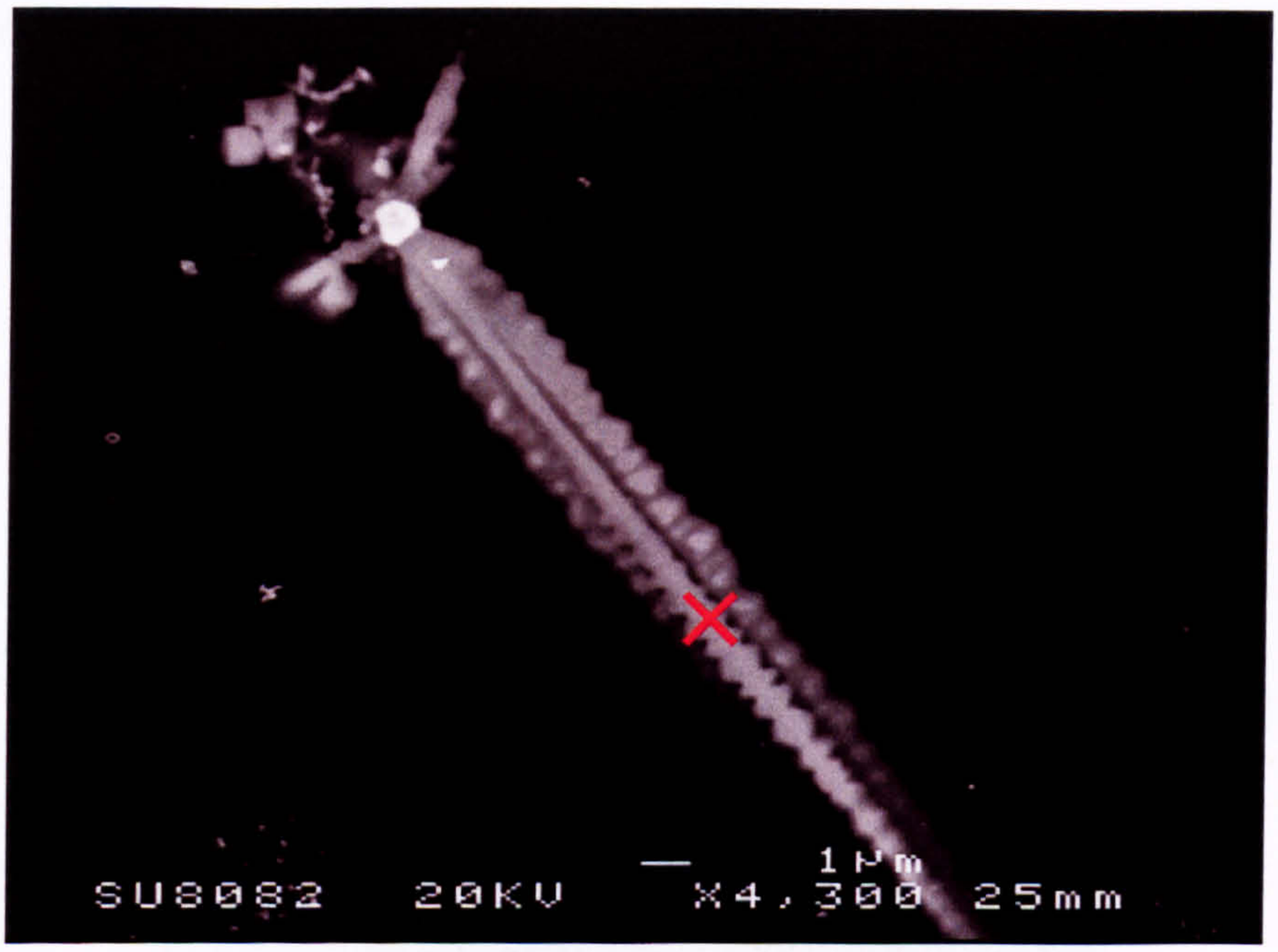


**Figure 4.2.4.14** BE SEM image of an Oxide HT sample, revealing dendritic (Na,Sr,Nd,La)$MoO_4$ which has nucleated and grown on metallic Pd-Te.

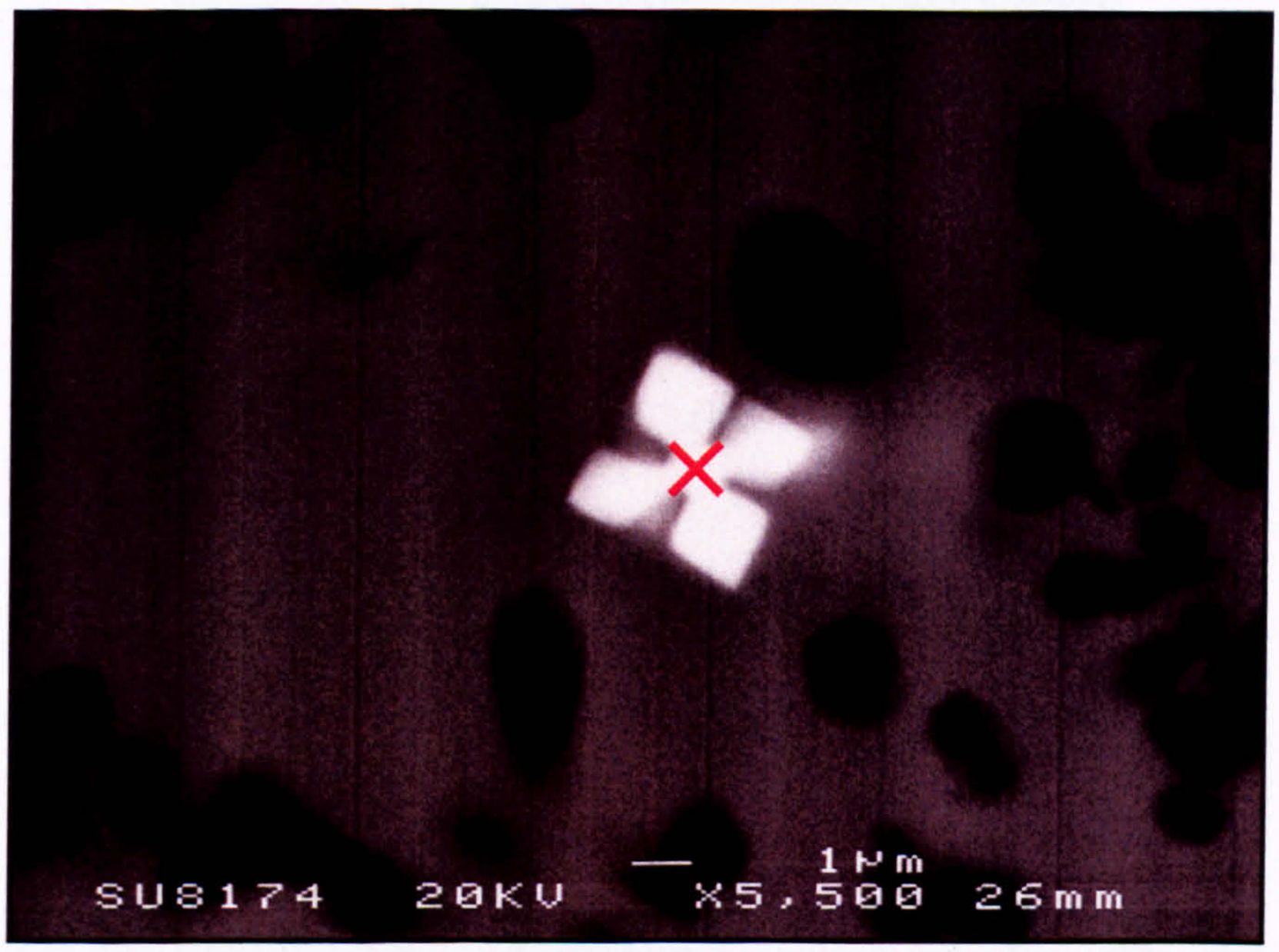


**Figure 4.2.4.15** BE SEM image of an Oxide HT sample, revealing dendritic (Na,Sr,Nd,La)$MoO_4$ (white) in an $\alpha$-cristobalite-rich region (black).

### 4.2.4.3 $Ce_{1-(x+y)}Zr_xGd_yO_{2-(y/2)}$

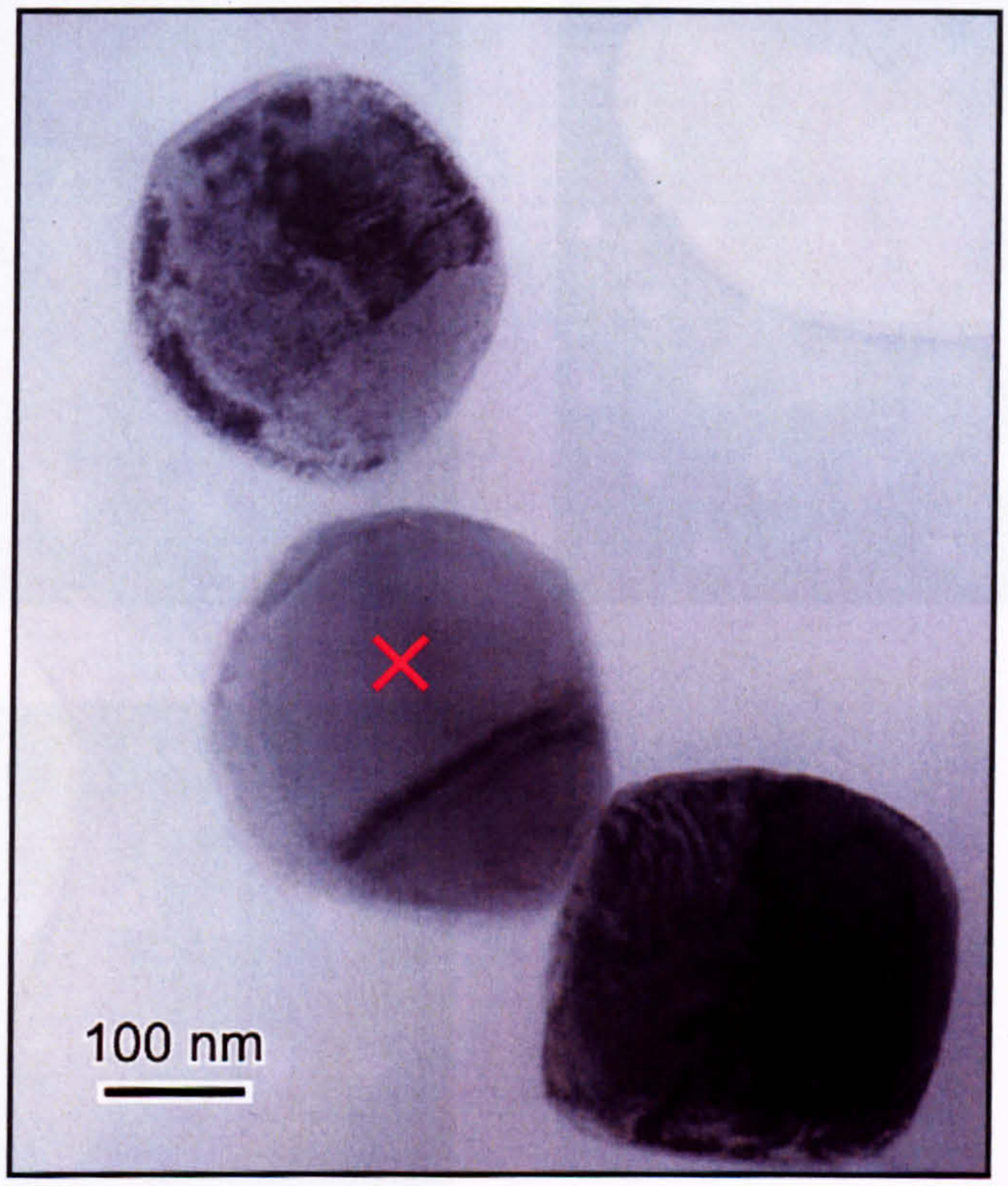


**Figure 4.2.4.16** Bright-field TEM micrograph of an Oxide HT sample, revealing spheroidal $Ce_{1-(x+y)}Zr_xGd_yO_{2-(y/2)}$. Crystal 'twinning' is observed.

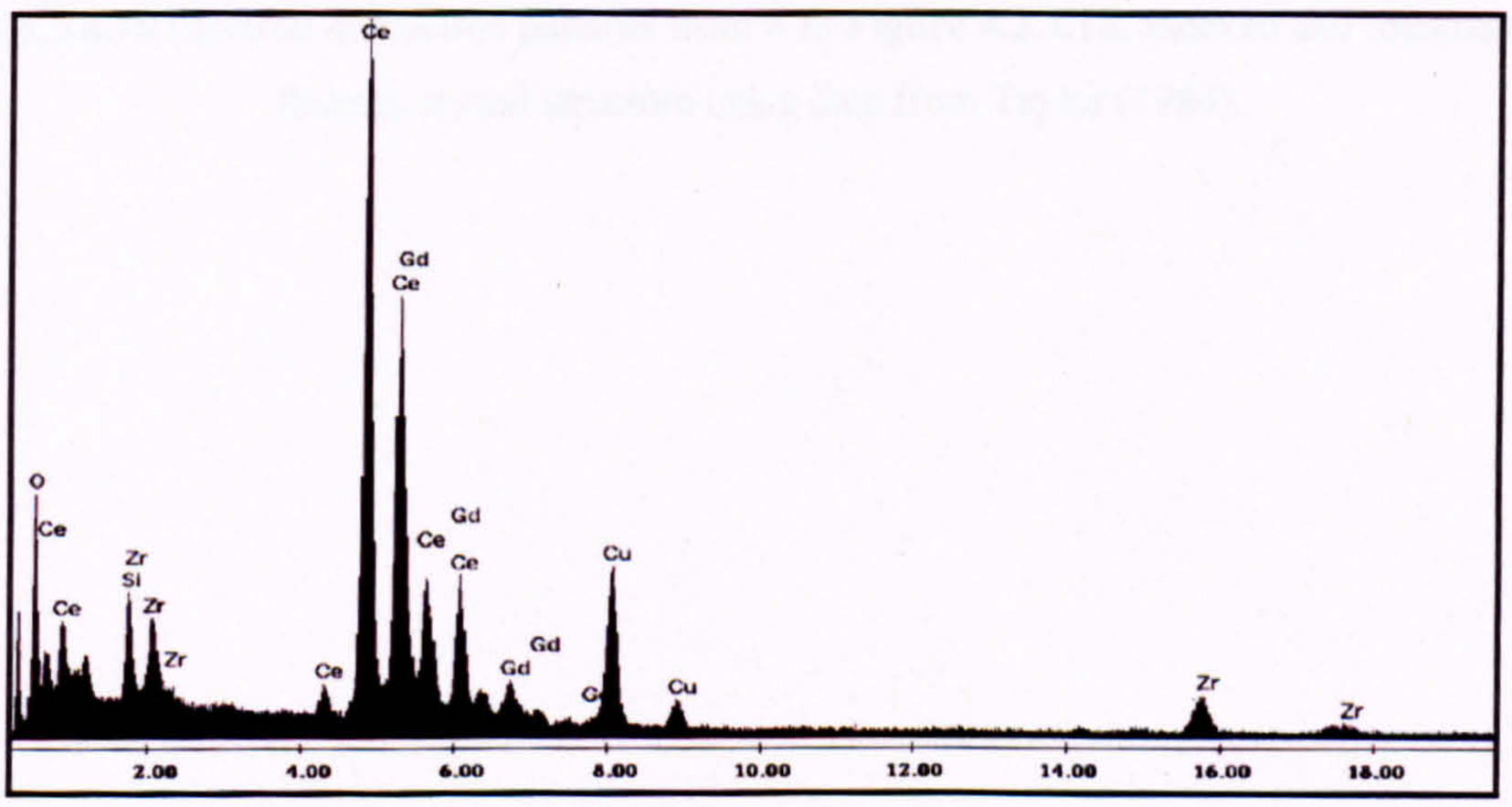


**Figure 4.2.4.17** Windowless EDX spectrum from × in **Figure 4.2.4.16** (*x*-axis = keV; *y*-axis = Intensity).

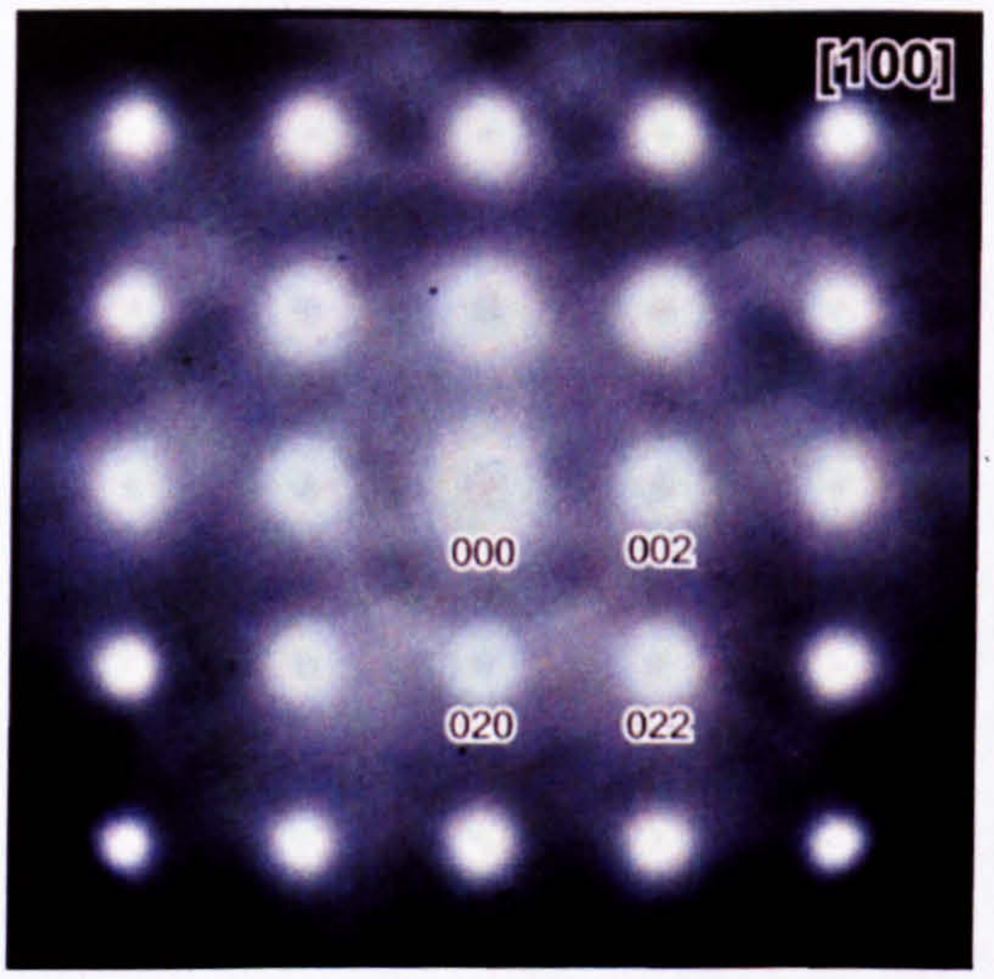


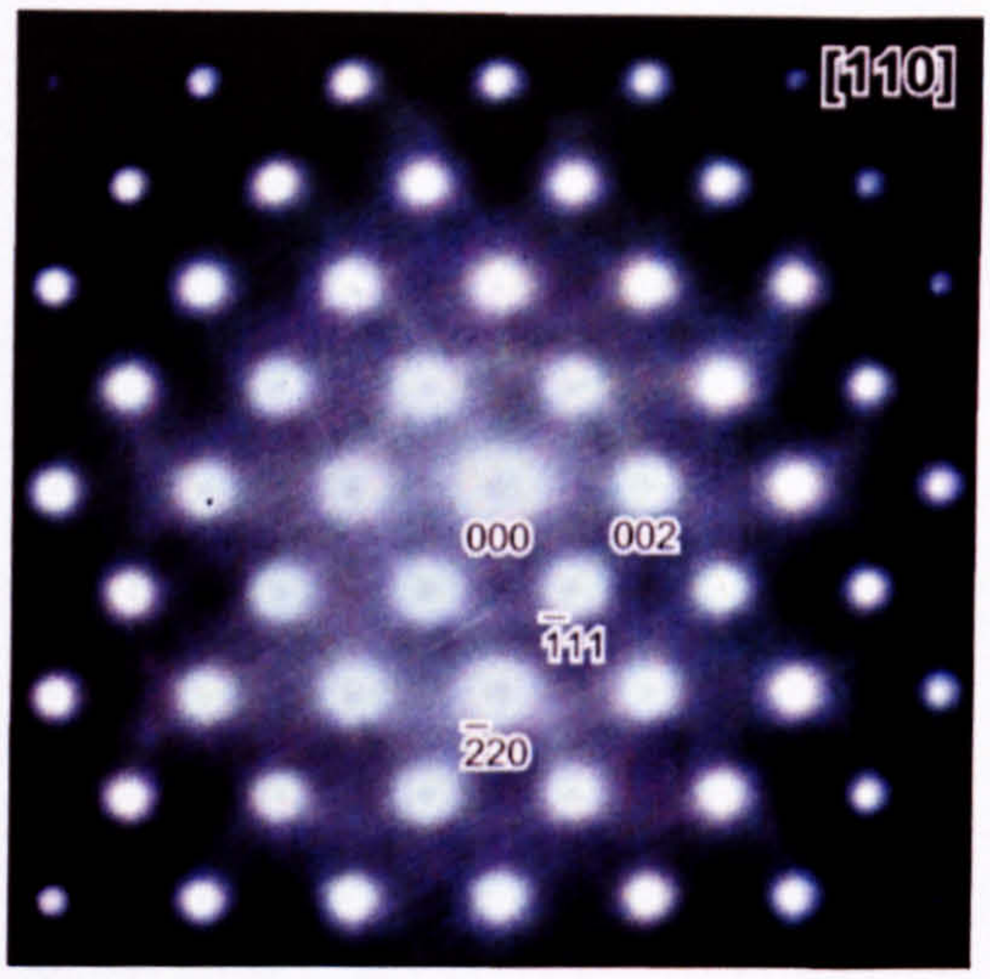


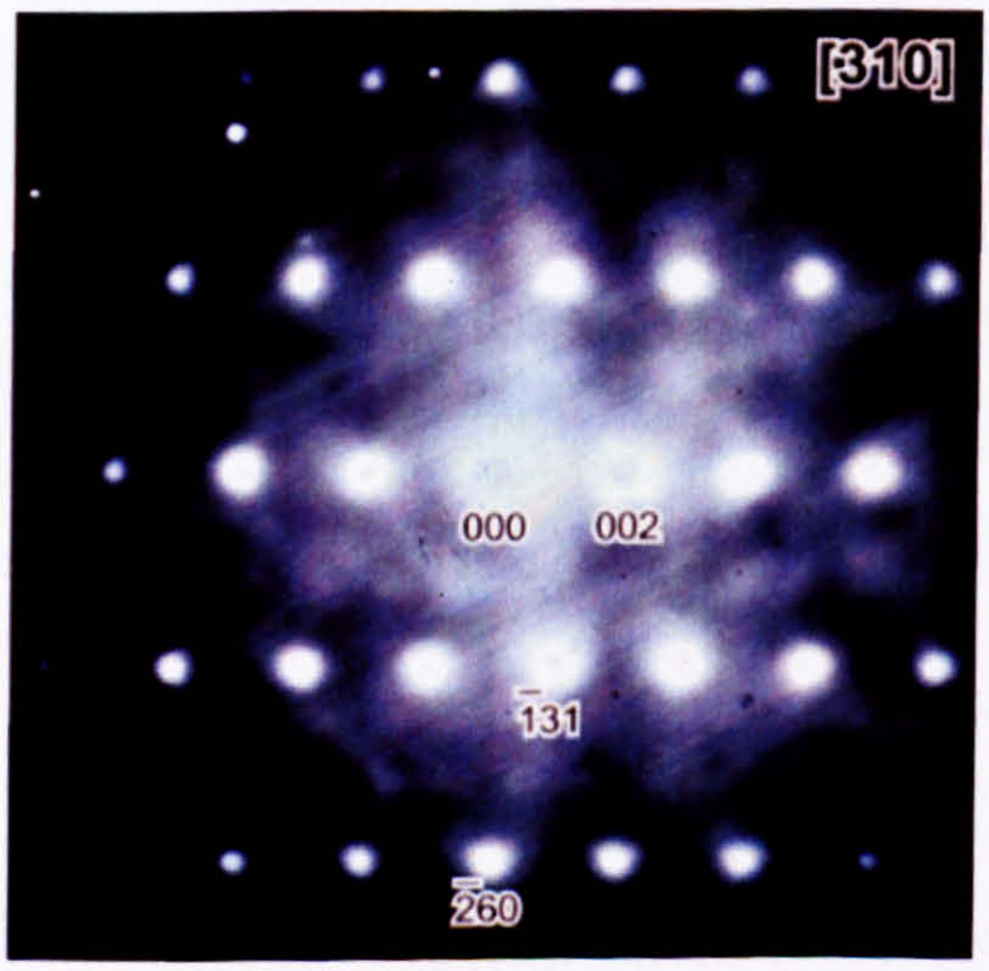


**Figure 4.2.4.18** Electron diffraction patterns from × in **Figure 4.2.4.16**, indexed and identified as the fluorite crystal structure using data from Taylor (1984).

*4.2.4.4 Ni-Rich Phase*

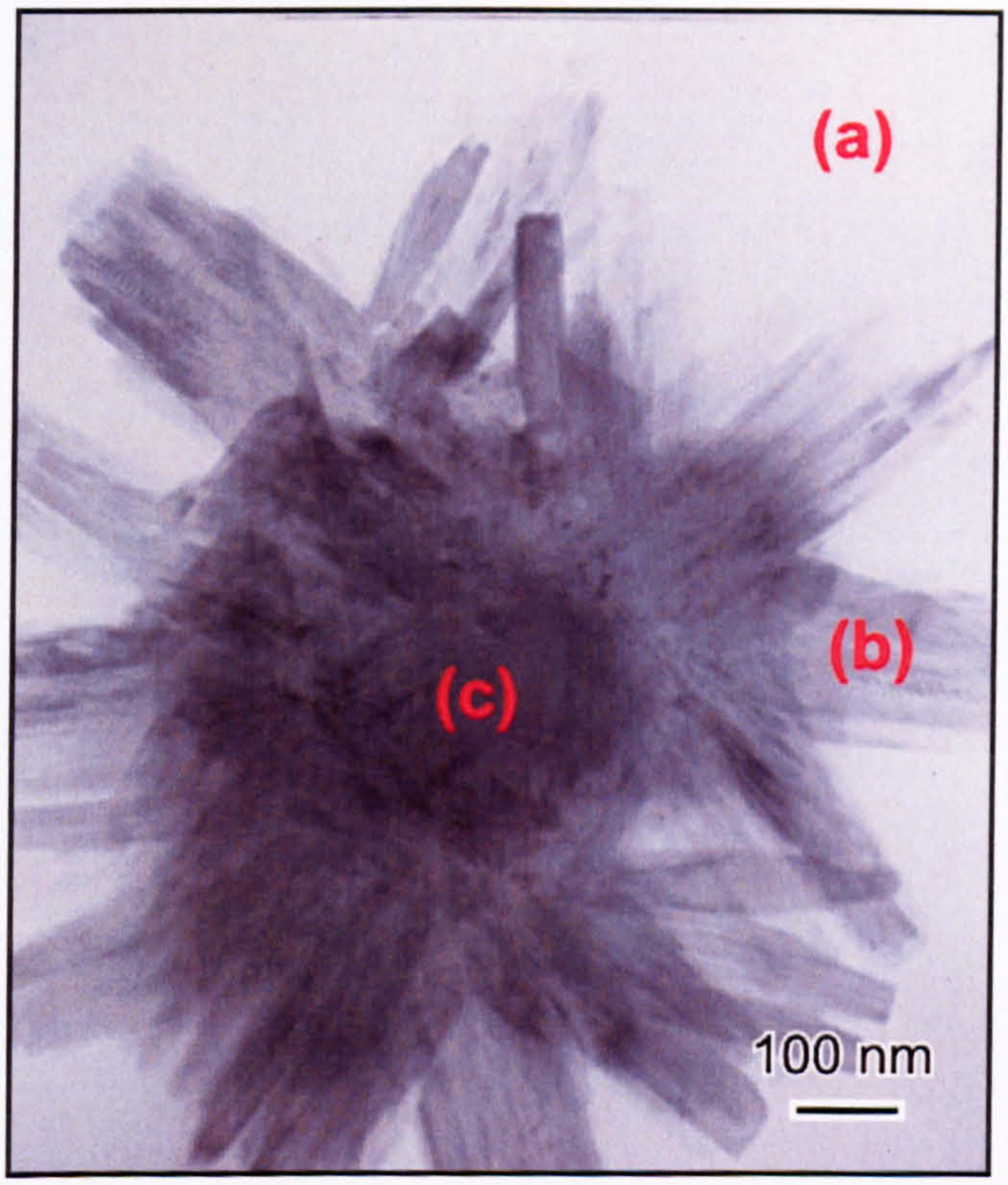


**Figure 4.2.4.19** Bright-field TEM micrograph of an Oxide HT sample, revealing a cluster of Ni-rich acicular crystals nucleated and grown on a $RuO_2$ core.

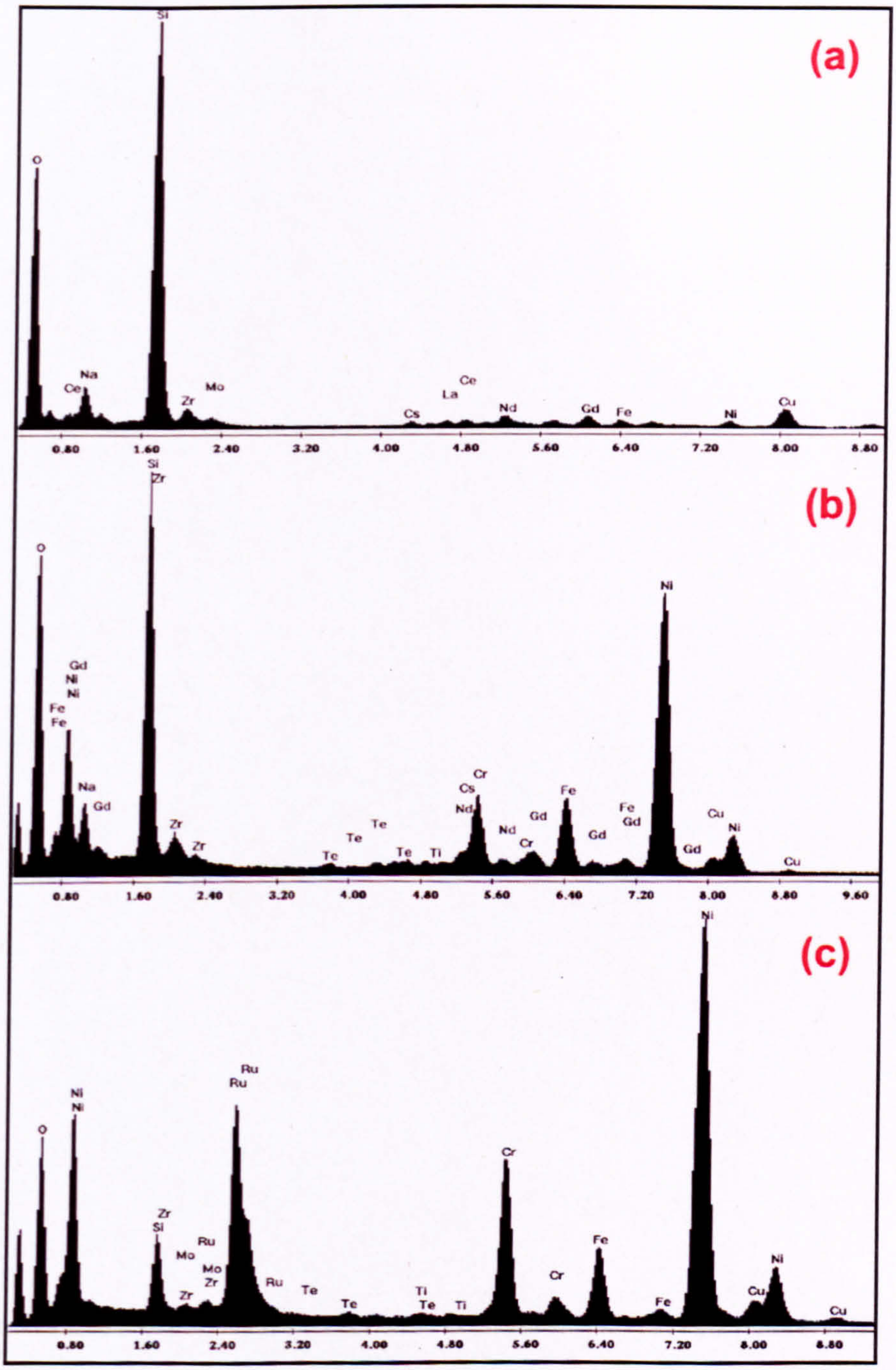


**Figure 4.2.4.20** Windowless EDX spectra from **(a)**, **(b)** and **(c)** in **Figure 4.2.4.19** (*x*-axis = keV; *y*-axis = Intensity).

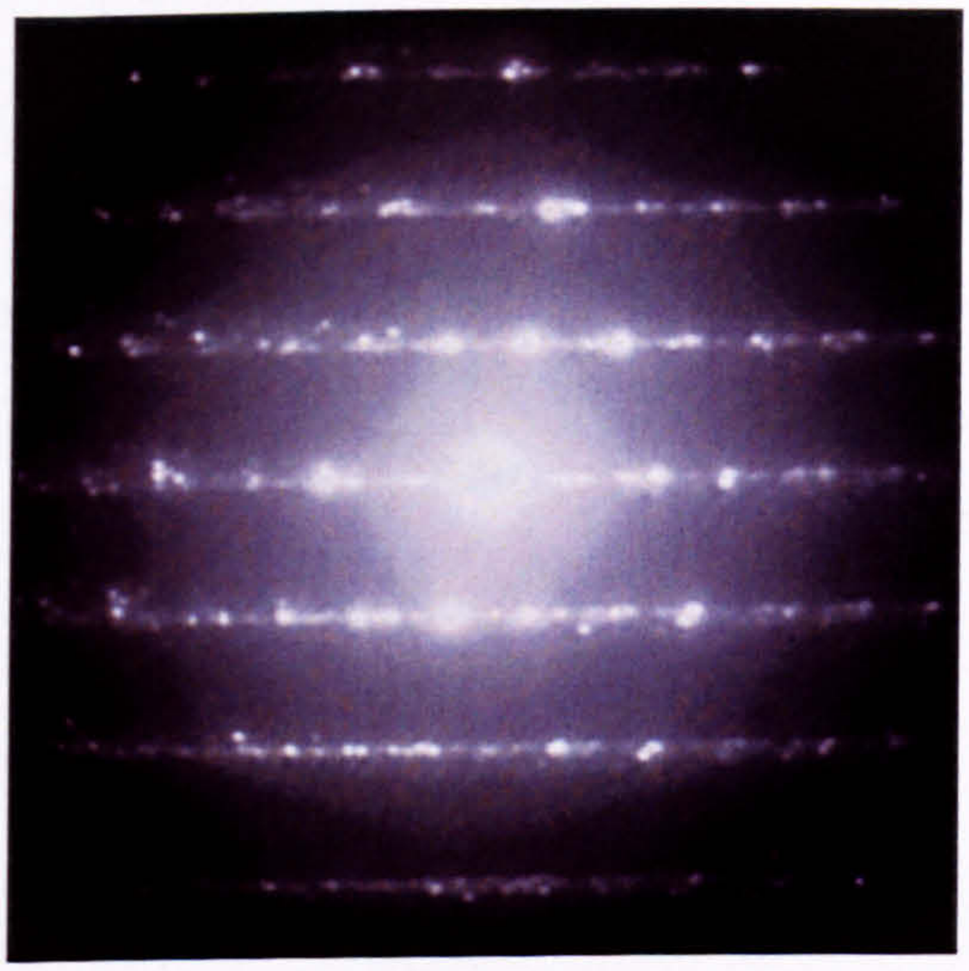

**Figure 4.2.4.21** Electron diffraction pattern from **(b)** in **Figure 4.2.4.19**.

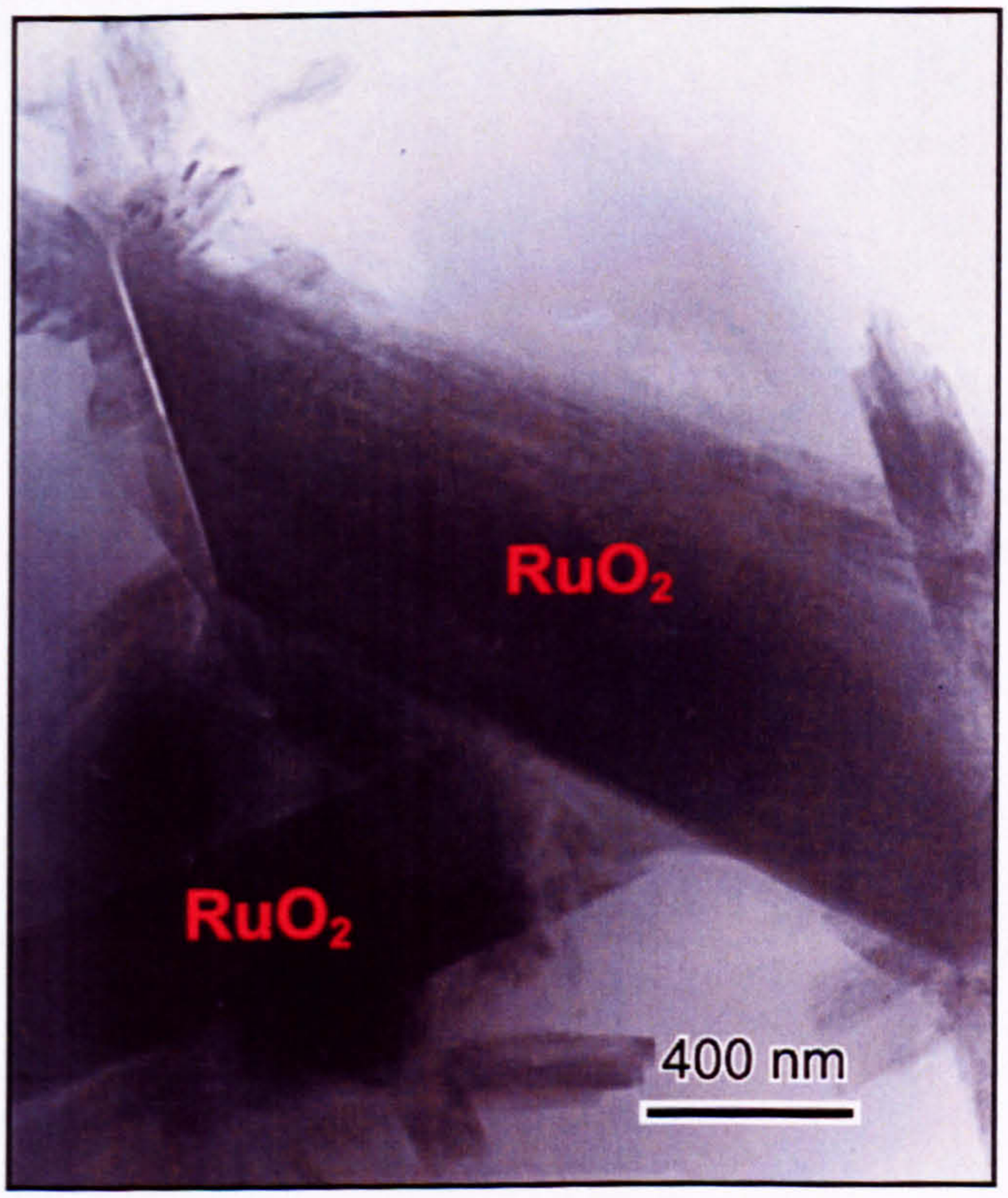


**Figure 4.2.4.22** Bright-field TEM micrograph of an Oxide HT sample, revealing Ni-rich acicular crystals nucleated and grown on $RuO_2$.

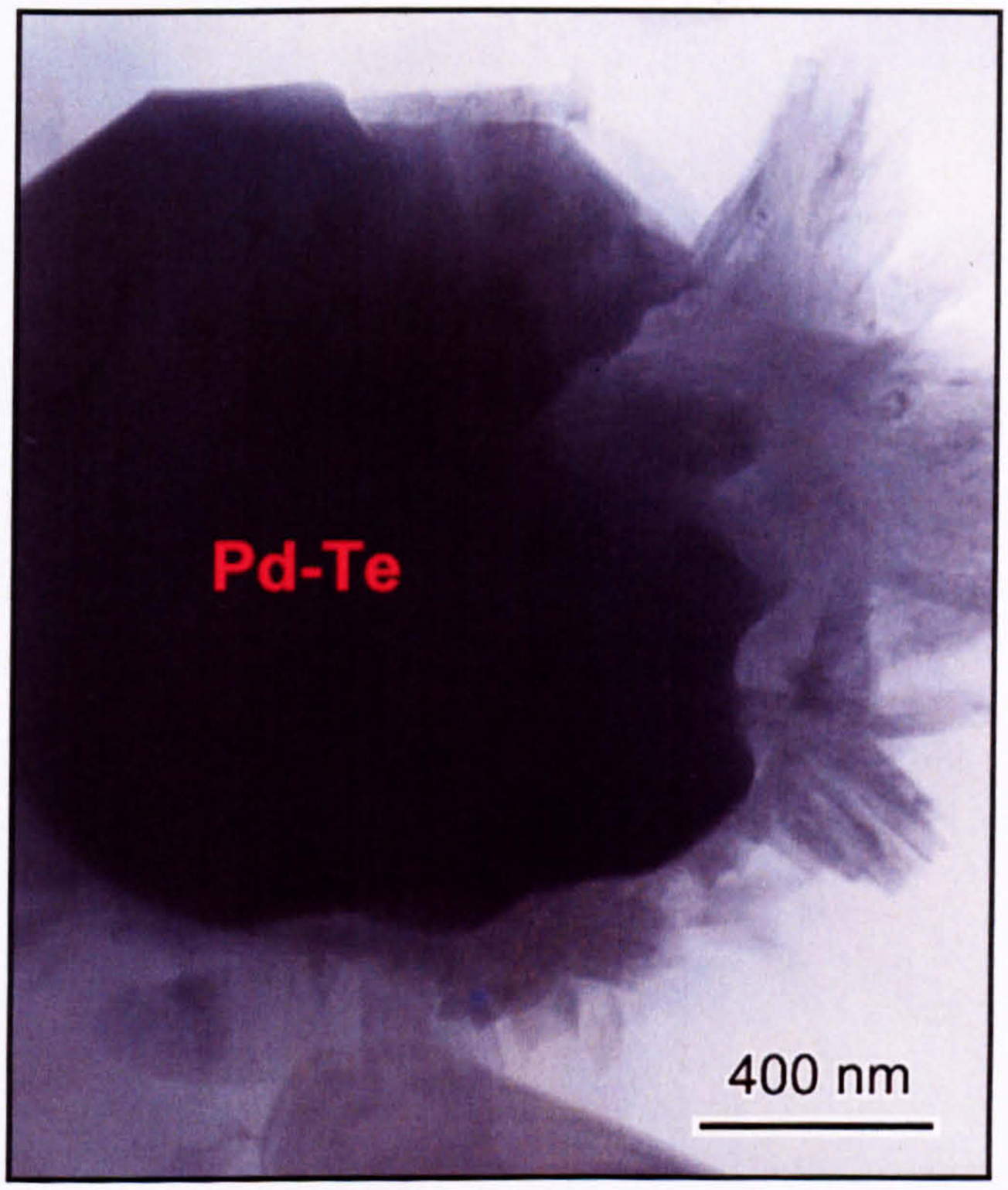


**Figure 4.2.4.23** Bright-field TEM micrograph of an Oxide HT sample, revealing Ni-rich acicular crystals nucleated and grown on metallic Pd-Te.

### *4.2.4.5 Lanthanide (Nd,Gd,La,Ce) Silicate*

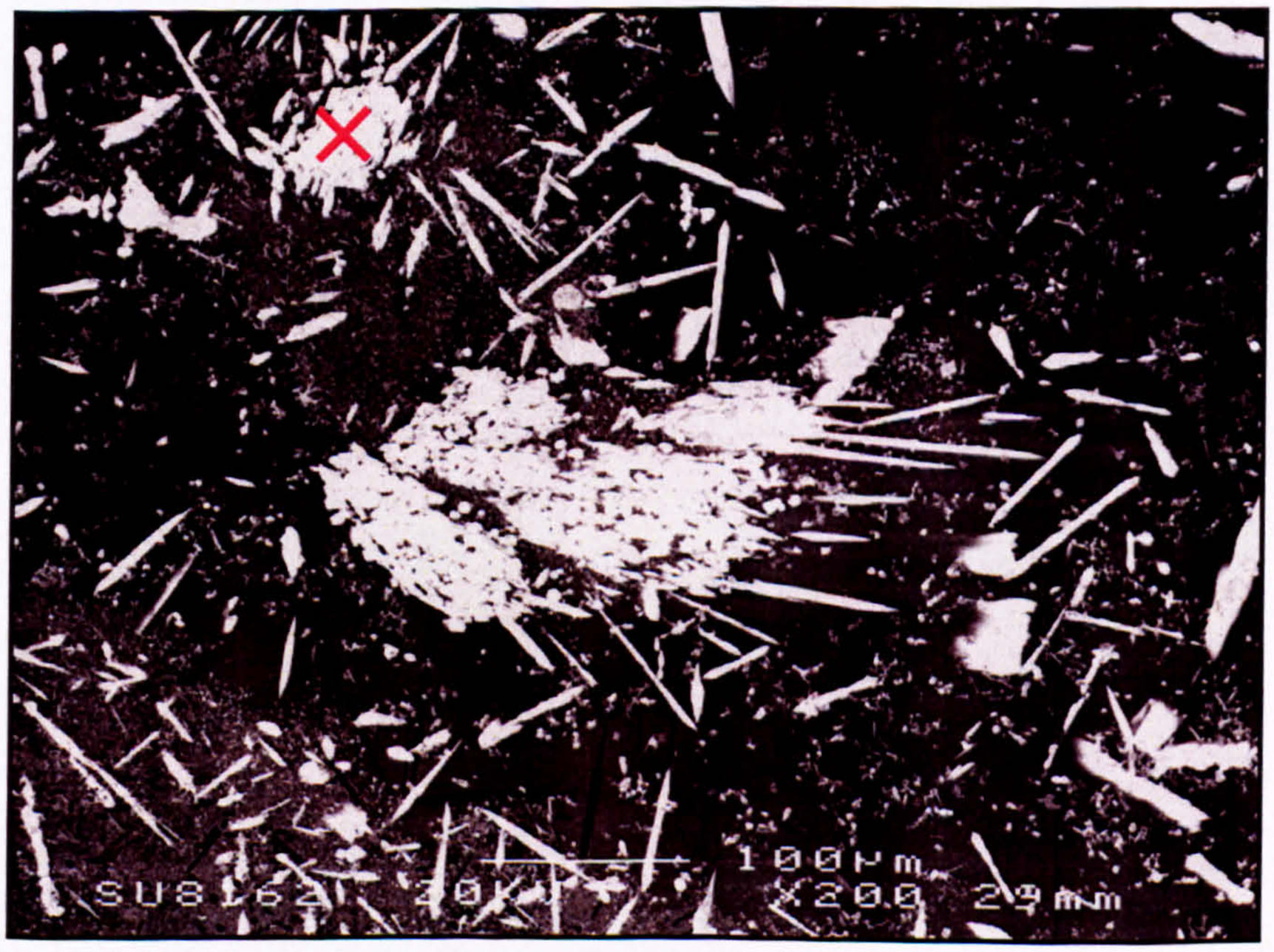


**Figure 4.2.4.24** BE SEM image of an Oxide HT sample, revealing acicular/platey lanthanide (Nd,Gd,La,Ce) silicate (white).

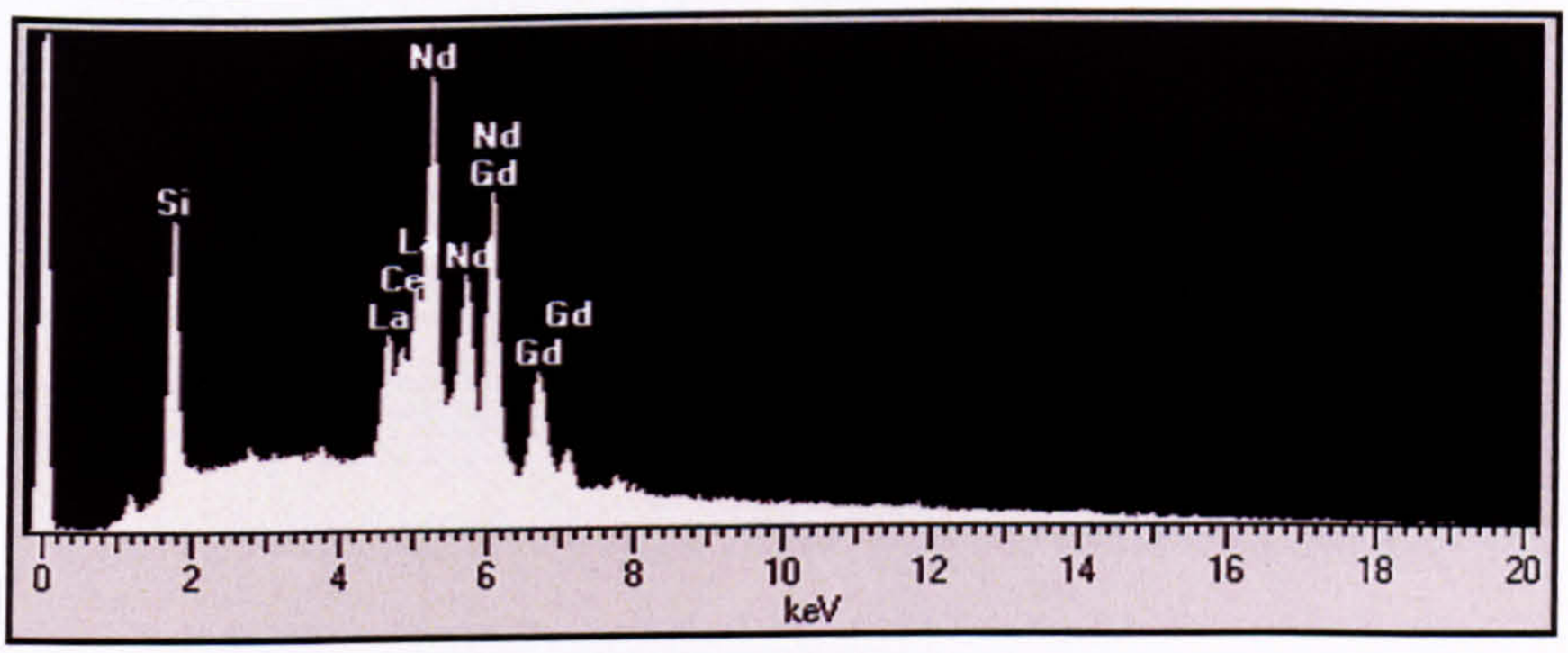


**Figure 4.2.4.25** EDX spectrum from × in **Figure 4.2.4.24** (*y*-axis = Intensity).

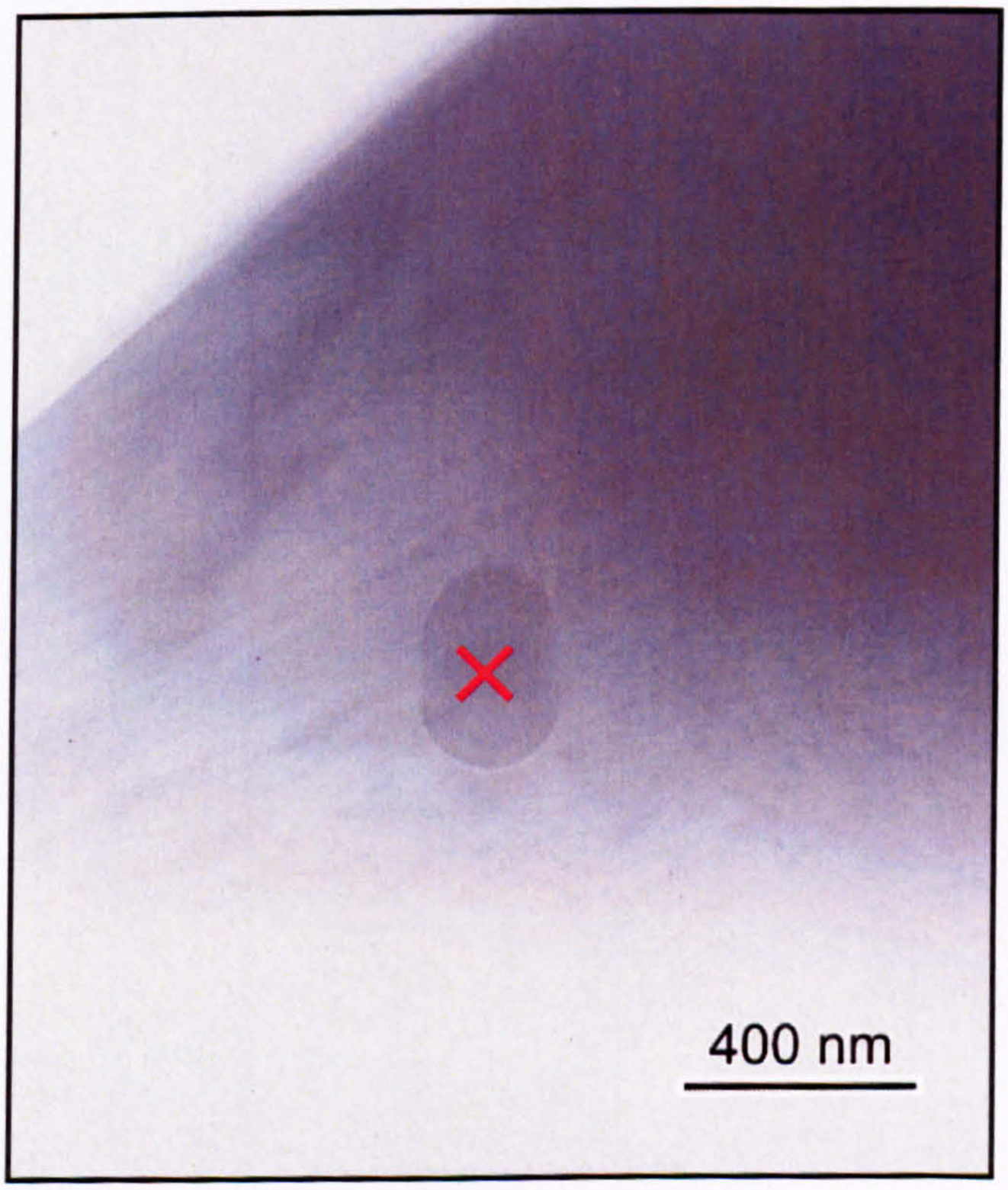


**Figure 4.2.4.26** Bright-field TEM micrograph of an Oxide HT sample, revealing an acicular/platey lanthanide (Nd,Gd,La,Ce) silicate crystal.

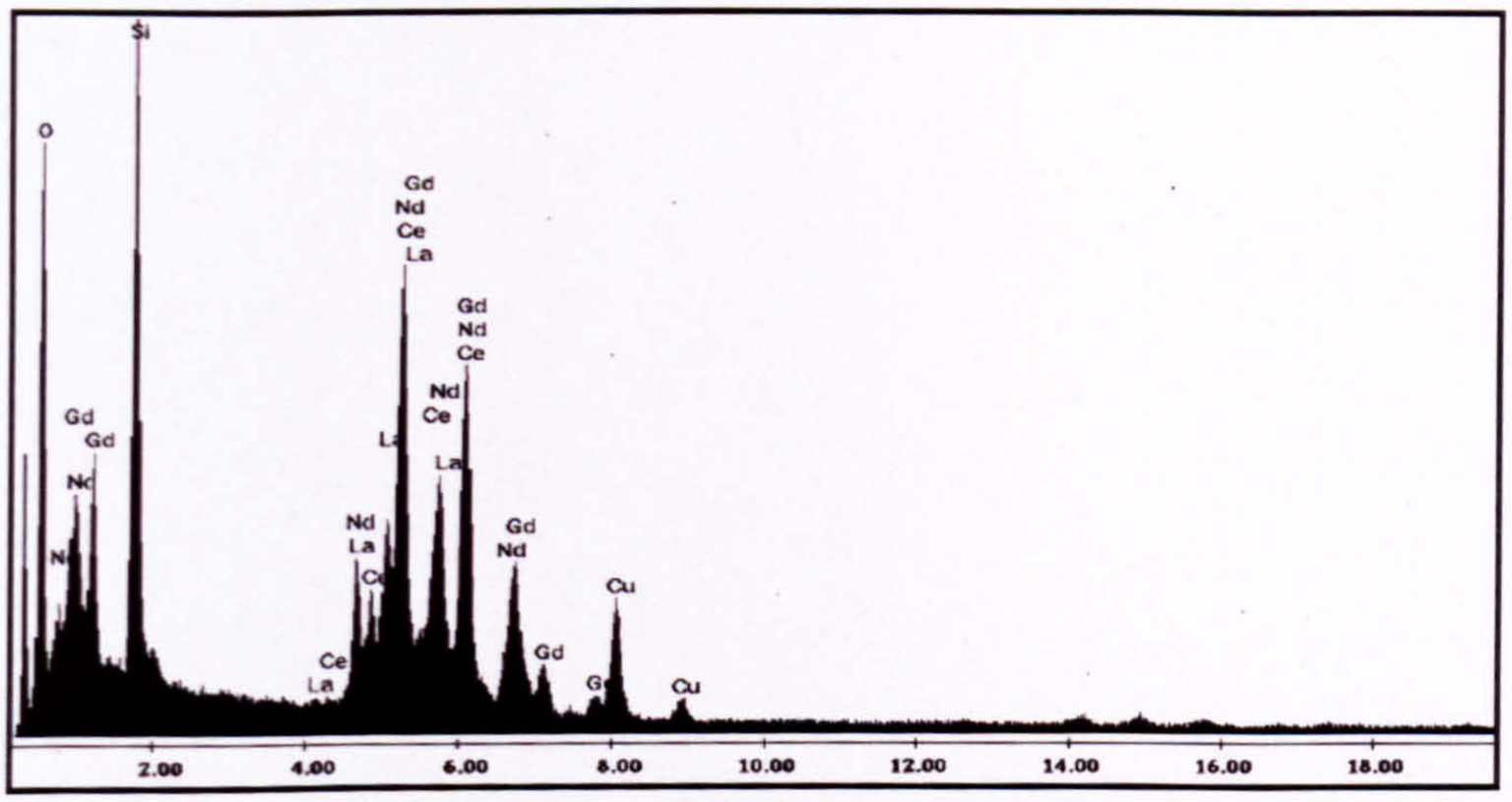


**Figure 4.2.4.27** Windowless EDX spectrum from × in **Figure 4.2.4.26** (*x*-axis = keV; *y*-axis = Intensity).

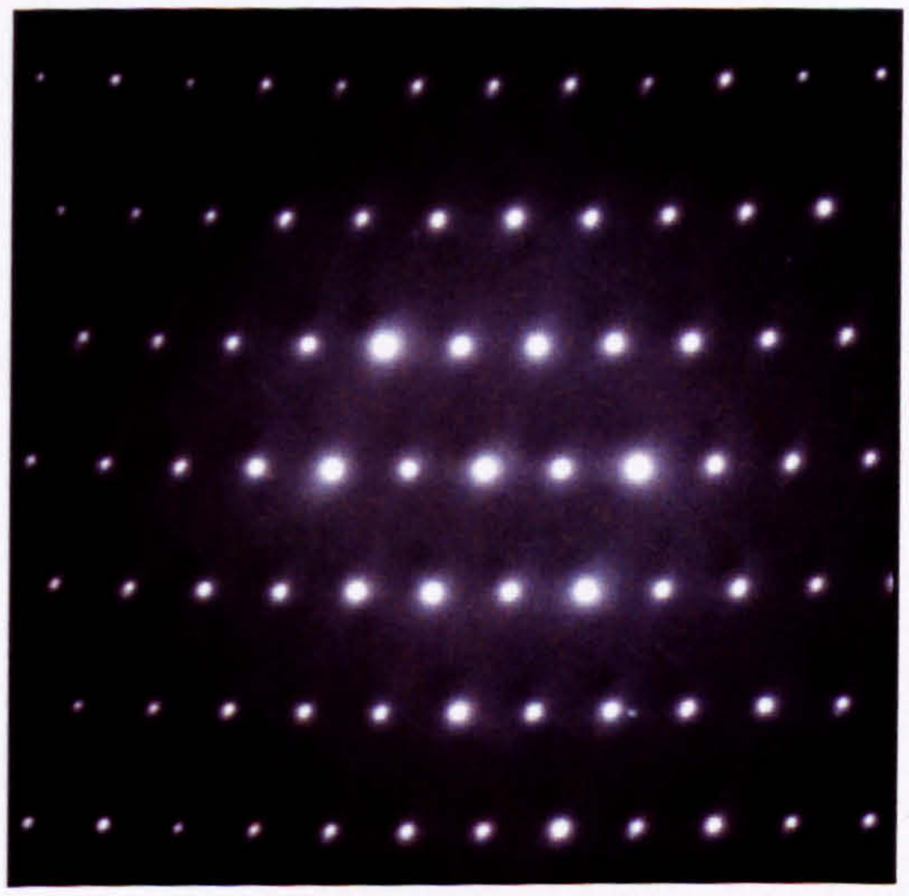

**Figure 4.2.4.28** Electron diffraction pattern from × in **Figure 4.2.4.26**.

### *4.2.4.6 $LiNaZrSi_6O_{15}$*

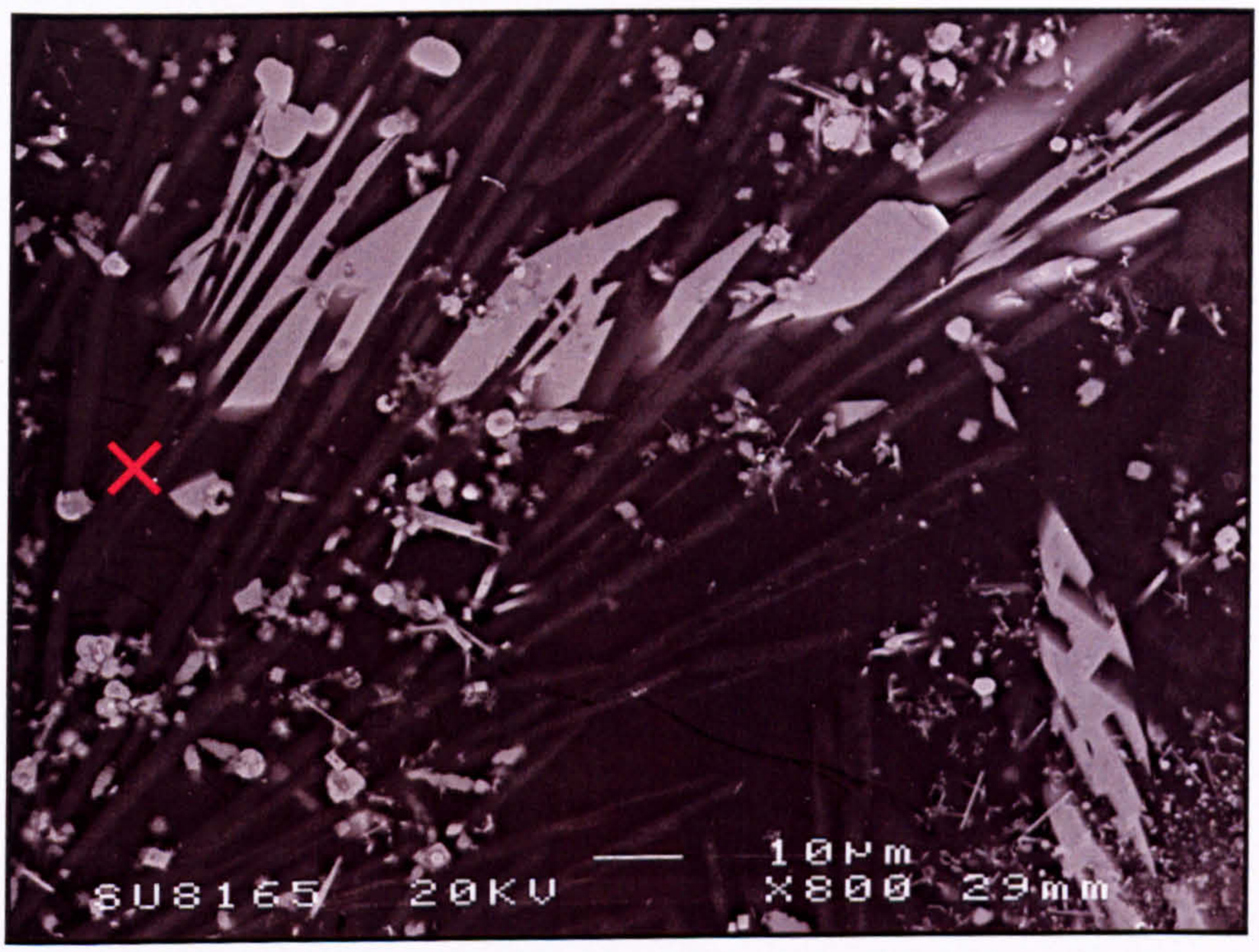


**Figure 4.2.4.29** SE SEM image of an Oxide HT sample, revealing acicular $LiNaZrSi_6O_{15}$ (dark grey) penetrating lanthanide (Nd,Gd,La,Ce) silicate (light grey) and cracking.

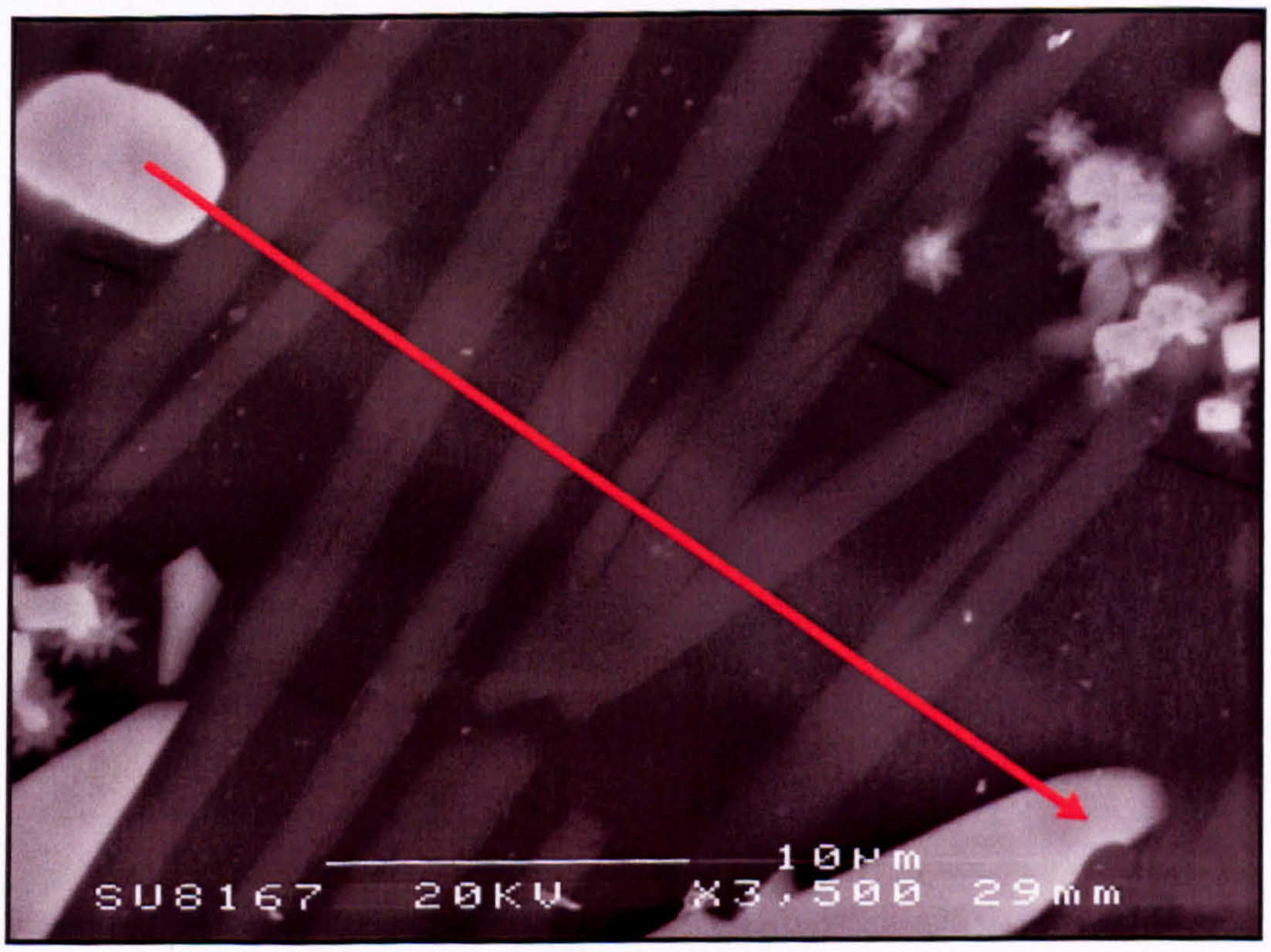


**Figure 4.2.4.30** SE SEM image of an Oxide HT sample with Type B microstructure. The red arrow indicates the location and direction of a linescan performed from a $Ce_{1-(x+y)}Zr_xGd_yO_{2-(y/2)}$ crystal (white) to a lanthanide (Nd,Gd,La,Ce) silicate crystal (light grey), passing across $LiNaZrSi_6O_{15}$ crystals (dark grey) (linescan length $\approx 32\ \mu m$). Image also reveals cracking.

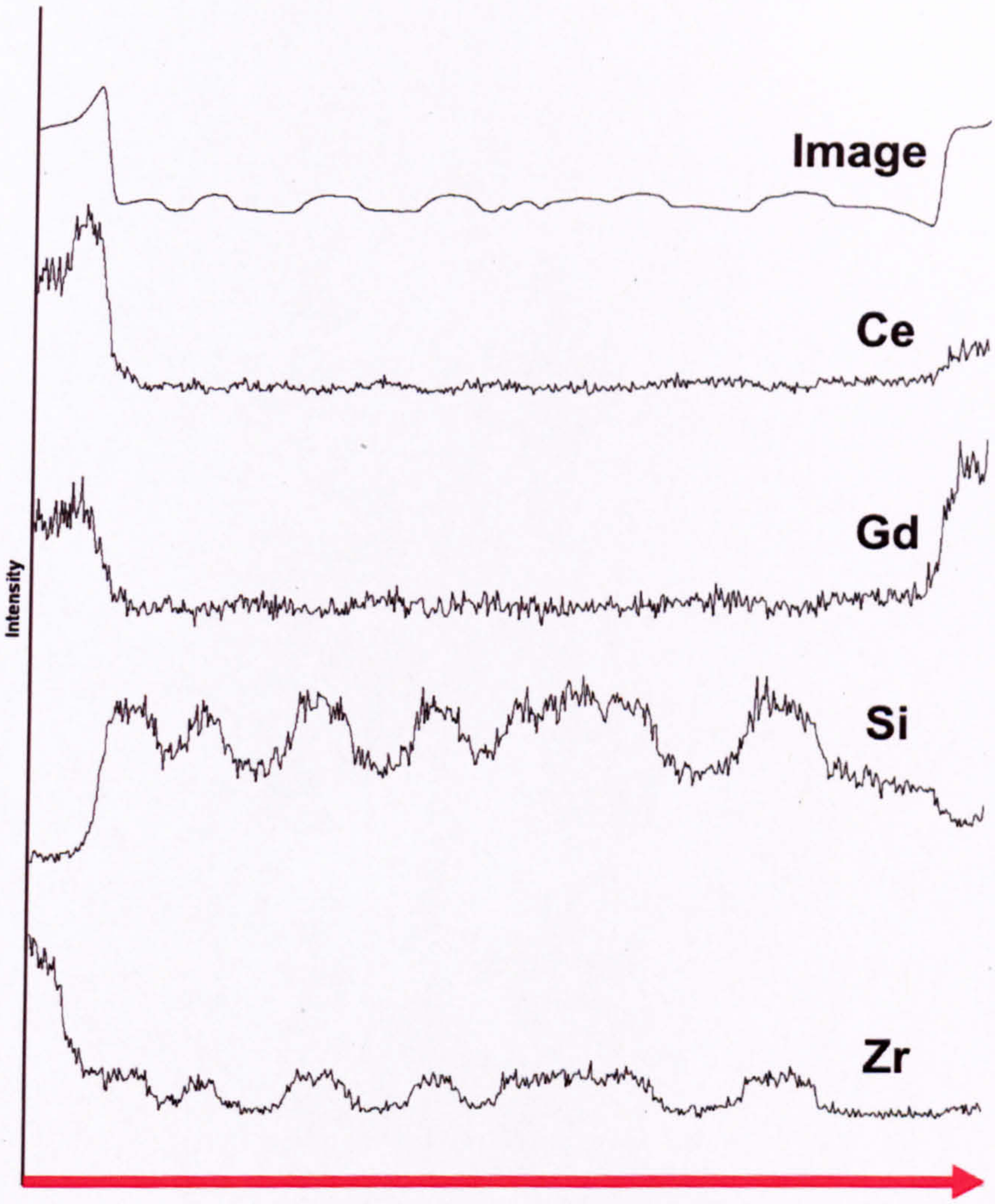


**Figure 4.2.4.31** Linescan performed where indicated in **Figure 4.2.4.30** ($x$-axis $\approx 32\ \mu$m).

# 4.3 Chemical (Aqueous) Durability Testing

## 4.3.1 Glass Leaching

Elements at concentrations below their DCP-AES detection limit in Blend AC, Oxide AC, Blend HT and Oxide HT leachate samples during modified PCT-B are listed in **Table 4.3.1.1.**

**Table 4.3.1.1** Elements at concentrations below their DCP-AES detection limit in Blend AC, Oxide AC, Blend HT and Oxide HT leachate samples during modified PCT-B.

| | |
|---|---|
| Ca | Ni |
| Fe | P |
| La | Ru |
| Mg | Ti |
| Mn | Zr |

Normalised elemental leach rates during modified PCT-B for Blend AC, Oxide AC, Blend HT and Oxide HT glasses are given in **Table 4.3.1.2**, with their elemental leached fractions reported in **Table 4.3.1.3**.

**Table 4.3.1.2** $NR_i$ (g $m^{-2}$ $d^{-1}$) during modified PCT-B.

| Glass | Element | Time (days) | | | | |
|---|---|---|---|---|---|---|
| | | 0 to 1 | 1 to 3 | 3 to 7 | 7 to 14 | 14 to 28 |
| Blend AC | Al | — | 0.0414 | 0.00583 | 0.0100 | –0.00148 |
| | B | 2.22 | 1.56 | 0.541 | 0.177 | 0.0896 |
| | Cr | 0.300 | 0.299 | 0.0794 | 0.0226 | 0.0118 |
| | K | 0.797 | 0.487 | 0.0826 | 0.102 | 0.0292 |
| | Li | 2.13 | 1.77 | 0.538 | 0.191 | 0.0362 |
| | Mo | 2.10 | 1.75 | 0.589 | 0.0816 | 0.0902 |
| | Na | 1.58 | 1.08 | 0.373 | 0.0805 | 0.0777 |
| | Si | 0.297 | 0.167 | 0.0133 | 0.0177 | 0.00497 |
| | Sr | — | 0.00623 | 0.00113 | 0.000225 | 0.000112 |
| Oxide AC | Al | — | 0.109 | 0.00626 | 0.00621 | 0.00406 |
| | B | 3.06 | 1.61 | 0.522 | 0.264 | 0.124 |
| | Ba | — | 0.00315 | 0.000323 | –0.000185 | 0.000036 |
| | Cr | 0.0888 | 0.0567 | 0.0166 | 0.0123 | 0.00328 |
| | Li | 2.89 | 1.81 | 0.509 | 0.327 | 0.0783 |
| | Mo | 2.60 | 1.31 | 0.371 | 0.0296 | 0.0319 |
| | Na | 2.34 | 1.20 | 0.338 | 0.167 | 0.130 |
| | Si | 0.428 | 0.264 | 0.0162 | 0.0357 | 0.00736 |
| | Sr | — | 0.0102 | 0.000198 | –0.000679 | — |
| Blend HT | Al | — | 0.0296 | 0.0105 | 0.00836 | –0.00155 |
| | B | 2.39 | 1.71 | 0.428 | 0.113 | 0.0821 |
| | Cr | 0.373 | 0.311 | 0.0843 | 0.0187 | 0.00689 |
| | K | 0.808 | 0.448 | 0.126 | 0.0935 | –0.00798 |
| | Li | 2.55 | 1.65 | 0.471 | 0.112 | 0.0279 |
| | Mo | 2.37 | 1.51 | 0.528 | 0.0286 | 0.0689 |
| | Na | 1.77 | 1.04 | 0.299 | 0.0569 | 0.0530 |
| | Si | 0.452 | 0.105 | 0.0171 | 0.00429 | 0.00411 |
| | Sr | 0.00689 | 0.00346 | 0.000984 | 0.000084 | 0.000082 |
| Oxide HT | Al | 0.254 | 0.0186 | 0.0507 | 0.00731 | 0.0106 |
| | B | 11.2 | 2.78 | 1.63 | 0.346 | 0.217 |
| | Ba | 0.0116 | 0.00240 | 0.00129 | –0.000251 | 0.000369 |
| | Cr | 0.697 | 0.184 | 0.0763 | 0.0247 | 0.00654 |
| | K | — | — | — | 0.430 | 0.0177 |
| | Li | 11.5 | 2.51 | 1.69 | 0.706 | 0.0753 |
| | Mo | 6.91 | 1.21 | 0.763 | 0.0202 | 0.122 |
| | Na | 7.95 | 1.79 | 0.983 | 0.230 | 0.140 |
| | Nd | 0.0221 | 0.00139 | 0.000182 | — | — |
| | Si | 0.931 | 0.137 | 0.0726 | 0.0283 | 0.0105 |
| | Sr | 0.0242 | 0.00309 | 0.00122 | –0.000345 | 0.000027 |

**Table 4.3.1.3** $LF_i$ (%) during modified PCT-B.

| Glass | Element | Time (days) | | | | |
|---|---|---|---|---|---|---|
| | | 1 | 3 | 7 | 14 | 28 |
| Blend AC | Al | — | 0.158 | 0.202 | 0.336 | 0.297 |
| | B | 4.23 | 10.2 | 14.3 | 16.7 | 19.1 |
| | Cr | 0.572 | 1.71 | 2.32 | 2.62 | 2.94 |
| | K | 1.52 | 3.38 | 4.01 | 5.37 | 6.14 |
| | Li | 4.07 | 10.8 | 14.9 | 17.5 | 18.4 |
| | Mo | 4.00 | 10.7 | 15.2 | 16.3 | 18.7 |
| | Na | 3.01 | 7.12 | 9.97 | 11.0 | 13.1 |
| | Si | 0.566 | 1.20 | 1.30 | 1.54 | 1.67 |
| | Sr | — | 0.0238 | 0.0324 | 0.0354 | 0.0384 |
| Oxide AC | Al | — | 0.430 | 0.480 | 0.565 | 0.677 |
| | B | 6.02 | 12.3 | 16.5 | 20.1 | 23.5 |
| | Ba | — | 0.0124 | 0.0150 | 0.0124 | 0.0134 |
| | Cr | 0.175 | 0.398 | 0.529 | 0.699 | 0.789 |
| | Li | 5.69 | 12.8 | 16.8 | 21.3 | 23.5 |
| | Mo | 5.11 | 10.3 | 13.2 | 13.6 | 14.5 |
| | Na | 4.61 | 9.32 | 12.0 | 14.3 | 17.9 |
| | Si | 0.844 | 1.88 | 2.01 | 2.50 | 2.71 |
| | Sr | — | 0.0402 | 0.0418 | 0.0324 | — |
| Blend HT | Al | — | 0.113 | 0.193 | 0.304 | 0.263 |
| | B | 4.55 | 11.1 | 14.4 | 15.9 | 18.1 |
| | Cr | 0.711 | 1.90 | 2.54 | 2.79 | 2.97 |
| | K | 1.54 | 3.25 | 4.21 | 5.46 | 5.25 |
| | Li | 4.87 | 11.2 | 14.8 | 16.3 | 17.0 |
| | Mo | 4.53 | 10.3 | 14.3 | 14.7 | 16.6 |
| | Na | 3.38 | 7.33 | 9.61 | 10.4 | 11.8 |
| | Si | 0.861 | 1.26 | 1.39 | 1.45 | 1.56 |
| | Sr | 0.0131 | 0.0263 | 0.0339 | 0.0350 | 0.0372 |
| Oxide HT | Al | 0.501 | 0.574 | 0.974 | 1.07 | 1.37 |
| | B | 22.1 | 33.1 | 45.9 | 50.7 | 56.7 |
| | Ba | 0.0229 | 0.0323 | 0.0425 | 0.0390 | 0.0492 |
| | Cr | 1.37 | 2.10 | 2.70 | 3.04 | 3.22 |
| | K | — | — | — | 5.93 | 6.42 |
| | Li | 22.7 | 32.6 | 45.9 | 55.7 | 57.7 |
| | Mo | 13.6 | 18.4 | 24.4 | 24.7 | 28.0 |
| | Na | 15.7 | 22.7 | 30.5 | 33.6 | 37.5 |
| | Nd | 0.0435 | 0.0490 | 0.0504 | — | — |
| | Si | 1.83 | 2.37 | 2.94 | 3.34 | 3.62 |
| | Sr | 0.0476 | 0.0598 | 0.0694 | 0.0646 | 0.0654 |

*4.3.1.1 Aluminium Leaching*

Generally, normalised aluminium leach rates (**Figure 4.3.1.1**) decreased as the modified PCT-B progressed. Heat treatment of Blend glass does not affect its aluminium leach rates significantly. However, heat treatment of Oxide glass increased its aluminium leach rates significantly. Aluminium leached fractions during modified PCT-B (**Figure 4.3.1.2**) reveal that heat treatment of Blend glass lowered the fraction of aluminium leached marginally, whilst heat treatment of Oxide glass increased it significantly.

For Blend AC and Blend HT their normalised aluminium leach rates were negative (the concentration of Al in their leachates decreased) for the 14 to 28 d period. This is reflected in their aluminium leached fractions, which were lower at 28 d than at 14 d.

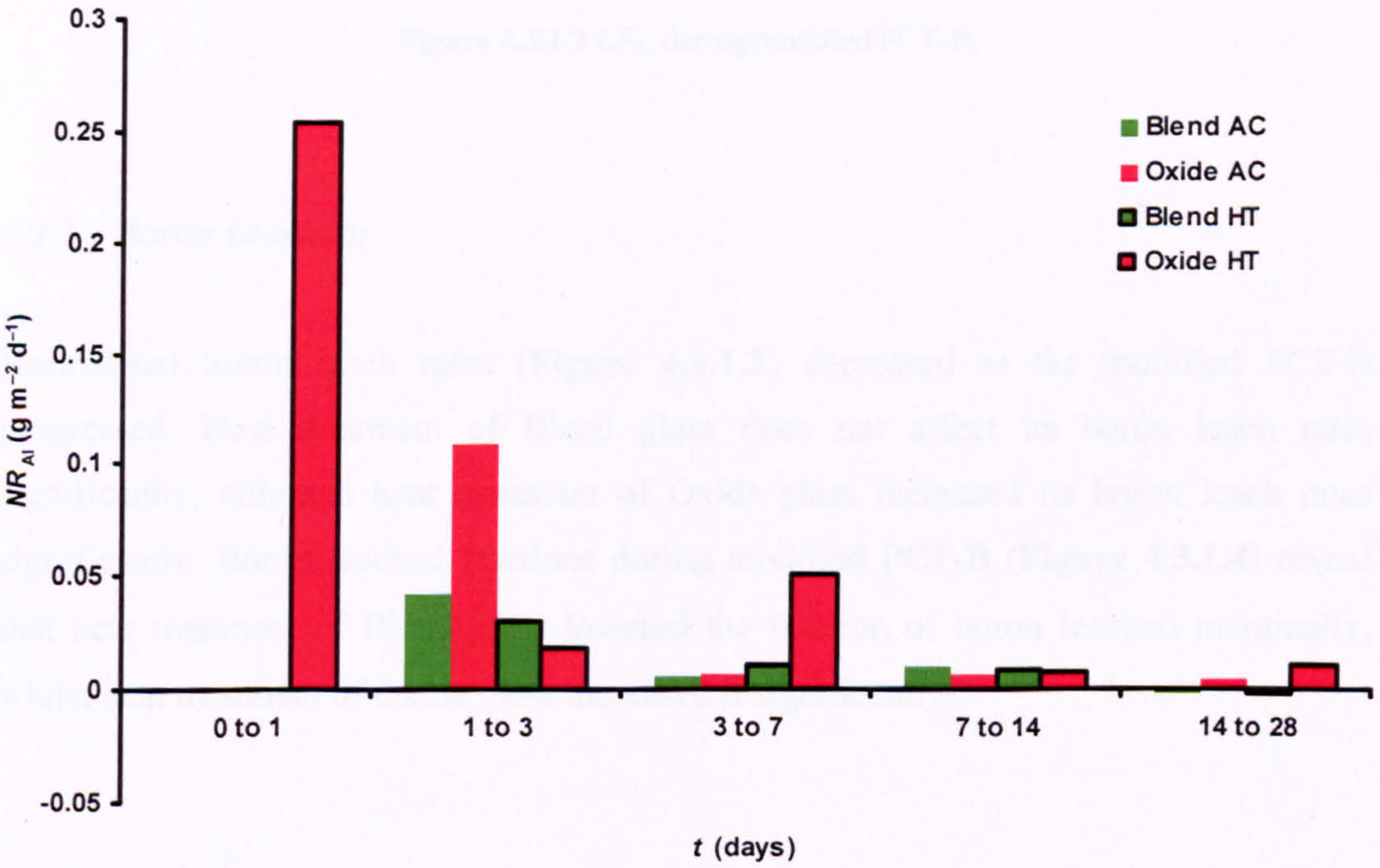


**Figure 4.3.1.1** $NR_{Al}$ during modified PCT-B.

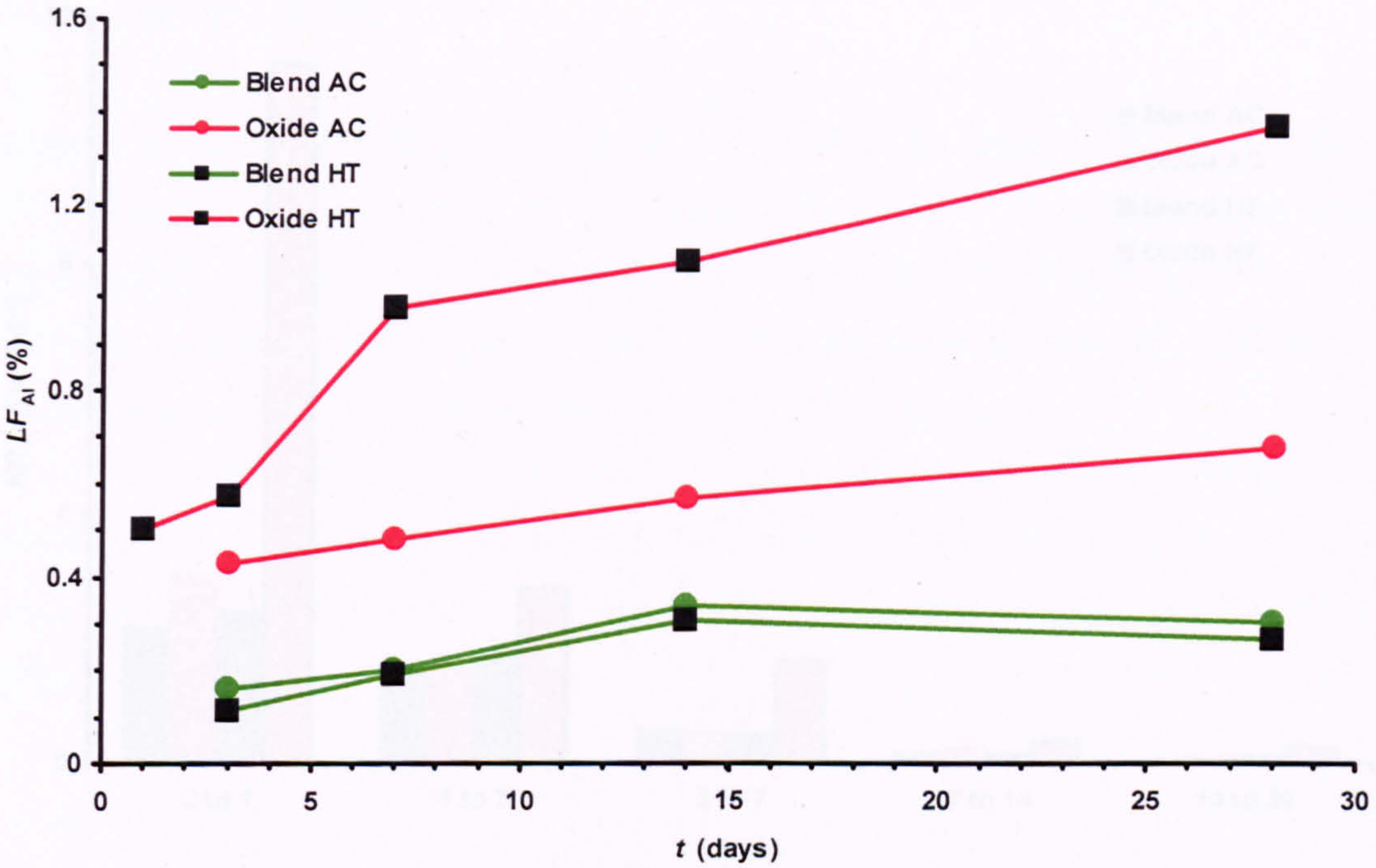


**Figure 4.3.1.2** $LF_{Al}$ during modified PCT-B.

### *4.3.1.2 Boron Leaching*

Normalised boron leach rates (**Figure 4.3.1.3**) decreased as the modified PCT-B progressed. Heat treatment of Blend glass does not affect its boron leach rates significantly, although heat treatment of Oxide glass increased its boron leach rates significantly. Boron leached fractions during modified PCT-B (**Figure 4.3.1.4**) reveal that heat treatment of Blend glass lowered the fraction of boron leached marginally, whilst heat treatment of Oxide glass increased it significantly.

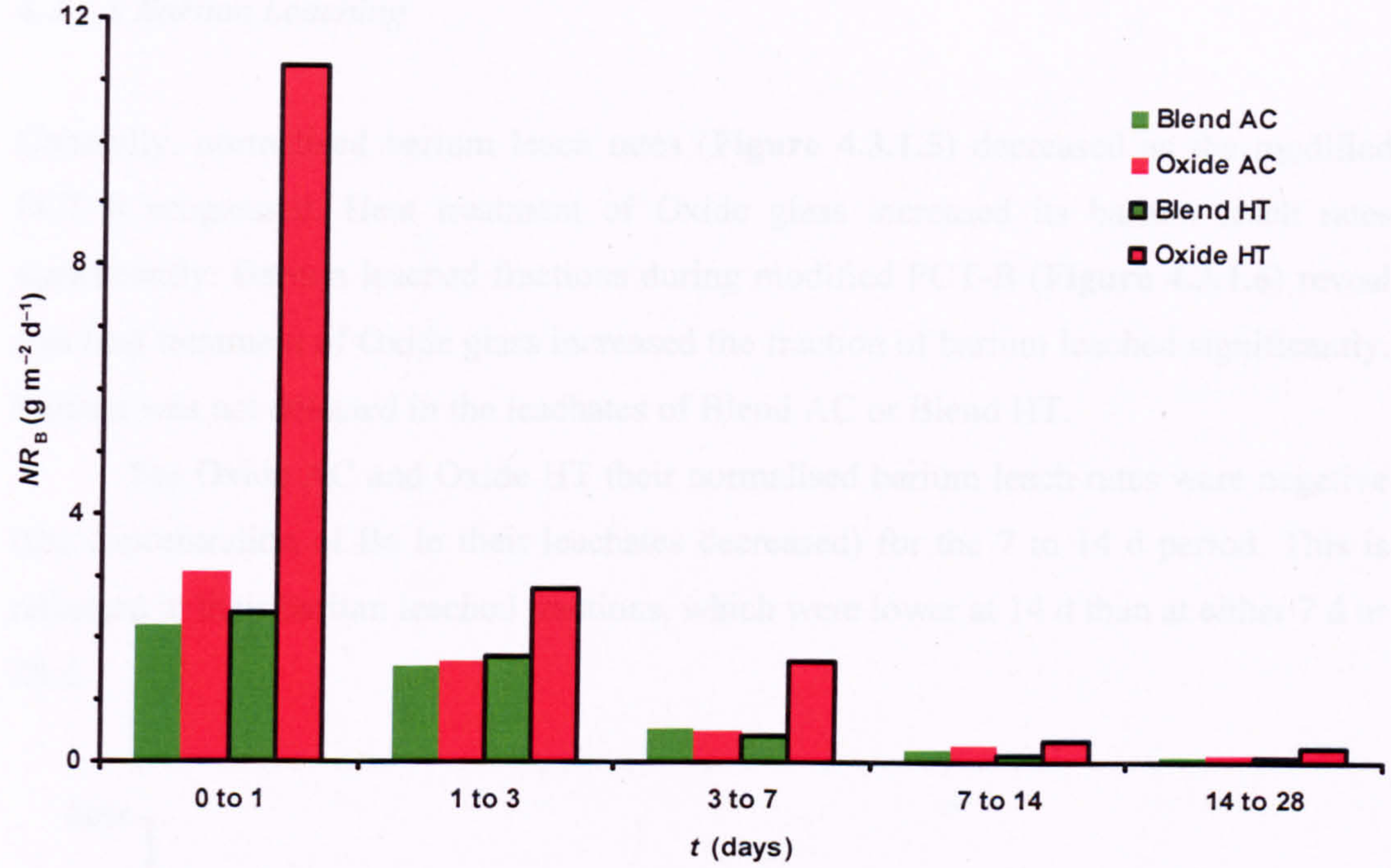


**Figure 4.3.1.3** $NR_B$ during modified PCT-B.

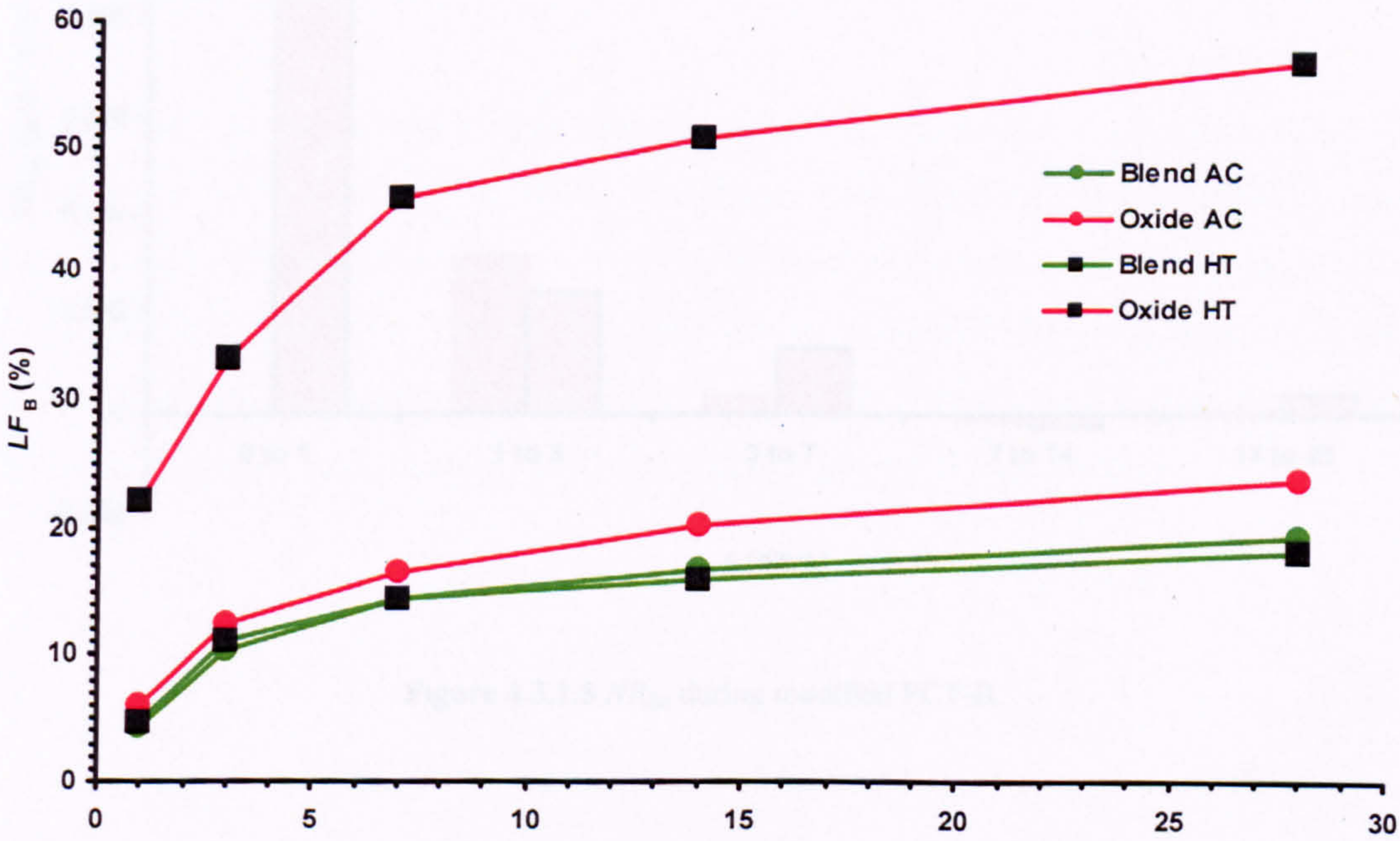


**Figure 4.3.1.4** $LF_B$ during modified PCT-B.

*4.3.1.3 Barium Leaching*

Generally, normalised barium leach rates (**Figure 4.3.1.5**) decreased as the modified PCT-B progressed. Heat treatment of Oxide glass increased its barium leach rates significantly. Barium leached fractions during modified PCT-B (**Figure 4.3.1.6**) reveal that heat treatment of Oxide glass increased the fraction of barium leached significantly. Barium was not detected in the leachates of Blend AC or Blend HT.

For Oxide AC and Oxide HT their normalised barium leach rates were negative (the concentration of Ba in their leachates decreased) for the 7 to 14 d period. This is reflected in their barium leached fractions, which were lower at 14 d than at either 7 d or 28 d.

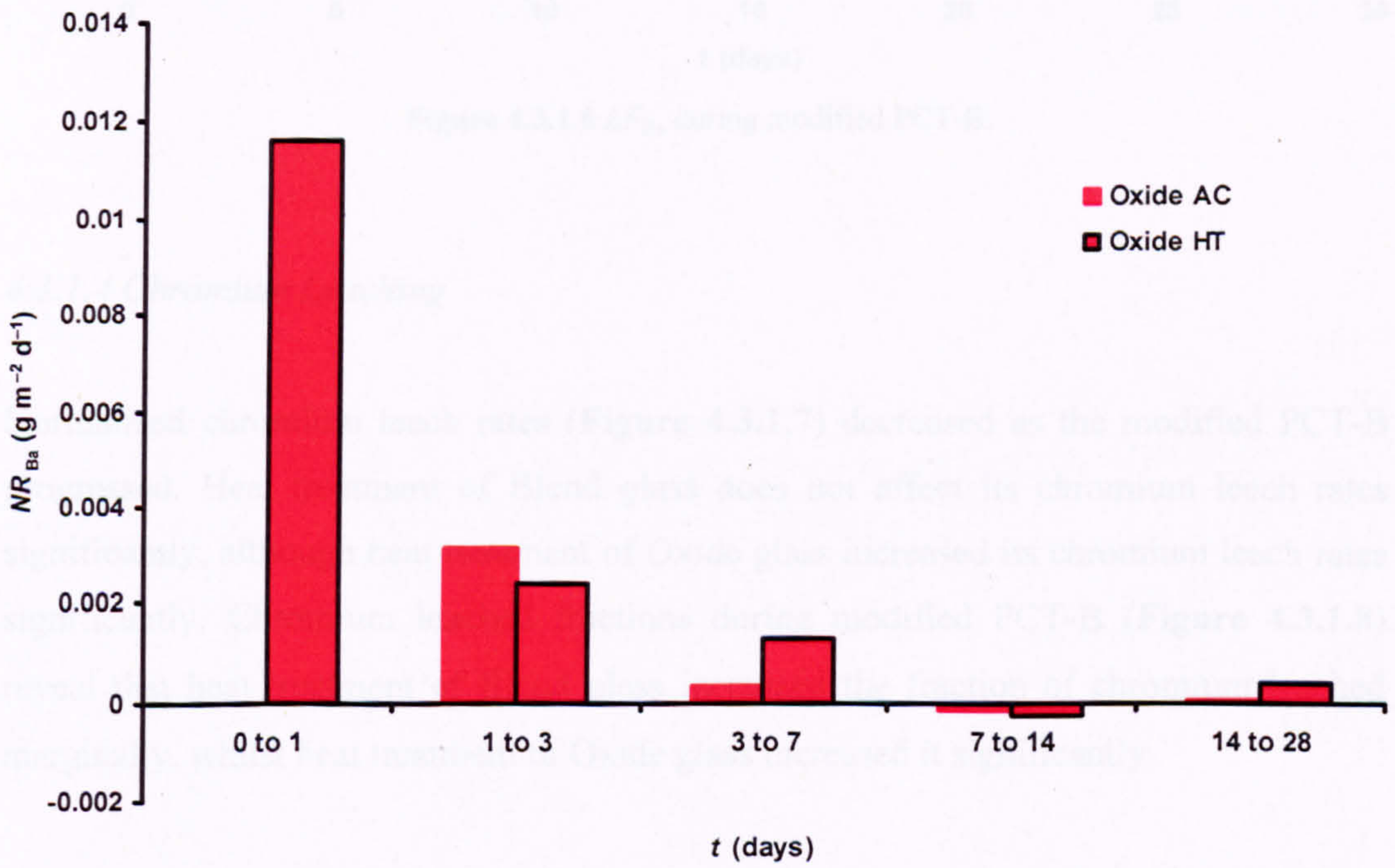


**Figure 4.3.1.5** $NR_{Ba}$ during modified PCT-B.

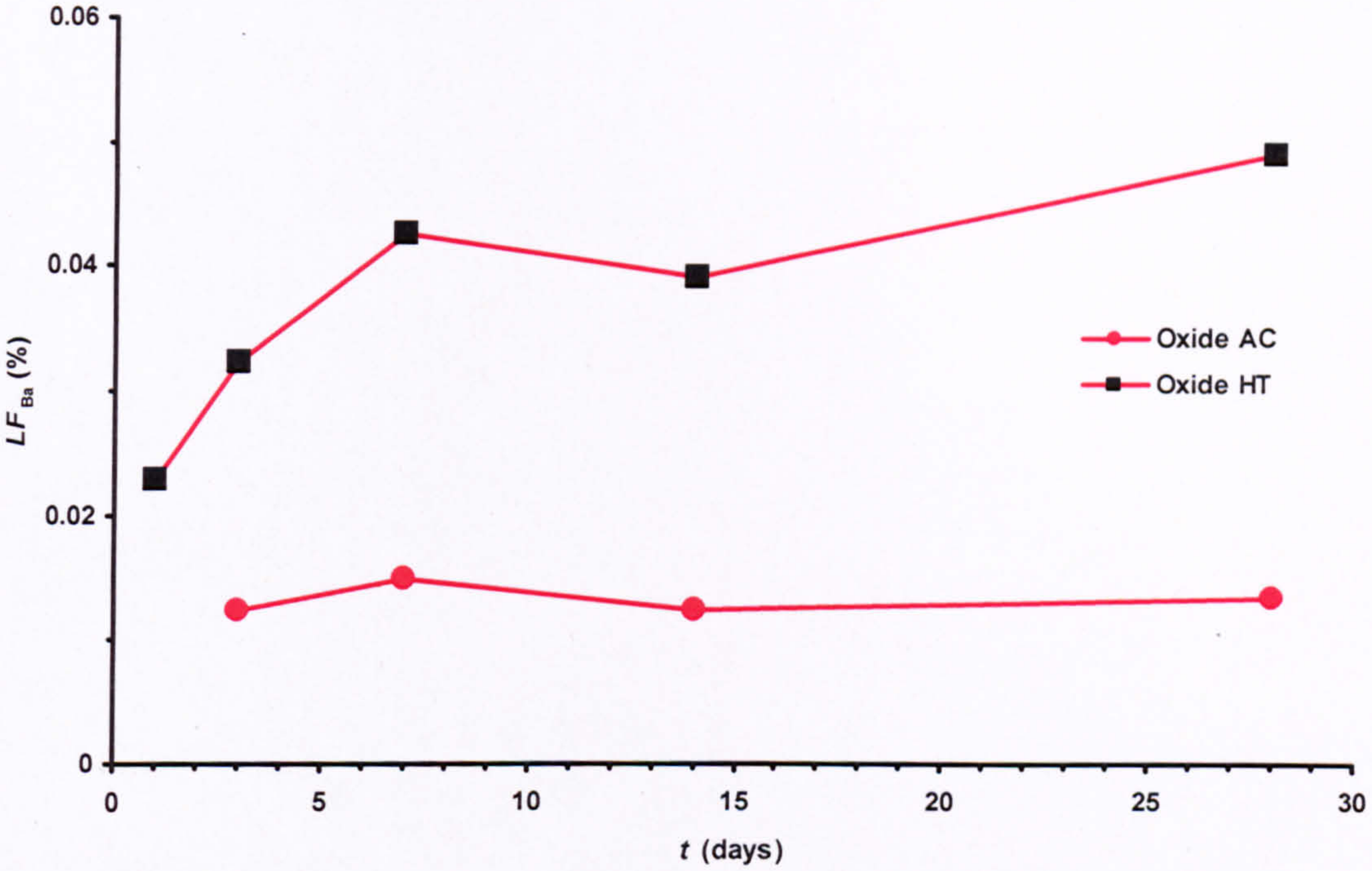


**Figure 4.3.1.6** $LF_{Ba}$ during modified PCT-B.

### *4.3.1.4 Chromium Leaching*

Normalised chromium leach rates (**Figure 4.3.1.7**) decreased as the modified PCT-B progressed. Heat treatment of Blend glass does not affect its chromium leach rates significantly, although heat treatment of Oxide glass increased its chromium leach rates significantly. Chromium leached fractions during modified PCT-B (**Figure 4.3.1.8**) reveal that heat treatment of Blend glass increased the fraction of chromium leached marginally, whilst heat treatment of Oxide glass increased it significantly.

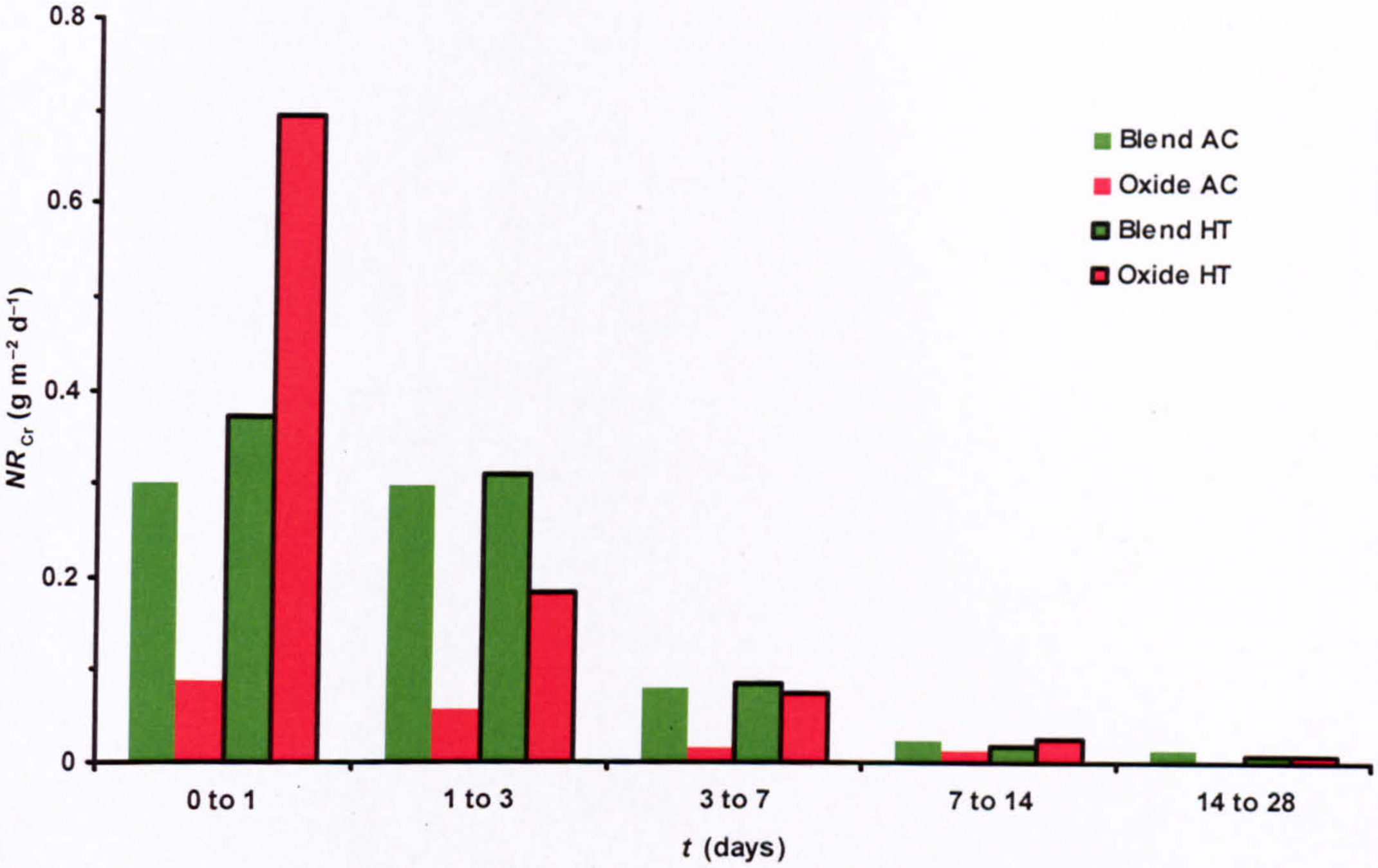


**Figure 4.3.1.7** $NR_{Cr}$ during modified PCT-B.

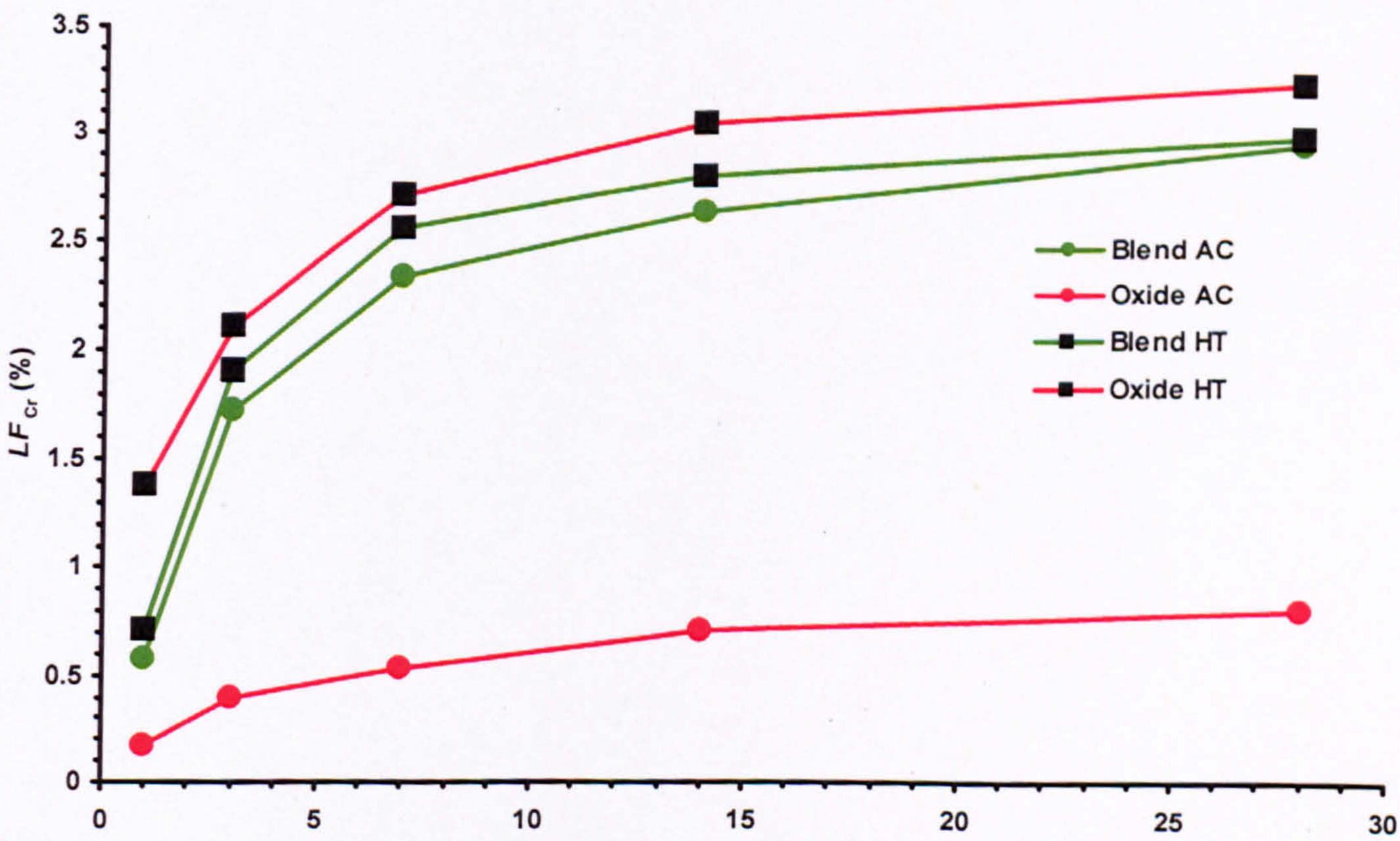


**Figure 4.3.1.8** $LF_{Cr}$ during modified PCT-B.

*4.3.1.5 Potassium Leaching*

Generally, normalised potassium leach rates (**Figure 4.3.1.9**) decreased as the modified PCT-B progressed. Heat treatment of Blend glass does not affect its potassium leach rates significantly. Heat treatment of Oxide glass increased its potassium leach rates enough to become detectable. Potassium leached fractions during modified PCT-B (**Figure 4.3.1.10**) reveal that heat treatment of Blend glass lowered the fraction of potassium leached marginally, whilst heat treatment of Oxide glass increased it enough to become detectable. Potassium was not detected in the leachate of Oxide AC.

For Blend HT its normalised potassium leach rate was negative (the concentration of K in its leachate decreased) for the 14 to 28 d period, reflected in its potassium leached fraction, which was lower at 28 d than at 14 d. Potassium became detectable in Oxide HT leachates during the 7 to 14 d period.

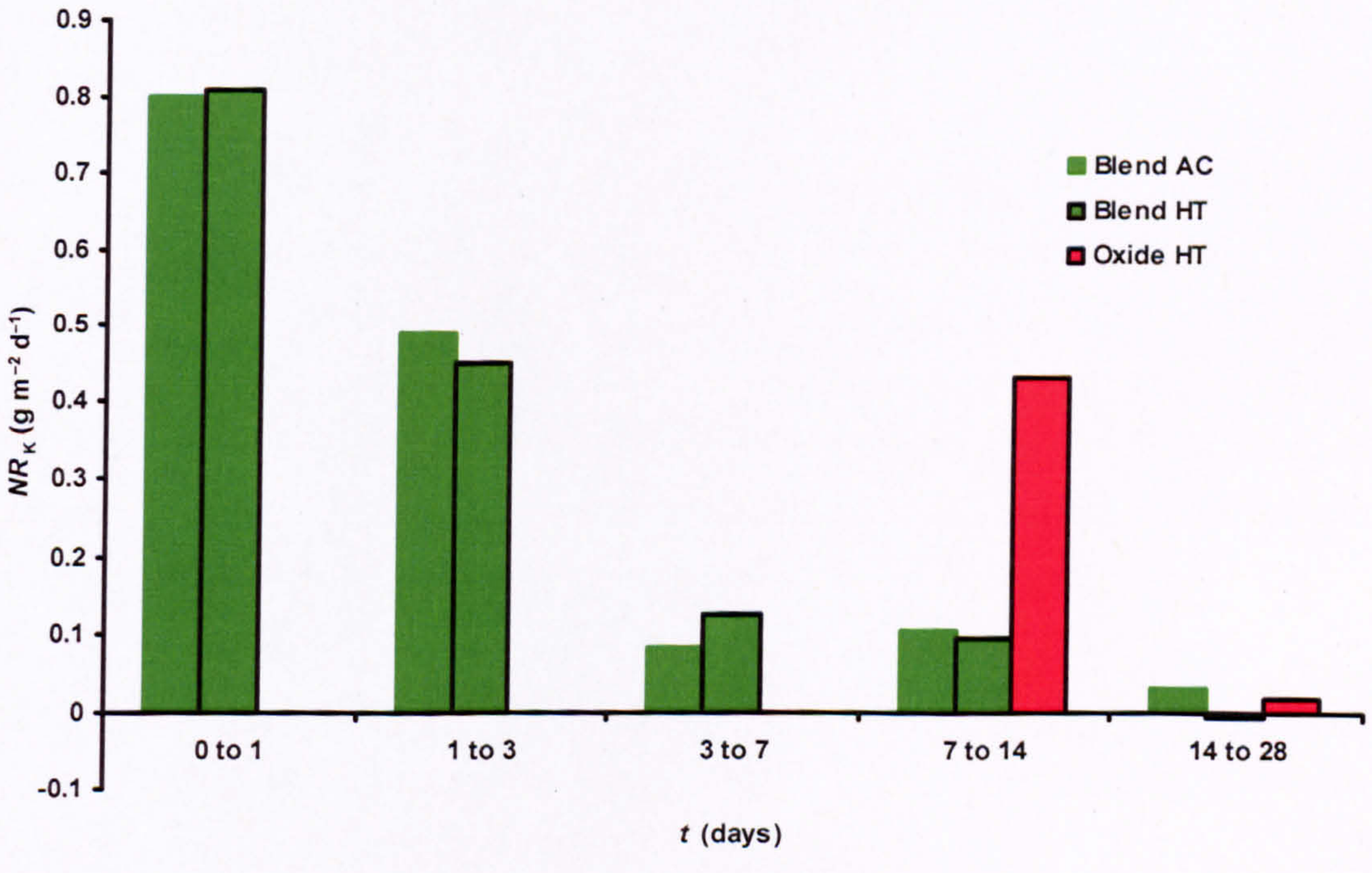


**Figure 4.3.1.9** $NR_K$ during modified PCT-B.

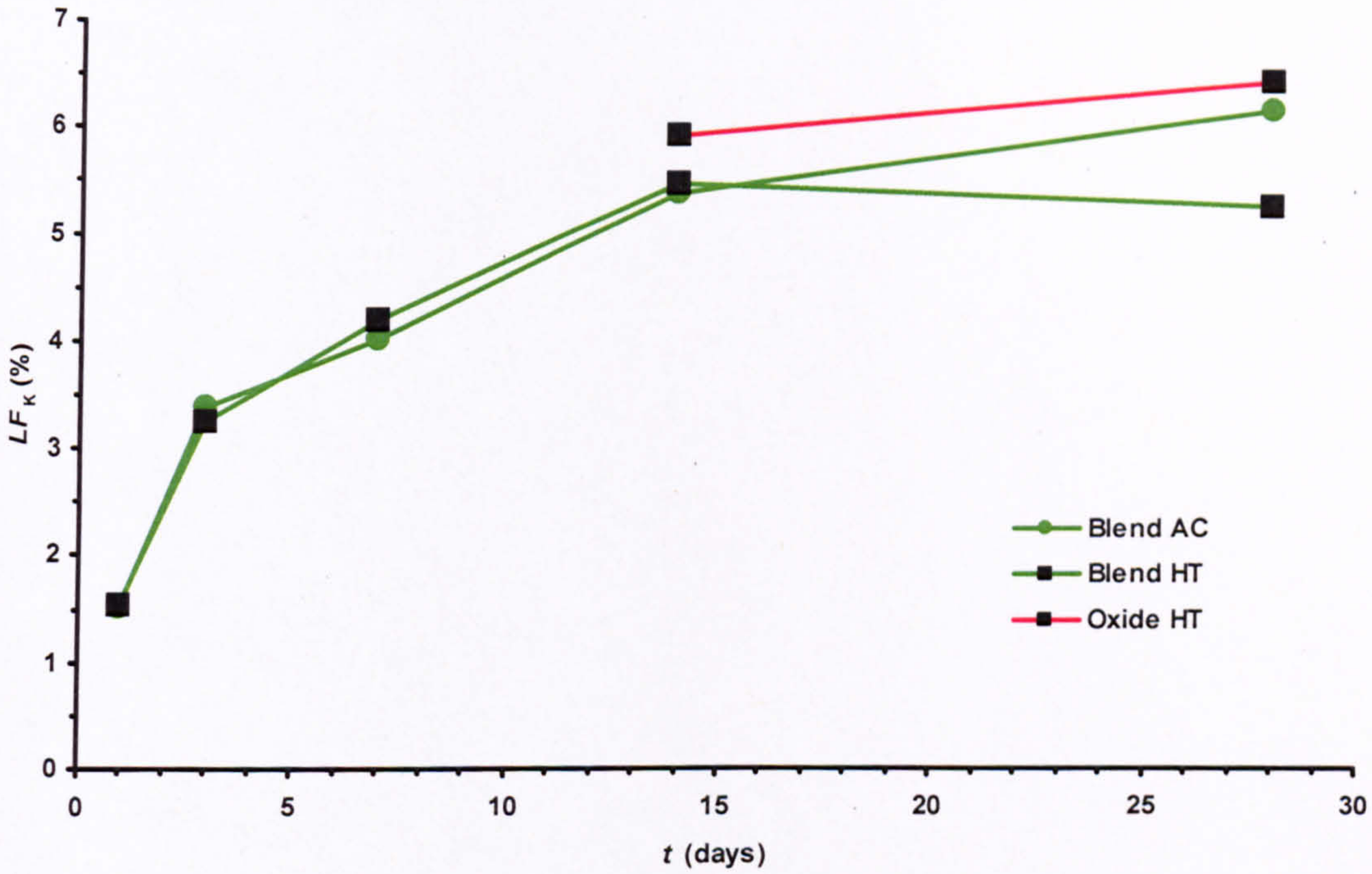


**Figure 4.3.1.10** $LF_K$ during modified PCT-B.

### *4.3.1.6 Lithium Leaching*

Normalised lithium leach rates (**Figure 4.3.1.11**) decreased as the modified PCT-B progressed. Heat treatment of Blend glass does not affect its lithium leach rates significantly, but heat treatment of Oxide glass increased its lithium leach rates significantly. Lithium leached fractions during modified PCT-B (**Figure 4.3.1.12**) reveal that heat treatment of Blend glass lowered the fraction of lithium leached marginally, whilst heat treatment of Oxide glass increased it significantly.

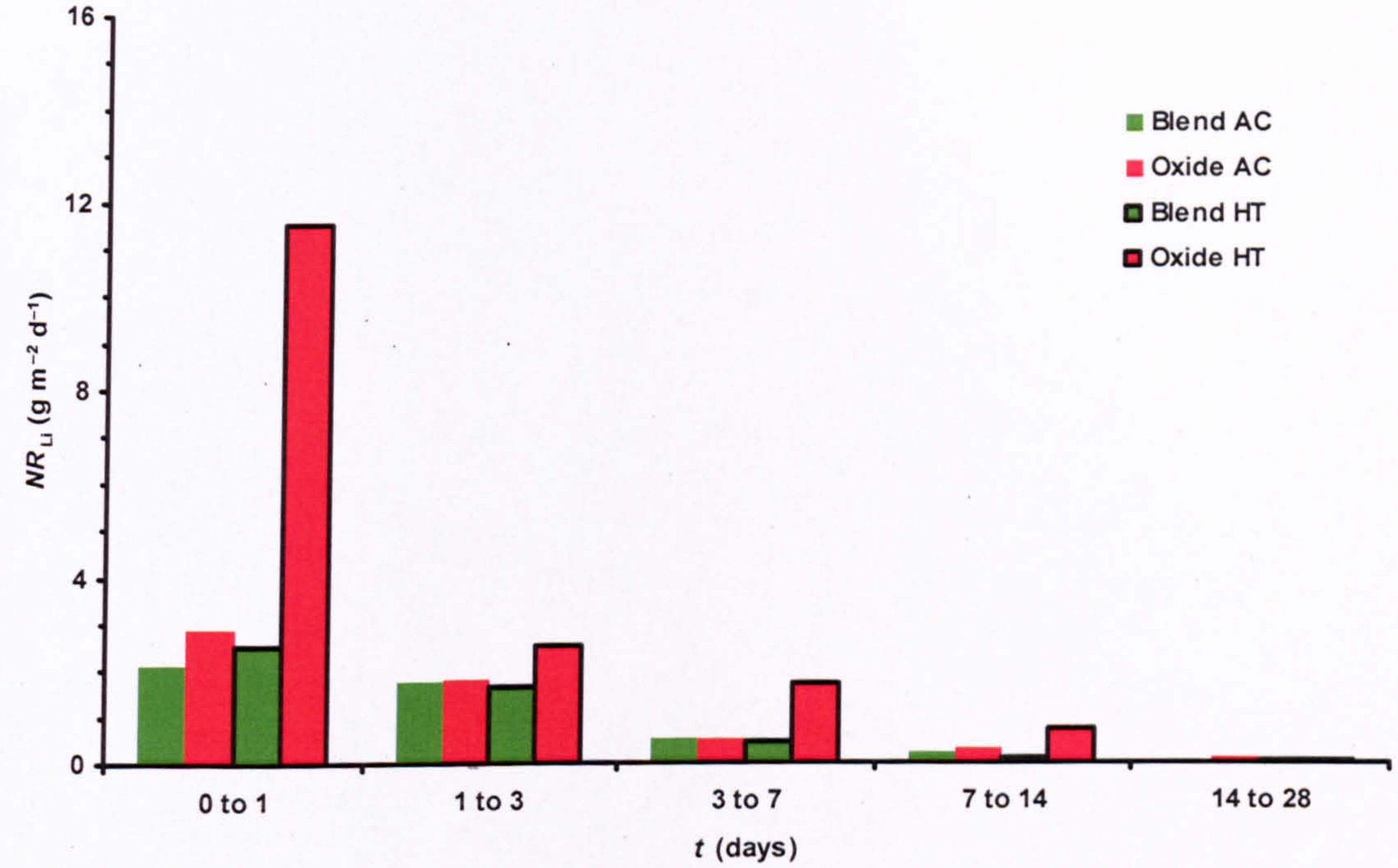


**Figure 4.3.1.11** $NR_{Li}$ during modified PCT-B.

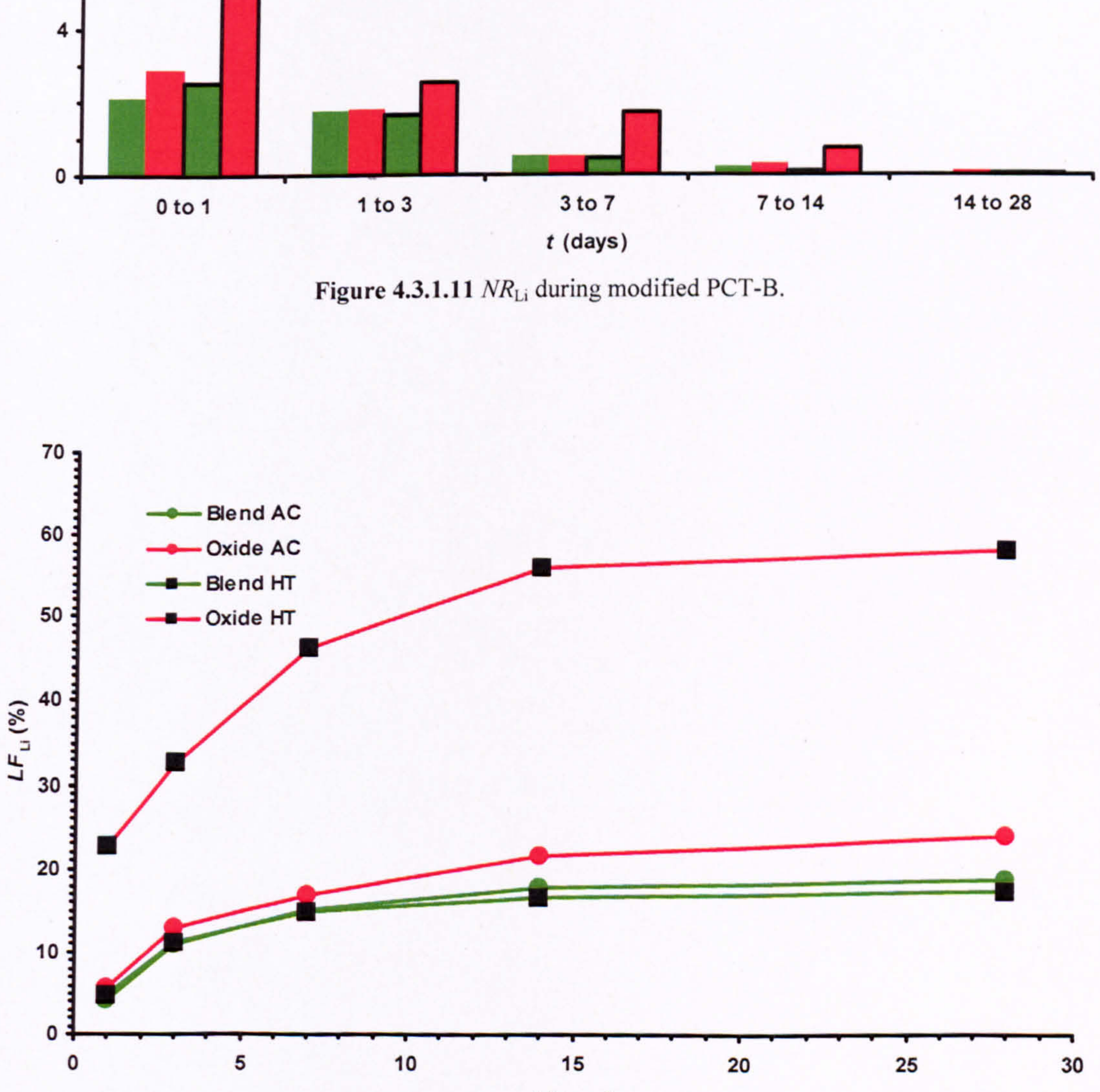


**Figure 4.3.1.12** $LF_{Li}$ during modified PCT-B.

*4.3.1.7 Molybdenum Leaching*

Generally, normalised molybdenum leach rates (**Figure 4.3.1.13**) decreased as the modified PCT-B progressed. Heat treatment of Blend glass does not affect its molybdenum leach rates significantly, although heat treatment of Oxide glass increased its molybdenum leach rates significantly. Molybdenum leached fractions during modified PCT-B (**Figure 4.3.1.14**) reveal that heat treatment of Blend glass lowered the fraction of molybdenum leached marginally, whilst heat treatment of Oxide glass increased it significantly.

For Blend AC, Oxide AC, Blend HT and Oxide HT their normalised molybdenum leach rates were lower during the 7 to 14 d period than either the preceding or subsequent period. This is reflected in their molybdenum leached fractions at 14 d, which were similar to those at 7 d.

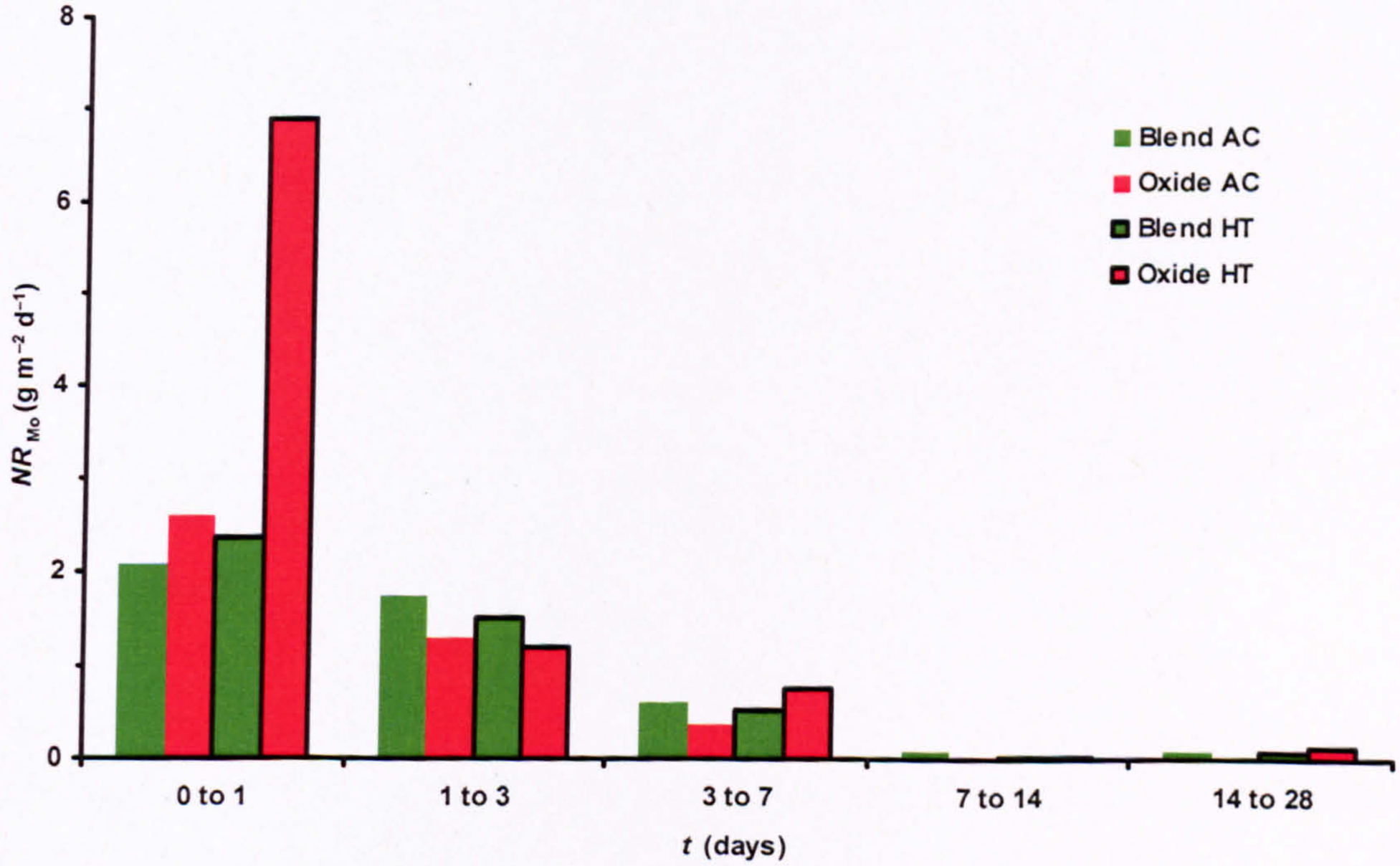


**Figure 4.3.1.13** $NR_{Mo}$ during modified PCT-B.

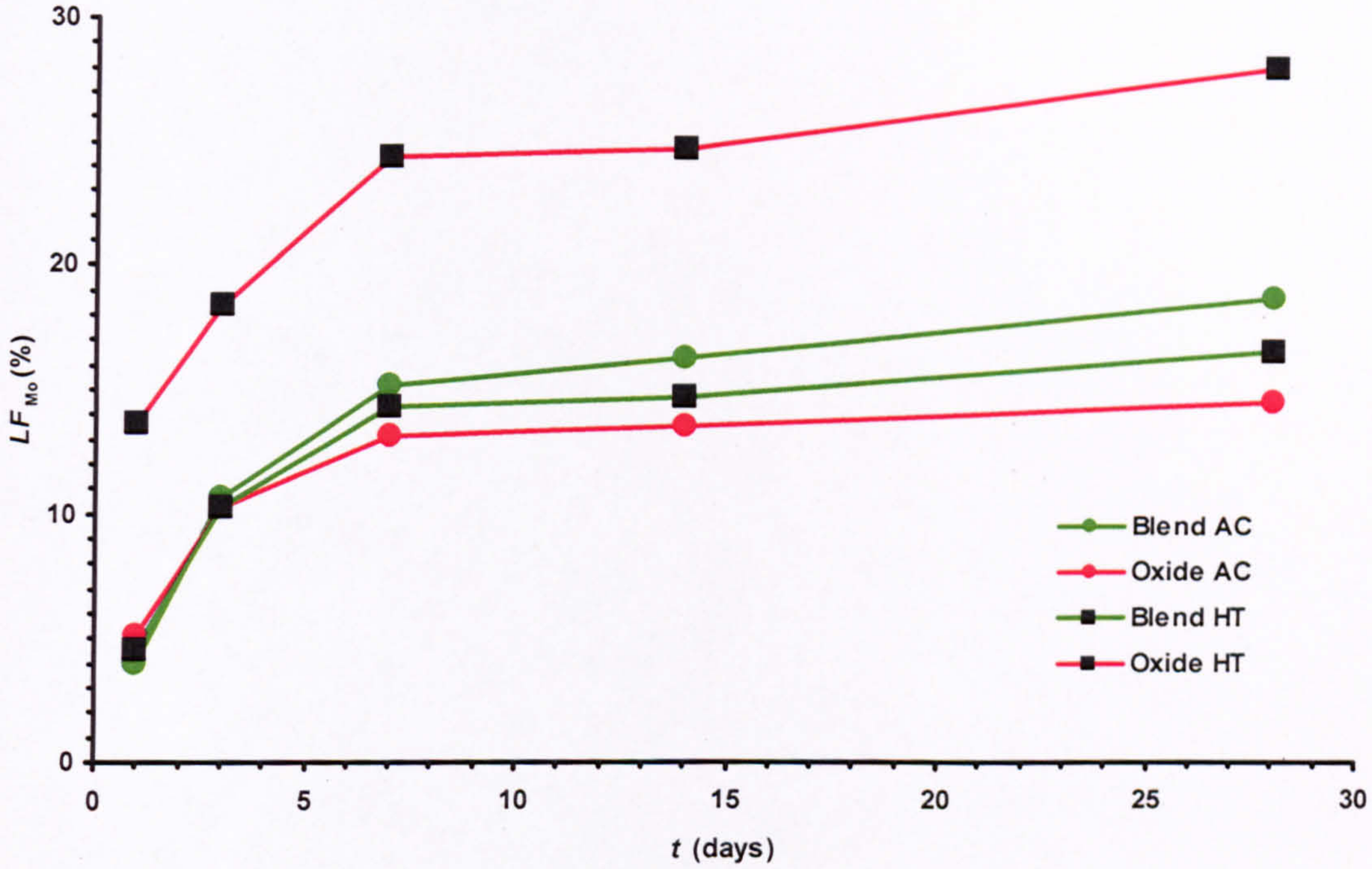


**Figure 4.3.1.14** $LF_{Mo}$ during modified PCT-B.

### *4.3.1.8 Sodium Leaching*

Normalised sodium leach rates (**Figure 4.3.1.15**) decreased as the modified PCT-B progressed. Heat treatment of Blend glass does not affect its sodium leach rates significantly. Heat treatment of Oxide glass increased its sodium leach rates significantly. Sodium leached fractions during modified PCT-B (**Figure 4.3.1.16**) reveal that heat treatment of Blend glass lowered the fraction of sodium leached marginally, whilst heat treatment of Oxide glass increased it significantly.

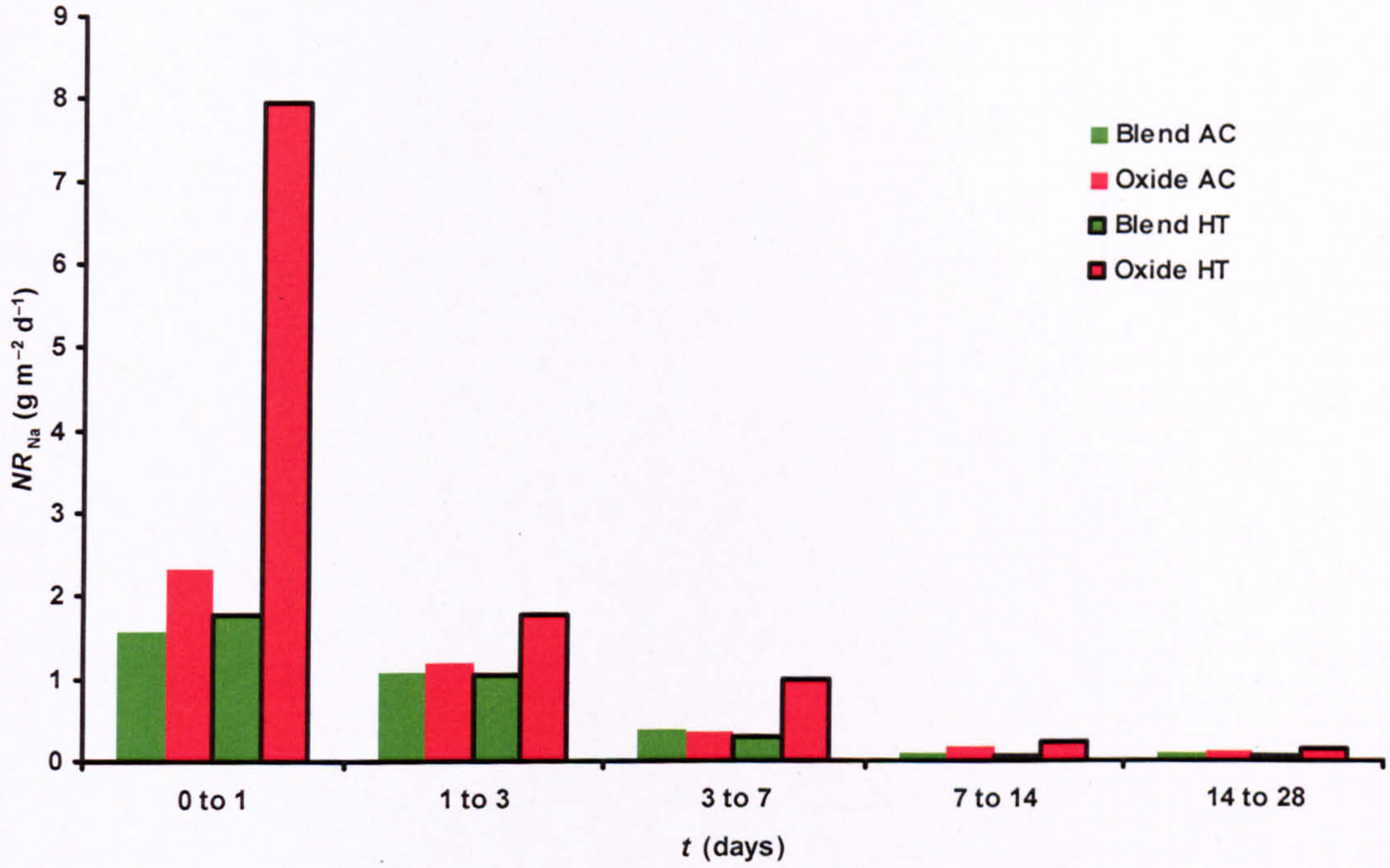


**Figure 4.3.1.15** $NR_{Na}$ during modified PCT-B.

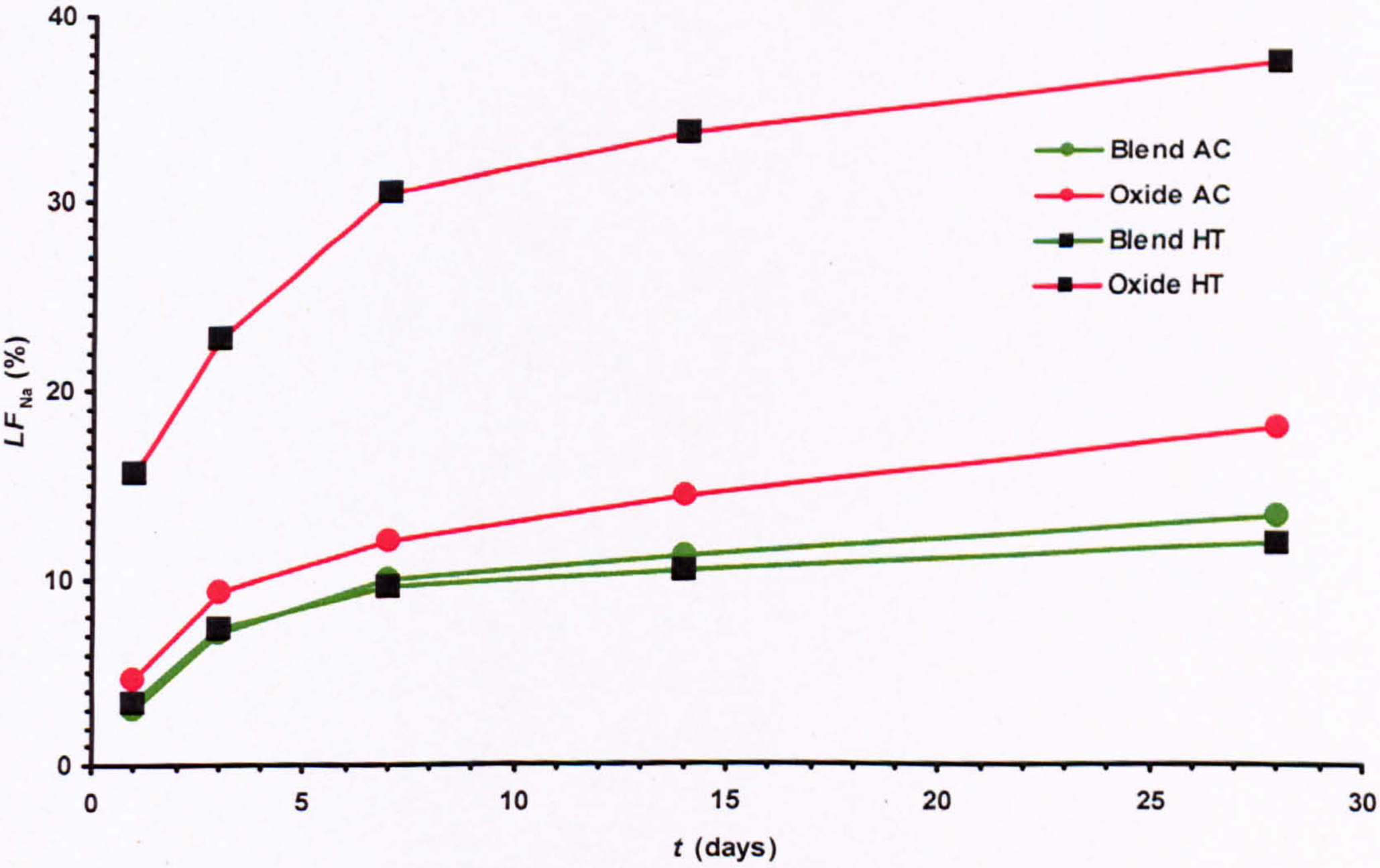


**Figure 4.3.1.16** $LF_{Na}$ during modified PCT-B.

*4.3.1.9 Neodymium Leaching*

Normalised neodymium leach rates (**Figure 4.3.1.17**) decreased as the modified PCT-B progressed. Heat treatment of Oxide glass increased its neodymium leach rate enough to become detectable. Neodymium leached fractions during modified PCT-B (**Figure 4.3.1.18**) reveal that heat treatment of Oxide glass increased the fraction of neodymium leached enough to become detectable. Neodymium was not detected in the leachates of Blend AC, Oxide AC and Blend HT.

Neodymium became undetectable in Oxide HT leachates during the 7 to 14 d period.

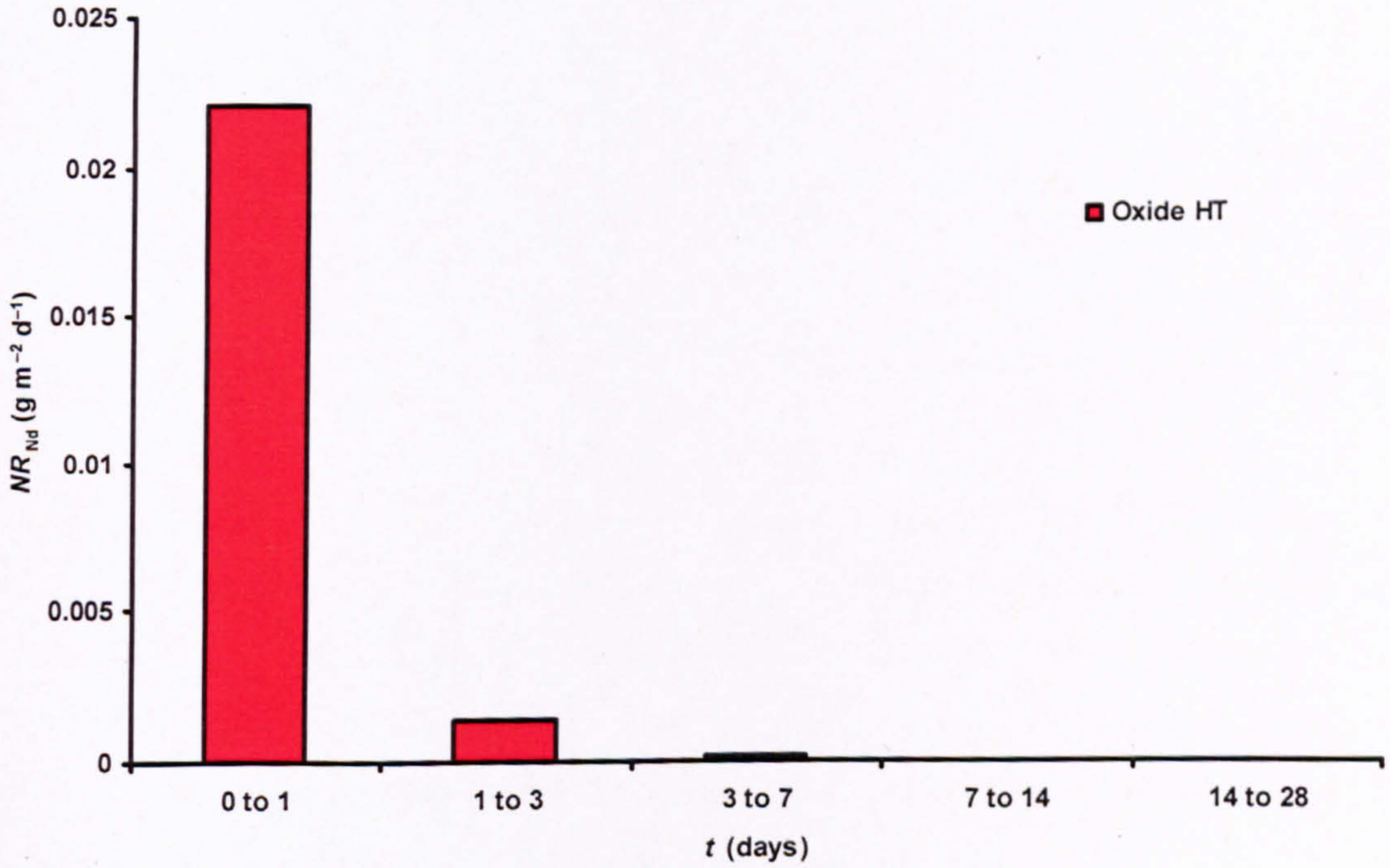


**Figure 4.3.1.17** $NR_{Nd}$ during modified PCT-B.

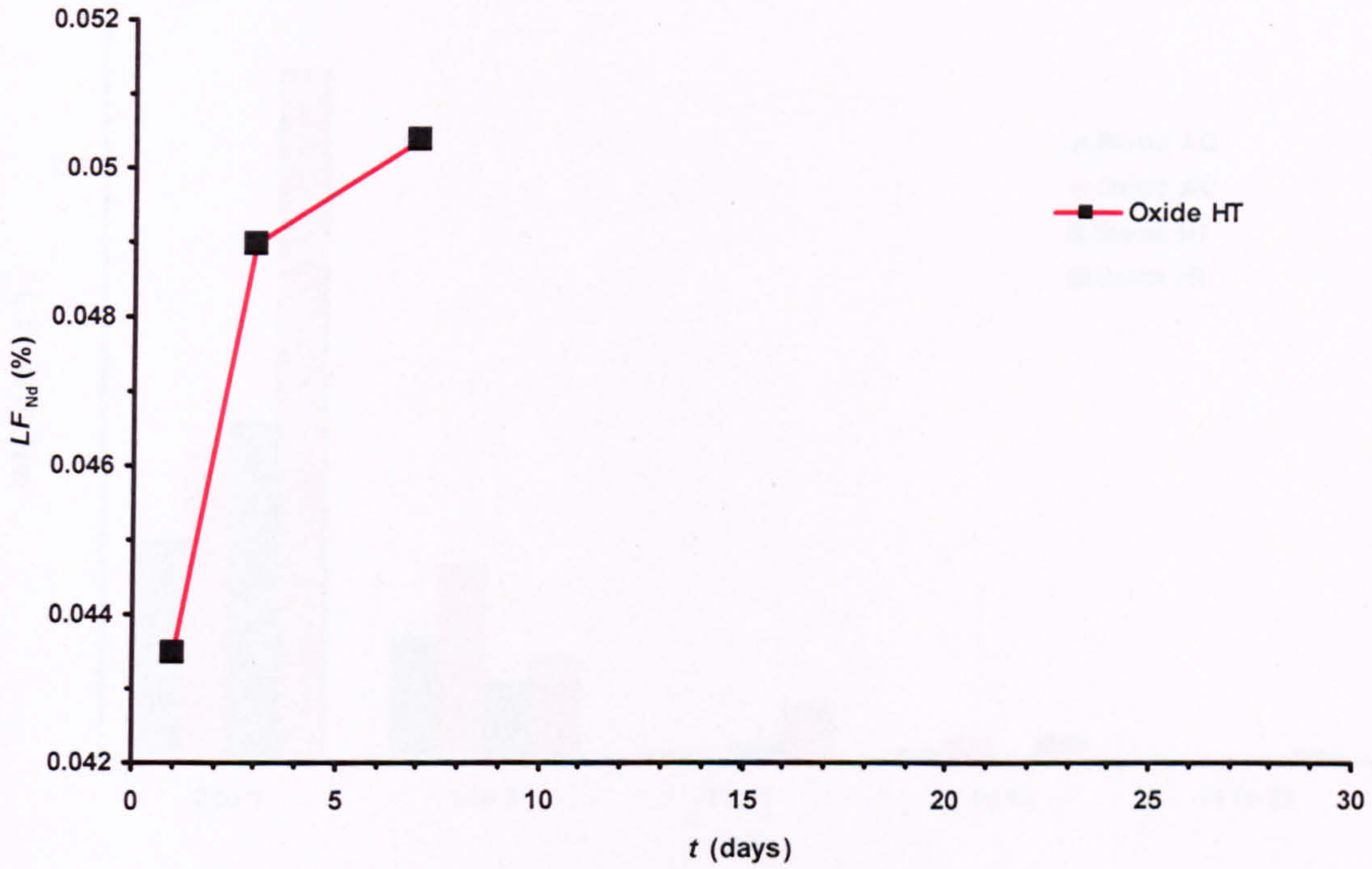


**Figure 4.3.1.18** $LF_{Nd}$ during modified PCT-B.

### *4.3.1.10 Silicon Leaching*

Generally, normalised silicon leach rates (**Figure 4.3.1.19**) decreased as the modified PCT-B progressed. Heat treatment of Blend glass does not affect its silicon leach rates significantly, but heat treatment of Oxide glass increased its silicon leach rates significantly. Silicon leached fractions during modified PCT-B (**Figure 4.3.1.20**) reveal that heat treatment of Blend glass lowered the fraction of silicon leached marginally, whilst heat treatment of Oxide glass increased it significantly.

For Blend AC and Oxide AC their normalised silicon leach rates were lower during the 3 to 7 d period than either the preceding or subsequent period. This is reflected in their silicon leached fractions at 7 d, which were similar to those at 3 d.

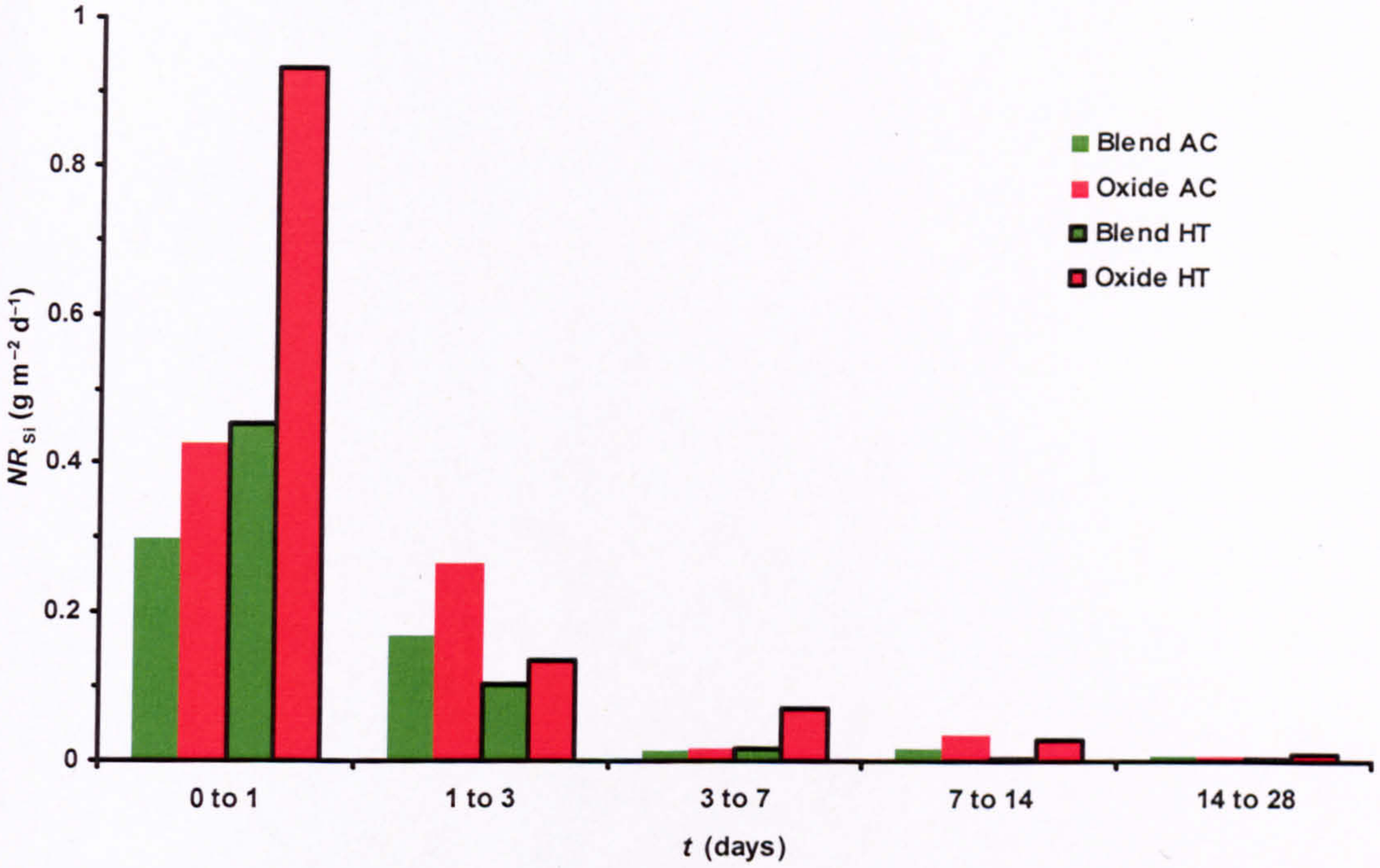


**Figure 4.3.1.19** $NR_{Si}$ during modified PCT-B.

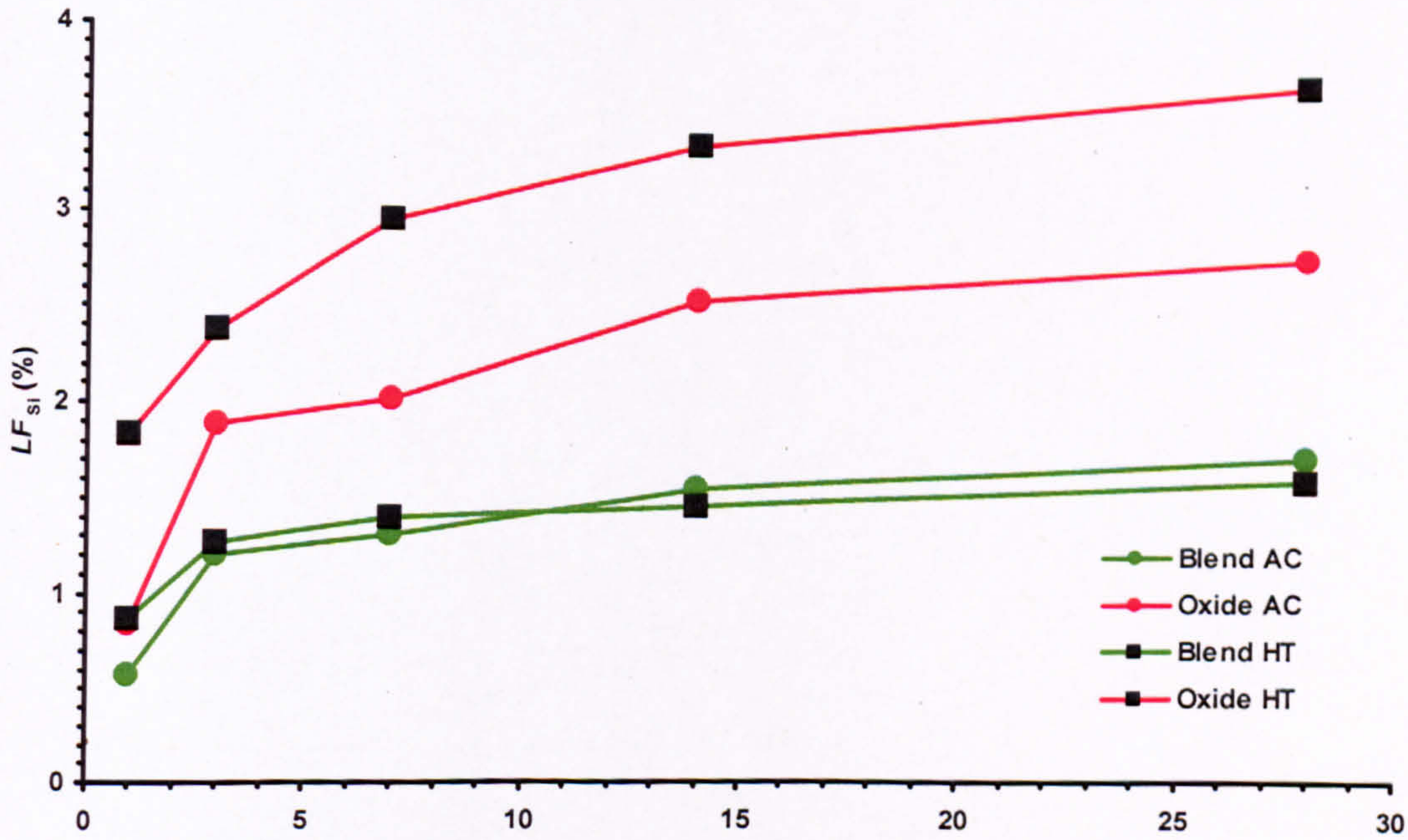


**Figure 4.3.1.20** $LF_{Si}$ during modified PCT-B.

*4.3.1.11 Strontium Leaching*

Generally, normalised strontium leach rates (**Figure 4.3.1.21**) decreased as the modified PCT-B progressed. Heat treatment of Blend glass does not affect its strontium leach rates significantly. Heat treatment of Oxide glass increased its strontium leach rates significantly. Strontium leached fractions during modified PCT-B (**Figure 4.3.1.22**) reveal that heat treatment of Blend glass lowered the fraction of strontium leached marginally, whilst heat treatment of Oxide glass increased it significantly.

For Oxide AC and Oxide HT their normalised strontium leach rates were negative (the concentration of Sr in their leachates decreased) for the 7 to 14 d period. This is reflected in their strontium leached fractions, which were lower at 14 d than at 7 d.

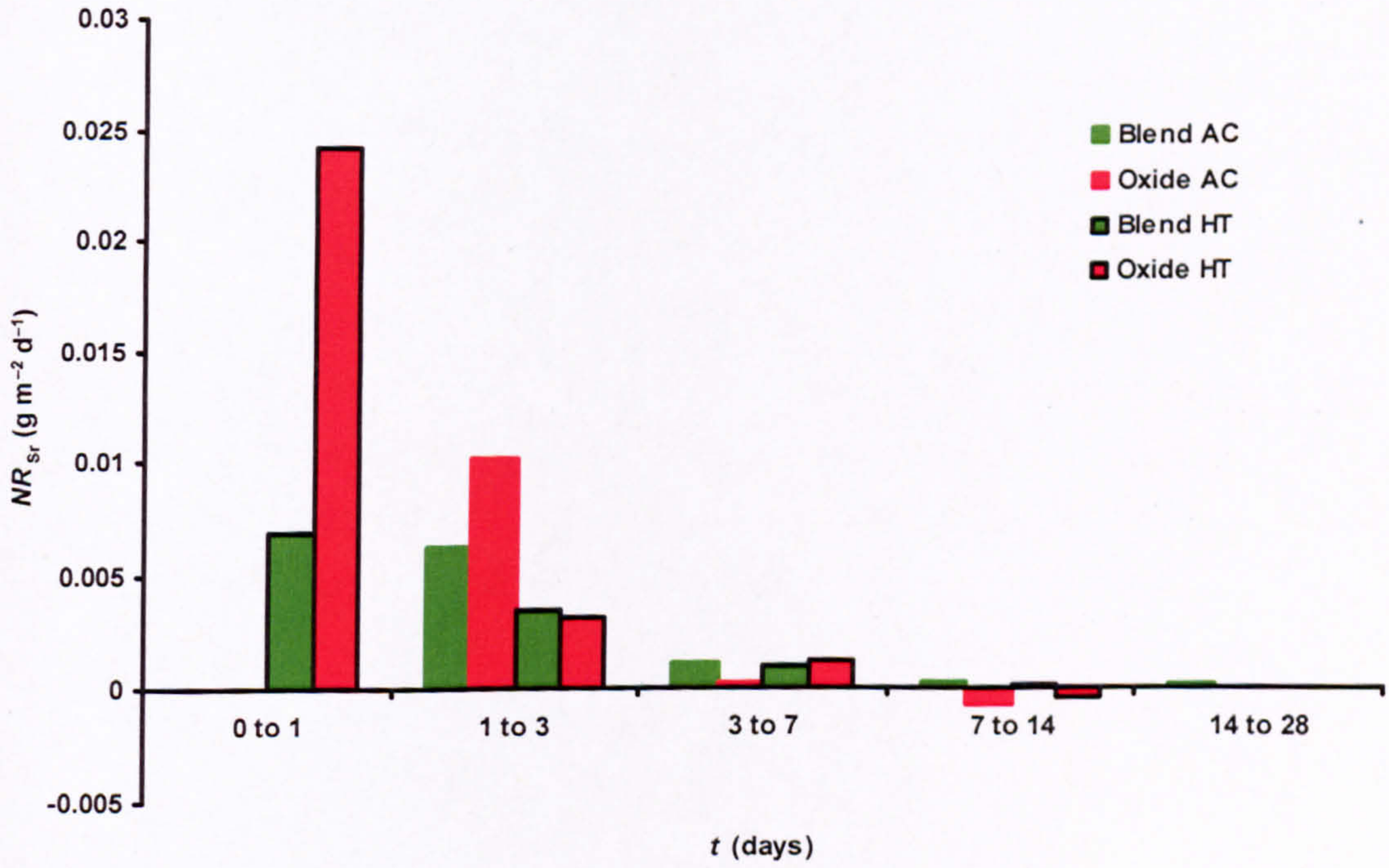


**Figure 4.3.1.21** $NR_{Sr}$ during modified PCT-B.

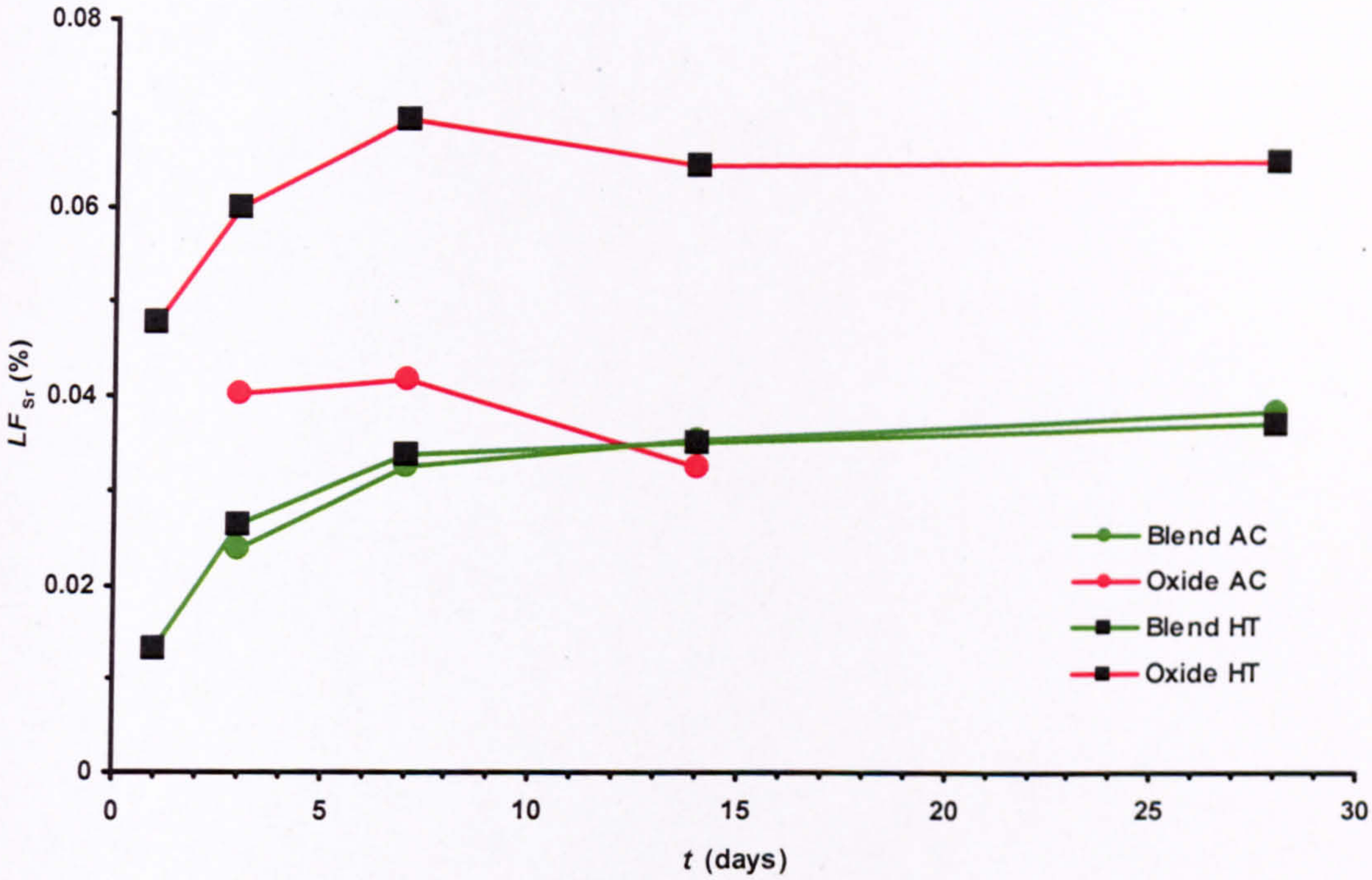


**Figure 4.3.1.22** $LF_{Sr}$ during modified PCT-B.

*4.3.1.12 Leachate pH*

Generally, leachate pH (**Figure 4.3.1.23**) increased as the modified PCT-B progressed. Heat treatment of Blend glass does not affect its leachate pH during modified PCT-B significantly. However, heat treatment of Oxide glass increases its leachate pH during modified PCT-B significantly.

For Blend AC, Oxide AC, Blend HT and Oxide HT their leachate pH values at 28 d were identical, if not lower, than at 14 d.

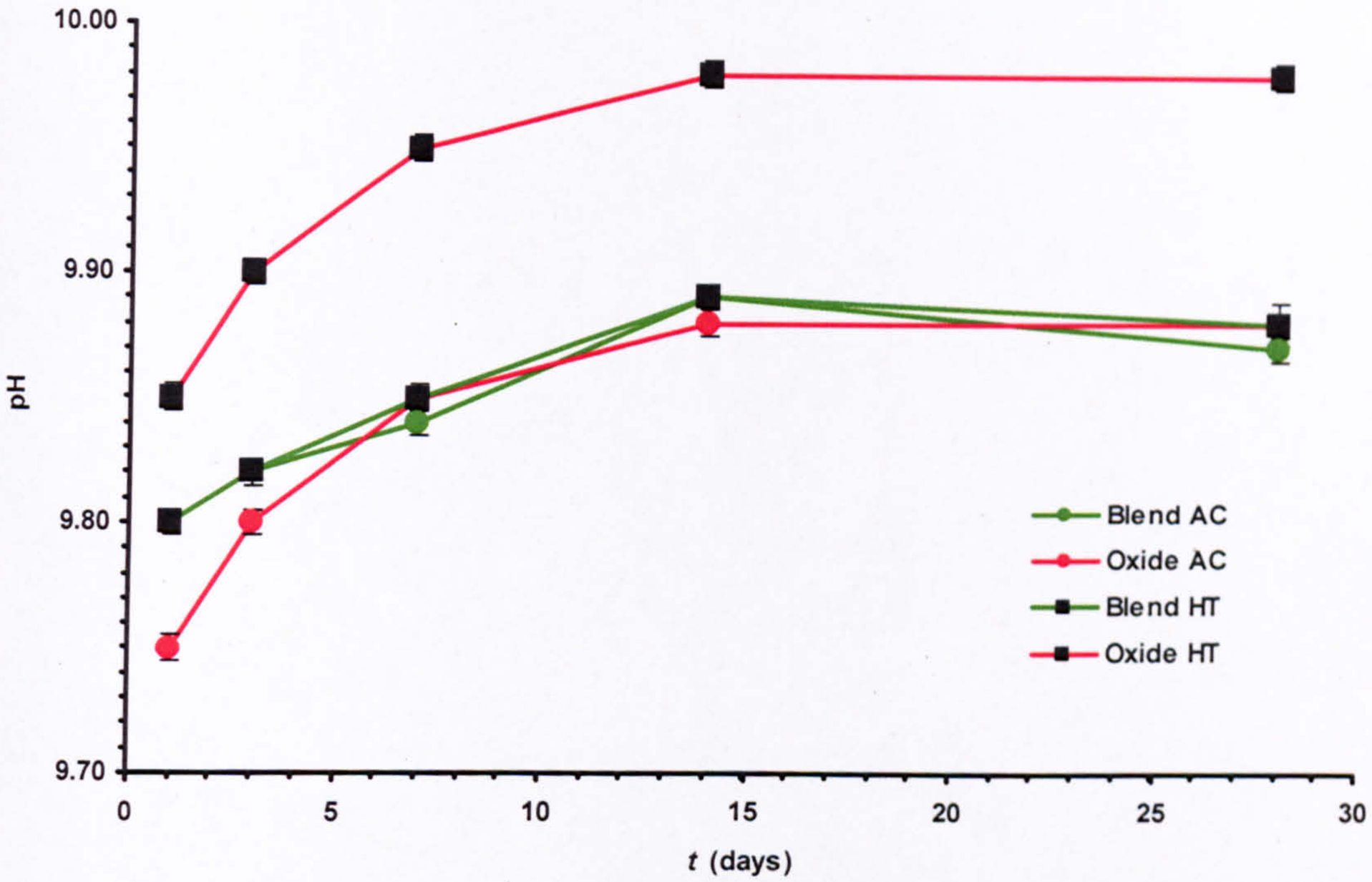


**Figure 4.3.1.23** Leachate pH (mean) during modified PCT-B (error bars indicate standard deviation ($1\sigma$)).

## 4.3.2 Leached Glass Analysis

### *4.3.2.1 As-Cast Blend Glass (Blend AC)*

Cross-sectional SEM of leached Blend AC (**Figure 4.3.2.1**) reveals an alteration (hydration) layer extending 4.5–8 $\mu$m into the glass. Acicular $RuO_2$ crystals (one of which is labelled × in **Figure 4.3.2.1**) have not dissolved during leaching.

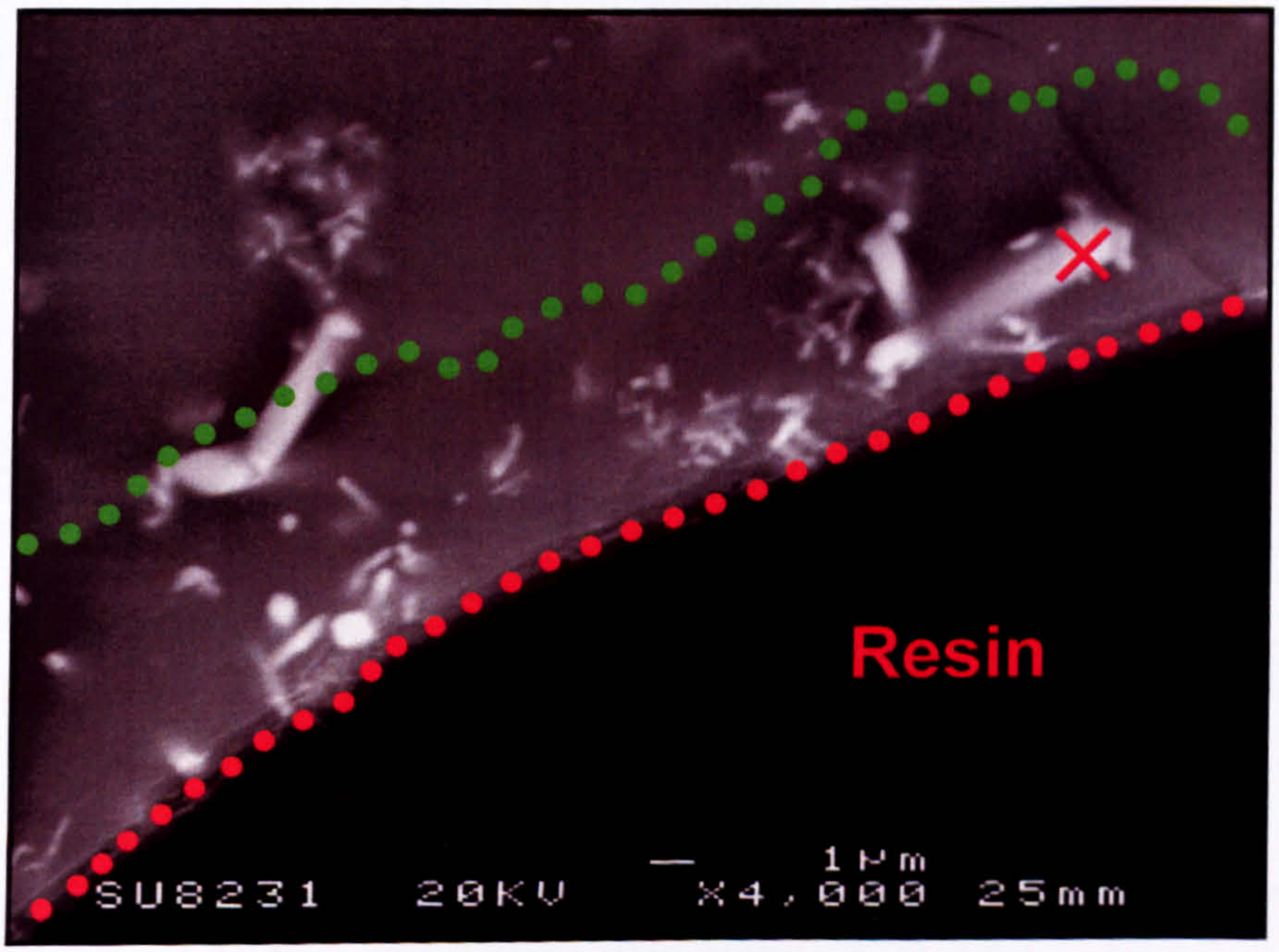


**Figure 4.3.2.1** Cross-sectional SE SEM image of a leached Blend AC 'powder' sample. Red dotted line indicates the sample surface; green dotted line indicates the visible extent of glass alteration (hydration).

*4.3.2.2 As-Cast Oxide Glass (Oxide AC)*

Cross-sectional SEM of leached Oxide AC (**Figure 4.3.2.2**) shows an alteration (hydration) layer extending 5–7.5 $\mu$m into the glass. The microstructure of these leached Oxide AC samples is Type I (**Section 4.2.2**). Acicular $RuO_2$ crystals (one of which is labelled × in **Figure 4.3.2.2**) and spheroidal metallic Pd-Te crystals (one of which is labelled + in **Figure 4.3.2.2**) have not dissolved during leaching.

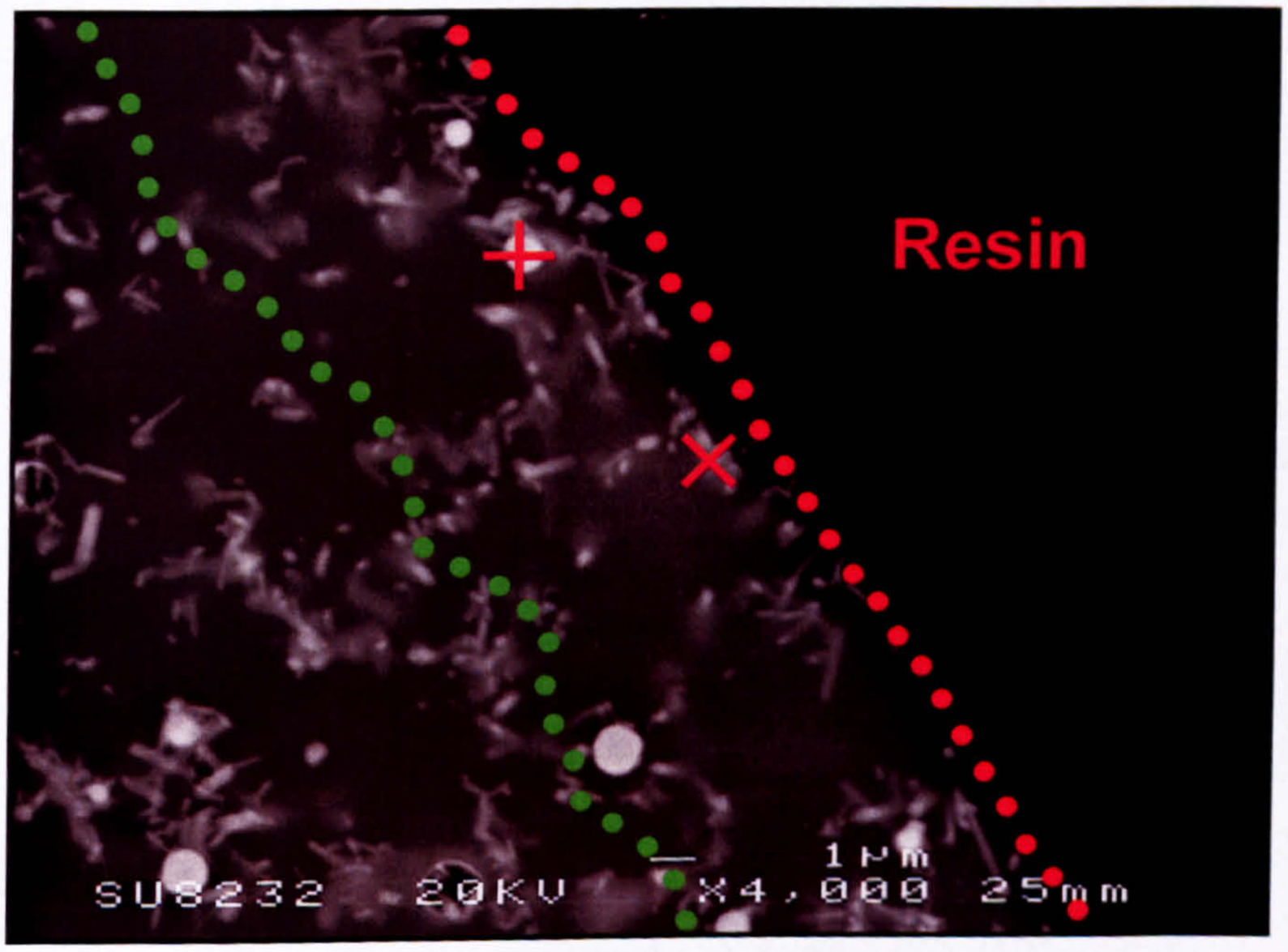


**Figure 4.3.2.2** Cross-sectional SE SEM image of a leached Oxide AC 'powder' sample with Type I microstructure. Red dotted line indicates the sample surface; green dotted line indicates the visible extent of glass alteration (hydration).

*4.3.2.3 Heat Treated Blend Glass (Blend HT)*

Cross-sectional SEM of leached Blend HT (**Figures 4.3.2.3**, **4.3.2.4** and **4.3.2.5**) reveal an alteration (hydration) layer extending 4.5–8.5 $\mu$m into the glass. Spheroidal $Ce_{1-(x+y)}Zr_xGd_yO_{2-(y/2)}$ crystals (one of which is labelled × in **Figure 4.3.2.3**) have not dissolved during leaching, but enhance glass alteration (hydration) around themselves. Dendritic (Sr,Nd,La) molybdate crystals (one of which is labelled × in **Figure 4.3.2.4**) have not dissolved during leaching. Facetted lanthanide (Nd,Gd,La,Ce) silicate crystals (one of which is labelled × in **Figure 4.3.2.5**) have not dissolved during leaching, but may enhance glass alteration around themselves (although this could be due to their proximity to spheroidal $Ce_{1-(x+y)}Zr_xGd_yO_{2-(y/2)}$ crystals in **Figure 4.3.2.5**).

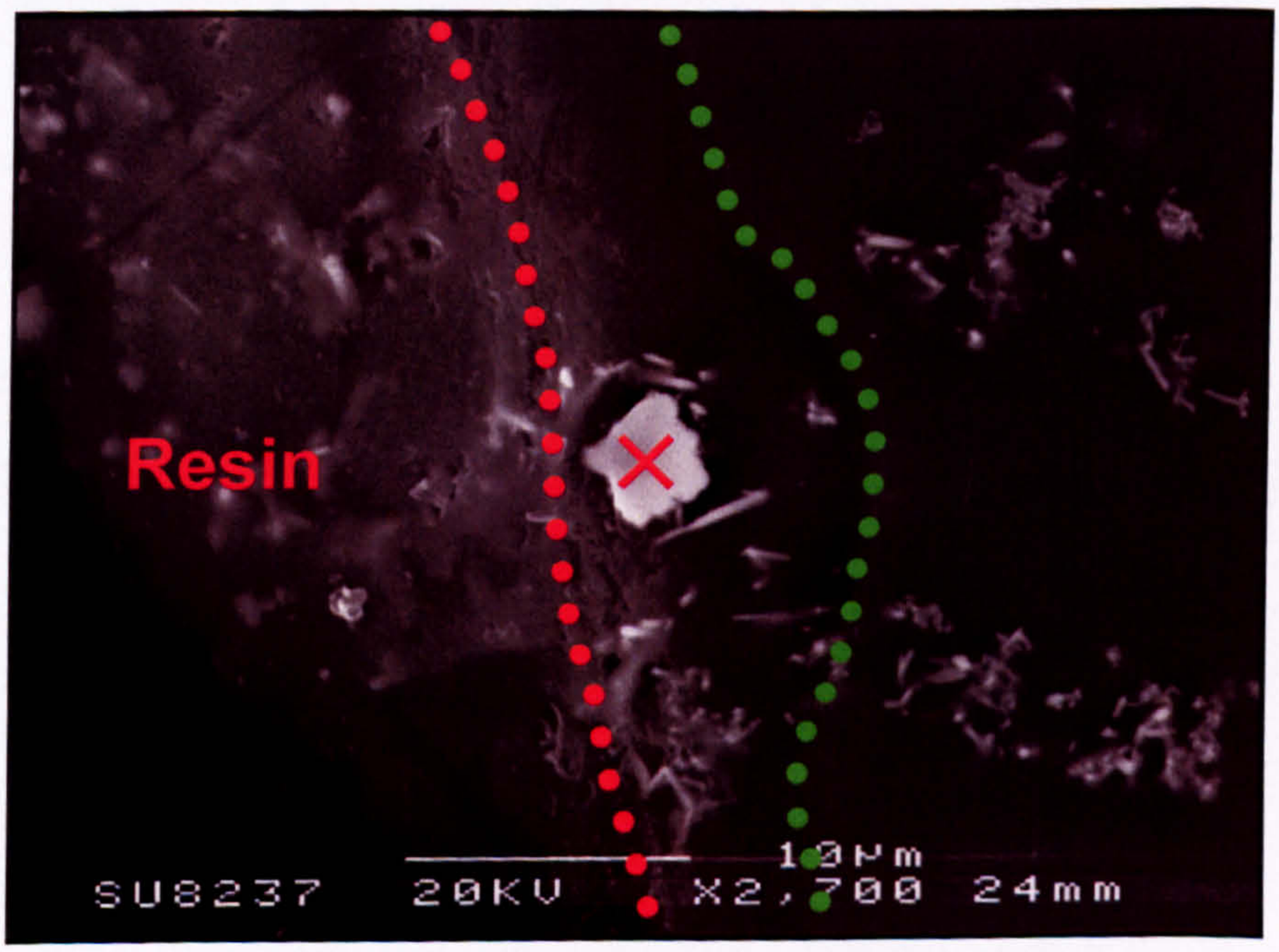


**Figure 4.3.2.3** Cross-sectional SE SEM image of a leached Blend HT 'powder' sample. Red dotted line indicates the sample surface; green dotted line indicates the visible extent of glass alteration (hydration).

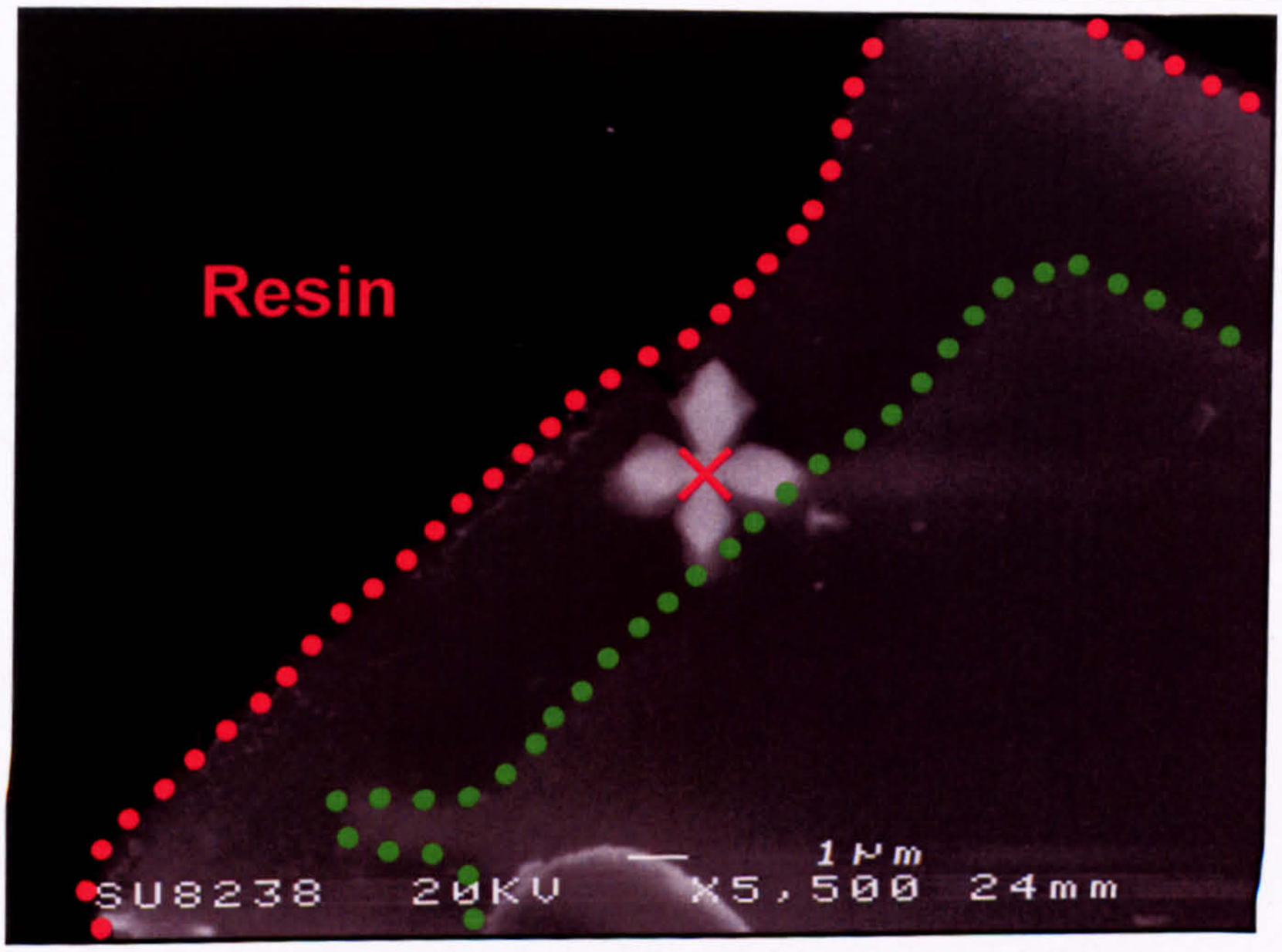


**Figure 4.3.2.4** Cross-sectional SE SEM image of a leached Blend HT 'powder' sample. Red dotted line indicates the sample surface; green dotted line indicates the visible extent of glass alteration (hydration).

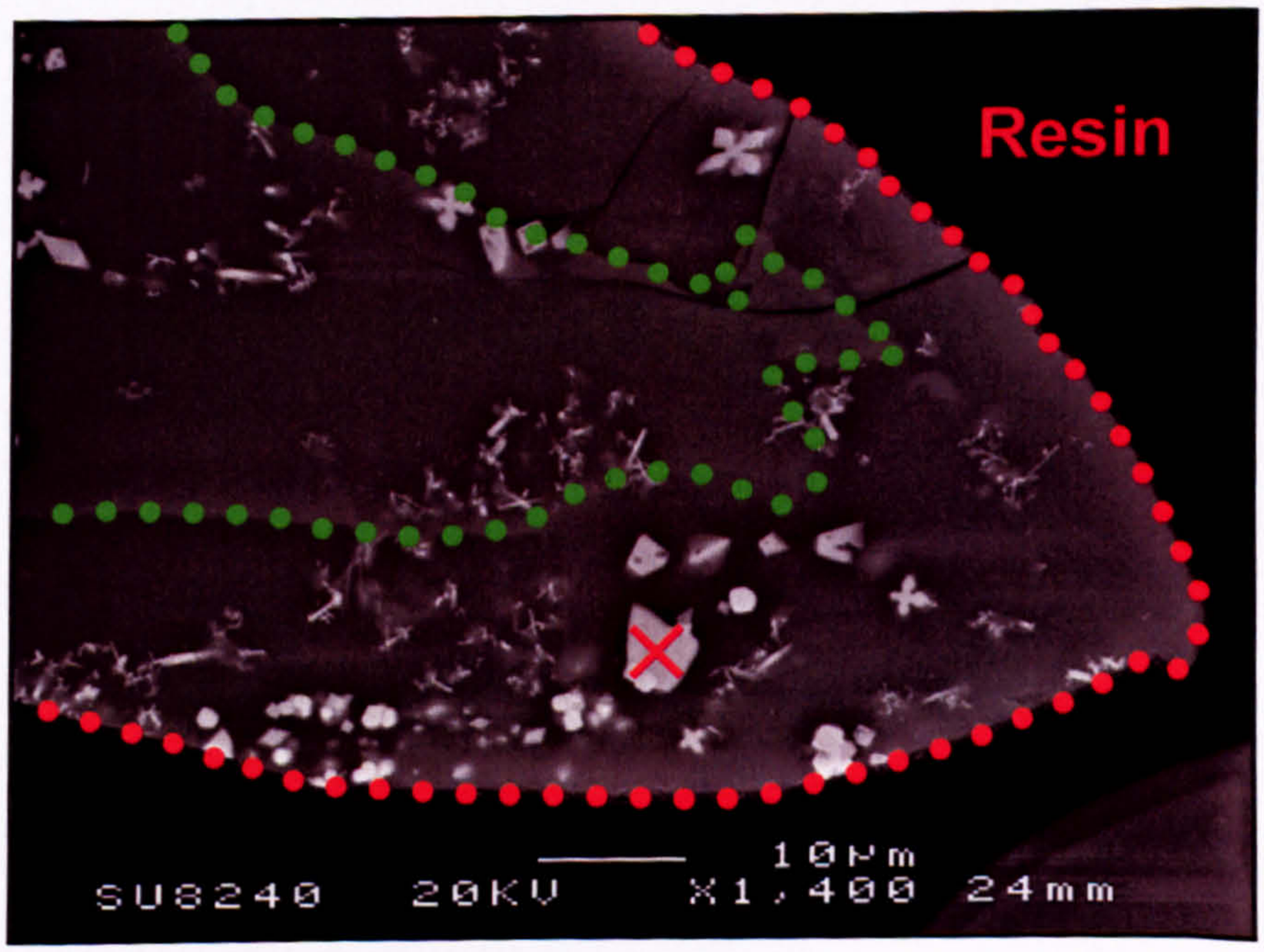


**Figure 4.3.2.5** Cross-sectional SE SEM image of a leached Blend HT 'powder' sample. Red dotted line indicates the sample surface; green dotted line indicates the visible extent of glass alteration (hydration).

*4.3.2.4 Heat Treated Oxide Glass (Oxide HT)*

Cross-sectional SEM of leached Oxide HT (**Figures 4.3.2.6**, **4.3.2.7** and **4.3.2.8**) reveal an alteration (hydration) layer extending 4.5–7 $\mu$m into the glass in some samples. The microstructure of these leached Oxide HT samples is Type A (**Section 4.2.4**). Dendritic $\alpha$-cristobalite crystals (one of which is labelled × in **Figure 4.3.2.6**) have not dissolved during leaching, but enhance glass alteration (hydration) around themselves (all of the surrounding glass has been hydrated). Dendritic (Na,Sr,Nd,La)$MoO_4$ crystals (one of which is labelled × in **Figure 4.3.2.7**) have not dissolved during leaching. Glass alteration (hydration) that was non-uniform in depth can be seen in **Figure 4.3.2.8**.

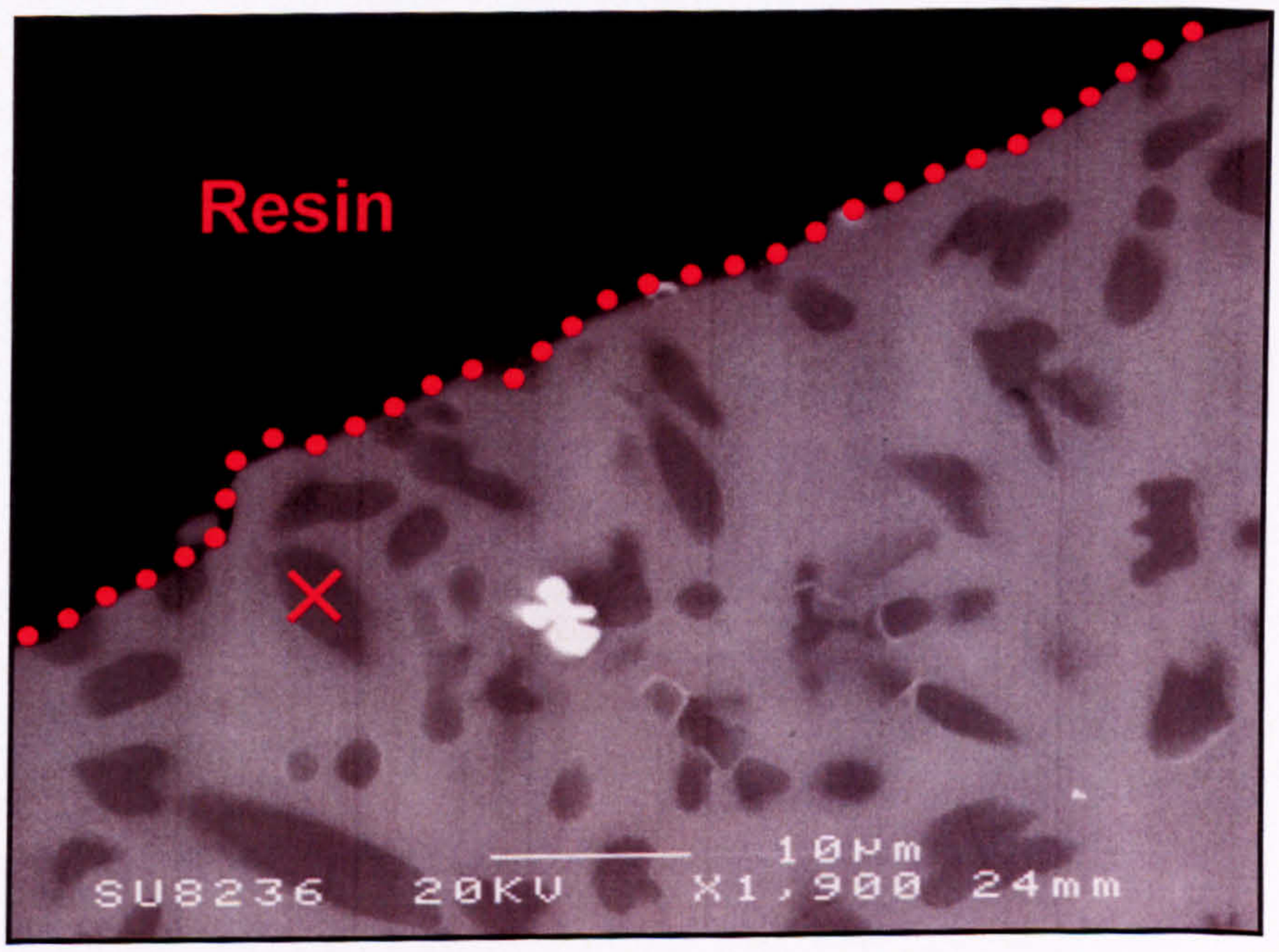


**Figure 4.3.2.6** Cross-sectional BE SEM image of a leached Oxide HT 'powder' sample with Type A microstructure. Red dotted line indicates the sample surface; no green dotted line as the glass is fully altered (hydrated).

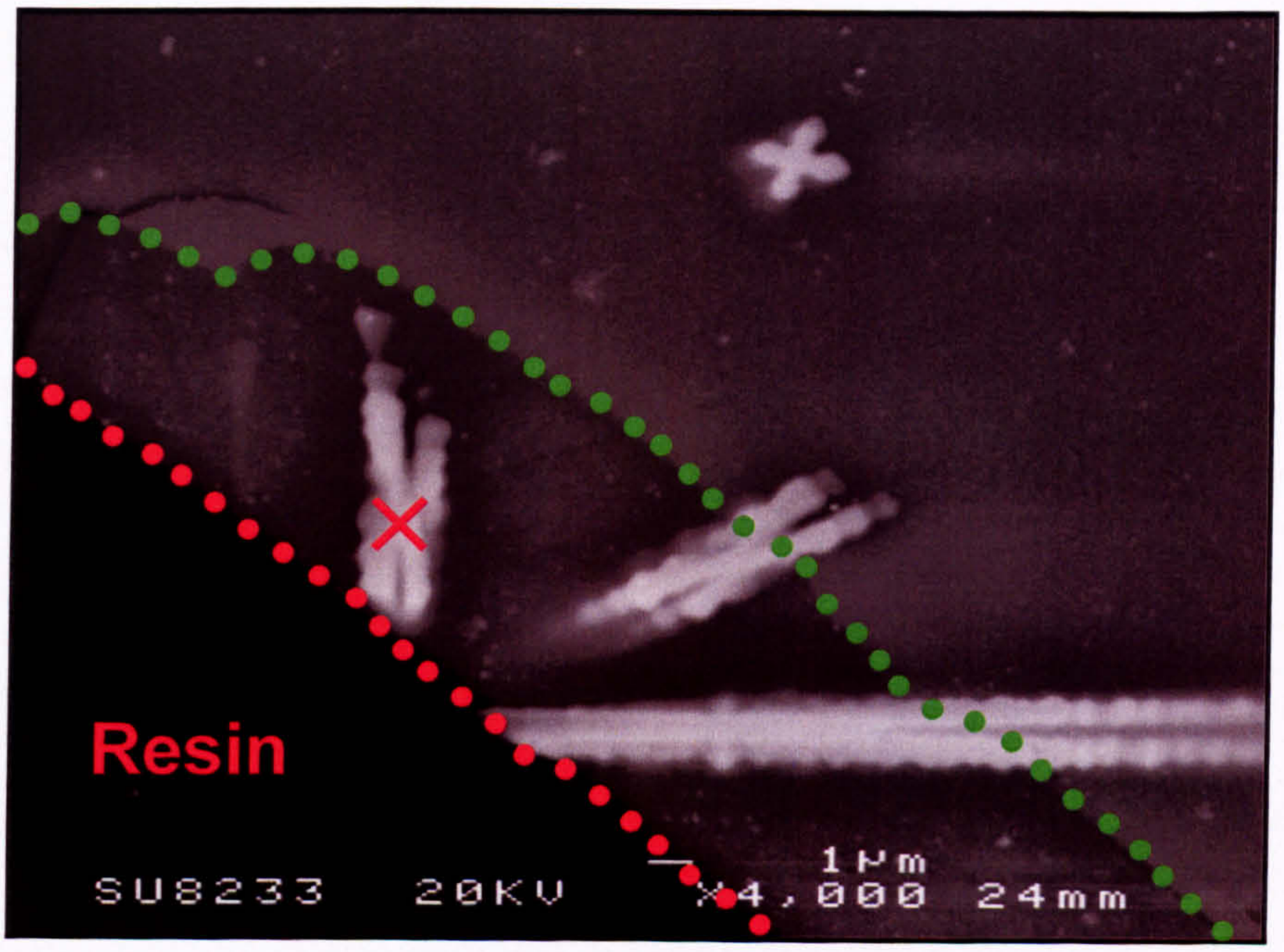


**Figure 4.3.2.7** Cross-sectional SE SEM image of a leached Oxide HT 'powder' sample with Type A microstructure. Red dotted line indicates the sample surface; green dotted line indicates the visible extent of glass alteration (hydration).

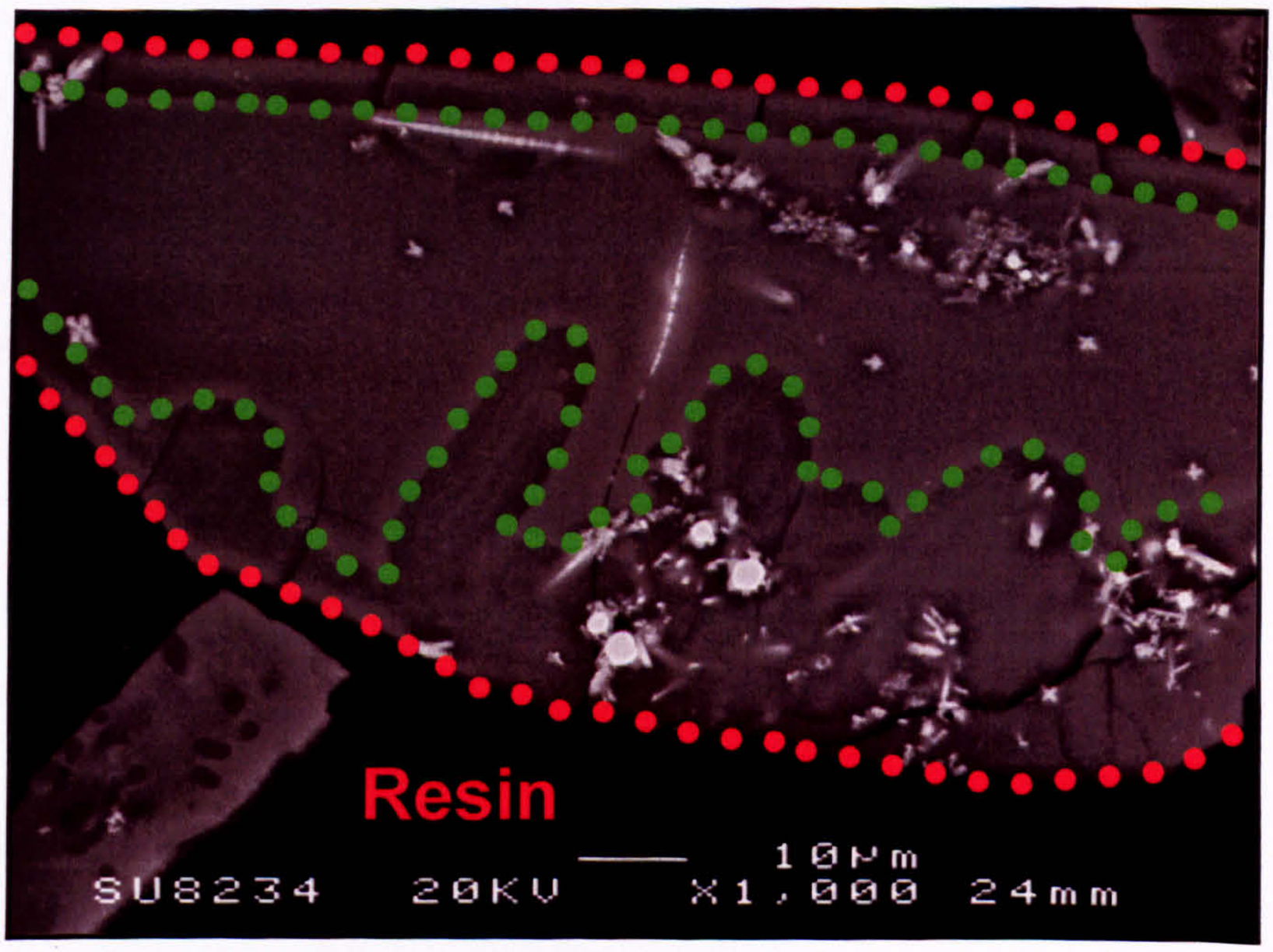


**Figure 4.3.2.8** Cross-sectional SE SEM image of a leached Oxide HT 'powder' sample with Type A microstructure. Red dotted line indicates the sample surface; green dotted line indicates the visible extent of glass alteration (hydration).

## 4.4 'Yellow Phase' Analysis

A sample of as-cast Oxide glass (Oxide AC) contained a 'yellow phase' inclusion, shown in **Figure 4.4.1**.

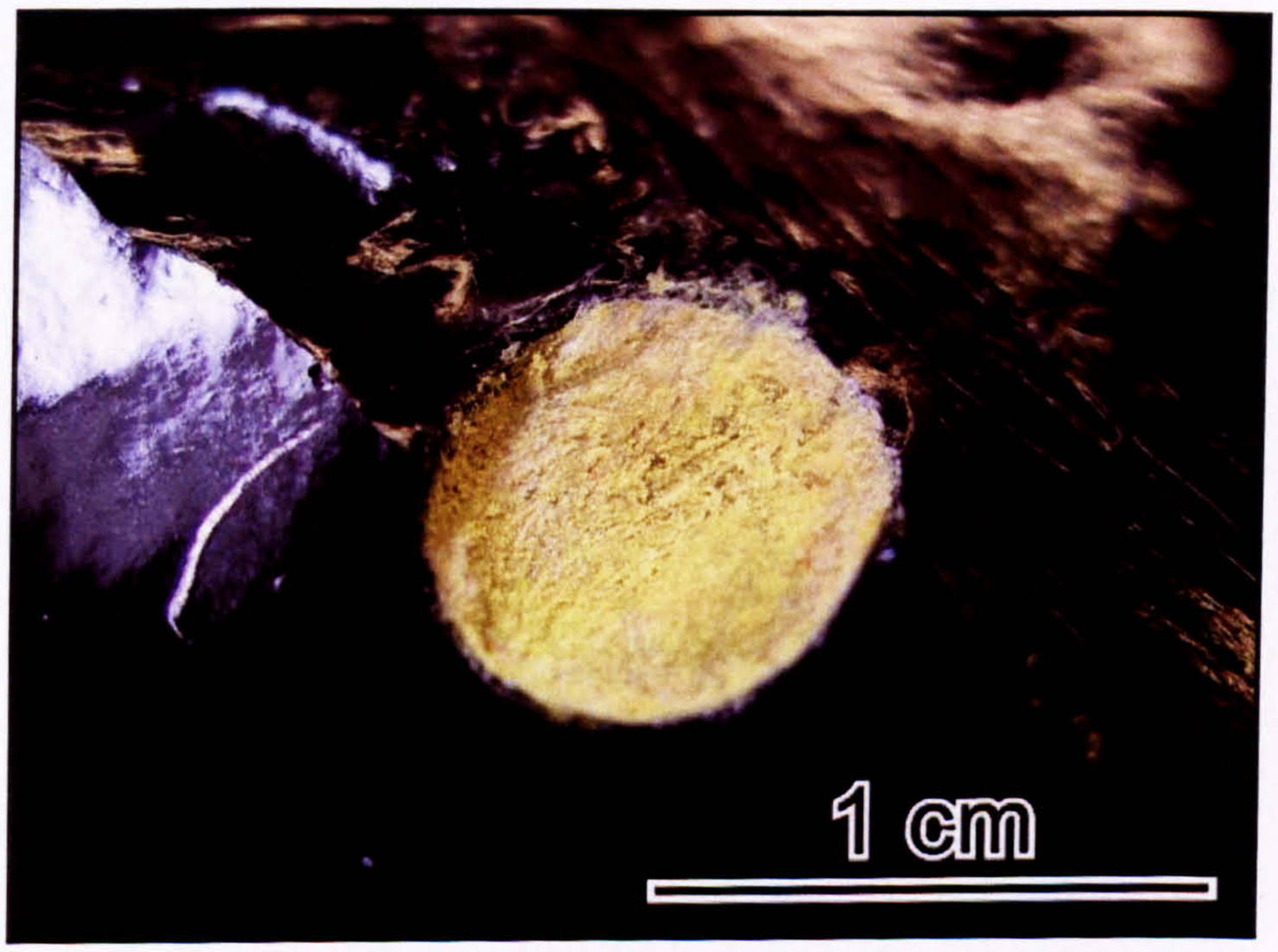


**Figure 4.4.1** Image of the 'yellow phase' inclusion in an Oxide AC sample.

**Table 4.4.1** gives the chemical composition of the 'yellow phase' inclusion.

**Table 4.4.1** Chemical composition of the 'yellow phase' inclusion in an Oxide AC sample.

| Component | Weight % | Molar % |
|---|---|---|
| $MoO_3$ | 55.4 | 46.2 |
| $Cs_2O$ | 19.9 | 8.5 |
| $Na_2O$ | 7.6 | 14.8 |
| $Li_2O$ | 4.5 | 17.9 |
| $Cr_2O_3$ | 3.8 | 3.0 |
| BaO | 1.9 | 1.5 |
| SrO | 1.5 | 1.7 |
| $TeO_2$ | 1.0 | 0.7 |
| $Nd_2O_3$ | 0.8 | 0.3 |
| Others | 4.0 | 5.4 |
| **Total** | **100.4** | **100.0** |

Relative to Oxide glass (**Table 4.1.1**), the 'yellow phase' inclusion is enriched in Mo, Cs, Na, Li, Cr, Ba, Sr and Te, but depleted in Nd and other major glass components.

An XRD trace of the 'yellow phase' inclusion (**Figure 4.4.2**) reveals it to be crystalline, with peak matches for cubic $CsLiMoO_4$ (labelled ❍; ICDD card [38-1238]),

rhombohedral $Na_3Li(MoO_4)_2 \cdot 6H_2O$ (labelled ▼; ICDD card [30-769]), tetragonal $AgCeMo_2O_8$ (labelled ■; ICDD card [49-381]) as well as other unidentified peaks – two of which are labelled in red and have *d*-spacings (Å) of 3.34 and 2.77.

The cubic $CsLiMoO_4$ crystal phase identified by XRD (**Figure 4.4.2**) has the space group $F\bar{4}3m$. The rhombohedral $Na_3Li(MoO_4)_2 \cdot 6H_2O$ crystal phase identified by XRD (**Figure 4.4.2**) has the space group $R\bar{3}c$ and was hydrated by atmospheric $H_2O$. The tetragonal $AgCeMo_2O_8$ crystal phase peak matched using XRD (**Figure 4.4.2**) is powellite (space group $I4_1/a$). This crystal phase is not present in the 'yellow phase' inclusion (as neither Ag nor Ce are present at significant levels in the 'yellow phase', as can be seen in **Table 4.4.1**; and Ag is not present in Oxide glass, as can be seen in **Table 4.1.1**); rather, a powellite crystal phase with matching lattice parameters but different chemical composition is present. Comparison of the $AgCeMo_2O_8$ XRD pattern with data from Short (2004) and the chemical composition of the 'yellow phase' inclusion (**Table 4.4.1**) indicates that the powellite crystal phase was of the composition $(Na,Sr,Nd)MoO_4$ (**Table 4.4.2**).

**Table 4.4.2** Comparison of observed powellite with likely powellites from the literature.

| Phase | *d*-spacing of (112) plane (Å) | Reference/ ICDD card |
|---|---|---|
| $SrMoO_4$ | 3.22 | (Short, 2004) |
| $Na_{0.25}Sr_{0.5}Nd_{0.25}MoO_4$ | 3.18 | (Short, 2004) |
| $Na_{0.5}Nd_{0.5}MoO_4$ | 3.14 | (Short, 2004) |
| Observed | 3.17 | This work |
| $AgCeMo_2O_8$ | 3.17 | [49-381] |
| $Ag_{0.5}Ce_{0.5}MoO_4$ | 3.17 | (Short, 2004) |

The two XRD peaks labelled in red (**Figure 4.4.2**) are indicative of another powellite crystal phase. Using the chemical composition of the 'yellow phase' inclusion (**Table 4.4.1**) and combining this with published data (**Table 4.4.3**) indicates the presence of a powellite crystal phase of composition $Ba_{1-x}Sr_xMoO_4$ (where $0 < x < 0.5$).

**Table 4.4.3** Comparison of observed powellite with likely powellites from the literature.

| Phase | *d*-spacing of (*hkl*) plane (Å) | | Reference/ ICDD card |
|---|---|---|---|
| | (112) | (200) | |
| $BaMoO_4$ | 3.36 | 2.79 | [29-193] |
| $(Ba_{0.5}Sr_{0.5})MoO_4$ | 3.31 | 2.74 | [30-157] |
| Observed | 3.34 | 2.77 | This work |

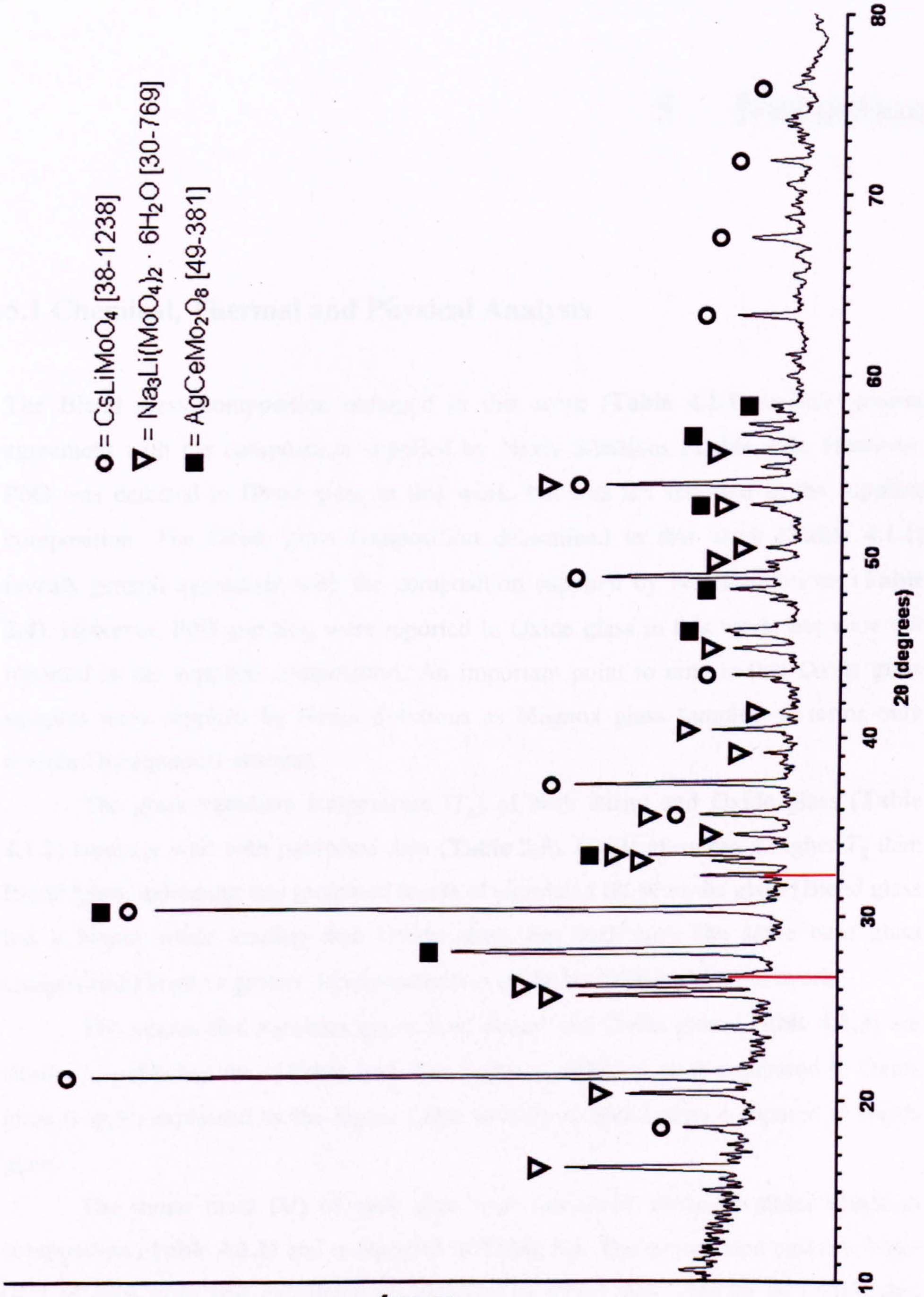


**Figure 4.4.2** XRD trace from the 'yellow phase' inclusion in an Oxide AC sample, illustrating its crystallinity. Two unidentified peaks have been labelled in red and have *d*-spacings (Å) of 3.34 and 2.77.

# 5 Discussion

## 5.1 Chemical, Thermal and Physical Analysis

The Blend glass composition obtained in this work (**Table 4.1.1**) reveals general agreement with the composition supplied by Nexia Solutions (**Table 2.4**). However, PbO was detected in Blend glass in this work, but was not reported in the supplied composition. The Oxide glass composition determined in this work (**Table 4.1.1**) reveals general agreement with the composition supplied by Nexia Solutions (**Table 2.4**). However, PdO and $SO_3$ were reported in Oxide glass in this work, but were not reported in the supplied composition. An important point to note is that Oxide glass samples were supplied by Nexia Solutions as Magnox glass samples, an error only revealed by chemical analysis.

The glass transition temperature ($T_g$) of both Blend and Oxide glass (**Table 4.1.2**) compare well with published data (**Table 2.5**). Oxide glass has a higher $T_g$ than Blend glass, indicating that increased levels of simulated HLW in the glass (Blend glass has a higher waste loading than Oxide glass, but both have the same base glass composition) leads to greater depolymerisation of the borosilicate glass network.

The unannealed densities ($\rho$) of both Blend and Oxide glass (**Table 4.1.3**) are similar to published data (**Table 2.5**). The higher $\rho$ of Blend glass compared to Oxide glass is again explained by the higher waste loading of Blend glass compared to Oxide glass.

The molar mass ($M$) of each glass was calculated using its molar chemical composition (**Table 4.1.1**) and is reported in **Table 5.1**. The unannealed molar volume ($V_m$) of each glass was calculated by dividing its molar mass ($M$) by its unannealed density ($\rho$) and is reported in **Table 5.1**.

**Table 5.1** Molar mass ($M$) and molar volume ($V_m$) of both glasses.

| Glass | Blend | Oxide |
|---|---|---|
| $M$ (g mol$^{-1}$) | 70.56 | 68.29 |
| $V_m$ (cm$^3$ mol$^{-1}$) | 25.02 | 25.01 |

Although not reported in **Chapter 4**, it should be noted that both Blend and Oxide glass displayed non-Newtonian viscosity behaviour (apparent viscosity decreases with increasing shear rate). This is thought to be caused by the presence of platinoid phases in both glasses, as has been previously observed (F. Bart *et al.*, 2001; Kawamura and Ohuchi, 1995; Krause and Luckscheiter, 1991).

## 5.2 Phase and Microstructural Analysis

### 5.2.1.1 As-Cast Blend Glass (Blend AC)

The glass matrices of as-cast Blend glass samples are compositionally homogeneous **(Section 4.2.1)**, indicating sufficient reaction time in the glass melter before pouring **(Section 2.6.2)**. $RuO_2$ crystals (rutile structure) found in the glass **(Section 4.2.1.1)** had acicular morphologies, a morphology which has been reported for $RuO_2$ in other borosilicate HLW glasses (F. Bart *et al.*, 2001; Galoisy *et al.*, 1998; Larkin, 1986; Mitamura *et al.*, 1985; Roth and Weisenburger, 2000; Simonnet and Grandjean, 2005). $RuO_2$ can incorporate Rh if it is present in the borosilicate HLW glass, forming $(Ru,Rh)O_2$ **(Table 2.8)**. The unusual 'sponge-like' agglomeration could be either $RuO_2$ or metallic Ru, we cannot tell. This $RuO_2$/metallic Ru agglomeration will settle quickly in a borosilicate HLW glass melter due to its large size (Sundaram and Perez, 2000), likely forming a 'sludge' layer at the bottom of the melter **(Section 2.6.1)**. $RuO_2$ will be present in 'real' (radioactive) borosilicate HLW glasses (Cheron *et al.*, 1995) and will act as nuclei for further crystallisation during the slow (retarded) cool of these glasses (Bickford and Jantzen, 1984; Buechele *et al.*, 1990; Izak *et al.*, 2001; Jantzen *et al.*, 1984; D.-S. Kim *et al.*, 1994; Mitamura *et al.*, 1985). The presence of platinoids (such as $RuO_2$) has been reported to have negligible (F. Bart *et al.*, 2001), if not a positive (Pacaud *et al.*, 1992), effect on the aqueous durability of borosilicate HLW glasses.

### 5.2.1.2 Heat Treated Blend Glass (Blend HT)

In heat treated Blend glass samples **(Section 4.2.3)**, $Ce_{1-(x+y)}Zr_xGd_yO_{2-(y/2)}$ crystals (defect fluorite structure) found in the glass **(Section 4.2.3.1)** were similar to previously reported phases **(Section 2.8.6)**. They can incorporate long-lived Pu and U **(Table 2.27)**, indicating $Ce_{1-(x+y)}Zr_xGd_yO_{2-(y/2)}$ is a potential actinide host. Phases similar to $Ce_{1-(x+y)}Zr_xGd_yO_{2-(y/2)}$ have been observed in 'real' borosilicate HLW glasses (Cheron

*et al.*, 1995) due to their radiation tolerance (Sickafus *et al.*, 2000). $Ce_{1-(x+y)}Zr_xGd_yO_{2-(y/2)}$ is a chemically-durable phase (Abdelouas *et al.*, 1997), so will be a good actinide host.

(Sr,Nd,La) molybdate crystals (powellite structure suspected) observed in the glass (**Section 4.2.3.2**) are expected to have the powellite crystal structure due to their morphological and compositional similarity to dendritic $(Na,Sr,Nd,La)MoO_4$ crystals (powellite structure) found in heat treated Oxide glass samples (**Section 4.2.4.2**). This implies Na (and possibly Li) is incorporated in the crystals. (Sr,Nd,La) molybdate was observed to nucleate and grow on $RuO_2$ crystals, and is a potential host for long-lived Am and Cm (Abdelouas *et al.*, 1997) due to their being in the +3 valence state in borosilicate HLW glasses (Caurant *et al.*, 2006 and references therein) and their similar ionic radii to Nd (Shannon, 1976). If, as suspected, this phase has the powellite crystal structure, it will be insoluble in water (Komarneni *et al.*, 1983; Schiewer *et al.*, 1982), making it a good host for short-lived $^{90}Sr$, as well as long-lived Am and Cm (if incorporated in the crystals). As well as reducing the leach rates of elements which are incorporated in powellite crystals (Mitamura *et al.*, 1986), the aqueous durability of the overall wasteform is improved slightly by their formation (F. Bart *et al.*, 2001). The stability of powellite crystals to radiation is demonstrated by their presence in 'real' borosilicate HLW glasses (Cheron *et al.*, 1995).

Lanthanide (Nd,Gd,La,Ce) silicate crystals (unidentified structure) are noted in the glass (**Section 4.2.3.3**). When consulting the literature, these crystals appeared most likely to be silicate apatite (**Section 2.8.4.6**) or stillwellite (**Section 2.8.4.7**). However, their morphological and compositional similarity to a crystal phase formed in heat treated Oxide glass which could not be matched to either of these crystal phases by XRD or TEM (using electron diffraction) (**Section 4.2.4.5**) indicates a different crystal phase. Lanthanide (Nd,Gd,La,Ce) silicate crystals are a potential host for long-lived Am and Cm due to their +3 valence state in borosilicate HLW glasses (Caurant *et al.*, 2006 and references therein) and similar ionic radii to the incorporated lanthanides (Shannon, 1976).

### 5.2.2.1 As-Cast Oxide Glass (Oxide AC)

As-cast Oxide glass samples had one of two microstructures (**Section 4.2.2**): (1) Type I microstructure had a compositionally homogeneous glass matrix; whereas (2) Type II microstructure had a compositionally inhomogeneous glass matrix and displayed

compositional 'banding', dissolving/relict calcine, matrix cracking and bubbles. Glass samples with Type I and Type II microstructures will not be from the same batch.

Type I microstructure indicates the glass samples had sufficient reaction time in the glass melter between the base glass frit and the calcine before pouring, forming a homogeneous glass **(Section 2.6.2)**.

Type II microstructure indicates that the glass frit and calcine had insufficient reaction time in the glass melter before pouring, <1 h – indicated by the dissolving/relict calcine particles/granules and bubbles (Bouchet *et al.*, 2000; Larkin, 1986; Morgan, 2005), and has not been sufficiently homogenised (indicated by compositional 'banding') (Abraitis, 1999; Morgan, 2005). The aqueous durability of the wasteform will be detrimentally affected by this compositional 'banding'; the 'bands' enriched in simulated HLW components being of lower aqueous durability than the 'bands' enriched in base glass (Abraitis, 1999). The internal microstructure of the dissolving/relict calcine consists of two crystal phases, $Zr_{1-(x+y)}Ce_xGd_yO_{2-(y/2)}$ (defect fluorite structure) and lanthanide (Nd,Gd,La,Ce) silicate (unidentified structure). These crystal phases precipitated upon cooling of the glass due to local supersaturation of their component elements in the glass (Bouchet *et al.*, 2000). Dissolving/relict calcine in borosilicate HLW glasses are preferentially leached, lowering the overall aqueous durability of the wasteform (Raman *et al.*, 2003).

$RuO_2$ crystals (rutile structure) present in the glass **(Section 4.2.2.1)** had acicular morphologies, a morphology commonly noted in other borosilicate HLW glasses (F. Bart *et al.*, 2001; Galoisy *et al.*, 1998; Larkin, 1986; Mitamura *et al.*, 1985; Roth and Weisenburger, 2000; Simonnet and Grandjean, 2005). $RuO_2$ can incorporate Rh if it is present in the borosilicate HLW glass, forming $(Ru,Rh)O_2$ **(Table 2.8)**. Cracks in the glass matrix were noted to radiate from a large $RuO_2$ crystal, although it is unknown whether these arose: during sample preparation or due to thermal expansion coefficient (TEC) mismatch between the $RuO_2$ crystal and the borosilicate glass matrix. The latter option seems most likely when comparing $RuO_2$ thermal expansion coefficients **(Table 5.2)** to borosilicate HLW glass thermal expansion coefficients **(Section 2.4.2)**.

**Table 5.2** Mean linear ($\alpha$) and volumetric ($\beta$) thermal expansion coefficients for $RuO_2$ in the stated temperature ranges. Calculated using data from Rao and Iyengar (1969).

| Temperature range (°C) | $\alpha$ ($\times 10^{-6}$ $K^{-1}$) | $\beta$ ($\times 10^{-6}$ $K^{-1}$) |
|---|---|---|
| 30–361 | *a*-axis = 9.7<br>*c*-axis = –2.6 | 16.8 |
| 361–608 | *a*-axis = 13.0<br>*c*-axis = –3.8 | 22.3 |

A Ru-rich phase with globular morphology was initially thought to be $RuO_2$. However, the morphology suggests the phase is metallic Ru, which can develop in borosilicate HLW glasses due to reducing melt conditions (Bickford and Jantzen, 1986) or prolonged heating (Krause and Luckscheiter, 1991). The large $RuO_2$ crystal will settle more quickly in a borosilicate HLW glass melter due to its large size (Sundaram and Perez, 2000), likely contributing to a 'sludge' layer at the bottom of the melter (**Section 2.6.1**). $RuO_2$ will form in 'real' borosilicate HLW glasses (Cheron *et al.*, 1995) and will act as nuclei for further crystallisation during the slow (retarded) cool of these 'real' borosilicate HLW glass (Bickford and Jantzen, 1984; Buechele *et al.*, 1990; Izak *et al.*, 2001; Jantzen *et al.*, 1984; D.-S. Kim *et al.*, 1994; Mitamura *et al.*, 1985). The presence of platinoids (such as $RuO_2$) has been noted to have negligible (F. Bart *et al.*, 2001), if not a positive (Pacaud *et al.*, 1992), effect on the aqueous durability of borosilicate HLW glasses. $RuO_2$ was observed in both Type I and Type II microstructures.

Metallic Pd-Te crystals (fcc structure) noted in the glass (**Section 4.2.2.2**) generally had spheroidal morphologies. Metallic Pd-Te with similar morphologies have been described elsewhere (Galoisy *et al.*, 1998; Mendel *et al.*, 1976). As XRD revealed cubic Pd to be present; some, if not all of the metallic Pd-Te crystals will have the fcc structure, indicating the Te content is ≤16.3 at% (Galoisy *et al.*, 1998). Also, as Pd and Rh form a complete solid solution above 910 °C (Okamoto, 1994), metallic Pd-Te would incorporate Rh if it is present in the borosilicate HLW glass. Because Te and Se have similar chemistries (both are from Group 16 in the Periodic Table), long-lived $^{79}Se$ could be incorporated into this phase, as has been previously reported (Sundaram and Perez, 2000). Metallic Pd-Te is an effective nucleating agent (Lutze, 1988; Mitamura *et al.*, 1985) and forms in 'real' borosilicate HLW glasses (Cheron *et al.*, 1995). Platinoids (such as metallic Pd-Te) can have negligible (F. Bart *et al.*, 2001), or even a positive (Pacaud *et al.*, 1992), effect on the aqueous durability of borosilicate HLW glasses. Metallic Pd-Te is noted in both Type I and Type II microstructures.

$(Cr,Fe,Ni)_3O_4$ crystals (spinel structure) observed in this glass (**Section 4.2.2.3**) were noted to contain the element Ru, as has been observed in natural spinels (Capobianco and Drake, 1990). Similar phases have been reported in other borosilicate HLW glasses (**Table 2.19**). A 'swarm' of these crystals is noted in the Type II microstructure, these will settle quickly in a borosilicate HLW glass melter (Sundaram and Perez, 2000); likely forming a 'sludge' layer (**Section 2.6.1**). The formation of this phase in borosilicate HLW glasses has negligible impact upon the aqueous durability of the wasteform (Hrma *et al.*, 2005; Lutze, 1988), probably as it does not consume network formers during crystallisation. This crystal phase is of higher aqueous durability than the borosilicate glass matrix (Yan *et al.*, 1995; Zhu *et al.*, 1986) and is radiation tolerant (Sickafus *et al.*, 2000), so will form in 'real' borosilicate HLW glasses (Cheron *et al.*, 1995; Hrma *et al.*, 2005). Spinels are known to nucleate and grow on platinoid inclusions (Bickford and Jantzen, 1986; Izak *et al.*, 2001; D.-S. Kim *et al.*, 1994; Sundaram and Perez, 2000), and these in turn can act as nucleation sites for other crystal phases. $(Cr,Fe,Ni)_3O_4$ was noted in both Type I and Type II microstructures.

$Na_3Li(MoO_4)_2 \cdot 6H_2O$ crystals (rhombohedral system) (**Figure 4.2.2.1**) are water soluble (**Table 2.18**) and a component of 'yellow phase'(**Section 4.4**). They are hydrated by atmospheric $H_2O$.

$Zr_{1-(x+y)}Ce_xGd_yO_{2-(y/2)}$ crystals (defect fluorite structure) (**Section 4.2.2.4**) are found exclusively within the dissolving/relict calcine particles/granules in Type II microstructures, along with bubbles. A similar cubic zirconia phase has previously been reported in borosilicate HLW glasses (O'Holleran *et al.*, 1998). For $Zr_{1-(x+y)}Ce_xGd_yO_{2-(y/2)}$ the incorporation of Ce and Gd helping to stabilise it in cubic form (Rebollo *et al.*, 2003; Yashima *et al.*, 1995). Due to its similar structure to $CeO_2$ crystals (fluorite structure) (**Section 2.8.6**), the long-lived actinides Pu and U could be incorporated within this phase (**Table 2.27**) if it were to form in a 'real' borosilicate HLW glass. The nano-crystalline nature of this phase is thought to be due to its precipitation from a glass melt locally supersaturated in respect of the component elements (Bouchet *et al.*, 2000). This explanation would also explain the regular size of the nano-crystals (10–20 nm), indicative of precipitation upon cooling due to supersaturation (Gong *et al.*, 2000). Nano-crystals of this size (<20 nm) will also help to stabilise the zirconia in cubic form (Martínez-Arias *et al.*, 1999 and references therein). This phase is radiation tolerant (Sickafus *et al.*, 2000), so will be able to form in a 'real' borosilicate HLW glass. A problem for this phase may be intergranular corrosion between the nano-crystals during

aqueous leaching (Zhu *et al.*, 1986). $Zr_{1-(x+y)}Ce_xGd_yO_{2-(y/2)}$ is found exclusively in Type II microstructures.

Lanthanide (Nd,Gd,La,Ce) silicate crystals (unidentified structure) (**Section 4.2.2.5**) are found exclusively within the dissolving/relict calcine particles/granules in Type II microstructures. These crystals were thought most likely to be silicate apatite (**Section 2.8.4.6**) or stillwellite (**Section 2.8.4.7**) due to their chemical compositions. This may not be the case however, as noted for a compositionally similar phase in heat treated Oxide glass (**Section 4.2.4.5**). This phase is likely formed by precipitation (upon cooling) from a glass supersaturated in respect to its component elements, found within the dissolving/relict calcine particles/granules (Bouchet *et al.*, 2000). As such they are associated with the $Zr_{1-(x+y)}Ce_xGd_yO_{2-(y/2)}$ crystals, cracking and bubbles. As the phase contains lanthanides it is a potential host for long-lived Am and Cm, as both are present in the +3 valence state in borosilicate glass (Caurant *et al.*, 2006 and references therein) and have similar ionic radii to the incorporated lanthanides (Shannon, 1976). Lanthanide (Nd,Gd,La,Ce) silicate is found exclusively in Type II microstructures.

### 5.2.2.2 Heat Treated Oxide Glass (Oxide HT)

Heat treated Oxide glass samples had one of two microstructures (**Section 4.2.4**); both descended from the two microstructures present in as-cast Oxide glass samples (**Section 4.2.2**).

Type A microstructure was Type I microstructure before heat treatment. It now displays extensive crystallisation and matrix cracking. This cracking will be detrimental to the aqueous durability of the glass due to the increase in wasteform surface area (Bickford *et al.*, 1990a).

Type B microstructure was Type II microstructure before heat treatment. It displays 'banded' crystallisation – crystallisation which has occured in the 'bands' enriched in simulated HLW components which were present in its parent microstructure.

$\alpha$-cristobalite crystals (tetragonal system) are the major crystal phase seen after heat treatment in Type A microstructures (**Section 4.2.4.1**) and have been noted in other borosilicate HLW glasses (**Table 2.20**). $\alpha$-cristobalite is responsible for the extensive glass matrix cracking (Arbab *et al.*, 2007; Caurant *et al.*, 2007), a cumulative effect of the $\beta$ to $\alpha$ phase transition (Arbab *et al.*, 2007; Matzke *et al.*, 1984) which results in a decrease in crystal volume (Matzke *et al.*, 1984; Peacor, 1973) on cooling, and also

thermal expansion coefficient (TEC) mismatch with the surrounding glass matrix (Jean *et al.*, 1995). Cristobalite thermal expansion coefficients (**Table 5.3**) and borosilicate HLW glass thermal expansion coefficients (**Section 2.4.2**), especially in the phase transition region, differ vastly.

**Table 5.3** Mean linear ($\alpha$) and volumetric ($\beta$) thermal expansion coefficients for cristobalite in the stated temperature ranges. Calculated using data from Peacor (1973), Pluth *et al.* (1985) and Swainson and Dove (1995).

| Temperature range (°C) | $\alpha$ ($\times 10^{-6}$ K$^{-1}$) | $\beta$ ($\times 10^{-6}$ K$^{-1}$) |
|---|---|---|
| 23–200 ($\alpha$-cristobalite) | $a$-axis = 19.1<br>$c$-axis = 34.2 | 72.9 |
| 200–300 ($\alpha$–$\beta$ phase transition region) | $a$-axis = 112<br>$c$-axis = 234 | 465 |
| 300–600 ($\beta$-cristobalite) | $a$-axis = 4.9 | 14.6 |

The formation of this phase is detrimental to the aqueous durability of the borosilicate HLW glass as it removes $SiO_2$ from the surrounding glass matrix (**Section 2.8.4.1**), generating a residual glass of lower aqueous durability than the parent glass (Mitamura *et al.*, 1985). This problem may not be encountered in 'real' borosilicate HLW glasses however, as this phase is electron beam sensitive in the TEM (McConville *et al.*, 1998) and therefore would not form in an environment with excessive $\beta$ and $\gamma$ radiation (Sun *et al.*, 2004), let alone $\alpha$ radiation. This would also explain why no cristobalite was observed during TEM examination of the glass. However, as amorphous phase separation (APS) has been noted to occur prior to cristobalite formation (Matzke *et al.*, 1984), and APS of alkali borosilicates is enhanced by irradiation (Sun *et al.*, 2004), the formation of a vitreous silica phase would have much the same effect (negative) on the durability of the residual alkali borate HLW-containing glass as cristobalite formation. As $Al_2O_3$ additions can inhibit cristobalite formation (Jean *et al.*, 1995), and there is little $Al_2O_3$ in Oxide glass compared to Blend glass (**Table 4.1.1**) it is suggested that increasing the $Al_2O_3$ content of the glass to above ~1.5 wt% may inhibit cristobalite formation (Jean *et al.*, 1995). $Al_2O_3$ additions have also been shown to suppress APS in sodium borosilicate glasses (Sproull *et al.*, 1994). $\alpha$-cristobalite is observed in Type A microstructures only.

$(Na,Sr,Nd,La)MoO_4$ crystals (powellite structure) are found in both Type A and Type B microstructures (**Section 4.2.4.2**) and similar phases are observed in borosilicate HLW glasses (**Table 2.15**). They have a dendritic morphology, previously noted in other borosilicate HLW glasses (Caurant *et al.*, 2007; Mendel *et al.*, 1976; Short, 2004;

Short *et al.*, 2005). This phase was observed to nucleate on both $RuO_2$ and metallic Pd-Te crystals. $(Na,Sr,Nd,La)MoO_4$ crystals are a potential host for short-lived $^{90}Sr$, as well as for long-lived Am and Cm as they are in the +3 valence state in borosilicate glasses (Caurant *et al.*, 2006 and references therein) and have similar ionic radii to Nd and La (Shannon, 1976). Li may also be present in this phase, but could not be detected. Formation of this crystal phase reduces the leach rate of elements which segregate to it (Mitamura *et al.*, 1986) and can slightly improve the overall aqueous durability of the wasteform (F. Bart *et al.*, 2001). As this phase has been reported to form in 'real' borosilicate HLW glasses (Cheron *et al.*, 1995) it must be radiation tolerant.

$Ce_{1-(x+y)}Zr_xGd_yO_{2-(y/2)}$ crystals (defect fluorite structure) formed predominantly in Type B microstructure (**Section 4.2.4.3**) and are similar to previously reported phases (**Section 2.8.6**). This phase is a potential host for the long-lived actinides Pu and U (**Table 2.27**) and as it is radiation tolerant (Sickafus *et al.*, 2000) it can (and does) form in 'real' borosilicate HLW glasses (Cheron *et al.*, 1995). This crystal phase is chemically durable (Abdelouas *et al.*, 1997), good news if actinides partition to it. Compositional 'zoning' of crystals formed in borosilicate HLW glasses (as noted for this crystal) has been observed previously (Mishra *et al.*, 2007). This zoning could indicate that the $Ce_{1-(x+y)}Zr_xGd_yO_{2-(y/2)}$ crystal exhibiting 'zoning' could have developed on a $Zr_{1-(x+y)}Ce_xGd_yO_{2-(y/2)}$ crystal core.

The Ni-rich crystal phase (unidentified crystal structure) (**Section 4.2.4.4**) containing Cr and Fe is found predominantly in Type B microstructures. Although its crystal structure could not be determined, a possibility is that it is bunsenite (NiO), with substitution of Cr and Fe on the Ni site and a Ni-site deficiency (if the Cr and Fe are not all +2 valent). This crystal phase nucleated and grew on both $RuO_2$ and metallic Pd-Te crystals. As it was beam stable in the TEM this indicates it may form in 'real' borosilicate HLW glasses, as the electron beam has been used to simulate the effect of $\beta$ and $\gamma$ radiation upon glasses (Sun *et al.*, 2004).

Lanthanide (Nd,Gd,La,Ce) silicate crystals (unidentified crystal structure) (**Section 4.2.4.5**) form exclusively in Type B microstructures. This acicular phase was not identified as either of the two most likely phases by XRD or TEM (using electron diffraction): silicate apatite (**Section 2.8.4.6**) or stillwellite (**Section 2.8.4.7**). As the phase contains lanthanides it is a potential host for long-lived Am and Cm, as both are present in the +3 valence state in borosilicate glass (Caurant *et al.*, 2006 and references therein) and have similar ionic radii to the incorporated lanthanides (Shannon, 1976). However, its stability under the electron beam suggests this phase may form in 'real'

borosilicate HLW glasses as the TEM has been used to simulate the effect of $\beta$ and $\gamma$ radiation upon glasses (Sun *et al.*, 2004). As this phase has a lower concentration of Si than the residual glass matrix, its formation should have a beneficial effect upon the aqueous durability of the residual glass.

Zektzerite ($LiNaZrSi_6O_{15}$) crystals (orthorhombic system) **(Section 4.2.4.6)** form exclusively in the Type B microstructure, and have previously been reported in borosilicate HLW glasses (Hyatt *et al.*, 2004). This crystal phase requires 6 of the 8 moles for its formation to be $SiO_2$, therefore it is likely that formation of this phase will be detrimental to the aqueous durability of the surrounding glass. That these crystals penetrate the lanthanide (Nd,Gd,La,Ce) silicate crystals indicates zektzerite crystallised before the lanthanide (Nd,Gd,La,Ce) silicate. Matrix cracking (possibly due to thermal expansion coefficient (TEC) mismatch between the crystal and the surrounding glass) around these crystals will increase the surface area exposed to any leaching media, lowering the overall aqueous durability of the wasteform (Bickford *et al.*, 1990a). Zektzerite thermal expansion coefficients **(Table 5.4)** and borosilicate HLW glass thermal expansion coefficients **(Section 2.4.2)** show mismatch.

**Table 5.4** Mean linear ($\alpha$) and volumetric ($\beta$) thermal expansion coefficients for zektzerite in the stated temperature ranges. Calculated using data from Marr and Glasser (1979).

| Temperature range (°C) | $\alpha$ ($\times 10^{-6}$ $K^{-1}$) | $\beta$ ($\times 10^{-6}$ $K^{-1}$) |
|---|---|---|
| 12–420 | *a*-axis = 4.3<br>*b*-axis = 3.1<br>*c*-axis = 4.8* | 12.2 |
| 420–630 | *a*-axis = 6.3<br>*b*-axis = 6.0<br>*c*-axis = 7.5* | 19.9 |

* A. M. Shaikh reports contraction of the *c*-axis when heating through the stated temperature ranges.

## 5.3 Chemical (Aqueous) Durability Testing

### 5.3.1 Glass Leaching

#### *5.3.1.1 As-Cast and Heat Treated Blend Glasses*

The relative normalised leach rates/leached fractions of the elements from Blend glasses (both as-cast and heat treated) are **(Tables 4.3.1.2** and **4.3.1.3)**: B ≈ Li ≈ Mo > Na >> K > Cr > Si >> Al >> Sr. Ba was below the DCP-AES detection limit in both as-cast and

heat treated glass leachates due to its low concentration in Blend glass (0.31 wt%; **Table 4.1.1**). Nd was below the DCP-AES detection limit in both as-cast and heat treated glass leachates due to the low solubility of lanthanides in aqueous solutions (Abdelouas *et al.*, 1997; Abraitis, 1999; Barkatt *et al.*, 1981, 1983; Calas *et al.*, 2002; Ménard *et al.*, 1998; Plodinec, 1986; Trocellier *et al.*, 2005).

Heat treatment of Blend glass reduced the normalised leach rates/leached fractions of Al, B, K, Li, Mo, Na, Si and Sr marginally, but increased those of Cr marginally. The pH of Blend glass leachates during modified PCT-B were not significantly altered by heat treatment (**Figure 4.3.1.23**).

### *5.3.1.2 As-cast and Heat Treated Oxide Glasses*

The relative normalised leach rates/leached fractions of the elements from Oxide glasses (both as-cast and heat treated) are (**Tables 4.3.1.2** and **4.3.1.3**): B ≈ Li > Na > Mo >> Si > Cr > Al >> Sr > Ba. K was below the DCP-AES detection limit in as-cast Oxide glass due to its low concentration (0.05 wt%; **Table 4.1.1**) and the better aqueous durability of this glass. Nd was below the DCP-AES detection limit in as-cast Oxide glass due to the low solubility of lanthanides in aqueous solutions (Abdelouas *et al.*, 1997; Abraitis, 1999; Barkatt *et al.*, 1981, 1983; Calas *et al.*, 2002; Ménard *et al.*, 1998; Plodinec, 1986; Trocellier *et al.*, 2005) and the better aqueous durability of this glass.

Heat treatment of Oxide glass increased the normalised leach rates/leached fractions of Al, B, Ba, Cr, Li, Mo, Na, Si and Sr significantly. Heat treatment also results in K and Nd becoming detectable in the leachate. The pH of Oxide glass leachates during modified PCT-B were significantly increased by heat treatment (**Figure 4.3.1.23**).

### *5.3.1.3 General Observations*

Significantly, both as-cast glasses (Blend and Oxide) had lower Si leach rates during the 3 to 7 d period than either the preceding or subsequent period (**Section 4.3.1.10**). This indicates a change in the dynamic equilibrium between silica dissolution and recondensation toward recondensation (Vernaz *et al.*, 2001) and is related to gel layer formation. For low durability glasses such as these, gel layer formation is reported to be complete within 10 d (Barkatt *et al.*, 1983).

Related to the above are the negative leach rates of Ba **(Section 4.3.1.3)** and Sr **(Section 4.3.1.11)** during the 7 to 14 d period for both as-cast and heat treated Oxide glass samples. During the same period the leach rates of Mo **(Section 4.3.1.7)** from both as-cast and heat treated Oxide glass samples are lower than either the preceding or subsequent period. It is proposed that these three elements are precipitating on/in the newly formed gel layer, forming either a powellite molybdate or an amorphous precursor phase, due to the low temperature at which the experiments were conducted. Abraitis (1999) observed decreasing Sr concentrations in solution over time, due to secondary processes such as gel layer formation and secondary phase precipitation. As-cast and heat treated Blend glass samples also have Mo leach rates lower during the 7 to 14 d period than either the preceding or subsequent period. It is proposed that Mo is precipitating on/in the newly formed gel layer.

Also related to gel layer formation is the Nd concentration in heat treated Oxide glass leachate samples **(Section 4.3.1.9)**, which becomes undetectable just after the gel layer forms, as has been noted previously (Gauthier *et al.* 2000), indicating it has precipitated on/in the gel layer as lanthanides have been reported as being enriched on/in these gel layers (Abdelouas *et al.*, 1997; Abraitis, 1999; Barkatt *et al.*, 1981, 1983; Calas *et al.*, 2002; Ménard *et al.*, 1998; Plodinec, 1986; Trocellier *et al.*, 2005).

In the period 14 to 28 d, Al is precipitated from the leachate of as-cast and heat treated Blend glass samples, on/in the gel layer **(Section 4.3.1.1)**. Abraitis (1999) observed decreasing Al concentrations in solution over time, due to secondary processes such as gel layer formation and secondary phase precipitation.

In all investigated glasses, the alkalis (Li and Na) **(Sections 4.3.1.6** and **4.3.1.8)**, boron **(Section 4.3.1.2)** and molybdenum **(Section 4.3.1.7)** are leached at rates much higher than silicon **(Section 4.3.1.10)**. If we accept the modified random network model of Greaves (1985), then alkali cations (and other network modifiers) will cluster together in the glass, forming 'percolation channels' throughout the glass structure if their concentration in the glass is high enough. As alkalis are preferentially associated with boron in 'traditionally' homogeneous alkali borosilicate glasses (Bourcier, 1994; Gou *et al.*, 2001 and references therein; Ledieu *et al.*, 2004), borate will be associated with these 'percolation channels'. Further to the above, molybdenum (as $[MoO_4]^{2-}$ oxyanions) is independent of the borosilicate glass network, located within these 'percolation channels', charge compensated by network modifying cations (Calas *et al.*, 2003; Short, 2004; Short *et al.*, 2005). Therefore, water contacting the glass will likely enter the glass structure via these percolation channels (Greaves, 1990; Hand and

Seddon, 1997), next, ion exchange will occur, releasing the soluble alkali cations into solution (**Section 2.10.2**). As borate network groups are preferentially associated with these 'percolation channels', the low durability 'borate glass' (Hall *et al.*, 1976; Ledieu *et al.*, 2004) will also dissolve. Because molybdenum forms $[MoO_4]^{2-}$ oxyanions in solution (Greenwood and Earnshaw, 2002) and is already present in this form in the 'percolation channels', it will leach rapidly. In 'real' borosilicate HLW glasses short-lived $^{137}Cs$ as well as long-lived $^{135}Cs$ (Abraitis, 1999; Ferrand *et al.*, 2006; Inagaki *et al.*, 1998; Lutze, 1988) and long-lived $^{99}Tc$ (ASTM, 2002 and references therein) leach at similar rates to B, Li, Na and Mo. The higher normalised leach rates/leached fractions of Li compared to Na observed in this work has been reported by other authors using similar experimental conditions, *e.g.* ~90 °C (Barkatt *et al.*, 1983; Clark *et al.*, 1982; Crum *et al.*, 2002; Hrma *et al.*, 2005; Inagaki *et al.*, 1998; Kawamura and Ohuchi, 1995; Langowski *et al.*, 1996b; H. Li *et al.*, 1996a; Lutze, 1988; Sheng *et al.*, 1999; Werme *et al.*, 1990).

Si leaching rates (**Section 4.3.1.10**) are much lower than those for elements such as Li, B, Na and Mo, due to the stability of the Si–Ø–Si bond in these mildly alkaline leachates (Abraitis, 1999; Trocellier *et al.*, 2005). Also, there is a dynamic equilibrium between silica dissolution (from the glass and gel layer) and its recondensation on/in the gel layer (Vernaz *et al.*, 2001). K present in these glasses leaches at similar rates (**Section 4.3.1.5**) to Si, although K is an alkali. Its leaching rates are lower than for Li and Na, possibly due to its larger size (Shannon, 1976). As Cr is a multivalent transition metal its leaching rate (**Section 4.3.1.4**) would be expected to be lower (Doremus, 1982), however some Cr in these glasses will be present as $[CrO_4]^{2-}$ oxyanions independent of the borosilicate glass network (Tilquin *et al.*, 1998) and associated with network modifiers, therefore leaching in a similar manner to $[MoO_4]^{2-}$ oxyanions. The main reason Cr will have a lower normalised leach rate/leached fraction than Mo is that it also occurs in glasses in the +3 valence state (Hrma *et al.*, 2006), whereas Mo is almost wholly in the +6 valence state (Short, 2004; Short *et al.*, 2005). The increased leaching of Cr after the heat treatment of Blend glass may be related to an increase in the $Cr^{6+}/\Sigma Cr$ ratio, leading to more $[CrO_4]^{2-}$ oxyanions independent of the borosilicate HLW glass network, which are easier to leach.

Al has lower leaching rates (**Section 4.3.1.1**) than Si and is generally found in the gel layer (Abdelouas *et al.*, 1997; Abraitis, 1999; Barkatt *et al.*, 1981, 1983; Calas *et al.*, 2002; Ménard *et al.*, 1998; Plodinec, 1986; Trocellier *et al.*, 2005).

Sr (**Section 4.3.1.11**) and Ba (**Section 4.3.1.3**) (alkaline earths) have the lowest leach rates, probably due to them stabilising the glass structure, much as Ca does (Lutze, 1988), as well as being present in the glasses at low levels (**Table 4.1.1**).

### *5.3.1.4 Leachate pH*

The leachate pH values for all four glasses were in the range of 9.70–10.00 throughout the 28 d modified PCT-B (**Section 4.3.1.12**). This pH level is mildly alkaline. The most striking feature of these glasses is the way the pH levels 'plateau' beyond 14 d. Leachate pH has been noted to stabilise at approximately constant values from 28 d and beyond (Feng and Pegg, 1994). This will be due to the high levels of dissolved boron (as boric acid) buffering the pH increase (Feng and Pegg, 1994; Lutze and Grambow, 1992; Macedo *et al.*, 1982) caused by the release of the alkalis, Li and Na. The stabilised pH level falls slightly for both as-cast and heat treated Blend glass samples at 28 d, thought to be due to the effect of leachate replenishment and possibly secondary phase formation on/in the gel layer (Feng and Pegg, 1994). However, the leachate pH values for the container 'blanks' (**Appendix, Table A.12**) indicate a continuous decline in leachate pH values over the course of the experiment which are unrelated to either leachate replenishment or secondary phase formation. It is proposed that atmospheric $CO_2$ was responsible for the fall in leachate pH values for the container 'blanks' as the experiment progressed.

## 5.3.2. Leached Glass Analysis

### *5.3.2.1 As-Cast and Heat Treated Blend Glasses*

Leached, as-cast Blend glass analysis (**Section 4.3.2.1**) reveals the $RuO_2$ crystals (rutile structure) did not dissolve during leaching. The presence of $RuO_2$ crystals in borosilicate HLW glasses has been reported to have negligible (F. Bart *et al.*, 2001) or even a slightly positive (Pacaud *et al.*, 1992), effect on their chemical durabilities. Leached, heat treated Blend glass analysis (**Section 4.3.2.3**) shows $Ce_{1-(x+y)}Zr_xGd_yO_{2-(y/2)}$ crystals (defect fluorite structure) did not dissolve during leaching, confirming the high aqueous durability of this phase (Abdelouas *et al.*, 1997). However, glass matrix alteration (hydration) is enhanced around these crystals. The (Sr,Nd,La) molybdate crystals (powellite structure suspected) did not dissolve during leaching, this is expected

if (as suspected) the phase has the powellite structure due to its high aqueous durability (Komarneni *et al.*, 1983; Schiewer *et al.*, 1982). As the $[MoO_4]^{2-}$ oxyanions (which are the building blocks of this phase) are independent of the borosilicate glass network and associated with network modifiers (+1, +2 and +3 valent cations), the crystallisation of this high aqueous durability phase within the modifier/boron 'percolation channels' would effectively 'plug' these easy routes for water ingress and ion exchange in the glass, reducing the connectivity of the 'percolation channels' and possibly being responsible for the slight increase in aqueous durability seen in heat treated Blend glass. The lanthanide (Nd,Gd,La,Ce) silicate crystals (unidentified structure) did not dissolve during leaching, suggesting a reasonable aqueous durability for this phase. The effect the formation of this phase has on glass matrix alteration (hydration) could not be determined due to its proximity to $Ce_{1-(x+y)}Zr_xGd_yO_{2-(y/2)}$ crystals (defect fluorite structure) which enhance matrix alteration (hydration).

### *5.3.2.2 As-Cast and Heat Treated Oxide Glasses*

Leached, as-cast Oxide glass analysis (**Section 4.3.2.2**) shows the microstructure of all glass samples to be Type I. $RuO_2$ crystals (rutile structure) and metallic Pd-Te crystals (fcc structure) did not dissolve during leaching. The presence of platinoids (such as $RuO_2$ and metallic Pd-Te crystals) in borosilicate HLW glasses has been reported to have negligible (F. Bart *et al.*, 2001) or even a slightly positive (Pacaud *et al.*, 1992), effect on their chemical durabilities. Leached, heat treated Oxide glass analysis (**Section 4.3.2.4**) shows the microstructure of all samples to be Type A. The (Na,Sr,Nd,La)$MoO_4$ crystals (powellite structure) did not dissolve during leaching, this is unsurprising as powellite crystals are insoluble in aqueous solutions (Komarneni *et al.*, 1983; Schiewer *et al.*, 1982), and their formation is thought responsible for the slight increase in the aqueous durability of Blend glass after heat treatment. The $\alpha$-cristobalite crystals (tetragonal system) did not dissolve during leaching. However, all of the glass surrounding these crystals is altered (hydrated), explaining the significant decrease in the aqueous durability of Oxide glass after heat treatment. **Figure 5.1** illustrates the difference between leached Oxide HT 'powder' samples depending on whether they contained cristobalite or not.

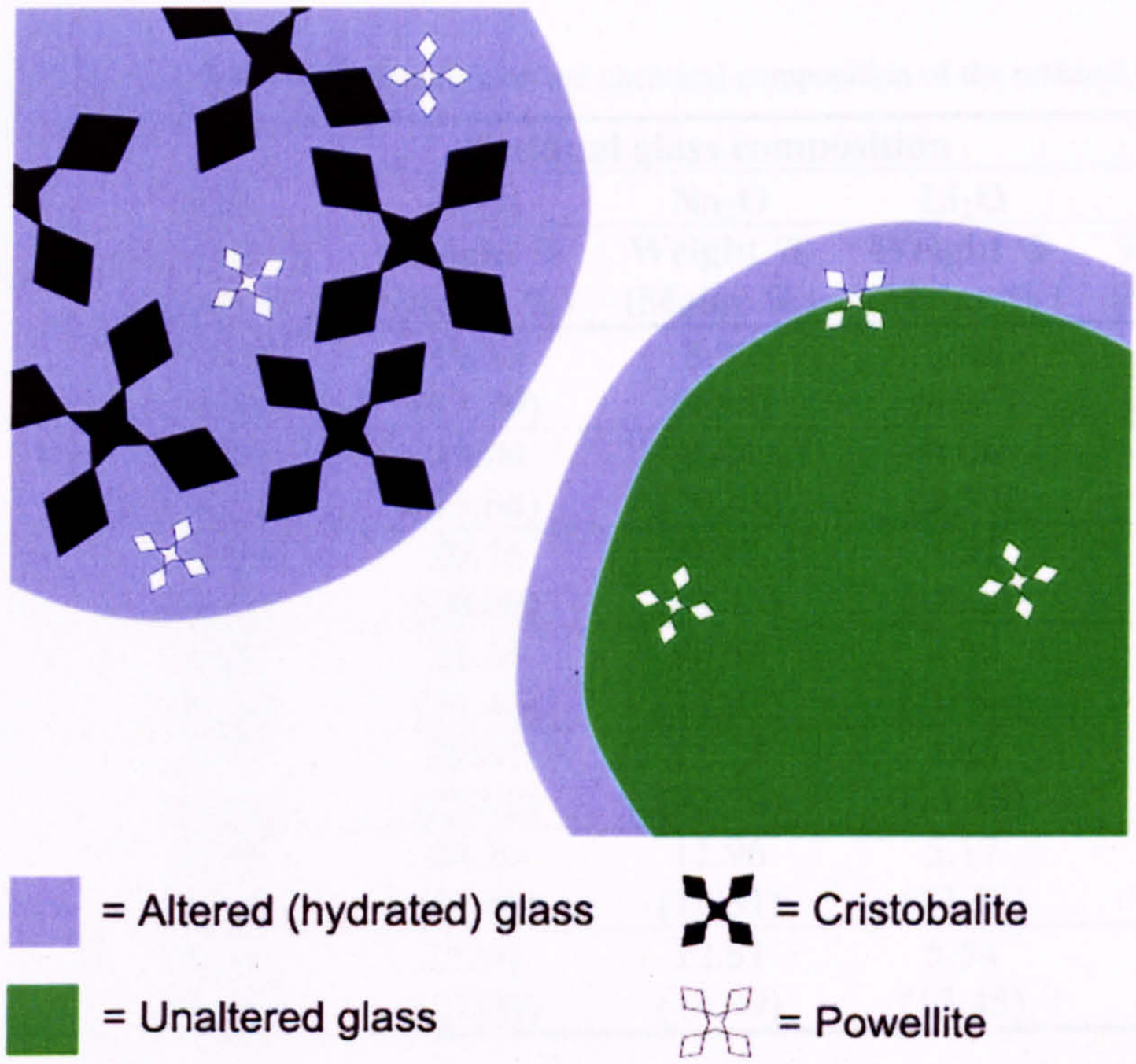


**Figure 5.1** Schematic of the alteration (hydration) of leached Oxide HT 'powder' samples, showing the effect of cristobalite crystallisation.

Calculation of the effect of $\alpha$-cristobalite formation on the chemical composition of the residual Oxide glass (**Table 5.5**) shows that as the amount of $\alpha$-cristobalite formed increases, the glass is increasingly impoverished in $SiO_2$, but enriched in all other glass components, leading to a lower aqueous durability glass (Hall *et al.*, 1976; Ledieu *et al.*, 2004).

**Table 5.5** Effect of cristobalite crystallisation on the chemical composition of the residual Oxide glass.

| Cristobalite | Residual glass composition | | | | |
|---|---|---|---|---|---|
| | $SiO_2$ | $B_2O_3$ | $Na_2O$ | $Li_2O$ | Waste |
| Weight % | Weight % (Molar %) | Weight % (Molar %) | Weight % (Molar %) | Weight % (Molar %) | Weight % (Molar %) |
| 0 | 49.19 (55.90) | 18.14 (17.79) | 8.97 (9.88) | 3.88 (8.87) | 19.82 (7.56) |
| 5 | 46.53 (53.27) | 19.09 (18.86) | 9.44 (10.48) | 4.08 (9.39) | 20.86 (8.00) |
| 10 | 43.55 (50.26) | 20.16 (20.08) | 9.97 (11.15) | 4.31 (10.00) | 22.01 (8.51) |
| 15 | 40.24 (46.86) | 21.35 (21.46) | 10.56 (11.92) | 4.56 (10.68) | 23.29 (9.08) |
| 20 | 36.47 (42.92) | 22.67 (23.02) | 11.21 (12.79) | 4.85 (11.48) | 24.80 (9.79) |
| 25 | 32.26 (38.41) | 24.19 (24.86) | 11.96 (13.81) | 5.17 (12.38) | 26.42 (10.54) |
| 30 | 27.42 (33.10) | 25.91 (27.00) | 12.81 (14.99) | 5.54 (13.45) | 28.32 (11.46) |

Even though the $SiO_2$ loss associated with cristobalite crystallisation will move the residual Oxide glass composition away from the 'traditional' immiscibility region in this system (Mazurin *et al.*, 1984), the alkalis and boron leached at rates expected for an amorphously phase separated alkali borosilicate glass with an interconnected alkali borate phase. Similarly, Ledieu *et al.* (2004) observed that sodium borosilicate glasses of similar composition (outside the 'traditional' immiscibility region) had leach rates for the soluble glass components similar to those which would be expected for an amorphously phase separated alkali borosilicate glass (where the soluble glass components are interconnected). A theory is now postulated to explain this behaviour. As Greaves (1985) notes, interconnected 'percolation channels' will form throughout the structure of a glass if the concentration of network modifiers is sufficient. Also, the borate and silicate network units of 'traditionally' homogeneous borosilicate glasses show demixing (non-random distribution) (**Section 2.4.1**), with borate units preferentially associated with network modifiers (the 'percolation channels') (Bourcier, 1994; Gou *et al.*, 2001 and references therein; Ledieu *et al.*, 2004). It is proposed that the structure of 'traditionally' homogeneous alkali borosilicate glasses are actually phase separated, but on a scale difficult for most traditional techniques, such as visual inspection, to observe. This would mean that the alkali borosilicate system is phase separated to a much greater extent (possibly completely) than indicated by the 'traditional' immiscibility region in ternary phase diagrams. Further to this, the only

difference may be that glasses whose compositions lie within the 'traditional' immiscibility region can coarsen their phase separated microstructures (either on cooling from the glass melting temperature or after heat treatment) to a scale observable by low resolution methods such as visual inspection, whereas glasses whose compositions lie outside this region do not undergo this microstructural coarsening, or at least not to such a degree.

The durability of the glass phase should improve the further from an $\alpha$-cristobalite crystal it is due to an increase in its $SiO_2$ levels (Mitamura *et al.*, 1985). Even though $(Na,Sr,Nd,La)MoO_4$ crystals (powellite structure) are unaffected by leaching, the small positive influence on glass durability of their formation (F. Bart *et al.*, 2001) is outweighed by the huge negative impact of $\alpha$-cristobalite crystallisation.

## 5.4 'Yellow Phase' Analysis

The 'yellow phase' inclusion in as-cast Oxide glass (**Section 4.4**) may have a slightly different chemical composition to that shown (**Table 4.4.1**), probably due to the levels of Cr and Te being too low. As 'yellow phase' is oxidising (Krause and Luckscheiter, 1991), yellow in colour (indicating the presence of chromates) (Buechele *et al.*, 1995; Hall *et al.*, 1976; Lutze, 1988) and other 'yellow phase' samples have Cr in the +6 valence state (Hrma *et al.*, 2006; Kaushik *et al.*, 2006; Morris and Chidley, 1976; Schiewer *et al.*, 1982; Sullivan *et al.*, 1995), the Cr component should actually be in its highest valence state, $CrO_3$. The same is true of Te, as 'yellow phase' is oxidising (Krause and Luckscheiter, 1991), Te would be expected to be in its +6 valence state, as $TeO_3$. In a corrected composition, $CrO_3$ and $TeO_3$ levels would be at a higher weight %, with other components being in proportionally decreased levels. In terms of the crystal phases observed (**Figure 4.4.2**), $CsLiMoO_4$ (cubic system) is important as a host for short-lived $^{137}Cs$ and long-lived $^{135}Cs$. It is water soluble (Klevtsova *et al.*, 1980), illustrating the problem of 'yellow phase' formation. $Na_3Li(MoO_4)_2 \cdot 6H_2O$ (rhombohedral system) will be water soluble (Caurant *et al.*, 2007; Schiewer *et al.*, 1982) and is hydrated by atmospheric $H_2O$.. The problem with these two phases is that due to their aqueous solubility large amounts of alkali cations will be released into solution upon 'yellow phase' contact with water. These alkalis will cause a steep rise in solution pH (Feng and Pegg, 1994), which will not be buffered by Mo release as the $[MoO_4]^{2-}$ oxyanions do not have a significant effect on solution pH (Greenwood and Earnshaw, 2002), unlike silicic (Feng and Pegg, 1994) or boric acid (Feng and Pegg,

1994; Lutze and Grambow, 1992; Macedo *et al.*, 1982). The rapid rise in pH of the contacting solution will be detrimental to borosilicate glass durability, increasing Si leach rates (Ebert and Mazer, 1994). The crystal phase $(Na,Sr,Nd)MoO_4$ (powellite structure) is a host for short-lived $^{90}Sr$ but would not be expected to host Am and Cm in 'yellow phase' due to the oxidising nature of 'yellow phase' (Krause and Luckscheiter, 1991), with both Am and Cm expected in the +4 valence state, if they even preferentially partition to 'yellow phase'. However, this phase is of high aqueous durability (Komarneni *et al.*, 1983; Schiewer *et al.*, 1982) and therefore a good radionuclide host. The crystal phase $Ba_{1-x}Sr_xMoO_4$ (where $0 < x < 0.5$) (powellite structure) is a potential $^{90}Sr$ host. This crystal phase is of high aqueous durability (as noted for the powellite phase above, and will behave similarly in solution). Although not detected by XRD, it is proposed that alkali chromates (as potential short-lived $^{137}Cs$ and long-lived $^{135}Cs$ hosts) and $BaCrO_4$ (with possible short-lived $^{90}Sr$ incorporation) could be present due to their presence in other 'yellow phase' samples (Kaushik *et al.*, 2006; Schiewer *et al.*, 1982) and the similar composition of this 'yellow phase' sample. Alkali chromates are water soluble (Schiewer *et al.*, 1982), whilst $BaCrO_4$ is not (Schiewer *et al.*, 1982). As tellurates have been inferred in the 'yellow phase' inclusion, two different types may be present, metatellurates $[TeO_4]^{2-}$ and/or orthotellurates $[TeO_6]^{6-}$ (Greenwood and Earnshaw, 2002). Metatellurates can form tellurates with powellite crystal structure (which can incorporate +1, +2 and +3 valent cations) and have been produced elsewhere (Schieber, 1965). Alkali metatellurates are also a possibility. Orthotellurates could form crystals of the type $A_6TeO_6$ ($A$ = +1 valence cation) and/or $A_3TeO_6$ ($A$ = +2 valence cation) (Greenwood and Earnshaw, 2002).

Mo and Tc behave similarly in borosilicate HLW glasses (Dé *et al.*, 1976; Langowski *et al.*, 1996a), as well as in SYNROC (a synthetic rock HLW storage/disposal matrix) – forming soluble molybdates and technetates if SYNROC is not produced under sufficiently reducing conditions (Donald *et al.*, 1997). As Mo and Tc also have similar structural roles in borosilicate HLW glasses (as oxyanions independent of the borosilicate glass network, associated with network modifying cations; **Table 2.3**) it is proposed that long-lived $^{99}Tc$, as the water soluble (Lutze, 1988; Marples, 1988) pertechnetate oxyanion ($[TcO_4]^-$) will preferentially partition to 'yellow phase' in 'real' borosilicate HLW glasses where 'yellow phase' forms. Further to this, the similarity in chemistry of S, Se and Te (all are from Group 16 in the Periodic Table), along with the preferential partitioning of S and Te to 'yellow phase' (**Section 2.6.2.1** and this work) indicate that long-lived $^{79}Se$ will also preferentially partition to 'yellow

phase', probably as the selenate oxyanion ($[SeO_4]^{2-}$) (Ramos *et al.*, 1992; Schreiber and Schreiber, 1993). Both of these oxyanions ($[TcO_4]^-$ and $[SeO_4]^{2-}$) are expected to form crystal phases with alkali and/or alkaline earth cations in 'yellow phase' (Dietzel, 1942). The cations As, Nb and Sb may also preferentially partition to 'yellow phase' if they are in the +5 valence state.

The chemical composition of the 'yellow phase' inclusion (**Table 4.4.1**) reveals that the cations which preferentially partitioned to 'yellow phase' either had low valencies (Cs, Li, Na, Ba, Sr) or high valencies (Mo, Cr, Te). Cations with intermediate valencies (+3 or +4) did not preferentially partition to 'yellow phase'. In addition to these observations; using lighter alkali oxides in alkali borosilicate HLW glasses is known to reduce the amount of 'yellow phase' that will form during glass melting (Dé *et al.*, 1976; Hall *et al.*, 1976), whilst Mg (an alkaline earth cation with a valence of +2) does not preferentially partition to 'yellow phase' (Morris and Chidley, 1976; Schiewer *et al.*, 1982).

The above indicates that there is more determining the partition coefficient of a cation between glass and 'yellow phase' than just its valence. Therefore, the field strength concept of Dietzel (1942) is introduced. The Dietzel field strength of a cation is a measure of its 'ordering' effect upon surrounding anions (generally $O^{2-}$) and the equation for its calculation is:

$$F = z/a^2 \qquad (5.1)$$

$F$ = Dietzel field strength of cation
$z$ = valence of cation
$a$ = cation-oxygen interatomic distance (Å)

When calculating $F$ in this work, $a$ is determined by adding the ionic radius of the cation of interest (of known $O^{2-}$ coordination number and valence) to that of $^{II}O^{2-}$ (1.35 Å), with ionic radii obtained from Shannon (1976). The $F$ of some cations of interest have been calculated using **Equation 5.1** and data from Shannon (1976); these are presented in **Table 5.6.**

**Table 5.6** Calculated Dietzel field strength (*F*) of some cations of interest (shown with their $^{II}O^{2-}$ coordination number and valence).

| Cation | *F* | Cation | *F* | Cation | *F* |
|---|---|---|---|---|---|
| $^{IV}S^{6+}$ | 2.78 | $^{IV}Se^{6+}$ | 2.26 | $^{VI}Te^{6+}$ | 1.64 |
| $^{IV}Tc^{7+}$ | 2.37 | $^{IV}P^{5+}$ | 2.16 | $^{III}B^{3+}$ | 1.62 |
| $^{IV}Re^{7+}$ | 2.34 | $^{IV}Mo^{6+}$ | 1.94 | $^{IV}Si^{4+}$ | 1.54 |
| $^{IV}Cr^{6+}$ | 2.31 | $^{IV}Te^{6+}$ | 1.89 | $^{IV}B^{3+}$ | 1.41 |

As can be seen from **Table 5.2**, the *F* of a cation cannot be the only factor determining its partition coefficient, otherwise the amount of $P_2O_5$ in the 'yellow phase' inclusion would be >>1 wt% (assuming a similar partition coefficient to $MoO_3$), but this is not the case. Calculating the *F* of cations present in 'yellow phase' has, however, explained why it is crystalline. Dietzel (1942) notes that when the $\Delta F$ between two cations is high, crystallisation occurs. This explains how the oxyanion-forming cations (with high *F*) present in the 'yellow phase' form crystalline phases with the alkali and/or alkaline earth cations (with low *F*).

A further example of why *F* is too simplistic can be found when comparing the behaviour of $[PO_4]^{3-}$ and $[MoO_4]^{2-}$ oxyanions. Despite $^{IV}P^{5+}$ having a higher *F* than $^{IV}Mo^{6+}$ (**Table 5.2**), $[PO_4]^{3-}$ oxyanions can bond directly to the borosilicate glass network (forming P–Ø–B linkages) depending upon borosilicate glass composition and/or processing conditions (Muñoz *et al.*, 2006), whereas $[MoO_4]^{2-}$ oxyanions remain independent of the borosilicate glass network regardless of borosilicate glass composition and/or processing conditions (Short, 2004; Short *et al.*, 2005).

A more sophisticated way to explain the partition coefficients is the bond valence model. According to this model the sum of the bond valencies relating to a bridging oxygen must be close to the theoretical value of 2.0 valence units. The valence of a bond is calculated (Brese and O'Keeffe, 1991):

$$v_{iO} = \exp[(R_{iO} - d_{iO})/0.37] \qquad (5.2)$$

$v_{iO}$ = valence of the bond between cation *i* and oxygen
$R_{iO}$ = bond-valence parameter for oxides of cation *i*
$d_{iO}$ = cation *i*-oxygen bond length (Å)

When calculating $v_{iO}$, $d_{iO}$ is determined by adding the ionic radius of the cation of interest (of known $O^{2-}$ coordination number and valence) to that of $^{II}O^{2-}$ (1.35 Å), with ionic radii obtained from Shannon (1976). $R_{iO}$ of the cation of interest (of known

valence) is taken from Brese and O'Keeffe (1991). The $v_{iO}$ of some cations of interest have been calculated using **Equation 5.2** and data from Shannon (1976) and Brese and O'Keeffe (1991); these are presented in **Table 5.7.**

**Table 5.7** Calculated bond valence ($v_{iO}$) of some cations of interest (shown with their $^{II}O^{2-}$ coordination number and valence).

| Cation | $v_{iO}$ | Cation | $v_{iO}$ | Cation | $v_{iO}$ |
|---|---|---|---|---|---|
| $^{IV}Re^{7+}$ | 1.91 | $^{IV}S^{6+}$ | 1.52 | $^{IV}Si^{4+}$ | 1.04 |
| $^{IV}Cr^{6+}$ | 1.64 | $^{IV}Mo^{6+}$ | 1.49 | $^{III}B^{3+}$ | 1.03 |
| $^{IV}Tc^{7+}$ | 1.63* | $^{IV}Te^{6+}$ | 1.45 | $^{VI}Te^{6+}$ | 1.02 |
| $^{IV}Se^{6+}$ | 1.53 | $^{IV}P^{5+}$ | 1.25 | $^{IV}B^{3+}$ | 0.79 |

* $R_{TcO}$ (used to calculate $v_{TcO}$) taken from 'Accumulated Table of Bond Valence Parameters v2.2' (http://www.ccp14.ac.uk/ccp/web-mirrors/i_d_brown/bond_valence_param/bvparm2006.cif)

**Table 5.3** shows $^{IV}Mo^{6+}$ has a greater $v_{iO}$ than $^{IV}P^{5+}$, which means $v_{iO}$ is better than $F$ in this case in correlating with observed partition behaviour. The bond valence model may offer a way to predict how radionuclides in 'real' borosilicate HLW glasses will partition between glass and 'yellow phase', although this will have to be experimentally determined.

The bond valence model also offers more detail on the P–Ø–B linkage observed by Muñoz *et al.*, (2006). $^{IV}P^{5+}$ must be bonded (via a bridging oxygen) to $^{IV}B^{3+}$ as the bond valencies total 2.04 valence units, whereas bonding (via a bridging oxygen) to $^{III}B^{3+}$ would result in a bond valence total of 2.28 valence units, leading to an 'overbonding' of the bridging $O^{2-}$ anion. The bond valence model also presents a reason for the preferential partitioning of Te to the 'yellow phase' inclusion, as well as indicating whether the Te is present as metatellurate or orthotellurate. For Te to preferentially partition to 'yellow phase' it requires the $Te^{6+}$ to be in IV-fold coordination to $O^{2-}$ anions (metatellurate), as VI-fold coordination (orthotellurate) results in both $F$ and $v_{iO}$ similar to the glass formers (which do not preferentially partition to 'yellow phase').

An explanation of why the alkalis Li and Na have not partitioned to the 'yellow phase' inclusion as strongly as might be expected is due to how they were added to the melter. All the $Na_2O$ in the final glass comes from the base glass frit, whilst half the $Li_2O$ in the final glass comes from the base glass frit. This will lead to lower partition coefficients for these alkalis between glass and 'yellow phase' compared to alkalis such as Cs and K, which are added to the glass melter as part of the calcine.

As 'yellow phase' has been noted to increase volatilisation of some elements which segregate to it (Langowski *et al.*, 1996a and references therein; Sullivan *et al.*,

1995), in an 'real' borosilicate HLW glass the radionuclides $^{137}Cs$, $^{135}Cs$, $^{90}Sr$, $^{99}Tc$ and $^{79}Se$ may be lost to the off-gas at increased levels if 'yellow phase' is allowed to form.

As 'yellow phase' segregation occurs during feed-to-glass conversion (H. Li *et al.*, 2001; Manara *et al.*, 2007; Morgan, 2005; Sullivan *et al.*, 1995) and 'yellow phase' is initially nitrate-based (Hrma *et al.*, 2006) it is proposed that the addition of lithium nitrate ($LiNO_3$) to the HLW calciner may enhance 'yellow phase' formation for the following reason. Lithium nitrate, with a melting point of approximately 255 °C (Greenwood and Earnshaw, 2002), is one of the first calcine components to melt (Morgan, 2005), forming a liquid phase (although all nitrates will have decomposed by approximately 700–750 °C when heating at 4 °C $min^{-1}$) (Izak *et al.*, 2001; Morgan, 2005). It is proposed that other 'yellow phase' components partition to this liquid phase (or are leached from the calcine by it) due to their already low compatibility with the borosilicate glass network, with the lithium nitrate acting as a reaction medium for the formation of crystal phases. A similar method has recently been developed to form powellite crystals at low temperatures using $LiNO_3$ as a reaction medium (Y. Wang *et al.*, 2007). Therefore, it is suggested that the omission of lithium nitrate from the calcine feed will slow the kinetics of 'yellow phase' formation. The omission of lithium nitrate from the calcine feed is also commercially desirable (Short, 2004). It is reported that reducing melt conditions prevent 'yellow phase' formation (Camara *et al.*, 1980, Horneber *et al.*, 1982; Lutze, 1988 and references therein); as well as lowering the temperature needed for complete HLW incorporation in the glass melt (Morgan, 2005); increasing glass melting rates (Bickford *et al.*, 1990b); reducing foaming in the melter (Bickford *et al.*, 1990b; Goldman, 1986; Plodinec, 1986); and also reducing Ru (Demin *et al.*, 1996), Tc (Darab and Smith, 1996; Demin *et al.*, 1996) and Se (Ramos *et al.*, 1992) volatilisation from the melter. An argument against mildly reducing melt conditions is that it encourages the formation of metallic inclusions from easily reducible glass components such as $Ag_2O$ and CdO, which may then act as nucleation sites during the slow cool of the 'real' radiogenic glass (Short, 2004). However, the levels of these components are very low in 'real' borosilicate HLW glasses (**Table 2.2**), and their relative retentions in the melter bottom are low when compared to Pd, Ru and Rh (Smith and Bickford, 2000), so their presence would make very little difference compared to the amount of platinoid melt insolubles.

# 6 Conclusions and Suggested Further Work

## 6.1 Conclusions

The chemical composition, glass transition temperature and density of both Blend and Oxide glass have been determined.

As-cast Blend glass samples had a compositionally homogeneous glass matrix. The crystal phase $RuO_2$ (rutile structure) was observed in these samples. After heat treatment of Blend glass samples (simulating the retarded cooling experienced by 'real' (radioactive) borosilicate HLW glasses after pouring) the crystal phases $Ce_{1-(x+y)}Zr_xGd_yO_{2-(y/2)}$ (defect fluorite structure), (Sr,Nd,La) molybdate (powellite structure suspected) and lanthanide (Nd,Gd,La,Ce) silicate (unidentified structure) were detected. $Ce_{1-(x+y)}Zr_xGd_yO_{2-(y/2)}$ is a potential host for Pu and U; (Sr,Nd,La) molybdate is a potential host for $^{90}Sr$, Am and Cm; lanthanide (Nd,Gd,La,Ce) silicate is a potential host for Am and Cm. Generally, aqueous durability testing of as-cast and heat treated Blend glass samples revealed heat treatment of Blend glass improved its aqueous durability marginally. The crystal phases $RuO_2$, $Ce_{1-(x+y)}Zr_xGd_yO_{2-(y/2)}$, (Sr,Nd,La) molybdate and lanthanide (Nd,Gd,La,Ce) silicate were not water soluble.

As-cast Oxide glass samples had either (1) a compositionally homogeneous glass matrix (Type I microstructure) or (2) a compositionally inhomogeneous glass matrix (Type II microstructure) resulting from insufficient reaction time in the glass melter. The crystal phases $RuO_2$ (rutile structure), metallic Pd-Te (fcc structure) and $(Cr,Fe,Ni)_3O_4$ (spinel structure) were observed in both Type I and Type II microstructures, with $Na_3Li(MoO_4)_2 \cdot 6H_2O$ (rhombohedral system) occasionally detected. The crystal phases $Zr_{1-(x+y)}Ce_xGd_yO_{2-(y/2)}$ (defect fluorite structure) and lanthanide (Nd,Gd,La,Ce) silicate (unidentified structure) were only detected in Type II microstructures. Metallic Pd-Te is a potential host for $^{79}Se$; $Zr_{1-(x+y)}Ce_xGd_yO_{2-(y/2)}$ is a potential host for Pu and U; lanthanide (Nd,Gd,La,Ce) silicate is a potential host for Am and Cm. After heat treatment of Oxide glass samples, what had been a Type I microstructure resulted in extensive crystallisation of the glass and extensive matrix

cracking (termed Type A microstructure) and what had been a Type II microstructure yielded 'banded' crystallisation (termed Type B microsturucture). The crystal phases $(Na,Sr,Nd,La)MoO_4$ (powellite structure), $Ce_{1-(x+y)}Zr_xGd_yO_{2-(y/2)}$ (defect fluorite structure) and a Ni-rich phase (unidentified structure) were detected in both Type A and Type B mictrostructures. The crystal phase $\alpha$-cristobalite (tetragonal system) was found exclusively in Type A microstructures, whilst the crystal phases lanthanide (Nd,Gd,La,Ce) silicate (unidentified structure) and zektzerite (orthorhombic system) were only detected in Type B microstructures. The formation of both $\alpha$-cristobalite and zektzerite depletes the glass surrounding them in $SiO_2$. $(Na,Sr,Nd,La)MoO_4$ is a potential host for $^{90}Sr$, Am and Cm; $Ce_{1-(x+y)}Zr_xGd_yO_{2-(y/2)}$ is a potential host for U and Pu; lanthanide (Nd,Gd,La,Ce) silicate is a potential host for Am and Cm. Aqueous durability testing of as-cast and heat treated Oxide glass samples (Type I and Type A microstructures only) revealed heat treatment of Oxide glass decreased its aqueous durability significantly, due to the formation of $\alpha$-cristobalite. The crystal phases $RuO_2$, metallic Pd-Te, $\alpha$-cristobalite and $(Na,Sr,Nd,La)MoO_4$ were not water soluble.

The chemical composition of the 'yellow phase' inclusion found in an as-cast Oxide glass sample showed it to be enriched in Mo, Cs, Na, Li, Cr, Ba, Sr and Te relative to the glass. This indicates that the radionuclides $^{137}Cs$, $^{135}Cs$ and $^{90}Sr$ will preferentially partition to 'yellow phase'. The radionuclides $^{99}Tc$ and $^{79}Se$ may preferentially partition to 'yellow phase', as $[TcO_4]^-$ and $[SeO_4]^{2-}$ oxyanions respectively. The 'yellow phase' inclusion was crystalline; with the crystal phases $CsLiMoO_4$ (cubic system), $Na_3Li(MoO_4)_2 \cdot 6H_2O$ (rhombohedral system), $(Na,Sr,Nd)MoO_4$ (powellite structure) and $Ba_{1-x}Sr_xMoO_4$ (where $0 < x < 0.5$) (powellite structure) present. $CsLiMoO_4$ is a potential host for $^{137}Cs$ and $^{135}Cs$; $(Na,Sr,Nd)MoO_4$ and $Ba_{1-x}Sr_xMoO_4$ (where $0 < x < 0.5$) are potential hosts for $^{90}Sr$. $CsLiMoO_4$ and $Na_3Li(MoO_4)_2 \cdot 6H_2O$ are water soluble.

## 6.2 Suggested Further Work

- Ideally, all of the experiments performed in this work would be repeated using the 'real' (radioactive) versions of these simulated borosilicate HLW glasses.
- Determine the crystal structure of the lanthanide (Nd,Gd,La,Ce) silicate phase(s) found in heat treated Blend glass, and both as-cast and heat treated Oxide glass. This will show whether all three phases are the same or not and may yield a new crystal phase to host +3 valent actinides, or even a crystal phase new to science.
- All crystal phases detailed in this work should be synthesised to: test their chemical durabilities; determine their thermal expansion coefficients; investigate if any crystal phase transitions occur as they cool, and to find out whether they are radiation tolerant.
- Investigate sodium borosilicate glasses whose compositions are outside the 'traditional' immiscibility region of the ternary phase diagram. Particular emphasis should be placed on determining whether there is Å- to nm-scale amorphous phase separation. Use samples of similar composition to those investigated by Ledieu *et al.* (2004).
- Study the near surface region of as-cast borosilicate HLW glasses in terms of the concentration of certain network modifiers and also cations which from oxyanions, relating these to the concentration of B and Si. Aqueous durability testing of these surfaces will reveal whether they are less durable than the bulk glass.
- Study whether Te and Se can form oxyanions independent of the borosilicate glass network and whether this is the case in nitrate salt melts.
- Look at the effect of removing $LiNO_3$ (but boosting the $Li_2O$ in the base glass) from the calcine on 'yellow phase' formation during glass melting.
- Experiments to investigate whether Tc, Se, Am, Cm, Np, as well as Nb, As and Sb preferentially partition to 'yellow phase' should be performed. Re is a good surrogate for Tc (Darab and Smith, 1996; Langowski *et al.*, 1996a; Lukens *et al.*, 2007) – except under reducing conditions (Lukens *et al.*, 2007), with Pr suggested as a surrogate for Am and Cm.
- Partition coefficients for all borosilicate HLW components between glass and 'yellow phase' should be determined, taking into account the volatilisation of some components as well as some elements being present in multiple valence

states. These partition coefficients can then be used to investigate whether they relate to the Dietzel field strength and/or bond valence of specific cations, or whether there is some other relationship.

- Produce crystal phases which were proposed to exist in the 'yellow phase' inclusion (chromates, tellurates and selenates) to see what elements they can incorporate and also use them to identify crystal phases observed in 'yellow phase' samples investigated in the future. Tests of whether they are hygroscopic, water soluble and the like would be very informative.

# References


Aagaard, P., and Helgeson, H. C. (1982) *Thermodynamic and kinetic constraints on reaction rates among minerals and aqueous solutions. I. Theoretical considerations* Am. J. Sci. **282**, 237–285.

Abdelouas, A., Crovisier, J.-L., Lutze, W., Grambow, B., Dran, J.-C., and Müller, R. (1997) *Surface layers on a borosilicate nuclear waste glass corroded in $MgCl_2$ solution* J. Nucl. Mater. **240**, 100–111.

Abraitis, P. K. (1999) *Dissolution of a Simulated Magnox Waste Glass in Aqueous Solutions at Temperatures Below 100 °C* Ph.D. Thesis, Department of Earth Sciences, University of Manchester.

Abraitis, P. K., Livens, F. R., Monteith, J. E., Small, J. S., Trivedi, D. P., Vaughan, D. J., and Wogelius, R. A. (2000) *The kinetics and mechanisms of simulated British Magnox waste glass dissolution as a function of pH, silicic acid activity and time in low temperature aqueous systems* Appl. Geochem. **15**, 1399–1416.

Alton, J., Plaisted, T. J., and Hrma, P. (2002) *Dissolution and growth of spinel crystals in a borosilicate glass* J. Non-Cryst. Solids **311**, 24–35.

Arbab, M., Marghussian, V. K., Sarpoolaky, H., and Kord, M. (2007) *The effect of RO oxides on microstructure and chemical durability of borosilicate glasses opacified by $P_2O_5$* Ceram. Int. **33** (6), 943–950.

ASTM (2002) *Standard test methods for determining chemical durability of nuclear, hazardous, and mixed waste glasses and multiphase glass ceramics: the product consistency test (PCT)* C 1285 – 02, ASTM International, West Conshohocken, PA.

Barkatt, Aa., Barkatt, Al., Phersson, P. E., Szoke, P., and Macedo, P. B. (1981) *Static and dynamic tests for the chemical durability of nuclear waste glass* Nucl. Chem. Waste Manag. **2**, 151–164.

Barkatt, Aa., Macedo, P. B., Sousanpour, W., Barkatt, Al., Boroomand, M. A., Fisher, C. F., Shirron, J. J., Szoke, P., and Rogers, V. L. (1983) *The use of a flow test and a flow model in evaluating the durability of various nuclear waste-form materials* Nucl. Chem. Waste Manag. **4**, 153–169.

Barkatt, Aa., Macedo, P. B., Gibson, B. C., Mowad, R., Sousanpour, W., Barkatt, Al., Boroomand, M. A., Adel-Hadadi, M., and Rogers, V. L. (1985) *The behavior of defense waste reference glass in a long-term pulsed-flow leach test* Waste Management '85 Conference, Tucson, AZ, 471–476.

Bart, F., Dussossoy, J. L., and Fillet, C. (2001) *Influence of platinum-group metals on nuclear glass properties: viscosity, thermal stability and alterability* Mater. Res. Soc. Symp. Proc. **663**, 161–167.

Bart, J. M., Ribes, A., Rigaud, D., Boubals, J. M., Bart, F., and Fillet, C. (2000) *Cerium oxide solubility in borosilicate glass* Ceram. Trans. **107**, 665–672.

Bates, J. K., Emery, J. W., Hoh, J. C., and Johnson, T. R. (1995) *Performance of high plutonium-containing glasses for the immobilization of surplus fissile materials* Ceram. Trans. **61**, 447–454.

Bickford, D. F., and Jantzen, C. M. (1984) *Devitrification behavior of SRL defense waste glass* Mater. Res. Soc. Symp. Proc. **26**, 557–566.

Bickford, D. F., and Jantzen, C. M. (1986) *Devitrification of defense nuclear waste glasses: role of melt insolubles* J. Non-Cryst. Solids **84**, 299–307.

Bickford, D. F., Applewhite-Ramsey, A., Jantzen, C. M., and Brown, K. G. (1990a) *Control of radioactive waste glass melters: I, preliminary general limits at Savannah River* J. Am. Ceram. Soc. **73** (10), 2896–2902.

Bickford, D. F., Hrma, P., and Bowan, B. W. (1990b) *Control of radioactive waste glass melters: II, residence time and melt rate limitations* J. Am. Ceram. Soc. **73** (10), 2903–2915.

Bouchet, L., Rivoallan, A., Milot, J. F., and Bart, F. (2000) *Phenomenological study of the reactions between glass frit and simulated fission products calcine* Atalante 2000 Conference, Avignon, France, P4-26.

Bourcier, W. L. (1991) *Overview of chemical modeling of nuclear waste glass dissolution* Mater. Res. Soc. Symp. Proc. **212**, 3–18.

Bourcier, W. L. (1994) *Waste glass corrosion modeling: comparison with experimental results* Mater. Res. Soc. Symp. Proc. **333**, 69–82.

Bouvier, P., Djuardo, E., Lucazeau, G., and Le Bihan, T. (2000) *High-pressure structural evolution of undoped tetragonal nanocrystalline zirconia* Phys. Rev. B **62** (13), 8731–8737.

Brese, N. E., and O'Keeffe, M. (1991) *Bond-valence parameters for solids* Acta Cryst. B **47** (2), 192–197.

Buechele, A. C., Feng, X., Gu, H., and Pegg, I. L. (1990) *Alteration of microstructure of West Valley glass by heat treatment* Mater. Res. Soc. Symp. Proc. **176**, 393–402.

Buechele, A. C., Muller, I. S., Pegg, I. L., Kim, C.-W., and Yaschenko, E. (1995) *Properties of glasses for Idaho mixed waste vitrification* Ceram. Trans. **61**, 203–211.

Bunker, B. C. (1987) *Waste glass leaching: chemistry and kinetics* Mater. Res. Soc. Symp. Proc. **84**, 493–507.

Bunker, B. C. (1994) *Molecular mechanisms for corrosion of silica and silicate glasses* J. Non-Cryst. Solids **179**, 300–308.

Burns, P. C., Hawthorne, F. C., MacDonald, D. J., Della Ventura, G., and Parodi, G. C. (1993) *The crystal structure of stillwellite* Can. Mineral. **31**, 147–152.

Cachia, J.-N., Deschanels, X., Den Auwer, C., Pinet, O., Phalippou, J., Hennig, C., and Scheinost, A. (2006) *Enhancing cerium and plutonium solubility by reduction in borosilicate glass* J. Nucl. Mater. **352** (1–3), 182–189.

Calas, G., Le Grand, M., Galoisy, L., and Ghaleb, D. (2003) *Structural role of molybdenum in nuclear glasses: an EXAFS study* J. Nucl. Mater. **322**, 15–20.

Camara, B., Lutze, W., and Lux, J. (1980) *An investigation on the valency state of molybdenum in glasses with and without fission products* in 'Scientific Basis for Nuclear Waste Management II' ed. Northrup, C. J. M., Plenum Press, New York, 93–102.

Capobianco, C. J., and Drake, M. J. (1990) *Partitioning of ruthenium, rhodium, and palladium between spinel and silicate melt and implications for platinum group element fractionation trends* Geochim. Cosmochim. Acta **54**, 869–874.

Caurant, D., Majerus, O., Loiseau, P., Bardez, I., Baffier, N., and Dussossoy, J. L. (2006) *Crystallization of neodymium-rich phases in silicate glasses developed for nuclear waste immobilization* J. Nucl. Mater. **354** (1–3), 143–162.

Caurant, D., Majérus, O., Fadel, E., Lenoir, M., Gervais, C., and Pinet, O. (2007) *Effect of molybdenum on the structure and on the crystallization of $SiO_2$–$Na_2O$–$CaO$–$B_2O_3$ glasses* J. Am. Ceram. Soc. **90** (3), 774–783.

Chêne, J., and Trocellier, P. (2004) *Investigation of alkali borosilicate glass durability using tritium tracing, β-autoradiography, scanning electron microscopy and ion beam analysis* J. Non-Cryst. Solids **337**, 86–96.

Cheron, P., Chevalier, Ph., Do Quang, R., Tanguy, G., Sourrouille, M., Woignier, S., Senoo, N., Banba, T., Kuramoto, K., Yamaguchi, T., Shimizu, K., Fillet, C., Jacquet-Francillon, N., Godard, J., Dussossoy, J. L., Pacaud, F., and Charbonnel, J. G. (1995) *Examination and testing of an active glass sample produced by Cogema* Mater. Res. Soc. Symp. Proc. **353**, 55–62.

Clark, D. E., and Hench, L. L. (1981) *An overview of the physical characterization of leached surfaces* Nucl. Chem. Waste Manag. **2**, 93–101.

Clark, D. E., and Zoitos, B. K. (1992) *Corrosion testing and characterization* in 'Corrosion of Glass, Ceramics and Ceramic Superconductors' eds. Clark, D. E., and Zoitos, B. K., Noyes Publications, New Jersey, 51–102.

Clark, D. E., Maurer, C. A., Jurgensen, A. R., and Urwongse, L. (1982) *Effects of waste composition and loading on the chemical durability of a borosilicate glass* Mater. Res. Soc. Symp. Proc. **11**, 1–11.

Clarke, D. R. (1983) *Ceramic materials for the immobilization of nuclear waste* Annu. Rev. Mater. Sci. **13**, 191–218.

Cousi, C., Bart, F., and Phalippou, J. (2004) *Phase separation and crystallisation induced by adding molybdenum and phosphorus to a soda–lime–silica glass* Glass Technol. **45** (2), 65–67.

Crichton, S. N., Barbieri, T. J., and Tomozawa, M. (1995) *Solubility limits for troublesome components in a simulated low level nuclear waste glass* Ceram. Trans. **61**, 283–290.

Crum, J. V., Schweiger, M. J., Hrma, P., and Vienna, J. D. (1997) *Liquidus temperature model for Hanford high-level waste glasses with high concentration of zirconia* Mater. Res. Soc. Symp. Proc. **465**, 79–85.

Crum, J. V., Vienna, J. D., Peeler, D. K., Reamer, I. A., and Pittman, D. J. (2002) *The effect of glass composition on crystallinity and durability for INEEL run 78 calcine waste simulant* Ceram. Trans. **132**, 267–275.

Curti, E., Crovisier, J. L., Morvan, G., and Karpoff, A. M. (2006) *Long-term corrosion of two nuclear waste reference glasses (MW and SON68): a kinetic and mineral alteration study* Appl. Geochem. **21**, 1152–1168.

Darab, J. G., and Smith, P. A. (1996) *Chemistry of technetium and rhenium species during low-level radioactive waste vitrification* Chem. Mater. **8** (5), 1004–1021.

Dé, A. K., Luckscheiter, B., Lutze, W., Malow, G., and Schiewer, E. (1976) *Development of glass ceramics for the incorporation of fission products* Am. Ceram. Soc. Bull. **55** (5), 500–503.

Della Giusta, A., Princivalle, F., and Carbonin, S. (1987) *Crystal structure and cation distribution in some natural magnetites* Mineral. Petrol. **37** (3–4), 315–321.

Demin, A. V., Fedorova, M. I., and Matyunin, Yu. I. (1996) *Localization of platinum-group elements and technetium and the solidification of high-level liquid wastes* Atomic Energy **80** (3), 178–181.

Dietzel, A. (1942) *Die kationenfeldstärken und ihre beziehungen zu entglasungsvorgängen, zur verbindungsbildung und zu den schmelzpunkten von silicaten* Z. Elektrochem. **48** (1), 9–23.

Donald, I. W., Metcalfe, B. L., and Taylor, R. N. J. (1997) *The immobilization of high level radioactive wastes using ceramics and glasses* J. Mater. Sci. **32**, 5851–5887.

Doremus, R. H. (1982) *Interdiffusion of alkali and hydronium ions in glass: partial ionization* J. Non-Cryst. Solids **48**, 431–436.

Du, L.-S., and Stebbins, J. F. (2003) *Nature of silicon-boron mixing in sodium borosilicate glasses: a high-resolution $^{11}B$ and $^{17}O$ NMR study* J. Phys. Chem. B **107** (37), 10063–10076.

Dunn, P. J., Rouse, R. C., Cannon, B., and Nelen, J. A. (1977) *Zektzerite: a new lithium sodium zirconium silicate related to tuhualite and the osumilite group* Am. Mineral. **62**, 416–420.

Ebert, W. L., and Mazer, J. J. (1994) *Laboratory testing of waste glass aqueous corrosion; effects of experimental parameters* Mater. Res. Soc. Symp. Proc. **333**, 27–40.

Ebert, W. L., and Wolf, S. F. (2000) *An interlaboratory study of a standard glass for acceptance testing of low-activity waste glass* J. Nucl. Mater. **282**, 112–124.

Ewing, R. C. (2001) *Nuclear waste form glasses: the evaluation of very long-term behaviour* Mater. Technol. **16** (1), 30–36.

Fábián, M., Sváb, E., Mészáros, Gy., Révay, Zs., Proffen, Th., and Veress, E. (2007) *Network structure of multi-component sodium borosilicate glasses by neutron diffraction* J. Non-Cryst. Solids **353**, 2084–2089.

Feld, R. H., and Stammler, M. (1982) *Quantitative determination of crystalline phases in nuclear waste glasses* Mater. Res. Soc. Symp. Proc. **11**, 261–271.

Feng, X., and Pegg, I. L. (1994) *A glass dissolution model for the effects of S/V on leachate pH* J. Non-Cryst. Solids **175**, 281–293.

Ferrand, K., Abdelouas, A., and Grambow, B. (2006) *Water diffusion in the simulated French nuclear waste glass SON 68 contacting silica rich solutions: experimental and modeling* J. Nucl. Mater. **355**, 54–67.

Fleming, B. A. (1986) *Kinetics of reaction between silicic acid and amorphous silica surfaces in NaCl solutions* J. Colloid Interface Sci. **110** (1), 40–64.

Frugier, P., Martin, C., Ribet, I., Advocat, T., and Gin, S. (2005) *The effect of composition on the leaching of three nuclear waste glasses: R7T7, AVM and VRZ* J. Nucl. Mater. **346**, 194–207.

Galoisy, L., Calas, G., Morin, G., Pugnet, S., and Fillet, C. (1998) *Structure of Pd-Te precipitates in a simulated high-level nuclear waste glass* J. Mater. Res. **13** (5), 1124–1127.

Gauthier, A., Le Coustumer, P., Motelica, M., and Donard, O. F. X. (2000) *Real time alteration of a nuclear waste glass and remobilization of lanthanide into an interphase* Waste Manag. **20**, 731–739.

Ghose, S., and Wan, C. (1978) *Zektzerite, $NaLiZrSi_6O_{15}$: a silicate with six-tetrahedral-repeat double chains* Am. Mineral. **63**, 304–310.

Goldman, D. S. (1986) *Melt foaming, foam stability and redox in nuclear waste vitrification* J. Non-Cryst. Solids **84**, 292–298.

Goldman, D. S., and Brite, D. W. (1986) *Redox characterization of simulated nuclear waste glass* J. Am. Ceram. Soc. **69** (5), 411–413.

Gong, W. L., Wang, L. M., Ewing, R. C., Vernaz, E., Bates, J. K., and Ebert, W. L. (1998) *Analytical electron microscopy study of surface layers formed on the French SON68 nuclear waste glass during vapor hydration at 200°C* J. Nucl. Mater. **254**, 249–265.

Gong, W. L., Lutze, W., and Ewing, R. C. (2000) *Reaction sintered glass: a durable matrix for spinel-forming nuclear waste compositions* J. Nucl. Mater. **278**, 73–84.

González-Calbet, J. M., Herrero, M. P., Alario-Franco, M. A., and Pernet, M. (1987) *High pressure synthesis of Ru-Cr mixed oxides and oxyhydroxides* J. Less-Common Met. **135** (1), 105–111.

Gou, F., Greaves, G. N., Smith, W., and Winter, R. (2001) *Molecular dynamics simulation of sodium borosilicate glasses* J. Non-Cryst. Solids **293–295**, 539–546.

Grambow, B. (1992) *Geochemical approach to glass dissolution* in 'Corrosion of Glass, Ceramics and Ceramic Superconductors' eds. Clark, D. E., and Zoitos, B. K., Noyes Publications, New Jersey, 124–152.

Greaves, G. N. (1985) *EXAFS and the structure of glass* J. Non-Cryst. Solids **71**, 203–217.

Greaves, G. N. (1990) *EXAFS for studying corrosion of glass surfaces* J. Non-Cryst. Solids **120**, 108–116.

Greenwood, N. N., and Earnshaw, A. (2002) *Chemistry of the Elements – Second Edition* Butterworth-Heinemann, Oxford.

Guber, W., Hussain, M., Kahl, L., Ondracek, G., and Saidl, J. (1979) *Preparation and characterization of an improved high level radio-active waste (HAW) borosilicate glass* in 'Scientific Basis for Nuclear Waste Management I' ed. McCarthy, G. J., Plenum Press, New York, 37–42.

Haaker, R. F., and Ewing, R. C. (1981) *Natural analogues for crystalline radioactive waste forms, part II: non-actinide phases* in 'Scientific Basis for Nuclear Waste Management III' ed. Moore, J. G., Plenum Press, New York, 299–306.

Hair, M. L., and Chapman, I. D. (1966) *Surface composition of porous glass* J. Am. Ceram. Soc. **49** (12), 651–654.

Hall, A. R., Dalton, J. T., Hudson, B., and Marples, J. A. C. (1976) *Development and radiation stability of glasses for highly radioactive wastes* in 'Management of Radioactive Wastes from the Nuclear Fuel Cycle' Proc. Symp. **2**, IAEA, Vienna, 3–14.

Hand, R. J., and Seddon, A. B. (1997) *An hypothesis on the nature of Griffith's cracks in alkali silicate and silica glasses* Phys. Chem. Glasses **38** (1), 11–14.

Hazen, R. M., Finger, L. W., and Mariathasan, J. W. E. (1985) *High pressure crystal chemistry of scheelite-type tungstates and molybdates* J. Phys. Chem. Solids **46** (2), 253–263.

Healey, J. T., Headley, T. J., Hlava, P. F., Strachan, D. M., and Kupfer, M. J. (1979) *Microstructural characterization of solidified simulated reactor wasteforms* in 'Scientific Basis for Nuclear Waste Management I' ed. McCarthy, G. J., Plenum Press, New York, 83–96.

Henry, N., Deniard, P., Jobic, S., Brec, R., Fillet, C., Bart, F., Grandjean, A., and Pinet, O. (2004) *Heat treatments versus microstructure in a molybdenum-rich borosilicate* J. Non-Cryst. Solids **333**, 199–205.

Hewitt, C. N. (2001) *Radioactivity in the environment* in 'Pollution: Causes, Effects and Control – Fourth Edition' ed. Harrison, R. M., The Royal Society of Chemistry, Cambridge, 474–499.

Horneber, A., Camara, B., and Lutze, W. (1982) *Investigation on the oxidation state and the behaviour of molybdenum in silicate glass* Mater. Res. Soc. Symp. Proc. **11**, 279–288.

Hrma, P. (2002) *Crystallization in high-level waste glasses* Ceram. Trans. **132**, 243–256.

Hrma, P., Vienna, J., Crum, J., and Piepel, G. (2000) *Liquidus temperature of high-level waste borosilicate glasses with spinel primary phase* Mater. Res. Soc. Symp. Proc. **608**, 671–676.

Hrma, P., Riley, B. J., and Vienna, J. D. (2003) *Corrosion of partially crystallized glasses* Ceram. Trans. **143**, 291–298.

Hrma, P., Crum, J. V., Bredt, P. R., Greenwood, L. R., Arey, B. W., and Smith, H. D. (2005) *Vitrification and testing of a Hanford high-level waste sample. Part 2: phase identification and waste form leachability* J. Nucl. Mater. **345**, 31–40.

Hrma, P., Vienna, J. D., Wilson, B. K., Plaisted, T. J., and Heald, S. M. (2006) *Chromium phase behavior in a multi-component borosilicate glass melt* J. Non-Cryst. Solids **352**, 2114–2122.

Hyatt, N. C., Taylor, K. J., Gibb, F. G. F., and Lee, W. E. (2004) *Crystallisation of Magnox waste glass under conditions of high temperature, very deep, geological disposal* Glass Technol. **45** (2), 68–70.

IAEA (2003) *Scientific and technical basis for the geological disposal of radioactive wastes* Technical Reports Series No. 413, IAEA, Vienna, Austria.

Inagaki, Y., Furuya, H., Idemitsu, K., and Arima, T. (1998) *Review of waste glass corrosion and associated radionuclide release as a part of safety assesment of entire disposal system* Prog. Nucl. Energy **32** (3–4), 501–508.

Ipser, H., and Schuster, W. (1986) *Transition-metal-chalcogen systems X: the Pd-Te phase diagram* J. Less-Common Met. **125**, 183–195.

Izak, P., Hrma, P., Arey, B. W., and Plaisted, T. J. (2001) *Effect of feed melting, temperature history, and minor component addition on spinel crystallization in high-level waste glass* J. Non-Cryst. Solids **289**, 17–29.

Jacquet-Francillon, N., Pacaud, F., and Queille, P. (1982) *An attempt to assess the long-term crystallization rate of nuclear waste glasses* Mater. Res. Soc. Symp. Proc. **11**, 249–259.

Jain, V., Barnes, S. M., Vethanayagam, T. K., and Pye, L. D. (1991) *Noble metal and spinel deposition on the floor of the joule-heated ceramic melter* J. Am. Ceram. Soc. **74** (7), 1559–1562.

Jantzen, C. M., Bickford, D. F., and Karraker, D. G. (1984) *Time-temperature-transformation kinetics in SRL waste glass* Adv. Ceram. **8**, 30–38.

Jantzen, C. M., Brown, K. G., and Pickett, J. B. (2001) *Impact of phase separation on durability in phosphate containing borosilicate waste glasses: relevance to vitrification of INEEL high level waste* Ceram. Trans. **119**, 271–280.

Jean, J.-H., Kuan, T.-H., and Gupta, T. K. (1995) *Crystallization inhibitors during sintering of Pyrex borosilicate glass* J. Mater. Sci. Lett. **14**, 1068–1070.

Kahl, L. (1981) *The hydrolytic durability of two high-level waste oxide borosilicate glasses (GP 98/12 and GP 98/26)* Nucl. Chem. Waste Manag. **2**, 143–146.

Kaushik, C. P., Mishra, R. K., Sengupta, P., Kumar, A., Das, D., Kale, G. B., and Raj, K. (2006) *Barium borosilicate glass – a potential matrix for immobilization of sulfate bearing high-level radioactive liquid waste* J. Nucl. Mater. **358**, 129–138.

Kawamura, K., and Ohuchi, J. (1995) *Characterization of highly waste loaded glass for HLW* Mater. Res. Soc. Symp. Proc. **353**, 87–93.

Kelm, M., and Oser, B. (1992) *The platinum metals in HLLW – glass products* Mater. Res. Soc. Symp. Proc. **257**, 177–182.

Kim, C.-W., Muller, I. S., Buechele, A. C., Pegg, I. L., and Macedo, P. B. (1996) *Redox state and transition metal concentration effects on microstructure of simulated simplified glasses for waste immobilization* Mater. Res. Soc. Symp. Proc. **412**, 149–156.

Kim, D.-S., Hrma, P., Smith, D. E., and Schweiger, M. J. (1994) *Crystallization in simulated glasses from Hanford high-level nuclear waste composition range* Ceram. Trans. **39**, 179–189.

Kim, D.-S., Peeler, D. K., and Hrma, P. (1995) *Effect of crystallization on the chemical durability of simulated nuclear waste glasses* Ceram. Trans. **61**, 177–185.

Klevtsova, R. F., Klevtsov, P. V., and Aleksandrov, K. S. (1980) *Synthesis and crystal structure of $CsLiMoO_4$* Sov. Phys. Dokl. **25** (12), 966–968.

Kleykamp, H. (1985) *The chemical state of the fission products in oxide fuels* J. Nucl. Mater. **131**, 221–246.

Komarneni, S., Roy, R., and Roy, D. M. (1983) *Evaluation of $SrMoO_4$ in repository simulating tests* Nucl. Technol. **62**, 71–74.

Krause, Ch., and Luckscheiter, B. (1991) *Properties and behavior of the platinum group metals in the glass resulting from the vitrification of simulated nuclear fuel reprocessing waste* J. Mater. Res. **6** (12), 2535–2546.

LaMont, M. J., and Hrma, P. (1998) *A crucible study of spinel settling in a high-level waste glass* Ceram. Trans. **87**, 343–348.

Langowski, M. H., Darab, J. G., and Smith, P. A. (1996a) *Volatility literature of chlorine, iodine, cesium, strontium, technetium, and rhenium; technetium and rhenium volatility testing* PNNL-11052 UC-512, Pacific Northwest National Laboratory, Richland, WA.

Langowski, M. H., Li, H., Hrma, P., Schweiger, M. J., and Smith, D. E. (1996b) *The effect of phosphate on crystallisation, viscosity, and chemical durability of simulated Hanford site high-level radioactive waste glasses* Ceram. Trans. **72**, 291–298.

Larkin, M. J. (1986) *Development of highly active waste conditioning at Sellafield* Nucl. Energy **25** (6), 343–354.

Ledieu, A., Devreux, F., Barboux, P., Sicard, L., and Spalla, O. (2004) *Leaching of borosilicate glasses. I. Experiments* J. Non-Cryst. Solids **343** (1–3), 3–12.

Li, H., Langowski, M. H., and Hrma, P. R. (1995) *Segregation of sulfate and phosphate in the vitrification of high-level wastes* Ceram. Trans. **61**, 195–202.

Li, H., Hrma, P., Langowski, M. H., and Hlaváč, J. (1996a) *Vitrification and chemical durability of simulated high-level nuclear waste glasses with high concentrations of* $Cr_2O_3$ *and* $Al_2O_3$ Ceram. Trans. **72**, 299–306.

Li, H., Vienna, J. D., Hrma, P., Schweiger, M. J., Smith, D. E., and Gong, M. (1996b) *Borosilicate based glasses for immobilization of plutonium-bearing materials* Ceram. Trans. **72**, 399–408.

Li, H., Hrma, P., and Vienna, J. D. (2001) *Sulfate retention and segregation in simulated radioactive waste borosilicate glasses* Ceram. Trans. **119**, 237–245.

Li, H., Hrma, P., Vienna, J. D., Qian, M., Su, Y., and Smith, D. E. (2003) *Effects of* $Al_2O_3$, $B_2O_3$, $Na_2O$, *and* $SiO_2$ *on nepheline formation in borosilicate glasses: chemical and physical correlations* J. Non-Cryst. Solids **331**, 202–216.

Li, L., Strachan, D. M., Li, H., Davis, L. L., and Qian, M. (2000a) *Crystallization of gadolinium- and lanthanum-containing phases from sodium alumino-borosilicate glasses* J. Non-Cryst. Solids **272**, 46–56.

Li, L., Strachan, D. M., Li, H., Davis, L. L., and Qian, M. (2000b) *Peraluminous and peralkaline effects on $Gd_2O_3$ and $La_2O_3$ solubilities in sodium-alumino-borosilicate glasses* Ceram. Trans. **107**, 131–138.

Li, L., Li, H., Qian, M., and Strachan, D. M. (2001a) *Gadolinium solubility in peralkaline borosilicate glasses* J. Non-Cryst. Solids **283**, 237–245.

Li, L., Qian, M., Li, H., and Strachan, D. M. (2001b) *Phase separation in La-containing sodium alumino-borosilicate glasses* Ceram. Trans. **119**, 263–270.

Lopez, C., Deschanels, X., Bart, J. M., Boubals, J. M., Den Auwer, C., and Simoni, E. (2003) *Solubility of actinide surrogates in nuclear glasses* J. Nucl. Mater. **312**, 76–80.

Luckscheiter, B., and Nesovic, M. (1996) *Development of glasses for the vitrification of high level liquid waste (HLLW) in a joule heated ceramic melter* Waste Manag. **16** (7), 571–578.

Lukens, W. W., Shuh, D. K., Muller, I. S., and McKeown, D. A. (2004) *X-ray absorption fine structure studies of speciation of technetium in borosilicate glasses* Mater. Res. Soc. Symp. Proc. **802**, 101–106.

Lukens, W. W., McKeown, D. A., Buechele, A. C., Muller, I. S., Shuh, D. K., and Pegg, I. L. (2007) *Dissimilar behavior of technetium and rhenium in borosilicate waste glass as determined by X-ray absorption spectroscopy* Chem. Mater. **19** (3), 559–566.

Lutze, W. (1988) *Silicate glasses* in 'Radioactive Waste Forms for the Future' eds. Lutze, W., and Ewing, R. C., North-Holland, Amsterdam, 1–159.

Lutze, W., and Ewing, R. C. (1995) *Glass and ceramic waste forms – applications and materials properties* Ceram. Trans. **61**, 357–364.

Lutze, W., and Grambow, B. (1992) *The effect of glass corrosion on near field chemistry* Radiochim. Acta **58/59**, 3–7.

Lutze, W., Borchardt, J., and Dé, A. K. (1979) *Characterization of glass and glass ceramic nuclear waste forms* in 'Scientific Basis for Nuclear Waste Management I' ed. McCarthy, G. J., Plenum Press, New York, 69–81.

Macedo, P. B., Barkatt, Aa., and Simmons, J. H. (1982) *A flow model for the kinetics of dissolution of nuclear waste glasses* Nucl. Chem. Waste Manag. **3**, 13–21.

Malow, G. (1989) *Thermal and radiation effects in the range of the glass transition temperature $T_g$* Mater. Res. Soc. Symp. Proc. **127**, 153–162.

Manara, D., Grandjean, A., Pinet, O., Dussossoy, J. L., and Neuville, D. R. (2007) *Sulfur behavior in silicate glasses and melts: implications for sulfate incorporation in nuclear waste glasses as a function of alkali cation and $V_2O_5$ content* J. Non-Cryst. Solids **353**, 12–23.

Marples, J. A. C. (1988) *The preparation, properties, and disposal of vitrified high level waste from nuclear fuel reprocessing* Glass Technol. **29** (6), 230–247.

Marr, J. M., and Glasser, F. P. (1979) *Synthesis and properties of zektzerite, $LiNaZrSi_6O_{15}$, and its isotypes* Mineral. Mag. **43**, 171–173.

Martínez-Arias, A., Fernández-García, M., Ballesteros, V., Salamanca, L. N., Conesa, J. C., Otero, C., and Soria, J. (1999) *Characterization of high surface area Zr-Ce(1:1) mixed oxide prepared by a microemulsion method* Langmuir **15**, 4796–4802.

Matzke, Hj. (1984) *Actinide behavior and radiation damage produced by α-decay in materials to solidify nuclear waste* Inorg. Chim. Acta **94** (1–3), 142–143.

Matzke, Hj., and Vernaz, E. (1993) *Thermal and physicochemical properties important for the long term behavior of nuclear waste glasses* J. Nucl. Mater. **201**, 295–309.

Matzke, Hj., Kahl, L., Saidl, J., and Routbort, J. L. (1984) *Effect of composition and radiation on the Hertzian indentation behavior of nuclear waste glasses* Adv. Ceram. **8**, 697–709.

Mazurin, O. V., Roskova, G. P., and Porai-Koshits, E. A. (1984) *Immiscibility diagrams of oxide glass-forming systems* in 'Phase Separation in Glass' eds. Mazurin, O. V., and Porai-Koshits, E. A., North-Holland, Amsterdam, 103–142.

McConville, C. J., Lee, W. E., and Sharp, J. H. (1998) *Microstructural evolution in fired kaolinite* Br. Ceram. Trans. **97** (4), 162–168.

McGrail, B. P., Bacon, D. H., Icenhower, J. P., Mann, F. M., Puigh, R. J., Schaef, H. T., and Mattigod, S. V. (2001a) *Near-field performance assessment for a low-activity waste glass disposal system: laboratory testing to modeling results* J. Nucl. Mater. **298**, 95–111.

McGrail, B. P., Icenhower, J. P., Shuh, D. K., Liu, P., Darab, J. G., Baer, D. R., Thevuthasen, S., Shutthanandan, V., Engelhard, M. H., Booth, C. H., and Nachimuthu, P. (2001b) *The structure of $Na_2O$–$Al_2O_3$–$SiO_2$ glass: impact on sodium ion exchange in $H_2O$ and $D_2O$* J. Non-Cryst. Solids **296**, 10–26.

McKeown, D. A., Muller, I. S., Buechele, A. C., Pegg, I. L., Kendziora, C. A., and Scales, C. R. (1999) *Formulation, testing, and structural characterization of high-zirconium high-level waste glasses* Mater. Res. Soc. Symp. Proc. **556**, 305–312.

McKeown, D. A., Muller, I. S., Gan, H., Pegg, I. L., and Kendziora, C. A. (2001) *Raman studies of sulfur in borosilicate waste glasses: sulfate environments* J. Non-Cryst. Solids **288**, 191–199.

McKeown, D. A., Muller, I. S., Gan, H., Pegg, I. L., and Stolte, W. C. (2004) *Determination of sulfur environments in borosilicate waste glass using X-ray absorption near-edge spectroscopy* J. Non-Cryst. Solids **333**, 74–84.

McKinley, J. P., Zeissler, C. J., Zachara, J. M., Serne, R. J., Lindstrom, R. M., Schaef, H. T., and Orr, R. D. (2001) *Distribution and retention of $^{137}Cs$ in sediments at the Hanford site, Washington* Environ. Sci. Technol. **35**, 3433–3441.

Ménard, O., Advocat, T., Ambrosi, J. P., and Michard, A. (1998) *Behaviour of actinides (Th, U, Np and Pu) and rare earths (La, Ce and Nd) during aqueous leaching of a nuclear glass under geological disposal conditions* Appl. Geochem. **13**, 105–126.

Mendel, J. E., Ross, W. A., Roberts, F. P., Turcotte, R. P., Katayama, Y. B., and Westsik, J. H. (1976) *Thermal and radiation effects on borosilicate waste glasses* in 'Management of Radioactive Wastes from the Nuclear Fuel Cycle' Proc. Symp. **2**, IAEA, Vienna, 49–61.

Menkhaus, T. J., Hrma, P., and Li, H. (2000) *Kinetics of nepheline crystallization from high-level waste glass* Ceram. Trans. **107**, 461–468.

Mishra, R. K., Sengupta, P., Kaushik, C. P., Tyagi, A. K., Kale, G. B., and Raj, K. (2007) *Studies on immobilization of thorium in barium borosilicate glass* J. Nucl. Mater. **360**, 143–150.

Mitamura, H., Murakami, T., and Banba, T. (1985) *Crystalline phases in a devitrified simulated high-level waste glass containing the elements of the platinum group* J. Nucl. Mater. **136**, 104–116.

Mitamura, H., Banba, T., and Murakami, T. (1986) *Effects of crystalline phases on leaching of a devitrified simulated high-level waste glass* Nucl. Chem. Waste Manag. **6**, 223–231.

Mokhosoev, M. V., Get'man, E. I., and Alekseev, F. P. (1969) *Double molybdates of rubidium and rare-earth elements of composition $RbLn(MoO_4)_2$* Russ. J. Inorg. Chem. **14** (12), 1691–1693.

Morgan, S. (2005) *Characterisation and Interaction of Simulated High Level, Radioactive Waste (HLW) with Borosilicate Glass* Ph.D. Thesis, Department of Engineering Materials, University of Sheffield.

Morris, J. B., and Chidley, B. E. (1976) *Preliminary experience with the new Harwell inactive vitrification pilot plant* in 'Management of Radioactive Wastes from the Nuclear Fuel Cycle' Proc. Symp. **1**, IAEA, Vienna, 241–258.

Muller, I. S., Buechele, A. C., Perez-Cardenas, F., Gan, H., and Pegg, I. L. (1999) *Partitioning of plutonium between glass, secondary phases, and contact refractories* Mater. Res. Soc. Symp. Proc. **556**, 271–278.

Muñoz, F., Montagne, L., Delevoye, L., Durán, A., Pascual, L., Cristol, S., and Paul, J.-F. (2006) *Phosphate speciation in sodium borosilicate glasses studied by nuclear magnetic resonance* J. Non-Cryst. Solids **352** (28–29), 2958–2968.

Nirex (2002) *Radioactive wastes in the UK: a summary of the 2001 inventory* DEFRA/RAS/02.003, Nirex Report N/041, United Kingdom Nirex Limited, Harwell.

O'Holleran, T. P., Johnson, S. G., Kong, P. C., and Staples, B. A. (1998) *Plutonium host phases derived from high-level waste at the Idaho chemical processing plant* Ceram. Trans. **87**, 541–550.

Ojovan, M., Moebus, G., Ojovan, N., McLeod, C., and Cox, A. (2005) *Surface structure of corroded nuclear waste glasses* ICP Inform. Newslett. **30** (10), 1022–1024.

Ojovan, M. I., Pankov, A., and Lee, W. E. (2006) *The ion exchange phase in corrosion of nuclear waste glasses* J. Nucl. Mater. **358**, 57–68.

Okamoto, H. (1994) *Comment on Pd-Rh (palladium-rhodium)* J. Phase Equilibria **15** (3), 369.

Orlhac, X., Fillet, C., and Phalippou, J. (1999) *Study of crystallization mechanisms in the French nuclear waste glass* Mater. Res. Soc. Symp. Proc. **556**, 263–270.

Pacaud, F., Fillet, C., and Jacquet-Francillon, N. (1992) *Effect of platinoids on French LWR reference glass properties* Mater. Res. Soc. Symp. Proc. **257**, 161–167.

Palmer, R. A. (1995) *History of radioactive waste – how did we get here?* Ceram. Trans. **61**, 99–104.

Paul, A. (1990) *Chemistry of Glasses – Second Edition* Chapman and Hall, London.

Peacor, D. R. (1973) *High-temperature single-crystal study of the cristobalite inversion* Z. Kristallogr. **138**, 274–298.

Pegg, I. L., and Joseph, I. (2001) *Vitrification* in 'Hazardous and Radioactive Waste Treatment Technologies Handbook' ed. Oh, C. H., CRC Press, Boca Raton, 4.2, 1–27.

Peuget, S., Cachia, J.-N., Jégou, C., Deschanels, X., Roudil, D., Broudic, V., Delaye, J. M., and Bart, J.-M. (2006) *Irradiation stability of R7T7-type borosilicate glass* J. Nucl. Mater. **354** (1–3), 1–13.

Pinet, O., Grandjean, A., Frugier, P., Rabiller, H., and Poissonnet, S. (2006) *Leaching behavior of a polyphase glass–ceramic containment matrix* J. Non-Cryst. Solids **352**, 3095–3102.

Plaisted, T., Hrma, P., Vienna, J., and Jiricka, A. (2000) *Liquidus temperature and primary crystallization phases in high-zirconia high-level waste borosilicate glass* Mater. Res. Soc. Symp. Proc. **608**, 709–714.

Plaisted, T., Mo, F., Wilson, B., Young, C., and Hrma, P. (2001) *Surface crystallization and composition of spinel and acmite in high-level waste glass* Ceram. Trans. **119**, 317–325.

Plodinec, M. J. (1986) *Vitrification chemistry and nuclear waste* J. Non-Cryst. Solids **84**, 206–214.

Pluth, J. J., Smith, J. V., and Faber, J. (1985) *Crystal structure of low cristobalite at 10, 293, and 473 K: variation of framework geometry with temperature* J. Appl. Phys. **57** (4), 1045–1049.

Quintas, A., Majérus, O., Caurant, D., Dussossoy, J.-L., and Vermaut, P. (2007) *Crystallization of a rare earth-rich aluminoborosilicate glass with varying $CaO/Na_2O$ ratio* J. Am. Ceram. Soc. **90** (3), 712–719.

Rafferty, A., Hill, R. G., and Wood, D. (2003) *An investigation into the amorphous phase separation characteristics of an ionomer glass series and a sodium-boro-silicate glass system* J. Mater. Sci. **38**, 2311–2319.

Raman, S. V. (1998) *The effect of mixed modifiers on nuclear waste glass processing, leaching, and Raman spectra* J. Mater. Res. **13** (1), 8–15.

Raman, S. V., Scholes, B. A., Erickson, A., and Zareba, A. A. (2003) *Phase equilibria, viscosity, durability, and Raman spectra in the system for Idaho nuclear waste forms* Ceram. Trans. **143**, 185–198.

Ramos, A., Levelut, C., and Petiau, J. (1992) *Local environment of selenium in silicate glasses* J. Non-Cryst. Solids **151**, 13–22.

Rao, K. V. K., and Iyengar, L. (1969) *X-ray studies on the thermal expansion of ruthenium dioxide* Acta. Cryst. A **25** (2), 302–303.

Rebollo, N. R., Fabrichnaya, O., and Levi, C. G. (2003) *Phase stability of Y+Gd co-doped zirconia* Z. Metallkd. **94** (3), 163–170.

Reynolds, J. G., and Hrma, P. (1997) *The kinetics of spinel crystallization from a high-level waste glass* Mater. Res. Soc. Symp. Proc. **465**, 65–69.

Riley, B. J., Hrma, P., Rosario, J., and Vienna, J. D. (2002) *Effect of crystallisation on high-level waste glass corrosion* Ceram. Trans. **132**, 257–265.

Roth, G., and Weisenburger, S. (2000) *Vitrification of high-level liquid waste: glass chemistry, process chemistry and process technology* Nucl. Eng. Des. **202**, 197–207.

Roth, G., Weisenburger, S., Grünewald, W., and Gauthier, Y. (2002) *Effect of canister filling by multiple pouring batches on quality properties of HLW glass product* Proc. 8th Int. Conf. Radioact. Waste Manag. Environ. Remed. (ICEM '01, Bruges, Belgium) **3**, ASME, 1563–1568.

Sales, B. C., White, C. W., and Boatner, L. A. (1983) *A comparison of the corrosion characteristics of synthetic monazite and borosilicate glass containing simulated nuclear defense waste* Nucl. Chem. Waste Manag. **4**, 281–289.

Sattler, J. P., and Nemarich, J. (1970) *Unusual electron paramagnetic resonance hyperfine spectra of $Yb^{3+}$ in scheelites* Phys. Rev. B **1** (11), 4256–4261.

Schieber, M. M. (1965) *Growth of rare earth scheelites by the flux method* Inorg. Chem. **4** (5), 762–763.

Schieber, M., and Holmes, L. (1964) *Crystal growth and magnetic susceptibilities of some rare-earth sodium molybdenum scheelites* J. Appl. Phys. **35** (3), 1004–1005.

Schiewer, E., Rabe, H., and Weisenburger, S. (1982) *The materials balance – scientific fundamentals for the quality assurance of vitrified waste* Mater. Res. Soc. Symp. Proc. **11**, 289–297.

Schreiber, H. D., and Schreiber, C. W. (1993) *Polyselenide formation in borosilicate glasses* J. Non-Cryst. Solids **155**, 209–220.

Scott, P. A., Goles, R. W., and Peters, R. D. (1985) *Technology of off-gas treatment for liquid-fed ceramic melters* PNL-5446 UC-70, Pacific Northwest National Laboratory, Richland, WA.

Sengupta, P., Mittra, J., and Kale, G. B. (2006) *Interaction between borosilicate melt and Inconel* J. Nucl. Mater. **350**, 66–73.

Shanggeng, L., Yaozhong, J., and Delu, L. (1990) *Devitrification behavior of GC-12/9B HLW-glass* Waste Manag. **10**, 23–27.

Shannon, R. D. (1976) *Revised effective ionic radii and systematic studies of interatomic distances in halides and chalcogenides* Acta Cryst. A **32** (5), 751–767.

Shelby, J. E. (1997) *Introduction to Glass Science and Technology* The Royal Society of Chemistry, Cambridge.

Sheng, J., Luo, S., and Tang, B. (1999) *The leaching behavior of borate waste glass SL-1* Waste Manag. **19**, 401–407.

Shi, F., Meng, J., and Ren, Y. (1995) *Preparation structure and physical properties of new silver lanthanide molybdenum oxides [$AgLnMo_2O_8$ (Ln = La–Nd and Sm)]* Mater. Res. Bull. **30** (11), 1401–1405.

Short, R. (2004) *Incorporation of Molybdenum in Nuclear Waste Glasses* Ph.D. Thesis, Department of Engineering Materials, University of Sheffield.

Short, R. J., Hand, R. J., Hyatt, N. C., and Möbus, G. (2005) *Environment and oxidation state of molybdenum in simulated high level nuclear waste glass compositions* J. Nucl. Mater. **340**, 179–186.

Sickafus, K. E., Minervini, L., Grimes, R. W., Valdez, J. A., Ishimaru, M., Li, F., McClellan, K. J., and Hartmann, T. (2000) *Radiation tolerance of complex oxides* Science **289**, 748–751.

Simonnet, C., and Grandjean, A. (2005) *Mixed ionic and electronic conductivity of $RuO_2$–glass composites from molten state to glassy state* J. Non-Cryst. Solids **351**, 1611–1618.

Sinclair, R. N., Desa, J. A. E., and Wright, A. C. (1983) *Neutron scattering studies of vitrified radioactive waste* J. Am. Ceram. Soc. **66** (1), 72–77.

Smith, M. E., and Bickford, D. F. (2000) *The behavior and effects of the noble metals in the integrated DWPF melter system* Ceram. Trans. **107**, 363–371.

Smith, M. E., Miller, D. H., and Lorier, T. H. (2004) *The impact of feed preparation acid stoichiometry and redox on melt rate for the SB3-frit 418 feed system* WSRC-TR-2004-00350, Savannah River National Laboratory, Aiken, SC.

Spilman, D. B., Hench, L. L., and Clark, D. E. (1986) *Devitrification and subsequent effects on the leach behavior of a simulated borosilicate nuclear waste glass* Nucl. Chem. Waste Manag. **6**, 107–119.

Sproull, J. F., Marra, S. L., and Jantzen, C. M. (1994) *High level radioactive waste glass production and product description* Mater. Res. Soc. Symp. Proc. **333**, 15–25.

Sullivan, G. K., Langowski, M. H., and Hrma, P. (1995) *Sulfate segregation in vitrification of simulated Hanford nuclear waste* Ceram. Trans. **61**, 187–193.

Sun, K., Wang, L. M., Ewing, R. C., and Weber, W. J. (2004) *Electron irradiation induced phase separation in a sodium borosilicate glass* Nucl. Instrum. Meth. Phys. Res. B **218**, 368–374.

Sundaram, S. K., and Perez, J. M. (2000) *Noble metals and spinel settling in high level waste glass melters* PNNL-13347, Pacific Northwest National Laboratory, Richland, WA.

Swainson, I. P., and Dove, M. T. (1995) *On the thermal expansion of β-cristobalite* Phys. Chem. Minerals **22** (1), 61–65.

Taylor, D. (1984) *Thermal expansion data: II. Binary oxides with the fluorite and rutile structures, $MO_2$, and the antifluorite structure $M_2O$* Trans. J. Br. Ceram. Soc. **83** (2), 32–37.

Teller, R. G. (1992) *Refinement of some $Na_{0.5-x}M'_{0.5+x/3}\square_{2x/3}MoO_4$, M = Bi, Ce, La, scheelite structures with powder neutron and X-ray diffraction data* Acta Cryst. C **48**, 2101–2104.

Tilquin, J.-Y., Duveiller, P., Glibert, J., and Claes, P. (1998) *Comparison between high temperature UV-visible spectroscopy and electrochemistry for the in situ study of redox equilibria in glass-forming melts* J. Non-Cryst. Solids **224**, 216–224.

Tomozawa, M. (1999) *A source of the immiscibility controversy of borate and borosilicate glass systems* J. Am. Ceram. Soc. **82** (1), 206–208.

Trocellier, P. (2001) *Chemical durability of high level nuclear waste forms* Ann. Chim. Sci. Mat. **26** (2), 113–130.

Trocellier, P., Djanarthany, S., Chêne, J., Haddi, A., Brass, A. M., Poissonnet, S., and Farges, F. (2005) *Chemical durability of alkali-borosilicate glasses studied by analytical SEM, IBA, isotopic-tracing and SIMS* Nucl. Instrum. Meth. Phys. Res. B **240**, 337–344.

Turcotte, R. P., Wald, J. W., and May, R. P. (1980) *Devitrification of nuclear waste glasses* in 'Scientific Basis for Nuclear Waste Management II' ed. Northrup, C. J. M., Plenum Press, New York, 141–146.

Turcotte, R. P., Wald, J. W., Roberts, F. P., Rusin, J. M., and Lutze, W. (1982) *Radiation damage in nuclear waste ceramics* J. Am. Ceram. Soc. **65** (12), 589–593.

Vernaz, E., Gin, S., Jégou, C., and Ribet, I. (2001) *Present understanding of R7T7 glass alteration kinetics and their impact on long-term behavior modeling* J. Nucl. Mater. **298**, 27–36.

Vienna, J. D., Hrma, P., and Smith, D. E. (1997) *Isothermal crystallization kinetics in simulated high-level nuclear waste glass* Mater. Res. Soc. Symp. Proc. **465**, 17–24.

Wang, E., Kuang, H., Matlack, K. S., Buechele, A. C., and Fu, S. S. (1994a) *Effect of fluoride on crystallization in high calcium and magnesium glasses* Mater. Res. Soc. Symp. Proc. **333**, 473–479.

Wang, E., Perez-Cardenas, F., Kuang, H., and Buechele, A. C. (1994b) *Liquid-liquid phase separation and phase diagrams of simulated Fernald waste glasses* Mater. Res. Soc. Symp. Proc. **333**, 481–486.

Wang, Y., Ma, J., Tao, J., Zhu, X., Zhou, J., Zhao, Z., Xie, L., and Tian, H. (2007) *Low temperature synthesis of $CaMoO_4$ nanoparticles* Ceram. Int. **33** (4), 693–695.

Weber, W. J., Ewing, R. C., Angell, C. A., Arnold, G. W., Cormack, A. N., Delaye, J. M., Griscom, D. L., Hobbs, L. W., Navrotsky, A., Price, D. L., Stoneham, A. M., and Weinberg, M. C. (1997) *Radiation effects in glasses used for immobilization of high level waste and plutonium disposition* J. Mater. Res. **12** (8), 1946–1978.

Webmineral (2006) *Mineralogy database* (http://www.webmineral.com).

Werme, L., Björner, I. K., Bart, G., Zwicky, H. U., Grambow, B., Lutze, W., Ewing, R. C., and Magrabi, C. (1990) *Chemical corrosion of highly radioactive borosilicate nuclear waste glass under simulated repository conditions* J. Mater. Res. **5** (5), 1130–1146.

Wescott, R. I., and Slate, S. C. (1981) *Vitrification of high-level wastes: a review of the computer thermal analyses for storage canisters* Nucl. Eng. Des. **67**, 447–458.

White, W. B. (1992) *Theory of corrosion of glass and ceramics* in 'Corrosion of Glass, Ceramics and Ceramic Superconductors' eds. Clark, D. E., and Zoitos, B. K., Noyes Publications, New Jersey, 2–28.

Wicks, G. G. (1986) *Nuclear waste vitrification – the geology connection* J. Non-Cryst. Solids **84**, 241–250.

Wicks, G. G. (1992) *Nuclear waste glasses: corrosion behavior and field tests* in 'Corrosion of Glass, Ceramics and Ceramic Superconductors' eds. Clark, D. E., and Zoitos, B. K., Noyes Publications, New Jersey, 218–268.

Williams, D. B., and Carter, C. B. (1996) *Transmission Electron Microscopy* Plenum Press, New York.

Wright, A. C., Shakhmatkin, B. A., and Vedishcheva, N. M. (2001) *The chemical structure of oxide glasses: a concept consistent with neutron scattering studies?* Glass Phys. Chem. **27** (2), 97–113.

Yamashita, M., Yamanaka, H., and Sasage, K.-I. (2004) *Dissolution and separation of ruthenium in borosilicate glass* J. Am. Ceram. Soc. **87** (5), 967–969.

Yan, Q., Buechele, A. C., Hu, S., Wang, E., and Fu, S. S. (1995) *Effect of crystallization on the durability of mixed waste glasses* Ceram. Trans. **61**, 167–176.

Yashima, M., Hirose, T., Katano, S., Suzuki, Y., Kakihana, M., and Yoshimura, M. (1995) *Structural changes of $ZrO_2$-$CeO_2$ solid solutions around the monoclinic-tetragonal phase boundary* Phys. Rev. B **51** (13), 8018–8025.

Yazawa, T., Kuraoka, K., Akai, T., Umesaki, N., and Du, W.-F. (2000) *Clarification of phase separation mechanism of sodium borosilicate glasses in early stage by nuclear magnetic resonance* J. Phys. Chem. B **104** (9), 2109–2116.

Zhao, D., Li, L., Davis, L. L., Weber, W. J., and Ewing, R. C. (2001) *Gadolinium borosilicate glass-bonded Gd-silicate apatite: a glass-ceramic nuclear waste form for actinides* Mater. Res. Soc. Symp. Proc. **663**, 199–206.

Zhu, B.-F., Clark, D. E., Hench, L. L., and Wicks, G. G. (1986) *Leaching behavior of nuclear waste glass heterogeneities* J. Non-Cryst. Solids **80**, 324–334.

# Appendix

**Table A.1** Chemical composition of NIST standard reference material 1412*. Values given in parentheses are not certified and are for information only.

| Component | Weight % | Component | Weight % | Component | Weight % |
|---|---|---|---|---|---|
| $Al_2O_3$ | 7.52 | $Fe_2O_3$ | (0.031) | PbO | 4.40 |
| $B_2O_3$ | 4.53 | $K_2O$ | 4.14 | $SiO_2$ | 42.38 |
| BaO | 4.67 | $Li_2O$ | (4.50) | SrO | 4.55 |
| CaO | 4.53 | MgO | (4.69) | ZnO | 4.48 |
| CdO | 4.38 | $Na_2O$ | 4.69 | **Total** | **(99.491)** |

* (https://srmors.nist.gov/certificates/view_cert2gif.cfm?certificate=1412)

**Table A.2** Chemical composition of LRM glass (adapted from Ebert and Wolf, 2000). '—' indicates value not reported, total added for information only.

| Component | Weight % | Component | Weight % | Component | Weight % |
|---|---|---|---|---|---|
| $Al_2O_3$ | 9.51 | HgO | — | NiO | 0.19 |
| $B_2O_3$ | 7.85 | I | — | $P_2O_5$ | 0.54 |
| BaO | — | $K_2O$ | 1.48 | PbO | 0.10 |
| CaO | 0.54 | $La_2O_3$ | 0.02 | $SO_3$ | 0.30 |
| CdO | 0.16 | $Li_2O$ | 0.11 | $SiO_2$ | 54.20 |
| Cl | — | MgO | 0.10 | $SnO_2$ | — |
| $Cr_2O_3$ | 0.19 | MnO | 0.08 | $TiO_2$ | 0.10 |
| F | 0.86 | $MoO_3$ | 0.10 | $ZrO_2$ | 0.93 |
| $Fe_2O_3$ | 1.38 | $Na_2O$ | 20.03 | **Total** | **98.77** |

**Table A.3** Raw concentration (mean) of element *i* (mg $l^{-1}$) in Blend AC leachate at each sampling during modified PCT-B (standard deviation (1$\sigma$) given in parentheses). '<DL' indicates concentration below detection limit.

| Element | Time (days) | | | | |
|---|---|---|---|---|---|
| | 1 | 3 | 7 | 14 | 28 |
| Al | <DL | 1.52 (± 0.04) | 1.80 (± 0.09) | 2.91 (± 0.06) | 2.24 (± 0.04) |
| B | 225.03 (± 0.76) | 519.28 (± 1.03) | 686.50 (± 7.01) | 743.33 (± 0.93) | 796.19 (± 1.39) |
| Ba | <DL | <DL | <DL | <DL | <DL |
| Cr | 1.06 (± 0.04) | 3.06 (± 0.04) | 3.87 (± 0.05) | 4.04 (± 0.02) | 4.22 (± 0.01) |
| K | 2.65 (± 0.07) | 5.62 (± 0.04) | 6.16 (± 0.13) | 7.91 (± 0.14) | 8.48 (± 0.12) |
| Li | 78.00 (± 0.59) | 199.71 (± 0.09) | 258.46 (± 1.53) | 281.55 (± 0.43) | 271.95 (± 3.04) |
| Mo | 78.12 (± 0.07) | 200.63 (± 0.26) | 268.31 (± 1.58) | 262.76 (± 1.48) | 283.53 (± 2.77) |
| Na | 190.73 (± 1.19) | 431.48 (± 3.04) | 568.46 (± 1.72) | 579.60 (± 1.30) | 652.97 (± 0.36) |
| Nd | <DL | <DL | <DL | <DL | <DL |
| Si | 114.33 (± 0.96) | 231.39 (± 0.95) | 228.70 (± 2.02) | 253.50 (± 1.23) | 254.97 (± 2.15) |
| Sr | <DL | 0.13 (± <0.01) | 0.16 (± 0.00) | 0.16 (± 0.00) | 0.16 (± 0.00) |

**Table A.4** Corrected concentration of element *i* (mg $l^{-1}$) in Blend AC leachate at each sampling during modified PCT-B.

| Element | Time (days) | | | | |
|---|---|---|---|---|---|
| | 1 | 3 | 7 | 14 | 28 |
| Al | — | 1.52 | 1.95 | 3.24 | 2.86 |
| B | 225.03 | 541.79 | 760.93 | 886.41 | 1013.61 |
| Ba | — | — | — | — | — |
| Cr | 1.06 | 3.16 | 4.28 | 4.84 | 5.42 |
| K | 2.65 | 5.89 | 6.99 | 9.35 | 10.71 |
| Li | 78.00 | 207.51 | 286.23 | 335.17 | 353.72 |
| Mo | 78.12 | 208.44 | 296.19 | 317.46 | 364.51 |
| Na | 190.73 | 450.56 | 630.68 | 698.67 | 829.99 |
| Nd | — | — | — | — | — |
| Si | 114.33 | 242.83 | 263.27 | 310.95 | 337.77 |
| Sr | — | 0.13 | 0.17 | 0.19 | 0.20 |

**Table A.5** Raw concentration (mean) of element *i* (mg $l^{-1}$) in Oxide AC leachate at each sampling during modified PCT-B (standard deviation (1$\sigma$) given in parentheses). '<DL' indicates concentration below detection limit.

| Element | Time (days) | | | | |
|---|---|---|---|---|---|
| | 1 | 3 | 7 | 14 | 28 |
| Al | <DL | 1.37 (± 0.10) | 1.39 (± 0.01) | 1.52 (± 0.04) | 1.72 (± 0.17) |
| B | 339.15 (± 1.73) | 661.89 (± 9.25) | 827.35 (± 1.68) | 950.07 (± 3.76) | 1047.70 (± 4.94) |
| Ba | <DL | 0.06 (± <0.01) | 0.07 (± 0.00) | 0.05 (± 0.00) | 0.05 (± 0.01) |
| Cr | 0.26 (± <0.01) | 0.57 (± 0.02) | 0.71 (± 0.04) | 0.90 (± 0.02) | 0.94 (± 0.03) |
| K | <DL | <DL | <DL | <DL | <DL |
| Li | 102.58 (± 0.85) | 220.53 (± 1.08) | 270.76 (± 0.75) | 324.90 (± 4.09) | 331.32 (± 2.37) |
| Mo | 91.01 (± 0.16) | 173.58 (± 0.18) | 208.23 (± 1.23) | 194.68 (± 2.99) | 190.84 (± 0.80) |
| Na | 306.68 (± 1.08) | 589.36 (± 3.68) | 707.70 (± 4.24) | 789.77 (± 2.39) | 949.89 (± 1.24) |
| Nd | <DL | <DL | <DL | <DL | <DL |
| Si | 194.03 (± 1.56) | 413.64 (± 1.16) | 401.71 (± 5.27) | 474.87 (± 2.31) | 474.04 (± 0.51) |
| Sr | <DL | 0.16 (± <0.01) | 0.15 (± <0.01) | 0.10 (± 0.00) | <DL |

**Table A.6** Corrected concentration of element *i* (mg $l^{-1}$) in Oxide AC leachate at each sampling during modified PCT-B.

| Element | Time (days) | | | | |
|---|---|---|---|---|---|
| | 1 | 3 | 7 | 14 | 28 |
| Al | — | 1.37 | 1.52 | 1.80 | 2.15 |
| B | 339.15 | 695.81 | 927.46 | 1132.91 | 1325.55 |
| Ba | — | 0.06 | 0.08 | 0.06 | 0.07 |
| Cr | 0.26 | 0.60 | 0.80 | 1.05 | 1.19 |
| K | — | — | — | — | — |
| Li | 102.58 | 230.79 | 303.07 | 384.29 | 423.19 |
| Mo | 91.01 | 182.68 | 234.69 | 241.96 | 257.59 |
| Na | 306.68 | 620.03 | 797.31 | 950.15 | 1189.24 |
| Nd | — | — | — | — | — |
| Si | 194.03 | 433.04 | 462.48 | 575.81 | 622.47 |
| Sr | — | 0.16 | 0.17 | 0.13 | — |

**Table A.7** Raw concentration (mean) of element *i* (mg $l^{-1}$) in Blend HT leachate at each sampling during modified PCT-B (standard deviation ($1\sigma$) given in parentheses). '<DL' indicates concentration below detection limit.

| Element | Time (days) | | | | |
|---|---|---|---|---|---|
| | 1 | 3 | 7 | 14 | 28 |
| Al | <DL | 1.09 (± 0.05) | 1.75 (± 0.01) | 2.65 (± 0.19) | 1.98 (± 0.04) |
| B | 241.97 (± 1.72) | 565.15 (± 2.43) | 682.24 (± 1.41) | 694.08 (± 1.53) | 741.15 (± 6.60) |
| Ba | <DL | <DL | <DL | <DL | <DL |
| Cr | 1.31 (± 0.06) | 3.37 (± 0.02) | 4.22 (± 0.04) | 4.26 (± 0.02) | 4.18 (± 0.09) |
| K | 2.69 (± 0.08) | 5.40 (± 0.11) | 6.53 (± 0.10) | 8.05 (± 0.10) | 6.88 (± 0.06) |
| Li | 93.39 (± 0.29) | 205.01 (± 2.56) | 253.48 (± 1.86) | 256.77 (± 2.41) | 245.38 (± 1.65) |
| Mo | 88.38 (± 1.41) | 192.29 (± 0.64) | 251.76 (± 2.03) | 234.05 (± 2.60) | 246.56 (± 3.01) |
| Na | 213.65 (± 1.96) | 442.34 (± 9.28) | 542.54 (± 0.54) | 536.32 (± 1.35) | 572.18 (± 4.84) |
| Nd | <DL | <DL | <DL | <DL | <DL |
| Si | 174.09 (± 0.30) | 237.51 (± 1.55) | 240.13 (± 3.07) | 227.68 (± 1.69) | 227.09 (± 0.97) |
| Sr | 0.07 (± 0.00) | 0.13 (± <0.01) | 0.16 (± 0.00) | 0.15 (± 0.00) | 0.15 (± <0.01) |

**Table A.8** Corrected concentration of element *i* (mg $l^{-1}$) in Blend HT leachate at each sampling during modified PCT-B.

| Element | Time (days) | | | | |
|---|---|---|---|---|---|
| | 1 | 3 | 7 | 14 | 28 |
| Al | — | 1.09 | 1.86 | 2.93 | 2.53 |
| B | 241.97 | 589.35 | 762.95 | 843.01 | 959.49 |
| Ba | — | — | — | — | — |
| Cr | 1.31 | 3.50 | 4.69 | 5.15 | 5.49 |
| K | 2.69 | 5.67 | 7.34 | 9.51 | 9.14 |
| Li | 93.39 | 214.35 | 283.32 | 311.96 | 326.25 |
| Mo | 88.38 | 201.13 | 279.83 | 287.30 | 323.21 |
| Na | 213.65 | 463.70 | 608.14 | 656.17 | 745.66 |
| Nd | — | — | — | — | — |
| Si | 174.09 | 254.92 | 281.29 | 292.86 | 315.03 |
| Sr | 0.07 | 0.14 | 0.18 | 0.19 | 0.20 |

**Table A.9** Raw concentration (mean) of element *i* (mg $l^{-1}$) in Oxide HT leachate at each sampling during modified PCT-B (standard deviation (1$\sigma$) given in parentheses). '<DL' indicates concentration below detection limit.

| Element | Time (days) | | | | |
|---|---|---|---|---|---|
| | 1 | 3 | 7 | 14 | 28 |
| Al | 1.59 (± 0.07) | 1.66 (± 0.07) | 2.77 (± 0.01) | 2.81 (± 0.04) | 3.45 (± 0.09) |
| B | 1245.50 (± 8.64) | 1737.93 (± 13.24) | 2288.90 (± 5.53) | 2329.00 (± 27.55) | 2433.33 (± 5.54) |
| Ba | 0.12 (± <0.01) | 0.15 (± <0.01) | 0.19 (± 0.00) | 0.15 (± <0.01) | 0.19 (± 0.03) |
| Cr | 2.07 (± 0.02) | 2.95 (± 0.04) | 3.56 (± 0.04) | 3.72 (± 0.03) | 3.62 (± 0.01) |
| K | <DL | <DL | <DL | 2.46 (± 0.17) | 2.42 (± 0.11) |
| Li | 409.96 (± 1.94) | 547.07 (± 3.91) | 732.18 (± 11.03) | 834.50 (± 0.97) | 788.50 (± 0.93) |
| Mo | 242.36 (± 0.76) | 302.72 (± 2.11) | 379.50 (± 0.76) | 346.51 (± 1.82) | 371.77 (± 1.38) |
| Na | 1042.40 (± 8.10) | 1407.20 (± 4.41) | 1781.77 (± 8.96) | 1814.47 (± 6.63) | 1889.27 (± 11.73) |
| Nd | 0.91 (± 0.00) | 0.93 (± <0.01) | 0.87 (± 0.02) | <DL | <DL |
| Si | 421.64 (± 1.79) | 503.35 (± 1.23) | 584.50 (± 0.44) | 615.89 (± 1.13) | 620.89 (± 1.50) |
| Sr | 0.19 (± <0.01) | 0.22 (± <0.01) | 0.24 (± 0.00) | 0.20 (± <0.01) | 0.18 (± 0.00) |

**Table A.10** Corrected concentration of element *i* (mg $l^{-1}$) in Oxide HT leachate at each sampling during modified PCT-B.

| Element | Time (days) | | | | |
|---|---|---|---|---|---|
| | 1 | 3 | 7 | 14 | 28 |
| Al | 1.59 | 1.82 | 3.09 | 3.41 | 4.34 |
| B | 1245.50 | 1862.48 | 2587.24 | 2856.23 | 3193.47 |
| Ba | 0.12 | 0.17 | 0.22 | 0.20 | 0.25 |
| Cr | 2.07 | 3.16 | 4.06 | 4.57 | 4.85 |
| K | — | — | — | 2.46 | 2.66 |
| Li | 409.96 | 588.07 | 827.89 | 1003.42 | 1040.87 |
| Mo | 242.36 | 326.96 | 434.01 | 438.97 | 498.88 |
| Na | 1042.40 | 1511.44 | 2026.73 | 2237.60 | 2493.85 |
| Nd | 0.91 | 1.02 | 1.05 | — | — |
| Si | 421.64 | 545.51 | 677.00 | 766.84 | 833.43 |
| Sr | 0.19 | 0.24 | 0.28 | 0.26 | 0.27 |

**Table A.11** Raw concentration (mean) of element *i* (mg $l^{-1}$) in LRM leachate at each sampling during modified PCT-B (standard deviation (1$\sigma$) given in parentheses). '<DL' indicates concentration below detection limit.

| Element | Time (days) | | | | |
|---|---|---|---|---|---|
| | 1 | 3 | 7 | 14 | 28 |
| Al | 6.50 (± 0.05) | 11.20 (± 0.25) | 13.78 (± 0.19) | 15.35 (± 0.15) | 16.23 (± 0.44) |
| B | 7.75 (± 0.22) | 18.38 (± 0.27) | 30.44 (± 0.24) | 39.33 (± 0.33) | 60.55 (± 0.19) |
| Ca | 0.09 (± 0.00) | 0.12 (± 0.01) | 0.11 (± <0.01) | 0.13 (± <0.01) | 0.10 (± <0.01) |
| Cr | <DL | 0.29 (± 0.06) | 0.49 (± 0.03) | 0.34 (± 0.01) | 0.55 (± 0.02) |
| Fe | <DL | 1.85 (± 0.07) | 2.43 (± 0.08) | 2.59 (± 0.20) | 3.25 (± 0.15) |
| K | 1.91 (± 0.09) | 3.31 (± 0.24) | 4.56 (± 0.03) | 6.33 (± 0.11) | 7.07 (± 0.04) |
| Na | 54.59 (± 0.29) | 109.25 (± 0.98) | 173.83 (± 0.36) | 208.73 (± 1.95) | 267.23 (± 1.88) |
| Ni | <DL | <DL | <DL | <DL | 0.95 (± 0.04) |
| Si | 46.05 (± 0.62) | 72.39 (± 1.48) | 83.50 (± 0.10) | 87.93 (± 0.26) | 96.21 (± 1.03) |
| Zr | <DL | 1.16 (± 0.02) | 1.67 (± 0.04) | 1.73 (± 0.05) | 1.90 (± 0.05) |

**Table A.12** Leachate pH (mean) at each sampling during modified PCT-B (standard deviation (1$\sigma$) given in parentheses).

| Glass | Time (days) | | | | |
|---|---|---|---|---|---|
| | 1 | 3 | 7 | 14 | 28 |
| Blend AC | 9.80 (± <0.01) | 9.82 (± <0.01) | 9.84 (± <0.01) | 9.89 (± <0.01) | 9.87 (± <0.01) |
| Oxide AC | 9.75 (± <0.01) | 9.80 (± <0.01) | 9.85 (± <0.01) | 9.88 (± <0.01) | 9.88 (± 0.01) |
| Blend HT | 9.80 (± <0.01) | 9.82 (± <0.01) | 9.85 (± <0.01) | 9.89 (± <0.01) | 9.88 (± 0.01) |
| Oxide HT | 9.85 (± <0.01) | 9.90 (± <0.01) | 9.95 (± <0.01) | 9.98 (± <0.01) | 9.98 (± <0.01) |
| LRM | 10.28 (± <0.01) | 10.67 (± 0.01) | 11.03 (± <0.01) | 11.11 (± <0.01) | 11.23 (± 0.01) |
| 'blanks' | 6.13 (± 0.01) | 6.12 (± 0.01) | 6.11 (± 0.01) | 6.09 (± 0.01) | 6.07 (± 0.01) |